OPTIMIZATION AND THERMAL PERFORMANCE ANALYSIS OF SUPERCRITICAL CARBON DIOXIDE BRAYTON CYCLES DRIVEN BY SOLAR THERMAL POWER TOWER SYSTEMS

BY

MAIMOON ATIF

A Thesis Presented to the
DEANSHIP OF GRADUATE STUDIES

KING FAHD UNIVERSITY OF PETROLEUM & MINERALS

DHAHRAN, SAUDI ARABIA

In Partial Fulfillment of the
Requirements for the Degree of

MASTER OF SCIENCE

In

MECHANICAL ENGINEERING

OCTOBER 2014

KING FAHD UNIVERSITY OF PETROLEUM & MINERALS
DHAHRAN- 31261, SAUDI ARABIA
DEANSHIP OF GRADUATE STUDIES

This thesis, written by **MAIMOON ATIF** under the direction of his thesis advisor and approved by his thesis committee, has been presented and accepted by the Dean of Graduate Studies, in partial fulfillment of the requirements for the degree of **MASTER OF SCIENCE IN MECHANICAL ENGINEERING.**

Dr. Fahad A. Al-Sulaiman
(Advisor)

Dr. Zuhair Mattoug Gasem
Department Chairman

Dr. Esmail M. A. Mokheimer
(Member)

Dr. Salam A. Zummo
Dean of Graduate Studies

Dr. Haitham M. S. Bahaidarah
(Member)

11/2/15

Date

To my late mathematics’ teacher, Khawaja Abdul Qadeer, who always believed in me

To my Father and Mother, without their prayers and moral support I would not have been able to come this far

To my Wife, for her continuous encouragement

To my younger brothers, Saadoon and Haroon, for their support and backing

To my teachers, for their guidance and counsel

To my friends, for being the source of motivation

ACKNOWLEDGMENTS

In the Name of Allah, the Most Beneficent, the Most Merciful

“*Indeed, in the creation of the heavens and the earth and the alteration of the night and the day are signs for those of understanding*.” Al-Qur’an (3:190)

All praise and glory to Allah, the Almighty, the Creator, who gave me the strength, the patience, the aptitude; without whose help, I would not have been able to complete this work.

I acknowledge, the support, the assistance, the time, and the guidance provided to me at every step of my research work by my advisor Dr. Fahad A. Al-Sulaiman. I would also like to thank him for supporting me through all the work, for providing helpful comments and for being a source of inspiration for me. I am especially thankful to my thesis committee members Dr. Esmail M. A. Mokheimer and Dr. Haitham M. S. Bahaidarah for their review of the thesis and the useful comments on the research conducted.

During this course of work and study, my parents were a constant source of motivation and support for me. Their prayers and love helped me to achieve this milestone. Special thanks are owed to my wife who supported me in numerous ways throughout my MSc study.

I would also like to acknowledge the support of King Fahd University of Petroleum & Minerals (KFUPM), Dhahran, Saudi Arabia, for this work through project # SB121010.

I am very grateful to Mr. M. Usama Siddiqui and Mr. M. Waqar Ahmed for helping me out with MATLAB whenever I needed their assistance. I am also thankful to Mr. Amine Kouta for his help and suggestions regarding the thermal storage modeling. Special thanks to Mr. Furqan Tahir, Mr. Binash Imtiyaz, Mr. Ahmer Ali Bozdar Baloch, Dr. Haider Ali and Mr. Yasir Jamil for their support during my Master's course. I also appreciate the guidance of my senior post graduate colleagues Mr. Bilal Tanweer, Mr. Adnan Saeed, Mr. Khalid Naseem, Mr. Osama Hassan, Mr. Waqas Akram, Mr. Sheraz Khalid and Mr. Waqas Khalid. I would also like to thank my friends Mr. Mohsin Attiq and Mr. Talha Hussam Qureshi for their support and encouragement. Thanks to all my colleagues in the University for making my time in the university memorable.

TABLE OF CONTENTS

ACKNOWLEDGMENTS V

TABLE OF CONTENTS VII

LIST OF TABLES X

LIST OF FIGURES XI

LIST OF ABBREVIATIONS XXII

ABSTRACT XXIV

ملخص الرسالة XXVI

CHAPTER 1 INTRODUCTION 1

1.1 Concentrating solar power (CSP) technologies 2

1.2 Current technologies for CSP power production plants 2
  1.2.1 Linear Fresnel reflectors 3
  1.2.2 Parabolic trough 4
  1.2.3 Solar dish 5
  1.2.4 Solar tower 5

1.3 Comparison of CSP technologies 9

1.4 Thermal storage 10

1.5 Motivation and significance 12

1.6 Objectives of the current study 14

CHAPTER 2 LITERATURE REVIEW 15

2.1 Central receiver and heliostat field layout 15

2.2 Supercritical CO_2 thermodynamic cycles 23

2.3 Thermal energy storage 26

2.4 Summary 32

CHAPTER 3 MATHEMATICAL MODELING 33

3.1 Generating a preliminary heliostat field 34
3.1.1 The characteristic diameter 34
3.1.2 The radial spacing 36
3.1.3 The azimuthal spacing 38
3.1.4 Number of rows 38
3.1.5 Number of heliostats 39
3.1.6 Radius of the first ring of the zones 41
3.1.7 Land area covered by the heliostat field 41

3.2 Solar positioning model 41

3.3 Optical efficiency of the heliostat field 42
3.3.1 Cosine factor 42
3.3.2 Atmospheric attenuation factor 43
3.3.3 Shadowing and blocking factor 43
3.3.4 Intercept factor 47

3.4 Optimization 49
3.4.1 Differential evolution (DE) algorithm 49
3.4.2 Daily averaged annual optimization 54
3.4.3 Insolation weighted daily averaged annual optimization 54
3.4.4 Monthly averaged annual optimization 55

3.5 Central receiver 56
3.5.1 Radiation heat losses 56
3.5.2 Convection heat losses 56
3.5.3 Receiver thermal efficiency 57

3.6 Supercritical CO_2 Brayton cycle modeling 58
3.6.1 Simple closed loop sCO_2 Brayton cycle 58
3.6.2 Regenerative closed loop sCO_2 Brayton cycle 59
3.6.3 Pre-compression closed loop Brayton cycle 61
3.6.4 Re-compression closed loop Brayton cycle 63
3.6.5 Split expansion closed loop Brayton cycle 65
3.6.6 Thermal efficiency of the Brayton cycles 68
3.6.7 Validation of sCO_2 modeling 68

3.7 Thermal efficiency of the integrated system 69

3.8 Thermal storage 69
3.8.1 Hot storage tank 70
3.8.2 Cold storage tank 70
3.8.3 Storage heat exchanger 71

CHAPTER 4 RESULTS AND DISCUSSION..73

4.1 Optimization of heliostat field layout.. 73
4.1.1 Optimization of heliostat field using one and two variables...73
4.1.2 Optimization of heliostat field using four variables 82
4.1.3 Optimization of normalized ratio of optical performance to the land area covered by the heliostat field...99
4.1.4 Annual Optimization of heliostat field 114

4.2 Central receiver.. 123

4.3 Supercritical CO_2 Brayton cycles.. 128
4.3.1 Simple closed loop sCO_2 Brayton cycle 142
4.3.2 Regenerative closed loop sCO_2 Brayton cycle 145
4.3.3 Pre-compression closed loop sCO_2 Brayton cycle 148
4.3.4 Re-compression closed loop sCO_2 Brayton cycle 151
4.3.5 Split expansion closed loop sCO_2 Brayton cycle 154

4.4 sCO_2 recompression Brayton cycles for different locations in Saudi Arabia 157

4.5 sCO_2 Brayton cycle integrated with two tank thermal storage 171

CHAPTER 5 CONCLUSIONS AND RECOMMENDATIONS 183

5.1 Conclusions... 183

5.2 Recommendations 186

NOMENCLATURE 187
List of Greek symbols...190

REFERENCES... 193

VITAE 202

LIST OF TABLES

Table 1.1 The four CSP technologies [1] 3

Table 1.2 Specifications of the four main CSP technologies [12] 8

Table 3.1 Validation of the calculation of the shadowing and blocking factor 46

Table 3.2 Recommended average days of month [84,97] 56

Table 4.1 Basic design and operating parameters of the heliostat field [41,102] 78

Table 4.2 Optimization results of single and two variable optimization 78

Table 4.3 Optimization results of four variable optimization 88

Table 4.4 Computation configuration of the optimization 89

Table 4.5 Optimization results using four variables for optimizing the normalized ratio 104

Table 4.6 Computation costs of the optimization 105

Table 4.7 Optimization results of heliostat field on annual basis with considering the extra security distance 118

Table 4.8 Optimization results of the heliostat field on monthly averaged annual basis with *dsep=0* 118

Table 4.9 Basic design and operating parameters used for the heliostat field and the central receiver [17,42,102] 133

Table 4.10 Basic design and operating parameters used for the sCO_2 Brayton cycles .. 133

Table 4.11 Performance comparison of different locations of Saudi Arabia 161

LIST OF FIGURES

Figure 3.1 Fundamental definitions of the heliostat field 34

Figure 3.2 Vertical and horizaontal clearanaces 36

Figure 3.3 Fundamental definitions of the central receiver 37

Figure 3.4 Projection following $-\hat{t}\,(-\hat{d}_{rec})$ for parallel planes [87]................................. 44

Figure 3.5 Flow chart summarizing the procedure of differential evolution 51

Figure 3.6 Crossover operation 53

Figure 3.7 Simple closed loop supercritical carbon dioxide Brayton cycle 59

Figure 3.8 Regenerative closed loop supercritical carbon dioxide Brayton cycle 61

Figure 3.9 Pre-compression closed loop supercritical carbon dioxide Brayton cycle 63

Figure 3.10 Re-compression closed loop supercritical carbon dioxide Brayton cycle 65

Figure 3.11 Split Expansion closed loop supercritical carbon dioxide Brayton cycle 67

Figure 3.12 A re-compression closed loop sCO_2 Brayton cycle (Figure 2 of reference [100]) 68

Figure 3.13 Temperature (T) – entropy (s) diagram for validation with figure 2 of reference [100] 69

Figure 3.14 Two tank molten salt thermal storage integrated with the central receiver... 71

Figure 4.1 Contours of the optical efficiency of the un-optimized heliostat field for 21st December, solar time 8:00 a.m. 79

Figure 4.2 Contours of the optical efficiency of the optimized heliostat field for 21st December, solar time 8:00 a.m. with x_1 = 14.3803 (Case 1) 79

Figure 4.3 Contours of the optical efficiency of the optimized heliostat field for 21st December, solar time 8:00 a.m. with x_1 =0 and x_2 = 2.1838 (Case 2 and Case 3) 80

Figure 4.4 Contours of the optical efficiency of the un-optimized heliostat field for 21st June, solar noon 80

Figure 4.5 Contours of the optical efficiency of the optimized heliostat field for 21st June, solar noon with x_1 = 2.87633 (Case 2) 81

Figure 4.6 Contours of the optical efficiency of the optimized heliostat field for 21st June, solar noon with x_1 = 0 and x_2 = 1.2744 (Case 2 and Case 3) 81

Figure 4.7 Contours of the shadowing and blocking factor of the un-optimized heliostat field for 21st December, solar time 8:00 a.m. 89

Figure 4.8 Contours of the intercept factor of the un-optimized heliostat field for 21st December, solar time 8:00 a.m. 90

Figure 4.9 Contours of the optical efficiency of the un-optimized heliostat field for 21st December, solar time 8:00 a.m. 90

Figure 4.10 Contours of the shadowing and blocking factor of the optimized heliostat field for 21st December, solar time 8:00 a.m. (Case 1) 91

Figure 4.11 Contours of the intercept factor of the optimized heliostat field for 21st December, solar time 8:00 a.m. (Case 1) 91

Figure 4.12 Contours of the optical efficiency of the optimized heliostat field for 21st December, solar time 8:00 a.m. (Case 1) 92

Figure 4.13 Contours of the shadowing and blocking factor of the optimized heliostat field for 21st December, solar time 8:00 a.m. (Case 2) 92

Figure 4.14 Contours of the intercept factor of the optimized heliostat field for 21st December, solar time 8:00 a.m. (Case 2) 93

Figure 4.15 Contours of the optical efficiency of the optimized heliostat field for 21st December, solar time 8:00 a.m. (Case 2) 93

Figure 4.16 A zoomed view of the contours of the optical efficiency of the optimized heliostat field of first two zones for 21st December, solar time 8:00 a.m. (Case 2).. 94

Figure 4.17 Contours of the optical efficiency of the un-optimized heliostat field for 21st December, solar time 9:00 a.m.. 94

Figure 4.18 Contours of the optical efficiency of the optimized heliostat field for 21st December, solar time 9:00 a.m. (Case 1) 95

Figure 4.19 Contours of the optical efficiency of the optimized heliostat field for 21st December, solar time 9:00 a.m. (Case 2) 95

Figure 4.20 Contours of the optical efficiency of the un-optimized heliostat field for 21st June, solar noon.. 96

Figure 4.21 Contours of the optical efficiency of the optimized heliostat field for 21st June, solar noon (Case 1) 96

Figure 4.22 Contours of the optical efficiency of the optimized heliostat field for 21st June, solar noon (Case 2) 97

Figure 4.23 Contours of the optical efficiency of the un-optimized heliostat field for 21st March, solar noon.. 97

Figure 4.24 Contours of the optical efficiency of the optimized heliostat field for 21st March, solar noon (Case 1) 98

Figure 4.25 Contours of the optical efficiency of the optimized heliostat field for 21st March, solar noon (Case 2) 98

Figure 4.26 Contours of the optical efficiency of the un-optimized heliostat field with *dsep =0* for 21st December, solar time 9:00 a.m. 105

Figure 4.27 Contours of the optical efficiency of the optimized heliostat field with *dsep =0* for 21st December, solar time 9:00 a.m.(Case 1) 106

Figure 4.28 Contours of the optical efficiency of the optimized heliostat field with *dsep =0* for 21st December, solar time 9:00 a.m.(Case 2) 106

Figure 4.29 Contours of the optical efficiency of the unoptimized heliostat field with *dsep =3* for 21st December, solar time 9:00 a.m.. 107

Figure 4.30 Contours of the optical efficiency of the optimized heliostat field with *dsep =3* for 21st December, solar time 9:00 a.m.(Case 1) 107

Figure 4.31 Contours of the optical efficiency of the optimized heliostat field with *dsep =3* for 21st December, solar time 9:00 a.m.(Case 2) 108

Figure 4.32 Contours of the optical efficiency of the un-optimized heliostat field with *dsep =0* for 21st June, solar noon 108

Figure 4.33 Contours of the optical efficiency of the optimized heliostat field with *dsep =0* for 21st June, solar noon (Case 1) 109

Figure 4.34 Contours of the optical efficiency of the optimized heliostat field with *dsep =0* for 21st June, solar noon (Case 2) 109

Figure 4.35 Contours of the optical efficiency of the un-optimized heliostat field with *dsep =3* for 21st June, solar noon (same as Case 2) 110

Figure 4.36 Contours of the optical efficiency of the optimized heliostat field with *dsep =3* for 21st June, solar noon (Case 1) 110

Figure 4.37 Contours of the optical efficiency of the un-optimized heliostat field with *dsep =0* for 21st March, solar noon 111

Figure 4.38 Contours of the optical efficiency of the optimized heliostat field with *dsep =0* for 21st March, solar noon (Case 1) 111

Figure 4.39 Contours of the optical efficiency of the optimized heliostat field with *dsep =0* for 21st March, solar noon (Case 2) 112

Figure 4.40 Contours of the optical efficiency of the un-optimized heliostat field with *dsep =3* for 21st March, solar noon (same as case 2) 112

Figure 4.41 Contours of the optical efficiency of the optimized heliostat field with *dsep =3* for 21st March, solar noon (Case 1) 113

Figure 4.42 Contours of the optical efficiency of the annually un-optimized heliostat field on daily averaged basis.. 119

Figure 4.43 Contours of the optical efficiency of the annually optimized heliostat field on daily averaged basis... 119

Figure 4.44 Contours of the optical efficiency of the annually un-optimized heliostat field on monthly averaged basis 120

Figure 4.45 Contours of the optical efficiency of the annually optimized heliostat field on monthly averaged basis 120

Figure 4.46 Contours of the optical efficiency of the annually unoptimized heliostat field on monthly averaged basis with *dsep=0* 121

Figure 4.47 Contours of the optical efficiency of the annually optimized heliostat field on monthly averaged basis with *dsep=0* 121

Figure 4.48 Contours of the optical efficiency of the annually un-optimized heliostat field on insolation weighted daily averaged basis 122

Figure 4.49 Contours of the optical efficiency of the annually optimized heliostat field on insolation weighted daily averaged basis 122

Figure 4.50 Net energy gained for 16th March, Dhahran, Saudi Arabia 125

Figure 4.51 Net energy gained for 11th June, Dhahran, Saudi Arabia 125

Figure 4.52 Net energy gained for 10th December, Dhahran, Saudi Arabia 126

Figure 4.53 Optical efficiency of the heliostat field and the net energy gained at the receiver for 16th March, solar noon, Dhahran, Saudi Arabia 126

Figure 4.54 Optical efficiency of the heliostat field and the net energy gained at the receiver for 11th June, solar noon, Dhahran, Saudi Arabia......................... 127

Figure 4.55 Optical efficiency of the heliostat field and the net energy gained at the receiver for 10th December, solar noon, Dhahran, Saudi Arabia 127

Figure 4.56 Contours of the net optical efficiency of the heliostat field at solar noon, March 16, Dhahran, Saudi Arabia 134

Figure 4.57 Contours of the net optical efficiency of the heliostat field at solar noon, June 11, Dhahran, Saudi Arabia 134

Figure 4.58 Contours of the net optical efficiency of the heliostat field at solar noon, December 10, Dhahran, Saudi Arabia 135

Figure 4.59 Comparison of net power output for 16th of March, Dhahran, Saudi Arabia 135

Figure 4.60 Comparison of net power output for 11th of June, Dhahran, Saudi Arabia . 136
Figure 4.61 Comparison of net power output for 10th of December, Dhahran, Saudi Arabia 136
Figure 4.62 Comparison of thermal efficiency for 16th of March, Dhahran, Saudi Arabia 137
Figure 4.63 Comparison of thermal efficiency for 11th of June, Dhahran, Saudi Arabia 137
Figure 4.64 Comparison of thermal efficiency for 10th of December, Dhahran, Saudi Arabia 138
Figure 4.65 Comparison of system efficiency for 16th of March, Dhahran, Saudi Arabia 138
Figure 4.66 Comparison of system efficiency for 11th of June, Dhahran, Saudi Arabia 139
Figure 4.67 Comparison of system efficiency for 10th of December, Dhahran, Saudi Arabia 139
Figure 4.68 Comparison of turbine inlet temperature (TIT) for 16th of March, Dhahran, Saudi Arabia 140
Figure 4.69 Comparison of turbine inlet temperature (TIT) for 11th of June, Dhahran, Saudi Arabia 140
Figure 4.70 Comparison of turbine inlet temperature (TIT) for 10th of December, Dhahran, Saudi Arabia 141
Figure 4.71 Simple sCO_2 cycle's components energy analysis for 16th of March, Dhahran, Saudi Arabia 143
Figure 4.72 Simple sCO_2 cycle's components energy analysis for 11th of June, Dhahran, Saudi Arabia 143

Figure 4.73 Simple sCO_2 cycle's components energy analysis for 10th of December, Dhahran, Saudi Arabia 144

Figure 4.74 Regenerative sCO_2 cycle's components energy analysis for 16th of March, Dhahran, Saudi Arabia 146

Figure 4.75 Regenerative sCO_2 cycle's components energy analysis for 11th of June, Dhahran, Saudi Arabia 146

Figure 4.76 Regenerative sCO_2 cycle's components energy analysis for 10th of December, Dhahran, Saudi Arabia 147

Figure 4.77 Pre-compression sCO_2 cycle's components energy analysis for 16th of March, Dhahran, Saudi Arabia 149

Figure 4.78 Pre-compression sCO_2 cycle's components energy analysis for 11th of June, Dhahran, Saudi Arabia 149

Figure 4.79 Pre-compression sCO_2 cycle's components energy analysis for 10th of December, Dhahran, Saudi Arabia 150

Figure 4.80 Re-compression sCO_2 cycle's components energy analysis for 16th of March, Dhahran, Saudi Arabia 152

Figure 4.81 Re-compression sCO_2 cycle's components energy analysis for 11th of June, Dhahran, Saudi Arabia 152

Figure 4.82 Re-compression sCO_2 cycle's components energy analysis for 10th of December, Dhahran, Saudi Arabia 153

Figure 4.83 Split expansion sCO_2 cycle's components energy analysis for 16th of March, Dhahran, Saudi Arabia 155

Figure 4.84 Split expansion sCO_2 cycle's components energy analysis for 11th of June, Dhahran, Saudi Arabia 155
Figure 4.85 Split expansion sCO_2 cycle's components energy analysis for 10th of December, Dhahran, Saudi Arabia. 156
Figure 4.86 Re-compression closed loop supercritical carbon dioxide Brayton cycle with auxiliary heater. 161
Figure 4.87 Contours of the optical efficiency of the optimized heliostat field on annual basis for Tabouk, Saudi Arabia 162
Figure 4.88 Contours of the optical efficiency of the optimized heliostat field on annual basis for Madinah, Saudi Arabia 162
Figure 4.89 Contours of the optical efficiency of the optimized heliostat field on annual basis for Dhahran, Saudi Arabia 163
Figure 4.90 Contours of the optical efficiency of the optimized heliostat field on annual basis for Riyadh, Saudi Arabia 163
Figure 4.91 Contours of the optical efficiency of the optimized heliostat field on annual basis for Bishah, Saudi Arabia 164
Figure 4.92 Contours of the optical efficiency of the optimized heliostat field on annual basis for Najran, Saudi Arabia 164
Figure 4.93 Average heat collected at the central receiver for Tabouk, Saudi Arabia ... 165
Figure 4.94 Average heat collected at the central receiver for Madinah, Saudi Arabia . 165
Figure 4.95 Average heat collected at the central receiver for Dhahran, Saudi Arabia . 166
Figure 4.96 Average heat collected at the central receiver for Riyadh, Saudi Arabia 166
Figure 4.97 Average heat collected at the central receiver for Bishah, Saudi Arabia 167

Figure 4.98 Average heat collected at the central receiver for Najran, Saudi Arabia 167

Figure 4.99 Percentage of hybridization required for Tabouk, Saudi Arabia................ 168

Figure 4.100 Percentage of hybridization required for Madinah, Saudi Arabia............. 168

Figure 4.101 Percentage of hybridization required for Dhahran, Saudi Arabia 169

Figure 4.102 Percentage of hybridization required for Riyadh, Saudi Arabia 169

Figure 4.103 Percentage of hybridization required for Bishah, Saudi Arabia................ 170

Figure 4.104 Percentage of hybridization required for Najran, Saudi Arabia 170

Figure 4.105 Re-compression closed loop supercritical carbon dioxide Brayton cycle integrated with solar tower through two tank thermal storage 176

Figure 4.106 Net power gained on 11th of June for different storage options 176

Figure 4.107 Net power gained on 11th of June for different storage options 177

Figure 4.108 Net power gained on 10th of December for different storage options 177

Figure 4.109 Mass flow rate of the storage medium through the receiver 178

Figure 4.110 Change in mass of molten salt in the storage tanks with time for whole day operation on 16th of March.. 178

Figure 4.111 Change in mass of molten salt in the storage tanks with time for whole day operation on 11th of June... 179

Figure 4.112 Change in mass of molten salt in the storage tanks with time for whole day operation on 10th of December 179

Figure 4.113 Change in mass of molten salt in the storage tanks with time for daylight hours operation on 16th of March.. 180

Figure 4.114 Change in mass of molten salt in the storage tanks with time for daylight hours operation on 11th of June.. 180

Figure 4.115 Change in mass of molten salt in the storage tanks with time for daylight hours operation on 10th of December.. 181

Figure 4.116 Change in mass of molten salt in the storage tanks with time for sunrise till the end of the day operation on 16th of March.. 181

Figure 4.117 Change in mass of molten salt in the storage tanks with time for sunrise till the end of the day operation on 11th of June... 182

Figure 4.118 Change in mass of molten salt in the storage tanks with time for sunrise till the end of the day on 10th of December... 182

LIST OF ABBREVIATIONS

CPC	:	Compound parabolic collector
CPV	:	Concentrated photovoltaic
CRS	:	Central receiver system
CRS4-2	:	Research software for central receiver solar system simulations
CRT	:	Central receiver technology
CSP	:	Concentrated solar power
DE	:	Differential evolution
HFLD	:	Heliostat field layout design
HFLODE	:	Heliostat field layout optimization using differential evolution
HTF	:	Heat transfer fluid
HTR	:	High temperature regenerator
LCOE	:	Levelized cost of electricity
LFR	:	Linear Fresnel reflectors
LTR	:	Low temperature regenerator

PCM : Phase change material

PDC : Parabolic dish collectors

PTC : Parabolic trough collectors

PV : Photovoltaic

sCO2 : Supercritical carbon dioxide

STPP : Solar tower power plant

STPT : Solar thermal power tower

TIT : Turbine inlet temperature

ABSTRACT

Full Name : Maimoon Atif

Thesis Title : Optimization and thermal performance analysis of supercritical carbon dioxide Brayton cycles driven by solar thermal power tower systems

Major Field : Mechanical Engineering (Thermo-Fluids)

Date of Degree : October 2014

In this study, thermodynamic analysis of a solar thermal power tower integrated with supercritical CO_2 cycles is presented. A mathematical model was developed to achieve the objectives of the present study. The first part of the model deals with generating a preliminary heliostat field in a conventional radial staggered configuration. The heliostat field is then tested for its optical performance. There are five parameters which constitute the optical performance of a solar tower, namely the cosine factor, the atmospheric attenuation factor, the shadowing and blocking factor, the intercept factor and the mirror reflectivity. The generated field is then optimized against the above mentioned parameters by changing the heliostat positions to attain the maximum possible annual optical performance using differential evolution, which is an evolutionary algorithm. The optimized heliostat field has an insolation weighted annually averaged efficiency of 0.5634. Using the results of the optimization, comparison of net power outputs and thermal efficiencies of different Brayton cycles was performed. The Brayton cycles analyzed were simple Brayton cycle, regenerative Brayton cycle, recompression Brayton cycle, pre-compression Brayton cycle, and split expansion Brayton cycle. The results indicate that the highest thermal efficiency is achieved using recompression Brayton cycle on June noontime. The regenerative Brayton cycle, although simpler in configuration also shows comparable performance. Furthermore, the recompression Brayton cycles was selected to be integrated with solar tower through two tank molten salt thermal storage; as it achieves the highest efficiency. Three cases were studied in which the thermal storage was operational for different ranges of time. Firstly, when it was operational only for daylight hours, secondly when it was operational from sunrise till the end of the day, and lastly when it was operational for the whole day. For the case when the net power output is uniform for the whole day, 17 MW is produced in March,

22 MW in June, and 10 MW in December. Similar observations were made for the other cases. This analysis was carried out for Dhahran, Saudi Arabia.

In addition, a complete thermodynamic analysis of a solar thermal tower system when integrated with a sCO_2 recompression Brayton cycle was performed for six different locations in Saudi Arabia considering the local solar irradiation intensity for each location. The selected cities were Tabouk (North), Madinah (West), Dhahran (East), Riyadh (Central), Bishah (South), and Najran (South). The findings revealed that the highest annual average heat collected was for Madinah, 938,400 kWh/day, and the second highest was for Tabouk, 933,100 kWh/day. Consequently, the least amount of annual average fuel hybridization required was 5.82% for Madinah and 6.34% for Tabouk during daytime hours.

ملخص الرسالة

الاسم الكامل: ميمون عاطف

عنوان الرسالة: تحليل الأداء الأمثل لدورات برايتون فوق الحرجة باستخدام ثاني أكسيد الكربون مدمجة مع برج الطاقة الحرارية الشمسية

التخصص: الهنسة لاميكانيكية (علوم حرارية)

تاريخ الدرجة العلمية: اكتوبر 2014

في هذه الدراسة تم تحليل أداء برج الطاقة الحرارية الشمسية المركزة مع دورات ثاني أكسيد الكربون فوق الحرجة. وقد تم تطوير نموذج رياضي لتحقيق أهداف هذه الدراسة. الجزء الأول من النموذج تعامل مع توليد حقل المرايا الأولي على شكل اشعاعي متداخل التكوين. ثم تم اختبار نتائج النموذج الرياضي لتقييم الأداء البصري لحقل المرايا. هناك خمسة معامل التي تشكل الأداء البصري لحقل المرايا مع البرج الشمسي وهي عامل جيب التمام، وعامل التوهين في الغلاف الجوي، و عامل التظليل والعرقلة وعامل الإعتراض وعامل إنعكاسية المرآة. ثم تم استخدام هذه المعامل لإيجاد أقصى قدر ممكن من الأداء البصري السنوي باستخدام طريقة التطور التفاضلي، التي تعتبر خوارزمية تطورية. بلغ المتوسط السنوي الأمثل للكفاءة البصرية للنظام الشمسي 0.5634 باستخدام نتائج التحسين. تم إجراء مقارنة بين مخرجات الطاقة الصافية والكفاءة الحرارية لدورات برايتون الي تعمل بثاني اكسيد الكربون. الدورات التي تم اخيارها هي دورة برايتون التقليدية ودورة برايتون المتجدده و دورة إعادة الضغط ودورة قبل ضغط ودورة توسيع الانقسام. واشارة النتائج إلى أن الدورة التي تحقق أعلى كفاءة حرارية هي دورة إعادة الضغط وكانت في الظهيرة بشهر يونيو حزيران. أداء دورة برايتون المتجددة كان أقل بقليل من دورة إعادة الظغط. ثم بعد ذلك تمت دراسة تفصيلية باستخدام دورة إعادة الضغط بسب اداءها العالي. حيث تم اختيارها واضافة خزان للحرارة المكتسبة من البرج الشمسي و من ثم تحليل هذا النظام متكاملا. تمت دراسة ثلاث حالات كان فيها التخزين الحراري التشغيلي لنطاقات مختلفة من الزمن. أولا عندما كان النظام يعمل فقط لساعات النهار، وثانيا عندما كان التشغيل من شروق الشمس حتى نهاية اليوم في منتصف الليل، وأخيرا عندما كان التشغيل ليوم كامل لمدة 24 ساعة. بالنسبة للحالة عندما يكون صافي انتاج الطاقة موحد ليوم كامل، تم إنتاج 17 ميغاواط في شهر مارس، 22 ميغاواط في شهر يونيو، و 10 ميغاواط في

ديسمبر كانون الاول. أبديت ملاحظات مماثلة للحالات الأخرى. أجري هذا التحليل لمدينة الظهران بالمملكة العربية السعودية. وبالإضافة إلى ذلك تم إجراء تحليل الأداء لنظام برج الطاقة الشمسية الحرارية عند دمجه مع دورة إعادة الضغط لستة مواقع مختلفة في المملكة العربية السعودية وإعتبار تغيّر شدة الإشعاع الشمسي لكل مدينة. وكانت المدن المختارة تبوك (شمال) والمدينة المنورة (غرب) والظهران (شرق) والرياض (وسط) وبيشة (جنوب) ونجران (جنوب). في هذه الحالة تم استخدام الوقود الإحفوري عند ضعف التركيز الأشعاعي للأشعة الشمسية ولايوجد خزانات للحرارة المتولدة وتم تحليل اداء النضام خلال ساعات النهار. وكشفت النتائج أن أعلى متوسط للحرارة السنوية التي تم جمعها كان للمدينة المنورة بمقدار 938400 كيلو واط ساعة / يوم، وكان ثاني أعلى معدل لتبوك بمقدار933100 كيلو واط ساعة / يوم. ونتيجة لذلك، كان أقل قدر من التهجين السنوي المتوسط للوقود اللازم 5.82٪ للمدينة المنورة و 6.34٪ لتبوك.

CHAPTER 1

INTRODUCTION

The world is facing an ever increase in its energy demands and the conventional fossil fuel resources are being consumed at an alarming rate. This predicament needs to be addressed and more sustainable and reliable energy resources are required which will compensate for the uncertainty in the supply of conventional fuels. Renewable energy sources such as solar, biomass, geothermal, wind, and hydro, can be good alternatives to the conventional fuel sources. These sustainable energy sources are available in sufficient quantities and have minimal impact on the environment.

Solar energy is one such alternative and there are two ways in which this energy can be harnessed to generate electrical power through photovoltaic, and solar thermal or concentrated solar power (CSP). Photovoltaic technology provides a direct method to convert solar radiation into electricity. This implies that the photovoltaics can only be employed during the daylight hours because storing electrical energy is not an efficient process. On the other hand, in a solar thermal system, a device which collects the solar energy (solar collector) is used to run a thermodynamic engine (heat engine) which runs a generator to produce electricity. There are different working fluids which are used to run the thermodynamic cycle like oil, water, air, helium, and carbon dioxide. Alternatively, storing heat is far easier and efficient as compared to storing electricity. The heat which is stored during the daylight hours can be utilized in the night by converting it into electricity. Because of this capability, concentrated solar power is emerging as a potential technology among other sustainable technologies [1–12].

1.1 Concentrating solar power (CSP) technologies

In a concentrating solar power (CSP) technology, the solar radiations are reflected and concentrated using reflectors (mirrors) to heat up a fluid in order to operate a thermodynamic cycle and to obtain power just as in a conventional power plant.

Unlike nuclear reactors or conventional fossil fuel power plants, CSP augments clean solar radiations with the help of concentrators/reflectors to provide the required heat for the power production. CSP also offers an advantage over the photovoltaics with its ability to be equipped with thermal storage system in order to generate power on a cloudy day or even after the sunset. Moreover, it enables the production of dispatchable electricity, facilitating the grid integration and hence increasing the economic viability [2].

1.2 Current technologies for CSP power production plants

CSP plants can be broken down into two groups, based on

Line-focusing systems are those that concentrate the sun rays along a focal line and these include parabolic trough and linear Fresnel plants and have single-axis tracking systems.

Point-focusing systems are those solar collectors that concentrate the sun rays on a single focal point and these include solar dish systems and solar tower power plants and include two-axis tracking systems to concentrate the solar radiation onto the receiver.

Table 1.1 The four CSP technologies [1]

Focus type / Receiver type	Line focus	Point focus
Fixed Fixed receivers are stationary devices that remain independent of the plant's focusing device. This eases the transport of collected heat to the power block.	Linear Fresnel Reflectors	Towers (CRS)
Mobile Mobile receivers move together with the focusing device. In both line focus and point focus designs, mobile receivers collect more energy.	Parabolic Troughs	Parabolic Dishes

1.2.1 Linear Fresnel reflectors

Linear Fresnel reflectors (LFRs) utilize a series of slightly curved or long flat reflectors or mirrors which are placed at an angle such that it focuses the sun's incident radiations on either side of a fixed receiver, which is located several meters above the primary mirror field. In order to ensure that the sun rays are always focused on the fixed receiver, each mirrors line is equipped with an automatic tracking system, rotating on a single axis and optimized individually according to their position. The receiver consists of a long, selectively-coated absorber tube.

Unlike Parabolic Trough collectors (PTCs), LFRs inability to focus the sunlight sharply on the focal line causes astigmatism. This problem can be solved by refocusing the rays missing the tube with the help of a mirror above the tube or a secondary reflector.

Another solution is to introduce several parallel tubes forming a multi-tube receiver such that it is wide enough to capture most of the focused sunlight without a secondary reflector [2].

1.2.2 Parabolic trough

The parabolic trough collectors (PTC) comprises of three basic components: a solar concentrator, a central receiver tube and a support structure. The parabolic-shaped reflecting surface/material concentrates the incoming solar radiations onto a central receiver tube which is situated at the focal line of the collector. The width of these parabolic apertures is around 5-6m and the total length of the array of mirrors can be 100m or longer. The whole system is generally equipped with a single axis tracking mechanism such that both solar collectors and heat receiver are oriented towards the sun. The central receiver is generally a metallic tube which is placed inside an evacuated glass envelope to prevent heat loses. The absorber tube, usually a stainless tube, is coated with a spectrally selective coating that absorbs the solar (short wave) irradiation well, but emits very little infrared (long wave) radiation. Therefore, most of the radiation absorbed is converted into heat energy.

Heat transfer fluid (HTF) absorbs heat from the central tube walls and transfer it to the thermal power cycle or to the heat storage system. Synthetic oils are generally used as a HTF, which are stable up to 400 ^{o}C. Some new studies have shown that the use of molten salt at 540 ^{o}C for heat transfer as well as for thermal storage system can considerably improve the thermal storage performance.

Around 220 MW of installed CSP capacity in 2010 utilized parabolic trough technology and accounted for virtually all of the installed CSP capacity today. Therefore, parabolic trough technology is the most popular and mature of the CSP technologies [1].

1.2.3 Solar dish

Solar dish or parabolic dish collector (PDC) comprises of mirrors arranged in the shape of a dish and concentrates the solar radiations at the focal point above the center of the dish. Generally, an engine/generator, like Stirling engine or micro-turbine, is attached at the focus of the dish. Therefore, the need of a HTF is eliminated with this design.

PDC offers the highest solar-to-electric conversion performance of any CSP system. Some of the advantages of PDC are that these eliminate the need of cooling water and have compact size. On the contrary, PDC systems have low compatibility with thermal storage and hybridization. This makes PDC a very good competitor of PV modules, especially concentrating photovoltaics (CPV). Very large dishes also have provisions for thermal storage and fuel back up as add-ons. Promoters claim that mass production will allow dishes to compete with larger solar thermal systems.

Major disadvantage of PDC is its size limitation which is typically tens of kW or smaller. This necessitates a large number of dishes to be co-located and connected to create a large scale plant. Alternatively, the other CSP technologies have much higher capacities starting as low as 1 MW [1].

1.2.4 Solar tower

Solar tower or central receiver technology comprises of a field of mirrors on the ground which directs the solar radiation on a receiver mounted high on a central tower. The receiver converts the solar radiation into heat and drives a thermodynamic cycle, which is usually a Rankine cycle or a Brayton cycle, to generate power. Each individual mirror in the field is called a heliostat and it is equipped with a two axis tracking system. As compared to parabolic trough and LFR, solar towers can achieve higher temperature as more sunlight can be concentrated on a single receiver and loss of heat can be minimized.

Currently, water/steam, air, or molten salt is used as a working fluid in the heat exchanger. Normal working temperature is around 600 ^{o}C with current molten salt design but it may vary from 250 ^{o}C to as high as 1000 ^{o}C, depending on the working fluid used and design of the receiver. Currently, the capacity of the solar tower power plants is in the range of 10 MW to 50 MW. However, with the increase in annual power demand, the solar field size is required to be increased, which leads to a greater distance between the outer mirrors in the field and the receiver. Longer distance brings with it problems like optical losses due to attenuation or absorption, unavoidable angular mirror deviation due to imperfections in the mirrors, and slight errors in mirror tracking.

Synthetic oil or molten salt is used as HTF and thermal energy storage medium. Operating temperature for synthetic oil is 390 ^{o}C which, in turn, limits the efficiency of the thermodynamic cycle. The use of molten salt as HTF can significantly increase the operating temperature to around 650 ^{o}C, enough to allow higher efficiency supercritical cycles (steam or carbon dioxide); however, at the cost of higher initial investment.

Some of the advantages of solar towers that make these a very promising CSP technology are:

- Higher operating temperature increases efficiency of the thermodynamic cycle as well as reduces water consumption for cooling the condenser;
- Thermal energy storage for schedulable power generation is also enhanced by higher operating temperature; and
- Higher temperature also makes room for greater temperature differentials in the storage system which ultimately reduces the storage cost.

Hence, solar towers provide an opportunity to increase the capacity factor by using thermal storage system and to maximize the power generated by allowing flexible generation strategy along with higher efficiency levels. With these advantages, solar tower can be a tough competitor to parabolic trough in the future market with gained operating experience and reduced cost [2].

Table 1.2 Specifications of the four main CSP technologies [12]

Collector type	Description	Relative thermodynamic efficiency	Concentration ratio (sun)	Operating temp Range (°C)	Relative cost	Technology maturity
PTC	- Parabolic sheet of reflective material (aluminum, acrylic) - Linear receiver (metal pipe with heat transfer fluid)	Low	15–45	50–400	Low	Very mature
LFR	- Linear Fresnel mirror array focused on tower or high-mounted pipe as receiver	Low	10–40	50–300	Very low	Mature
CRS	- Large heliostat field with tall tower in its center - Can be used for continuous thermal storage	High	150–1500	300–2000	High	Most recent
PDC	- Large reflective parabolic dish with Stirling engine receiver at focal point - Heat engine produces electricity directly from reflected thermal energy (in this case, thermal storage cannot be achieved by the system)	High	100–1000	150–1500	Very high	Recent

1.3 Comparison of CSP technologies

In Table 1.1 and Table 1.2, a comparison of the major features of the four main types of CSP technologies — Fresnel reflectors and Parabolic trough, Parabolic dish and Solar tower — are reviewed. Apart from technical and economic aspects, all of these CSP technologies differ significantly in terms of maturity, reliability, and operational experience in utility scale conditions.

Although, parabolic trough is the most widely commercially used CSP technology, improvement in performance and cost reduction are still needed. Most of PTC systems do not have thermal energy storage system and therefore these can only operate in daylight hours. PTC or solar tower when integrated with thermal energy storage can meet the requirements of utility-scale, schedulable power plant.

Solar towers operating at high temperatures using molten salt or other alternatives as HTF and storage medium offers higher efficiency, cost reduction, and expanded energy storage opportunities and hence, these are the most promising CSP technology for the future.

In addition to solar towers, there is an increasing interest in sCO_2 Brayton cycles due to the high thermodynamic efficiencies which can reach as high as 50% at high concentration ratios.

The levelized cost of electricity (LCOE) of solar tower, unlike that of PTC system, tends to decrease as the capacity factor increases. Solar towers can offer more opportunities for local manufacturing than PTC system, creating more job opportunities and local economic development [2].

1.4 Thermal storage

Thermal energy storage technologies operate with a goal of storing energy for later use as a heating or cooling capacity. Thermal storage technologies are well suited for an array of applications including seasonal storage on the supply-side and demand management services.

Some thermal energy storage technologies have already realized significant levels of deployment in electricity and heat networks. Furthermore, some end-use technologies that have already been deployed to meet other societal requirements include thermal energy storage capabilities.

The well known and most researched form of thermal energy storage for high temperature applications is molten salts. This material is used to increase the dispatchability of power from CSP facilities by storing several hours of thermal energy for use in electricity generation. Heat storage by phase change materials, thermochemical energy storage and waste heat utilization methods offer many potential opportunities. However these technologies will need to overcome containment vessel design and material stability challenges at very high temperatures before they can achieve widespread deployment [13].

The concept of thermal storage for CSP plants is such that surplus heat is directed to a storage substance (for example molten salts). This excess stored heat is released into the thermodynamic cycle after the sunset, and the plant continues to operate depending upon the storage capacity.

All CSP plants have the ability to store excess thermal energy and therefore have the mitigate capacity that allows the electricity production to smoothen considerably and purge the short-term variations occurring due to cloudy days or any other reason.

The required solar field size is relatively larger to incorporate storage i.e. the plant has a higher solar multiple to make certain that there is adequate electricity production. As a consequence, at peak hours, the solar collectors will generate more heat than the turbine is designed for.

In the absence of storage, the operators would need to defocus some of the unneeded solar collectors. Storage allows for extended production after the sun has set and avoids losing this energy.

The CSP plants having large storage capacities may be able to generate power day and night, hence making it possible for CSP plants to compete with traditional fossil fuel power plants that release high levels of carbon dioxide.

Currently the industry’s focus is to reduce the thermal storage costs and to significantly increase the temperature to improve overall efficiency of CSP plants. Enhanced thermal energy storage would help expand production and capacity. The concept of storage makes solar only power plants possible, although hybrid plants have their own advantages [1,14].

1.5 Motivation and significance

The world is facing a challenging time to fulfill its energy requirements with depletion of the fossil fuel resources. In these hard times, research is being carried out to effectively utilize sustainable energy resources to fulfill the increase in the energy demands.

Of all the CSP technologies solar tower in the near future is expected to become the technology of choice. This is mainly due to the anticipated performance improvement and cost reductions associated with technology innovations of the three main subsystems, i.e. the heliostat, the receiver, and the integrated thermodynamic cycle within the near future. Compared with other CSP options, the solar tower or the central receiver system (CRS) could not only provide cheaper electricity than parabolic trough and solar dish systems but also superior performance [15]. Other advantages include higher temperatures and thus higher efficiency of the integrated thermodynamic cycle and it has the flexibility to be easily integrated in fossil fuel plants for hybrid operation. As already mentioned it has the potential for generating electricity with high annual capacity factors through the use of thermal storage.

The supercritical power cycles take advantage of real gas behaving in order to achieve high thermal efficiency. In supercritical CO_2 (sCO_2)cycle, main improvement of the cycle efficiency comes from the compressor work reduction due to the change in properties when it is compressed near the critical point and due to low critical temperature. Therefore, it is possible to include water at ambient temperatures as a coolant for such cycles [16]. sCO_2 when incorporated as a heat transfer fluid (HTF) can attain thermodynamic efficiencies above 50% at concentration ratios and temperatures achievable by concentrating solar power tower [17]. Due to the high operating pressures, small sized components can be incorporated. Moreover, as compared to steam and organic based Rankine cycles, sCO_2 can achieve high efficiency over wide temperature ranges of heat sources with compact components resulting in lower operating and capital costs. sCO_2 technology can displace steam for bottom cycling on gas turbines by providing higher output power with lower operation & maintenance costs and lower installment costs which can reduce levelized cost of electricity by up to 10 to 20 percent. In addition, the associated greenhouse emissions are reduced by an improvement in the overall energy production efficiency [18].

As can be observed the concentrated solar power production using solar tower is the most promising concentrated solar power technology. Therefore, this technology has been selected. On the other hand, only limited number of studies has been performed on sCO_2 cycles. However, among these studies, no study considered complete thermodynamic modeling of sCO_2 cycles when integrated with a solar tower. In this study, solar tower power system and its feasibility for electrical power production was studied in details. The reference location for this study is Dhahran, Saudi Arabia. A comparative analysis was carried out for different sCO_2 closed loop Brayton cycles. In addition, a complete thermodynamic analysis of a solar thermal tower system when integrated with a sCO_2 recompression Brayton cycle was performed for different locations in Saudi Arabia considering the local solar irradiation intensity for each location.

1.6 Objectives of the current study

The overall objective of this study is to perform thermal analysis of solar thermal power tower systems when integrated with supercritical CO_2 Brayton cycles. The specific objectives are:

1. Development of a mathematical code to deploy a conventional radial staggered heliostat field layout.
2. Development of a mathematical code for the effective optimization of the heliostat field.
3. Assessment of the heliostat field layout size for a selected power production range under different operating conditions considering solar irradiation intensity for Dhahran, Saudi Arabia.
4. Thermodynamic modeling of the solar thermal power tower systems when integrated with different supercritical CO_2 Brayton cycles for Dhahran, Saudi Arabia.
5. Comparative performance analysis of solar power tower driven sCO_2 recompression Brayton cycle with an auxiliary heater installed for different locations of Saudi Arabia.
6. Thermodynamic modeling of two tank thermal storage when integrated with supercritical CO_2 Brayton cycles driven by solar thermal power tower systems for Dhahran, Saudi Arabia.

CHAPTER 2

LITERATURE REVIEW

In this chapter, a detailed literature review is presented to identify the gap in the literature. The details of the literature review are organized as follows. It starts with the review of the studies on the solar thermal power tower (solar central receiver) systems and the heliostat field layout (HFL). Then, the review is presented on thermodynamic cycles using supercritical carbon dioxide as the working fluid. Lastly, the review of the studies focusing on solar thermal storage systems is presented and discussed.

2.1 Central receiver and heliostat field layout

Recently, several studies had been conducted to examine different performance parameters of the solar central receiver system. Solar central receiver systems (solar towers) are characterized by high temperatures operation using high temperature heat transfer fluid, usually molten salt or synthetic oil. Furthermore, they can incorporate storage medium due to the potential of higher efficiency, cost reduction, and prolonged energy storage opportunities. These operating features are based on their high capacity factor achievable, lower energy storage costs, greater efficiency of the integrated thermodynamic cycle, and their firm output capability [2,15,17].

Chiesi et al. [19] proposed parallel algorithms for the design and analysis of a heliostat field layout systems. Their work focused on studying mirror imperfections and non planar geometries using multiple graphical processing units (GPUs) to have an accurate and fast simulation environment. Processing times that usually take hours was reduced to a matter of minutes using this approach.

Garcia et al. [20] performed a detailed review study on the codes for the calculation of solar flux concentration. The codes were divided into two main categories: those codes which are used for optimization and the codes which are designed for the calculation of the optical performance parameters. Another similar review was performed by Romero and Steinfield [21] on concentrating solar thermal power and solar thermochemical fuels. It was concluded in their study that the implementation of CSP systems is rapidly increasing. Furthermore, the next generation of technologies allows surprising 1000 °C and thus enables higher efficiencies.

Renzi et al. [22] performed analysis on the performance of a non-imaging focusing heliostat for a small solar concentration plant. A prototype plant consisting of 90 two axis tracking heliostats was simulated using a ray tracing technique. These simulations also took into account tracking errors conforming to the real conditions. It was concluded from the study that flat mirror heliostat can perform well in terms of optical efficiency.

A study was conducted by Ali [23] on the factors which affect the heliostat field design in a central receiver plant. It was concluded that the shadowing length is about twice the length of the size of the mirror (heliostat) and the optimal distance from the tower up to which the heliostats can be placed is about 1.25 times the height of the tower.

A cell wise approach was proposed for optimizing a solar tower system by Lipps and Vant-hull [24–26]. In the approach described by them, the whole heliostat field was divided into cells and a layout of the heliostat was generated based on the optimization of these cells by determining an optimum value for the figure of merit. This figure of merit is defined as the ratio of the cost of the thermal system to the annual thermal energy collected. Lastly, the conversion from the optimum spacing from the cells to the individual heliostats was mainly based on the shadowing and blocking, and the insolation data [26].

A mathematical graphical method for generating a no-blocking radial staggered heliostat field layout was presented by Siala and Elayeb[27]. The field was divided into groups or zones to increase the density and it was reported that the proposed field layout is simple as compared to cell-wise method.

The German Aerospace Center developed a code for optimizing a heliostat field based on annual performance which is called HFLCAL[28,29]. This code computes the energy spot sent to a heliostat by describing the reflected image of each heliostat as a circular normal distribution. Thus, the intercept of each heliostat in the field can be calculated which is described by an analytical function. This code starts the optimization with a set of supposed heliostat positions and then the performance of these heliostats is calculated.

Pitz-Paal et al. [30] performed optimization of the heliostat field for solar tower systems by coupling genetic algorithm and the Nelder-Mead algorithm for maximum annual solar to chemical conversion energy efficiency for solar fuels production. It was concluded that the chemical process selected has high impact on the basic design parameters and the performance.

An improved configuration considered a biomimetic pattern for the heliostat field layout based on annual performance using discretization of the heliostat surface into cells was suggested by Noone et al. [31]. It was concluded that these patterns have better annual efficiency and cover less land area; thus, levelized cost of electricity is reduced. The discretization approach was used to calculate the shadowing and blocking factor and the intercept factor. For this purpose, the heliostat surface was divided into cells ranging from 9 to 100 for validation. This approach implies that in a full optimization process, which includes thousands of heliostats, it can be time consuming especially if the interception is calculated locally for each cell.

Optimization of the same heliostat field layout that was suggested by Noone et al. [31] was also studied by Besarati and Goswami [32]. Instead of using a discretization approach for the calculation of shadowing and blocking factor and the intercept factor, different approaches were used and implemented. For the calculation of shadowing and blocking factor, the method described by Sassi[33] was implemented. On the other hand, for the calculation of the intercept factor, the HFLCAL model [28,29] was used.

A new code and method called HFLD (Heliostat Field Layout Design) was developed by Wei et al. [34] from the Chinese Academy of Science. In their method, optimization of the heliostat field was based on an efficiency factor and the receiver geometrical aperture. They had applied this method to the PS10 power plant; and as a result, they had proposed a new layout for the PS10 plant. Same authors, in a different study [35], further implemented a new module for the analysis of aspherical toroidal heliostat field. However, their code calculates the intercept factor using Monte Carlo ray tracing method. Consequently, the accuracy will depend upon the number of rays traced, which will result in a high computation time.

Huang and Xu [36] developed an analytical model using ray tracing method for determining the annual solar energy collected by a heliostat field. A quick algorithm using some simplified assumptions was proposed for the estimation of the collected annual energy. Nonetheless, the accuracy will depend upon the simplified assumptions and the number of rays traced.

Sanchez and Romero [37] worked on the software tool SCT-HGM which generates heliostat field layouts on yearly basis. Their code calculates the shadowing and blocking factor and the intercept factor using the Monte Carlo ray tracing method resulting in a high computation time. Furthermore, as the calculation of the shadowing and blocking factor is burdensome, some interpolations were made based on regular distributions.

Huang et al. [38] proposed several methods for fast and accurate calculations of shadowing and blocking by projecting the heliostats using the actual focus ray. These methods were compared and two models were recommended to calculate shadowing and blocking: one is from the actual projections of heliostats single vertex and the other one is from the projections of four vertices (called the quadrilateral method). Same authors, in a different study [39], also developed an analytical model for the calculation of the intercept factor of a heliostat over a flat receiver. Their model was validated using a ray tracing program and experimental data. The model can also be applied to calculate the performance of a flat, sphere, and combined facet in a circle or rectangle.

Collado [40] addressed the difficulty of generating a preliminary surrounding layout of a heliostat field. Thousands of heliostat co-ordinates were generated using only two parameters which are the additional security distance and the simplified blocking factor. A code named *Campo* was developed by Collado and Guallar [41] which performs accurate calculations of the shadowing and blocking factor and allows for the optimization of the preliminary layout of the heliostat field in which thousands of heliostats co-ordinates are considered for the optimization process. In a different study, optimized heliostat field layouts were reviewed by means of this code, Campo[42], using the literature data on *Gemasolar* (a CSP plant). Using the scarce data on *Gemasolar*, the Campo code was validated on annual energy bases and the optimization was executed by applying radial increments in all the zones of the heliostats manually and finally eliminating the heliostats from the third zone that were below a certain efficiency.

CRS4-2(Research software for central receiver solar system simulations) was developed by Leonardi and Aguanno [43] to calculate the optical performance of the heliostat field of diverse geometrical parameters. Their code divides each heliostat surface into cells same as done by Noone et al. [31] and projects the centers of these cells following the sun and the receiver for the calculation of shadowing and blocking, respectively. Nevertheless, the intercept factor was not considered in their study.

Energy analysis of a solar tower power plant without an energy storage was performed by Benammar et al. [44]. In their study, the solar tower was coupled with a steam Rankine cycle and the whole system was divided into four main subsystems, namely the heliostat field subsystem, the cavity receiver subsystem, the steam generation subsystem, and the power cycle subsystem. However, the heliostat field efficiency was taken as a constant value for the sake of analysis in their study, which did not provide the real performance of the system.

Thermodynamic and thermoeconomic analysis and optimization was performed on a combined cycle power plant integrated with solar central receiver system by Kribus et al. [45] and Spelling et al. [46]. It was concluded that solar thermal combined cycle power plants are both thermodynamically and economically promising, and their levelized energy costs are competitive with those for other kinds of solar thermal power plants. While Kribus et al. [45] also did a feasibility study of a hybrid (solar and fossil) tower combined cycle power plant with the solar tower reflecting the light onto a compound parabolic collector (CPC). New developments were incorporated like solar tower optics, solar to gas turbine interface and high performance air receivers.

Xu et al. [47] performed detailed energy and exergy analyses on a solar central receiver system using molten salt as a heat transfer fluid to determine the effect of the design parameters like DNI (direct normal irradiance), the concentration ratio, and the type of power cycle on the energy and exergy performance. It was found that the overall exergy and energy efficiencies of the plant can be increased to some extent by integrating advanced power cycles including supercritical Rankine cycles and reheat Rankine cycles.

In a study by Reddy et al. [48], evaluation of a solar tower power plant was performed using exergy analysis. The solar tower was integrated with a Rankine cycles for their study. It was concluded that the solar heliostat field receiver assembly had the highest exergetic losses followed by the boiler.

In an another study, first and second law analysis of a solar tower driven thermodynamic cycle for triple effect refrigeration was carried out by Agrawal et al.[49]. It was found that maximum irreversibility occurs in the central receiver and the second largest irreversibility occurs in the heliostat field. Furthermore, it was concluded that first law analysis is inadequate and second law analysis is more meaningful.

Assessment of solar steam reforming of methane was performed by Sheu and Mitsos [50] when a combined cycle was integrated with solar tower through a reformer. The operation of this hybrid solar fossil fuel plant was optimized to yield the highest annual work output. It was concluded that the tower reformer integration method is a promising integration method because it yields higher efficiency.

In a study by Yao et al.[51], a power plant was modeled using TRNSYS and integrated with HFLD [34,35] developed by the Chinese academy of Science for the demonstration of 1 MW CRS plant in Dahan, China. The basic flow calculation in the solar central receiver system and their integration to a plant were described.

Yu et al. [52] performed optimization of solar flux distribution inside a cavity receiver based on multi focal points of heliostat field. The target was to make the flux density uniform while keeping the spillage losses to a minimum. This was achieved by defining a multi aim point strategy on the receiver by distributing the heliostat field in different groups. The study was carried out for a 1MWe “DAHAN” solar tower power plant located in China.

Avila-Marin et al. [53] performed a parametric study of medium to large sized solar central receiver plants. The analysis was divided into four parts namely; size and location analysis, technology analysis, storage analysis, and component’s cost analysis. It was concluded that a molten salt nitrate system results in a lower LCOE (levelized cost of electricity) as compared to a direct steam generation system. It was further concluded that the solar field has a potential for larger reduction in LCOE.

Peng et al. [54] conducted a study on off-design thermodynamic performance of a solar assisted coal fired power plant located in China. The study was conducted under different turbine loads based on hourly intervals. Nonetheless, parabolic troughs aligned on a north-south horizontal axis were used for this purpose. It was suggested to change the direction tracking axis for different seasons for improving the annual performance of the system.

2.2 Supercritical CO_2 thermodynamic cycles

High temperature supercritical CO_2 (sCO2) Brayton cycles are emerging technologies due to the high thermodynamic efficiency, which can reach as high as 50%. Such efficient cycles can be attained through high solar irradiation concentration ratios and temperatures using concentrating solar power tower. [17]

Yann Le Moullec [55] performed a study on a coal fired power plant with a supercritical CO_2 power (Brayton) cycle and a post combustion CO_2 capture mechanism. The study was intended to explore the potential of this concept. A techno-economic evaluation of the designed power plant was performed as well. The results indicated that the reduction in the levelized cost of electricity (LCOE) was 15%, and the reduction of cost of avoided CO_2 was 45%, without transport and storage, as compared to a reference supercritical coal fired power plant equipped with a standard carbon capture process.

Yamaguchi and his Research Group [56–61] studied, in details the characteristics of solar powered supercritical CO_2 Rankine system experimentally for a low temperature heat source. An evacuated tube solar collector was used for carrying out this study. A number of parameters were studied, which include, the heat transfer characteristics, optimal arrangement of solar collector, effect of mass flow rate, pressure ratios, temperatures and solar heat input. Moreover, it was reported that sCO_2 Rankine cycles display good potential for combined heat and power generation.

Researchers at Sandia National Laboratories [62] investigated the application of Brayton cycles with sCO_2 as a working fluid. They had tested a variety of heat sources, including solar, fossil, nuclear, and geothermal energy. Additionally, they focused towards improving the cycle efficiency and extending the applicability of the sCO_2 power generation systems by developing, testing, and upgrading the sCO_2 components.

The transient effect of the solar heat input on a supercritical CO_2 split flow recompression Brayton cycle was studied by Iverson et al. [63]. They had studied the behavior of the turbomachinery of the Brayton cycle in response to a fluctuating solar heat source. In particular, the thermal input was cut by 50% and 100% for short durations to check the effect of these variations on power conditions. It was observed that the thermal mass in the system effectively enables the Brayton cycle to continue to run for short periods until the thermal input can recover. A comparison of short and long-term thermal storage options was also presented in which the thermal storage can alleviate the thermal fluctuations.

In different studies, parabolic trough concentrators with supercritical CO_2 as a heat transfer fluid for Brayton cycles were examined, [64–67]. Singh et al. [64,65] developed a control oriented model for the sCO_2 dynamic behavior. They highlighted the need of utilizing sCO_2 charge manipulations during summer and winter to sustain fully supercritical operation of the cycle. Furthermore, an extremum-seeking controller was proposed by Singh et al. [66] to maximize the power output of a direct heated supercritical CO_2 closed loop Brayton cycle as the solar heat input and the ambient temperature fluctuate. This was achieved by manipulating CO_2 mass inventory in a closed loop Brayton cycle and it was concluded that this control method compares favorably to the operation while retuning is not required between summer and winter seasons. Chapman and Arias [67] examined using sCO_2 in a thermocline storage system and stated that the sCO_2 thermal storage was not practical due to the high cost of pressure vessels. Furthermore, it was concluded that the use of sCO_2 has benefits over the steam cycles in terms of smaller and simpler turbomachinery when integrated with parabolic trough concentrators.

A closed loop sCO_2 recompression Brayton cycle was analyzed by C. S.Turchi [68]. From the analysis, it was concluded that using sCO_2 as a working fluid has the potential of higher thermal efficiency as compared to other cycles, such as the helium Brayton cycle, the supercritical steam cycle, and the superheated steam cycle. It was further reported that the uncertainties associated with the use of such technology is the lack of experience with closed loop Brayton cycles and the high pressure required. Ma and Truchi [69] recommended a small solar tower design for simplicity in the power block.

Comparative analysis was carried out between a supercritical, transcritical, and subcritical CO_2 operating in a closed loop regenerative Brayton cycle by Garg et al. [70]. It was concluded that the supercritical CO_2 is the most promising among the three. Chacartegui et al. [71] studied supercritical and transcritical CO_2 for solar thermal power plants. Three cycles were taken into account: a regenerative closed loop CO_2 Brayton cycle, a partial cooling closed loop CO_2 Brayton cycle, and a combined cycle comprising of a topping CO_2 Brayton cycle and a bottoming Rankine cycle using an organic fluid. From the preliminary results, it was concluded that CO_2 Brayton cycles have the potential to compete in terms of efficiency and cost with the conventional cycles. Different parameters were taken into account to examine the comparative performance of the two Brayton cycles, and it was concluded that the partial cooling Bratyon cycle exhibits higher thermal efficiency as compared to the simple regenerative Brayton cycle.

2.3 Thermal energy storage

Using thermal energy storage increases the annual capacity factor and improves the dispatchability of power from a CSP plant. The selection of an appropriate heat transfer fluid (HTF) is important for designing a cost-effective thermal storage system and to improve the cycle efficiency of the power plant [72].

Liu et al. [72] performed a comparison of different gaseous and liquid heat transfer fluids (HTFs) to determine their suitability for use in a high temperature thermal storage unit with flat slabs of phase change materials. This comparison was based on their heat transfer characteristics between the flat plates and the net power produced. For the capacity rate considered, liquid sodium was identified as the best HTF because it delivers the highest electrical energy to the grid, achieving 99.4% relative to the ideal case. Alternatively, solar salt achieved a value of 93.6%, while the gaseous fluids of atmospheric air, air at 10 bar, sCO_2 at 100 bar and steam at 10 bar achieved a value between 87.9% and 91.3% of the ideal delivered electricity. Gaseous fluids have the advantage of being able to be used as the working fluid in the power block. This study shows that gaseous fluids are comparable to liquid HTFs in PCM storage facilities.

Gil et al. [73] reviewed and classified different high temperature thermal energy storage concepts. It was concluded from their review that cost effective and efficient storage system allows a better dispatchability of the solar power plant and a higher capacity factor. Storage systems were classified into latent heat storage, sensible heat storage, and chemical heat storage. The systems are further classified into active systems where forced convection heat transfer takes place either directly with the storage media or indirectly if the storage media and heat transfer fluid are of different substances; and passive where the storage medium itself is not forced to circulate. Mostly employed systems are two tank active systems, both indirect and indirect, where molten salt is used as the storage media and in case of indirect systems normally oil is used for heat transfer. The passive systems including the phase change material (PCM) and solid media sensible heat storage are being investigated by different research groups. Among the liquid sensible heat storage, the molten salts which are commonly in use are the binary salt (60% NaNO3 and 40% KNO3) and a salt known as HitecXL (48% Ca(NO3)2, 7% NaNO3, and 45% KNO3). Further investigations are being performed to develop new salt mixtures to overcome the problem of high freezing points. Several materials are being analyzed and investigated, as it brings nearly constant temperature and higher storage density. For concentrated solar power, the chemical heat storage is promising, but it is even less developed than the latent heat technology. Investigations have also been performed upon the corrosion effects of molten salts in steel and stainless steel tanks. Impurities contained in the molten salts prepared from the constituents of alkali nitrates have little effect in corrosion of carbon and stainless steels.

A comparative review of different high temperature thermal energy storage systems (case studies) was performed by Medrano et al.[74]. It was inferred that among the different heat transfer fluids in the solar field which include mineral oils, molten salt, ammonia and steam; recent plants (most of them being in Spain) are using steam because it allows for higher temperature operation and the configuration is relatively simple. For the storage systems, lately high temperature concrete or castable ceramics are being investigated as cost effective alternative to molten salt [73,74]. In recent tower solar thermal power plant technologies (in Spain), a comparative case study was carried out using steam as a heat transfer fluid and a combination of steam and ceramic as a thermal storage.

Kuravi et al. [75] performed a detailed review of thermal energy storage system design methodologies suited for CSP plants. The study discussed the thermal energy storage system designs presented in the literature along with thermal and exergy efficiency analyses of various thermal energy storage systems. Though all basic types of thermal storage media that are the sensible, latent and thermo-chemical have the potential to make solar power plants practical, more research is still needed to improve the thermo-economics of these systems. Nano-based technologies and advanced manufacturing techniques are being employed for this purpose.

A detailed review of solar collectors (concentrating and non-concentrating) and thermal energy storage systems for solar thermal applications was performed by Tian et al. [76] . A comparison was presented between different materials and different categories for high temperature thermal storage systems. The ideal materials considered for high temperature thermal storage would be molten salts with excellent properties. To overcome the poor heat transfer in these applications heat transfer enhancement by graphite composites and metal foams was recommended.

A transient heat loss model of two tank molten salt thermal energy storage was developed by Zaversky et al. in Modelica[77]. A fully transient storage tank model was developed and simulated over three sets of six reference days. The model was successfully validated against real application in molten salt thermal energy storage tanks. It was concluded that this can be a suitable tool for CSP performance simulations.

Yang and Garimella [78] performed thermal analysis of solar thermal energy storage in a molten salt thermo-cline. Molten salt HITEC was considered for illustration with quartzite rocks as a filler. Volume-averaged mass and momentum equations were employed, with the Brinkman Forchheimer extension to the Darcy law used to model the porous-medium resistance and the governing equations were solved using a finite volume approach. Thermal characteristics and discharge efficiency of the tank were investigated and guidelines were developed for designing solar thermo cline systems. The discharge efficiency was found to be improved at larger tank heights and small Reynolds numbers.

Cyclic operation of molten-salt thermal energy storage in thermoclines for solar power plants was also studied by Yang and Garimella [79] . Guidelines were developed for designing the dimensions and the salt flow rates for the thermo cline systems of different power capacities. The cycle efficiency was found to be improved at larger length ratios, smaller Reynolds numbers, and larger tank heights. The filler particle diameter and the tank volume were found to strongly influence the cycle efficiency.

Rovira et al. [80] devised two systems for CSP plants to improve the overall plant performance by reducing the losses coming from the respective sources. Firstly, double thermal energy storage was formulated with different functionalities for each storage. It was intended to keep the plant working at nominal capacity during post sunset hours. Secondly, the solar field was subdivided into specialized sectors; the purpose was to divide the thermal requirement through an intermediate heat exchanger for each sector. An increase of 1.7% of annual electricity generation was observed for the double thermal energy storage case and 3.9% for the solar collector field case as compared to a reference solar thermal power plant.

A dynamic simulation was presented by Powell and Edgar [81] for a two tank direct thermal energy storage used in (parabolic trough) concentrated solar power. The tests were performed on a sunny day, an intermittent cloudy day, and a cloudy day. It was concluded that for thermal energy storage of eight hours, the supplementary fuel requirement can be reduced by 43% and it can increase the solar share of the power plant by 47% for a thermal output of 1MW on a sunny day. A little improvement was noticed during cloudy days; however, the main benefit of adding storage is the ability to maintain a constant power output.

Heller and Gauche [82] developed a mathematical model of a thermocline based rock bed thermal storage suitable for air cooled solar central receiver systems. The study focused on the storage as the center of in and outgoing thermal energy and the derived storage model had one spatial dimension which was justified by the high tube-to-particle diameter ratio. The calculated LCOE was in agreement with other studies on combined thermal power cycle driven by concentrated solar power plants.

It was thoroughly investigated by Wagner and Rubin [83] about the economic implications of thermal energy storage for concentrated solar thermal power. An engineering economic model was developed that directly compared the cost, profit, and the performance of a 110 MW parabolic trough concentrated solar power plant operating with thermal energy storage system, natural gas fired backup system, and with no backup system. It was concluded that the molten salt thermal energy storage of a concentrated solar power plant with hourly solar radiation increased the annual capacity factor from around 30% with no backup to with up to 55% with 12 hour of storage when the solar field area is selected to provide the lowest levelized cost of electricity. Using thermal energy storage as compared to natural gas fired heater increased capital costs but decreased annual operating and maintenance costs. If higher capacity factors i.e. greater than 50% were to be encouraged that are based more on sustainable energy, additional incentives might be required to make thermal energy storage more attractive as compared to natural gas backup.

2.4 Summary

A detailed literature review on the solar central receiver system (solar tower), heliostat field layout, supercritical CO_2 thermodynamic cycles, and thermal energy storage was performed. From the literature review, it can be observed that only few studies have been conducted on supercritical CO_2 Brayton cycles when integrated with solar thermal power tower systems. However, those studies have not considered modeling of the solar power tower and used the results of the modeling to assess the performance of the sCO_2 Brayton cycles. They rather assumed a heat source that has similar heat outputs as the solar power tower. Therefore, this research is original. The current study demonstrates the relation between the heat produced from the solar power tower system and power produced using sCO_2 Brayton cycles with different thermal storage options.

CHAPTER 3

MATHEMATICAL MODELING

A mathematical model was developed to achieve the objectives of the present study. The first part of the mathematical model deals with generating a preliminary heliostat field in a radial staggered configuration. The generated heliostat field is then tested for its optical performance, and there are five parameters which constitute the optical performance of the heliostat field layout namely the cosine efficiency, the atmospheric attenuation factor, the shadowing and blocking factor, the intercept factor and the actual mirror reflectivity. The generated heliostat field is then optimized on annual basis using an evolutionary algorithm called the differential evolution (HFLODE). While the other part deals with the integration of the sCO_2 thermal cycles with the receiver. Five different cycles were modeled, i.e. the simple Brayton cycle, regenerative Brayton cycle, recompression Brayton cycle, precompression Brayton cycle and split expansion Brayton cycle and a comparative analysis between these cycles was performed when integrated with a solar tower system. Furthermore, analysis of sCO_2 recompression cycle integrated with solar tower through two tank molten salt storage was also performed for Dhahran, Saudi Arabia. In addition, a complete thermodynamic analysis of a solar thermal tower system when integrated with a sCO_2 recompression Brayton cycle was performed for six different locations in Saudi Arabia considering the local solar irradiation intensity for each location. The selected cities were Tabouk (North), Madinah (West), Dhahran (East), Riyadh (Central), Bishah (South), and Najran (South).

3.1 Generating a preliminary heliostat field

A preliminary heliostat field was generated in a radial staggered configuration using the method outlined in [40,41]. This method addresses the problem of generating and managing thousands of heliostats in an efficient manner. In this section, the method to calculate the characteristic diameter, radial spacing, azimuthal spacing, number of rows, number of heliostats, and the land area covered by the heliostat field are presented.

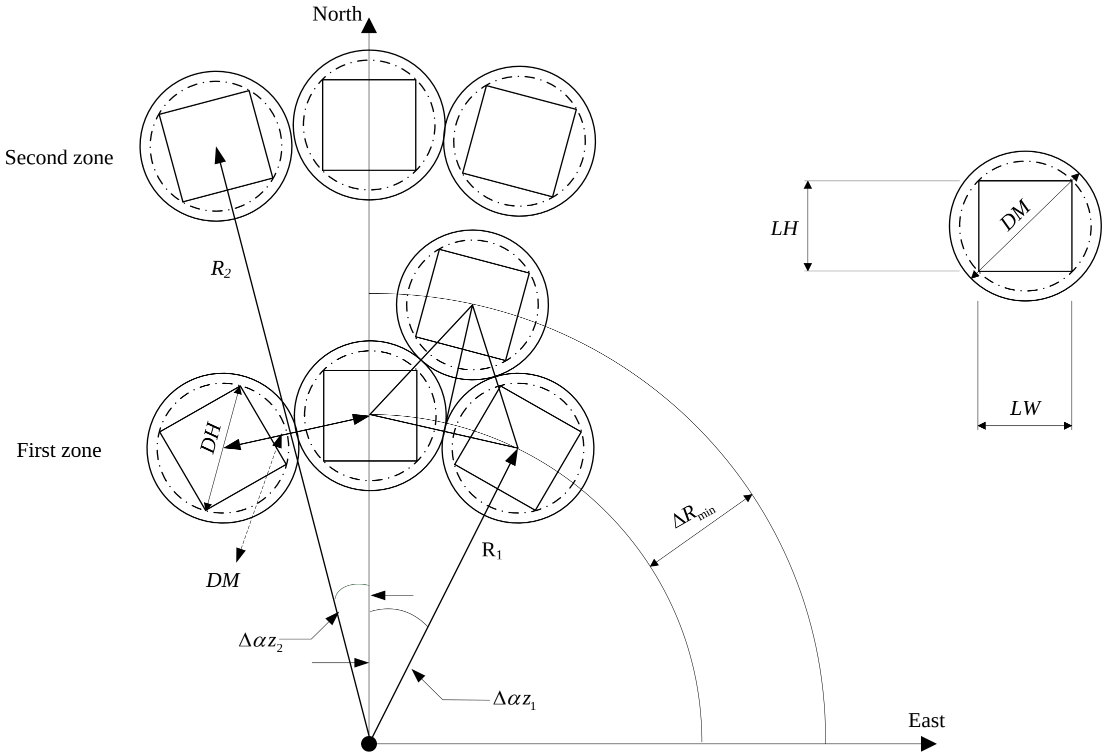

Figure 3.1 Fundamental definitions of the heliostat field

3.1.1 The characteristic diameter

The characteristic diameter (Figure 3.1) is the distance between the center of the adjacent heliostats and it is defined by

$$DH = \sqrt{1 + wr^2}\, LH \tag{1}$$

$$DM = \left(\sqrt{1 + wr^2} + ds\right) LH \tag{2}$$

This equation can also be written as

$$DM = DH + dsep \tag{3}$$

and it is also equal to

$$DM = LW + h_{clear} \tag{4}$$

where

$$dsep = ds \times LH \tag{5}$$

The above equation, 3, was modified as follows for optimization by introducing the factor x_1

$$DM = DH + dsep + x_1 \tag{6}$$

where DM is the characteristic diameter, DH is the heliostat diagonal and $dsep$ is any additional security distance between the heliostats, which is equal to $ds \times LH$; wr is the ratio of the width to the height of the heliostat, LH is the height of the heliostat, LW is the width of the heliostat, and h_{clear} is the horizontal clearance. Here, x_1 is one of the optimizing parameters. By varying the value of this paramter, we can control the azimuthal spacing between the adjacent heliostats.

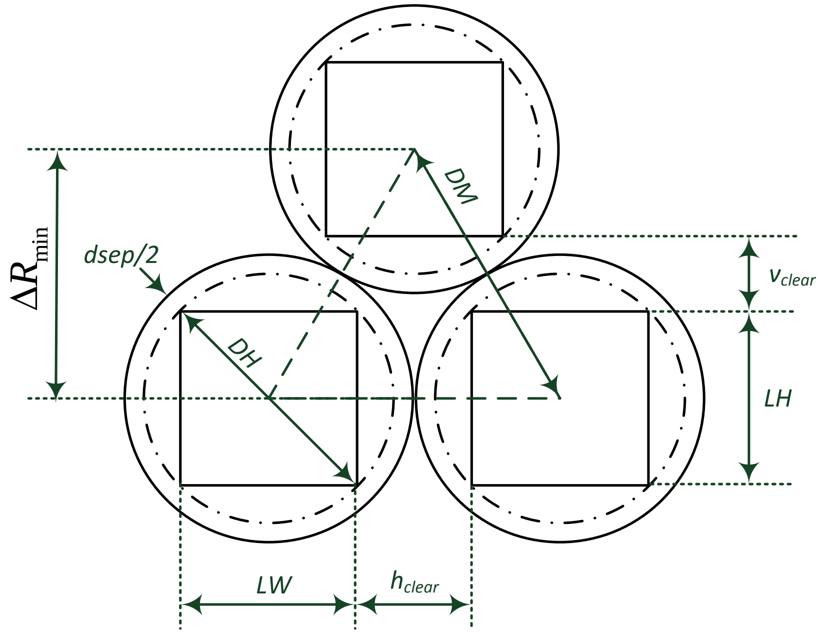

Figure 3.2 Vertical and horizaontal clearanaces

3.1.2 The radial spacing

The minimum radial distance (Figure 3.1 and Figure 3.2) between the heliostat rows is equal to the height of an equilateral triangle and is defined as

$$\Delta R_{\min} = DM \cos 30° - h \tag{7}$$

where

$$h = R_1 - \sqrt{R_1^2 - (DM^2/4)} \tag{8}$$

However, due to large values of R_1 in relation to DM, h has been neglected[41]. Hence, we have

$$\Delta R_{\min} = DM \cos 30° \tag{9}$$

and from this the vertical clearance can be defined as

$$v_{clear} = \Delta R_{\min} - LH \tag{10}$$

The above equation, (9) for minimum radial distance is modified for optimization as

$$\Delta R_i = x_{2,i} DM \cos 30° \tag{11}$$

where $x_{2,i}$ is the second optimizing parameter and i denotes the zone of heliostats and v_{clear} is the vertical clearance between heliostats. Using the parameter $x_{2,i}$ the radial spacing between the rows of the heliostats can be controlled and in turn the optical performance of the heliostats.

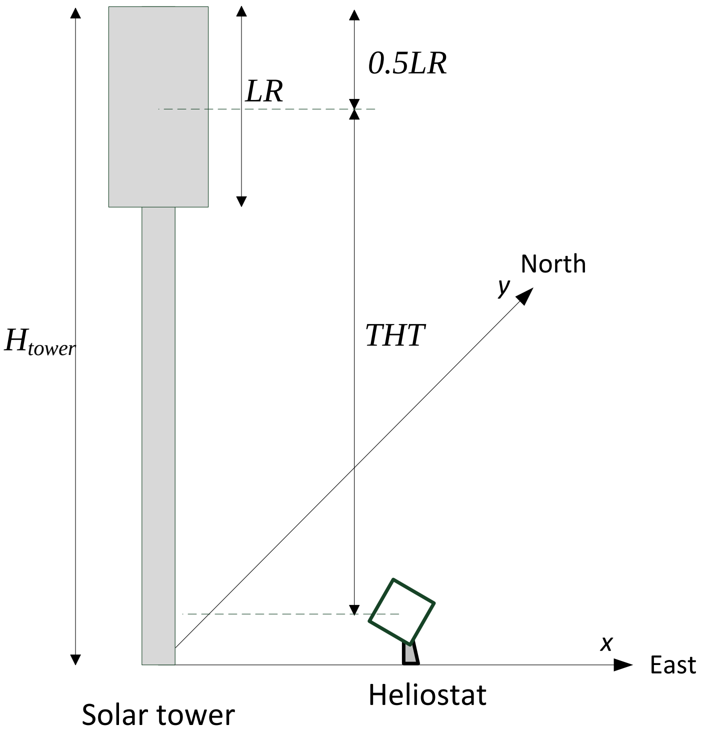

Figure 3.3 Fundamental definitions of the central receiver

3.1.3 The azimuthal spacing

The azimuthal increment is the angular distance between adjacent heliostats of the first ring in each zone is given as

$$\Delta\alpha z_1 = 2\sin^{-1}\left(DM \big/ 2R_1\right) \cong DM / R_1 \tag{12}$$

where R_1 is the radius of the first ring in the first zone and a zone is a group of rings which have constant azimuthal spacing.

Due to the radial staggered configuration, as we progress in the rows, the azimuthal spacing between adjacent heliostats increases. When the azimuthal spacing becomes large enough so that an additional heliostat can be placed in this spacing, a need for redefining the azimuthal increment arises and thus a new zone is formed. Similarly, for the other zones we can define the azimuthal increment as

$$\Delta\alpha z_2 = \Delta\alpha z_1 / 2 \cong DM / R_2 \Rightarrow R_2 = 2\left(DM \big/ \Delta\alpha z_1\right) = 2R_1 \tag{13}$$

and

$$\Delta\alpha z_3 = \Delta\alpha z_1 / 4 \cong DM / R_3 \Rightarrow R_3 = 4\left(DM \big/ \Delta\alpha z_1\right) = 4R_1 \tag{14}$$

$\Delta\alpha z_2$ and $\Delta\alpha z_3$ are the azimuthal spacings for the second zone and the third zone, respectively.

3.1.4 Number of rows

Number of rows for each zone is defined as

$$Nrows_1 = {(R_2 - R_1)}\big/{\Delta R_{\min}} \cong round({R_1}\big/{\Delta R_{\min}}) \tag{15}$$

where the quotient is rounded off because it is an integer value.

Similarly,

$$Nrows_2 = {(R_3 - R_2)}\big/{\Delta R_{\min}} \cong round({2R_1}\big/{\Delta R_{\min}}) \tag{16}$$

and

$$Nrows_3 = {(R_4 - R_3)}\big/{\Delta R_{\min}} \cong round({4R_1}\big/{\Delta R_{\min}}) \tag{17}$$

$Nrows_1$, $Nrows_2$, and $Nrows_3$ refer to number of rows of first, second, and third zone, respectively. Note that in the above equations, the minimum radial distance given by equation (9) was used to calculate the number of rows.

3.1.5 Number of heliostats

There are two types of conventional heliostat field layouts, the polar (or northern for the northern hemisphere) and the surround heliostat field. The mathematical equations for calculating the number of heliostats for both types of fields are given below.

3.1.5.1 Polar or Northern Field

Number of heliostats per row is defined as

For odd rows

$$Nhel_i = 2 \times round(\frac{\psi_{\max} - \Delta\alpha z_i / 2}{\Delta\alpha z_i}) + 1 \tag{18}$$

For even rows

$$Nhel_i = 2 \times round(\psi_{\max} / \Delta\alpha z_i) + 1 \tag{19}$$

where $\psi_{\max}$ is the maximum angular distance from north axis to the last heliostat in radians.

3.1.5.2 Surround Field

Number of heliostats in each row for the first zone is defined as

$$Nhel_1 = 2\pi / \Delta\alpha z_1 = 2\pi R_1 / DM \Rightarrow R_1 = Nhel_1 DM / 2\pi \tag{20}$$

where *Nhel*$_1$ are the number of heliostats per row in the first zone.

Similarly, for the second zone and the third zone,

$$Nhel_2 = 2\pi / \Delta\alpha z_2 = 2\pi R_2 / DM = 4\pi R_1 / DM \tag{21}$$

$$Nhel_3 = 2\pi / \Delta\alpha z_3 = 2\pi R_3 / DM = 8\pi R_1 / DM \tag{22}$$

where *Nhel*$_2$ and *Nhel*$_3$ are number of heliostats in each row in the second and the third zone, respectively.

It can be observed from the above equations that R_1 is function of *Nhel*$_1$ and *DM*. By varying the azimuthal spacing during the optimization process, the factor *DM* will change and in turn will control the radius R_1, i.e. the radius of the first ring of the heliostats from the tower.

3.1.6 Radius of the first ring of the zones

The radius of the first ring of different zones can then be calculated as

$$R_i = \max((2R_{i-1}),(R_{i-1} + (Nrows_{i-1} - 1)x_{2,i-1}\Delta R_{\min} + x_{2,i-1}\Delta R_{\min})) \tag{23}$$

where *i* denotes the zone number and this equation is valid from zone 2 and onwards. By incorporating this equation, the distance between the last and the first row at the zone boundary is also optimized. Note that by using the command “max”, the code chooses the maximum value, either controlled by the azimuthal spacing or the radial spacing or both of these simultaneously so that the heliostats do not cross each other’s territories at the zone boundaries.

3.1.7 Land area covered by the heliostat field

The land area covered by the heliostat field radially outwards from the center of the tower towards the last row of the last zone can be calculated as

$$A_l = \pi(R_{last} + 0.5DM)^2 \tag{24}$$

where A_l is the land area covered by the heliostat field and R_{last} is the radius of the last row of the last zone of the heliostat field.

3.2 Solar positioning model

In order to calculate the instantaneous optical efficiency of the heliostat field, it is necessary to include a solar positioning model which can be defined as [84]

$$\delta = \frac{23.45\pi}{180}\sin(2\pi\frac{284 + n_d}{365}) \tag{25}$$

$$\omega_{sunrise} = \cos^{-1}(\tan\phi\tan\delta) - \pi = -\omega_{sunset} \tag{26}$$

$$\alpha_s = \sin^{-1}(\cos\phi\cos\delta\cos\omega_s + \sin\phi\sin\delta) \tag{27}$$

$$\gamma_s = \mathrm{sgn}(\omega_s)\left|\cos^{-1}\frac{\sin\alpha_s\sin\phi - \sin\delta}{\cos\alpha_s\cos\phi}\right| \tag{28}$$

where δ is the solar declination angle, ω_s is the hour angle, n_d is the day of the year, ϕ is the latitude angle, α_s is the solar altitude, and γ_s is solar azimuth angle. Note that all angles are in radians.

3.3 Optical efficiency of the heliostat field

The total optical efficiency as defined by [41,85] is

$$\eta_{opt}(x,y,t) = \rho\cos\omega(x,y,t)\, f_{at}(x,y)\, f_{sb}(x,y,t)\, f_{itc}(x,y,t) \tag{29}$$

where ρ is the reflectivity of the heliostats, $\cos\omega$ is the incidence cosine between the incident sun ray and the normal to the heliostat surface, f_{sb} is the shadowing and blocking factor, f_{itc} is the intercept factor accounting for the fraction of the reflected rays intercepted by the receiver, and f_{at} is the atmospheric attenuation efficiency. *x*, *y*, and *t* represent the two co-ordinates (Figure 3.1 and Figure 3.3) and time, respectively.

3.3.1 Cosine factor

The cosine factor is calculated using the law of specular reflection. The dot product of unitary sun vector (pointing towards the sun) and the unit normal vector to the heliostat surface gives us the cosine efficiency, which is defined as

$$\cos\omega = \widehat{d}_{sun} \cdot \widehat{d}_n \tag{30}$$

It can also be calculated from the dot product of unitary vector pointing towards the receiver and the unit normal vector to the heliostat surface, as given below

$$\cos\omega = \widehat{d}_{rec} \cdot \widehat{d}_n \tag{31}$$

where the unit normal vector of the heliostat surface can be calculated as :

$$\widehat{d}_n = \frac{\widehat{d}_{rec} + \widehat{d}_s}{|\widehat{d}_{rec} + \widehat{d}_s|} \tag{32}$$

$\widehat{d}_{rec}$ and $\widehat{d}_s$ represent the unit vector pointing towards the receiver and the sun respectively.

3.3.2 Atmospheric attenuation factor

The atmospheric attenuation efficiency calculates the beam losses of the reflected ray from the heliostat to the receiver and is given by [29,86]

$$f_{at} = 0.99321 - 0.0001176 S_{rec} + 1.97 \times 10^{-8} S_{rec}^2 \qquad \text{if} \qquad S_{rec} < 1000m \tag{33}$$

$$f_{at} = \exp(-0.0001106 S_{rec}) \qquad \text{if} \qquad S_{rec} \geq 1000m \tag{34}$$

where S_{rec} is the slant distance from the heliostat to the receiver.

3.3.3 Shadowing and blocking factor

The shadowing and blocking factor is defined as the fraction of the area of the heliostat that is free of shadowing and blocking. This factor was calculated using the procedure outlined in [33,41,87,88]. In this method, the projections of the edge points of the affecting heliostats are used on the problem heliostat. Due to the radial staggered configuration, the blocking heliostats are clearly defined, two in the next inner row, (named as shoulder blocking) and one in the inner second row directly in the front (named as nose blocking) [41]. As for shadowing, the shadowing heliostats are not clearly defined due to a continuous change in position of the sun with time. Accordingly, a total of nine surrounding heliostats were used in the modeling for projection onto the affecting heliostats. Moreover, the blocking heliostats were also checked for shadowing; in which fifteen projections were examined to calculate the shadowing and blocking factor. In the current study, the accuracy of the calculated shadowing and blocking factor is enhanced because we have selected fifteen projections. For simplification, the heliostats were taken as parallel planes. This approach implies that it is only necessary to project the center points of the affecting heliostats [41].

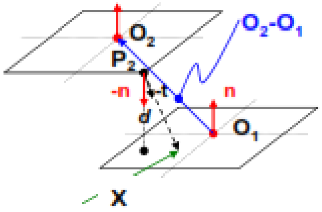

Figure 3.4 Projection following $-\hat{t}\,(-\hat{d}_{rec})$ **for parallel planes** [87]

Based on rules of geometry, the projection of one heliostat onto other (Figure 3.4) while considering them as parallel planes can be calculated using the following equations[87]

$$d=\hat{d}_n\cdot(\mathrm{O}_2-\mathrm{O}_1)=\lambda(\hat{t}\cdot\hat{n})=\lambda(\hat{d}_{rec}\cdot\hat{d}_{\mathrm{n}}) \tag{35}$$

$$\Rightarrow \lambda=\frac{(\mathrm{O}_2-\mathrm{O}_1)\cdot\hat{d}_n}{\hat{d}_{rec}\cdot\hat{d}_n} \tag{36}$$

$$(X - O_1) = \mathrm{P}_2 - \mathrm{O}_1 - \lambda \cdot \hat{d}_{rec} \tag{37}$$

Then the projection can be converted to a local coordinate system placed on the surface of the problem heliostat by the following equation:

$$TH = \begin{pmatrix} 1 & 0 & 0 \\ 0 & \cos\theta_n & \sin\theta_n \\ 0 & -\sin\theta_n & \cos\theta_n \end{pmatrix} \begin{pmatrix} \cos\gamma_n & -\sin\gamma_n & 0 \\ \sin\gamma_n & \cos\gamma_n & 0 \\ 0 & 0 & 1 \end{pmatrix} \tag{38}$$

where γ_n (origin South and positive towards West) and θ_n are the azimuthal and the zenith angle (complement of the altitude angle α_n) of the unit normal vector of the concerned heliostat.

3.3.3.1 The Sassi Procedure

As explained by Sassi [33], the heliostat is then divided into ‘n’ narrow vertical stripes and the height of the projection of the possible blocking or shadowing heliostat in each stripe is evaluated and so the mirror area that is free of blocking or shadowing is calculated based on these heights. During the process, the height is continuously updated for each stripe if a higher value has been found.

3.3.3.2 Validation of the shadowing and blocking factor

The shadowing and blocking factor calculation was validated with the Campo code [41]. In the current code, the total number of projections that were projected were 15 to enhance the accuracy, whereas, the campo code uses a total of 9 projections which cover the worst cases but reduces the computation time. Although the extra projections examined will have no or minor contribution to the shadowing and blocking factor calculation and it will further increase the computation time, but this will take into account those little contributions to the overlapping area for the calculation of shadowing and blocking factor. Therefore, the average shadowing and blocking factor for the whole heliostat field computed with this code was slightly less due to accumulative effect of 15 projections as compared with the 9 projections of the Campo code. The validation is demonstrated in Table 3.1. For case 1, the difference in the calculated values is higher because of closely packed heliostats, whereas for case 2 in the Table, the difference is smaller as compared to case 1 because of the increased distance between the heliostats and less projections causing the shadowing and blocking. Lastly, for case 3, the shadowing and blocking is caused by essentially the same projections of the heliostats for both codes because of solar noon, therefore the difference in the calculated values is almost negligible. These particular time instants were selected because for these time instants the calculation of shadowing and blocking factor was demonstrated in [41].

Table 3.1 Validation of the calculation of the shadowing and blocking factor

Sr. #	Case	current code	Campo code
1	Day 345, solar hour 9, *dsep*=0	0.6246	0.676
2	Day 345, solar hour 9, *dsep*=3	0.7113	0.747
3	Day 81, solar hour 12, *dsep*=0	0.7936	0.794

3.3.4 Intercept factor

The intercept factor is defined as the fraction of the reflected rays by the heliostat intercepted by the receiver. For the calculation of the intercept factor, the HFLCAL[28] model was used. The flux density expression of the HFCAL model is a circular normal distribution on the receiver plane and is given as

$$f_{itc} = \frac{1}{2\pi\sigma_{tot}^2} \int_{x'}\int_{y'} \exp\left(-\frac{x'^2 + y'^2}{2\sigma_{tot}^2}\right) dy'.dx' \tag{39}$$

where σ_{tot} is the total standard deviation on the receiver plane which is a result of convolution of four error functions, sun shape error σ_{sun} (standard deviation sun), beam quality error σ_{bq} , astigmatic error σ_{ast} , and tracking error σ_{track} . Here, x' and y' are the co-ordinates on the receiver plane.

The total standard deviation is given by

$$\sigma_{tot} = \sqrt{S_{rec}^2(\sigma_{sun}^2 + \sigma_{bq}^2 + \sigma_{ast}^2 + \sigma_t^2)} \tag{40}$$

The beam quality error can be defined as

$$\sigma_{bq}^2 = (2\sigma_s^2) \tag{41}$$

where σ_s is the mirror slope error caused by the imperfections of the mirror surface. This error is described statistically through a circular normal distribution. It is defined with respect to the surface normal vector, hence its effect is doubled in the reflected ray [28,29] as can be observed from the above equation.

The equivalent Gaussian circular distribution is defined as[89]

$$\sigma_s^2 = \frac{\sigma_h^2 + \sigma_v^2}{2} \tag{42}$$

where σ_h and σ_v are the horizontal and the vertical elliptical Gaussian distribution which here are assumed that of the slope error [42].

The standard deviation of astigmatic effect is defined as [28]

$$\sigma_{ast} = \frac{\sqrt{0.5(H_t^2 + W_s^2)}}{4S_{rec}} \tag{43}$$

where W_s and H_t are the image dimensions in the sagital and the tangential planes at distance S_{rec} from the mirror and are given by the following formulas

$$H_t = d_g \left| \frac{S_{rec}}{f} - \cos\omega \right| \tag{44}$$

$$W_s = d_g \left| \frac{S_{rec}}{f} \cos\omega - 1 \right| \tag{45}$$

where f is equal to the focal distance of the heliostat which was taken equal to S_{rec} and d is the general dimension of the heliostat and is assumed equal to the square root of the heliostat area [42].

$$d_g = \sqrt{LW \times LH} \tag{46}$$

For the sake of our analysis the standard deviation of sunshape error was assumed to be equal to the same value as the one selected in [90].

3.4 Optimization

Different approaches for the optimization of the heliostat on annual basis is discussed and presented. Moreover, the differential evolution optimization algorithm is discussed in detail and presented.

3.4.1 Differential evolution (DE) algorithm

The differential evolution is a population based optimization technique, which is characterized by its simplicity, robustness, few control variables, and fast convergence [91–93]. Because the DE technique is an evolutionary algorithm, it is suited for non-linear and non-differentiable optimization problems as well.

The strategy applied in this technique is to use the difference between randomly selected vectors to generate a new solution. For each solution in the original population, a trial solution is generated by performing the process of mutation, recombination, and selection operations. The old and new solutions are compared and the best solutions emerge in the next generation.

Vesterstrom and Thomsen [94] compared the DE with a well-known particle swarm optimization technique and it was concluded by the authors that the DE has better performance. Furthermore, the DE in most instances as compared to the annealed Nelder and Mead approach, adaptive simulating annealing and the breeder genetic algorithm outperformed all of the aforementioned optimization techniques in terms of the required number of function evaluations necessary to locate a global optimum of the test functions [93]. In addition, for several case studies; proof of convergence of global optimum solution by DE was shown in [92]. DE may not always be the fastest method; it is usually the one that produces the best results, although the number of cases in which it is also faster is significant. DE also proves itself to be robust, both in how the control parameters are chosen and in the regularity with which it finds the true optimum [92]. On the other hand, in a detailed review study by Das and Suganthan [95], it was concluded that DE exhibits remarkable performance in optimizing a wide variety of multi dimensional, multi objective and multimodal optimization problems. Therefore, the DE was selected in this study.

In this study, the differential evolution was programmed in Matlab as a minimization function, i.e. it will always minimize the objective function. Therefore, in order to maximize the objective function, the negative of the objective function is minimized, which in turn maximizes the objective function. The differential evolution generally performs three steps: initialization, creating new trial generation, and selection as explained next. Figure 3.5 shows the flow chart of the procedure of the differential evolution algorithm.

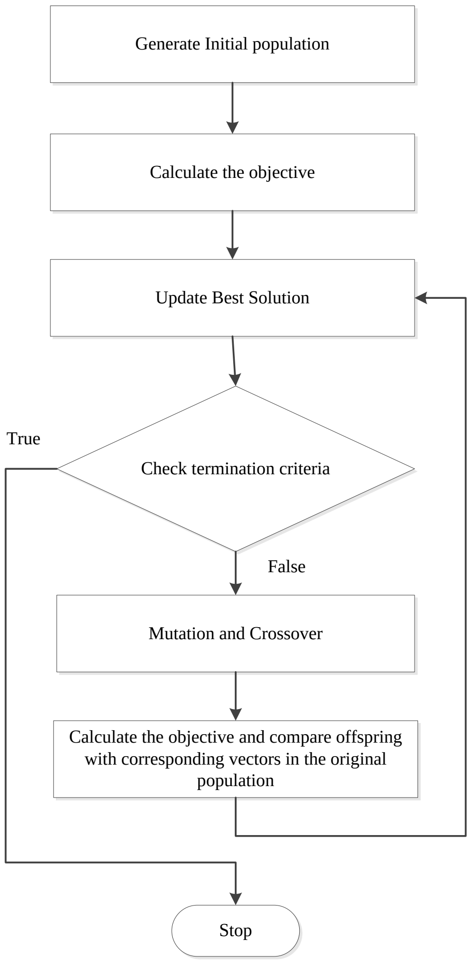

Figure 3.5 Flow chart summarizing the procedure of differential evolution

3.4.1 Initialization of population

The initialization of population used in the optimization is described next. First, vectors of initial population are generated equivalent to the population size. Values of various control variables, (in our case the optimizing parameters i.e. the radial and the azimuthal spacing) which represent a candidate solution are included in each of these vectors. This is accomplished by passing on random values for each parameter of solution, within the range defined for the corresponding variable. In an equation form, it can be defined as

$$\mathrm{X}_{i,j} = \mathrm{X}_{j,\min} + random\#(\mathrm{X}_{j,\max} - \mathrm{X}_{j,\min}) \tag{47}$$

where *i*=1-population size; *j*=1-number of control variables and X is any control variable.

3.4.2 Evaluating and finding the best solution

After the formation of initial population, the objective value (or the optical efficiency in our case) of each vector is evaluated and compared. Therefore, an optimal solution is obtained, and its value is stored externally and updated by comparison with all the values in each generation.

3.4.3 Mutation operation

For every solution (individual) X_i in the population in generation-i, a mutant vector V_i is generated using the following formula:

$$V_i^{(G+1)} = X_i^{(G)} + F(X_{best}^{(G)} - X_i^{(G)})) + F(X_{r1}^{(G)} - X_{r2}^{(G)}) \tag{48}$$

where $X_{r1}^{(G)}$ and $X_{r2}^{(G)}$ are randomly selected solution parameters from the i*th* generation which are different from each other. The variable $F \in [0,1]$ is the mutation factor, which is defined by the user and it depends upon the type of problem to be optimized, and $X_{best}^{(G)}$ is the solution that attaining the best value.

3.4.4 Crossover operation

The crossover operation is applied to further perturb the generated solutions and enhance the diversity. This is done by copying the parameters of the generated mutant vector and its corresponding vector *i* in the original population according to a crossover factor denoted by $CR \in [0,1]$. For each parameter, a random number in the range [0,1] is generated and compared with CR, and if its value is greater than or equal to *CR*, the parameter value is taken from the parent vector; otherwise, it will be taken from the mutant [96]. The process of the crossover operation is shown in Figure 3.6.

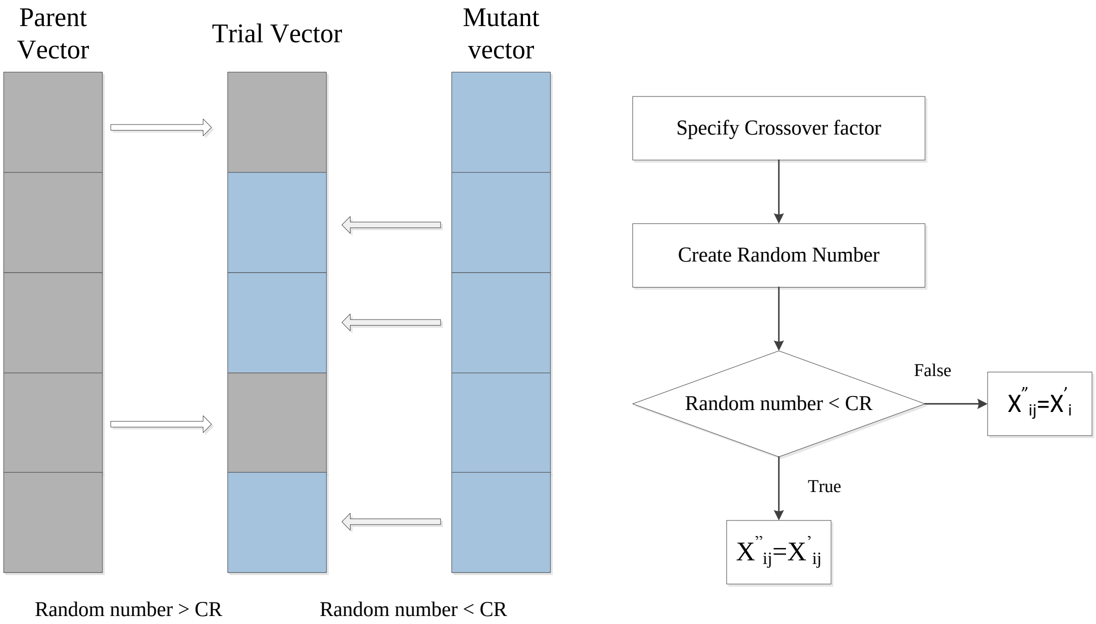

Figure 3.6 Crossover operation

3.4.6 Selection procedure

For the selection procedure, normally the solutions of the old population are compared with trial solutions for the generation of a new population. For this purpose, the objective function corresponding to each trial solution is evaluated and compared with the value of the parent solution. If the new solution does not perform better, the old solution is retained; otherwise, the new solution replaces the parent solution. Nevertheless, in this study, a special selection procedure was applied called the tournament selection. In this procedure, a group of solutions is randomly selected, in which these solutions are made to take part in a tournament (hence the name tournament selection came). That is, the solution which gives the best value for the objective function is selected. The main advantage of this procedure is that the best solutions will not dominate in the reproduction process and the worst solutions will not contribute to the construction of the next generation.

3.4.7 Termination criteria

After a new generation is formed, the algorithm updates the global best solution. Usually, a maximum number of iterations are defined as a termination or a stopping criterion. These criteria can also be defined by the user.

3.4.2 Daily averaged annual optimization

The following equation is used for calculating the daily averaged annual optical efficiency of the heliostat field:

$$\eta_{daa} = \frac{\sum_{j=1}^{365} \int_{t=sunrise}^{t=sunset} \eta_{opt} dt}{\sum_{j=1}^{365} \int_{t=sunrise}^{t=sunset} dt} \tag{49}$$

where η_{daa} is daily averaged annual heliostat field efficiency, the subscript *daa* denotes daily annual averaged, and *j* denotes the day of the year.

3.4.3 Insolation weighted daily averaged annual optimization

The following equation is used for calculating the insolation weighted daily averaged annual optical efficiency of the heliostat field [31]

$$\eta_{iwaa} = \frac{\sum_{j=1}^{365} \int_{t=sunrise}^{t=sunset} I \eta_{opt} dt}{\sum_{j=1}^{365} \int_{t=sunrise}^{t=sunset} I dt} \tag{50}$$

where η_{iwaa} is the insolation weighted daily averaged annual heliostat field efficiency, the subscript *iwaa* denotes insolation weighted annual averaged, and *j* denotes the day of the year.

3.4.4 Monthly averaged annual optimization

The following equation is used for calculating the monthly averaged annual optical efficiency of the heliostat field

$$\eta_{maa} = \frac{\sum_{j=1}^{12} \int_{t=sunrise}^{t=sunset} \eta_{opt} dt}{\sum_{j=1}^{12} \int_{t=sunrise}^{t=sunset} dt} \tag{51}$$

where η_{maa} is monthly averaged annual heliostat field efficiency, the subscript *maa* denotes monthly annual averaged, and *j* denotes the average day of each month from January to December for the whole year as given by Duffie and Beckman [84,97]. These days have been listed in Table 3.2

Table 3.2 Recommended average days of month [84,97]

	Month	Average day of Month (Date)	Day of the year (n_d)
1	January	17	17
2	February	16	47
3	March	16	75
4	April	15	105
5	May	15	135
6	June	11	162
7	July	17	198
8	August	16	228
9	September	15	258
10	October	15	288
11	November	14	318
12	December	10	344

3.5 Central receiver

The optical losses, heat radiation losses, and the convection heat losses were considered for the modeling of the central receiver as discussed next.

3.5.1 Radiation heat losses

The equation for the radiation heat losses from the central receiver was given by Sheu and Mitsos [50] as

$$Q_{rad} = F_{view} A_R \varepsilon \sigma (T_R + 273.15)^4 \tag{52}$$

where F_{view} is the radiation shape factor, A_R is the radiative area of the central receiver, ε is emissivity of the receiver, σ is the Stefan Boltzmann constant, and T_R is the receiver temperature.

3.5.2 Convection heat losses

The equation for convection heat losses from the central receiver is given as

$$Q_{conv} = A_R h_{conv}(T_R - T_{amb}) \tag{53}$$

where h_{conv} is calculated by Bejan correlation [98] for vertical chamber with natural convection and is defined as

$$h_{conv} = 0.557 \times 10^{-6} (\frac{T_R - T_{amb}}{H_{tower}})^{0.25} [\mathrm{kW/\,m^2 - {}^\circ C}] \tag{54}$$

where H_{tower} is the total height of the solar tower and T_{amb} is the ambient temperature.

3.5.3 Receiver thermal efficiency

The receiver thermal efficiency is defined as:

$$\eta_{th,R} = \frac{Q_{net}}{Q_{in}} \tag{55}$$

where

$$Q_u = Q_{net} = \alpha_R Q_{in} - (Q_{rad} + Q_{conv}) \tag{56}$$

$$Q_{in} = \eta_{opt} Q_{solar} \tag{57}$$

and

$$Q_{solar} = I A_h \tag{58}$$

Here, α_R is the absorptivity of the receiver, I is the direct normal incident radiation, A_h is the total area of the heliostats, Q_u (or Q_{net}) is the net useful energy gained at the receiver, Q_{solar} is the total incident radiation on the heliostats, and Q_{in} is the net energy intercepted at the receiver.

3.6 Supercritical CO_2 Brayton cycle modeling

The closed loop sCO_2 Brayton cycles were modeled using EES [99]. The modeling of five different cycles is presented next.

3.6.1 Simple closed loop sCO_2 Brayton cycle

The simple Brayton cycle (Figure 3.7) consists of a single compressor, a single turbine, a cooler and a heat source, which is the central receiver in our case. The net power output, the thermal efficiency, and the turbine inlet temperature are not high for this cycle because a lot of energy, which can be recuperated, is wasted. This cycle can be modeled using the following equations.

The compressor power is defined as

$$W_c = \dot{m}(h_2 - h_1) \tag{59}$$

where $\dot{m}$ is the mass flow rate of CO_2, and h is the specific enthalpy.

The isentropic efficiency of the compressor is defined as

$$\eta_c = \frac{h_{2s} - h_1}{h_2 - h_1} \tag{60}$$

The useful energy gained at the receiver is given as

$$Q_u = \dot{m}(h_3 - h_2) \tag{61}$$

The turbine power is defined as

$$W_T = \dot{m}(h_3 - h_4) \tag{62}$$

The isentropic efficiency of the turbine is defined as

$$\eta_T = \frac{h_3 - h_4}{h_3 - h_{4s}} \tag{63}$$

The energy rejected at the cooler is given by

$$Q_{out} = \dot{m}(h_4 - h_1) \tag{64}$$

The net power output of the cycle is defined as

$$W_{net} = W_T - W_C \tag{65}$$

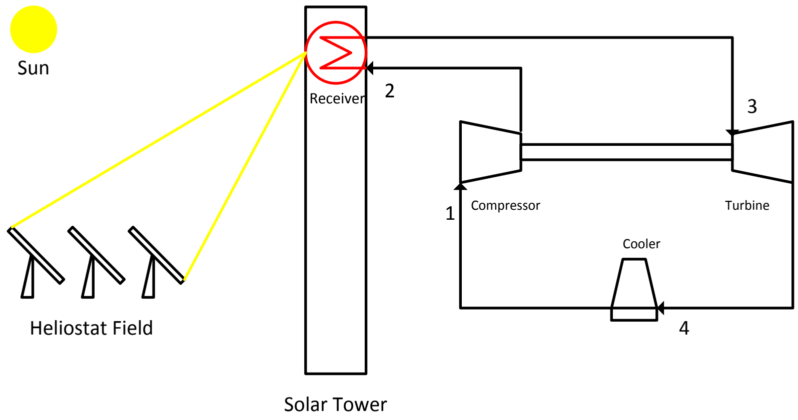

Figure 3.7 Simple closed loop supercritical carbon dioxide Brayton cycle

3.6.2 Regenerative closed loop sCO$_2$ Brayton cycle

For the case of regenerative Brayton cycle (Figure 3.8), one extra component is added to the configuration called the regenerator. The regenerator helps to recuperate the excess energy at the turbine exhaust. This cycle can be modeled using the following equations.

The compressor power is defined as

$$W_c = \dot{m}(h_2 - h_1) \tag{66}$$

The isentropic efficiency of the compressor is defined as

$$\eta_c = \frac{h_{2s} - h_1}{h_2 - h_1} \tag{67}$$

The effectiveness of the regenerator is defined as

$$\varepsilon_R = \frac{h_5 - h_2}{h_4 - h_2} \tag{68}$$

The useful energy gained at the receiver is given as

$$Q_u = \dot{m}(h_3 - h_5) \tag{69}$$

The turbine power is defined as

$$W_T = \dot{m}(h_3 - h_4) \tag{70}$$

The isentropic efficiency of the turbine is defined as

$$\eta_T = \frac{h_3 - h_4}{h_3 - h_{4s}} \tag{71}$$

Applying energy balance on the regenerator to obtain

$$h_5 - h_2 = h_4 - h_6 \tag{72}$$

The energy rejected at the cooler is given by

$$Q_{out} = \dot{m}(h_6 - h_1) \tag{73}$$

The net power output of the cycle is defined as

$$W_{net} = W_T - W_C \tag{74}$$

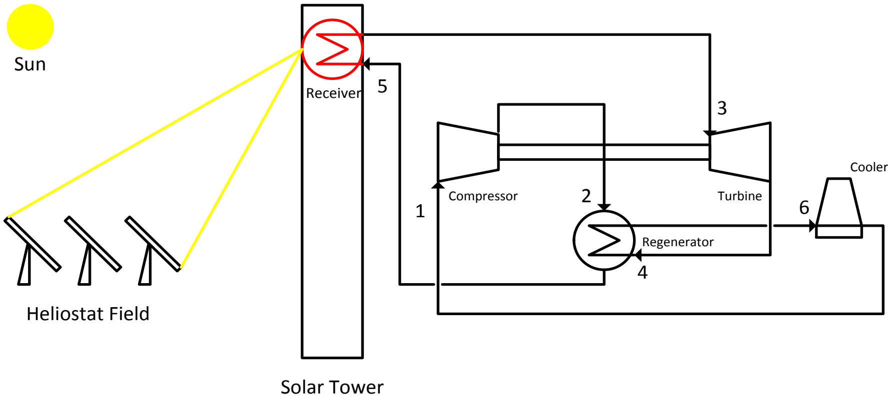

Figure 3.8 Regenerative closed loop supercritical carbon dioxide Brayton cycle

3.6.3 Pre-compression closed loop Brayton cycle

The pre-compression Brayton cycle (Figure 3.9) has two regenerators: one is a high temperature regenerator and the other is a low temperature regenerator; and two compressors. The advantage of this arrangement is the placement of the additional compressor, which makes place for further regeneration. This cycle can be modeled using the following equations.

The power input of the first compressor is defined as

$$W_c = \dot{m}(h_2 - \mathrm{h}_1) \tag{75}$$

The power input of the second compressor is defined as

$$W_{c2} = \dot{m}(h_9 - \mathrm{h}_8) \tag{76}$$

The isentropic efficiency of the first compressor is defined as

$$\eta_c = \frac{h_{2s} - h_1}{h_2 - h_1} \tag{77}$$

The isentropic efficiency of the second compressor is defined as

$$\eta_{c2} = \frac{h_{9s} - h_8}{h_9 - h_8} \tag{78}$$

The effectiveness of the high temperature regenerator is defined as

$$\varepsilon_{HTR} = \frac{h_5 - h_7}{h_4 - h_7} \tag{79}$$

The effectiveness of the low temperature regenerator is defined as

$$\varepsilon_{LTR} = \frac{h_7 - h_2}{h_9 - h_2} \tag{80}$$

The useful energy gained at the receiver is given as

$$Q_u = \dot{m}(h_3 - h_5) \tag{81}$$

The turbine power can be defined as

$$W_T = \dot{m}(h_3 - h_4) \tag{82}$$

The isentropic efficiency of the turbine is defined as

$$\eta_T = \frac{h_3 - h_4}{h_3 - h_{4s}} \tag{83}$$

Applying the energy balance on the high temperature regenerator to obtain

$$h_4 - h_8 = h_5 - h_7 \tag{84}$$

Applying the energy balance on the low temperature regenerator to obtain

$$h_7 - h_2 = h_9 - h_6 \tag{85}$$

The energy rejected at the cooler is defined as

$$Q_{out} = \dot{m}(h_6 - h_1) \tag{86}$$

The net power output of the cycle is defined as

$$W_{net} = W_T - W_C - W_{C2} \tag{87}$$

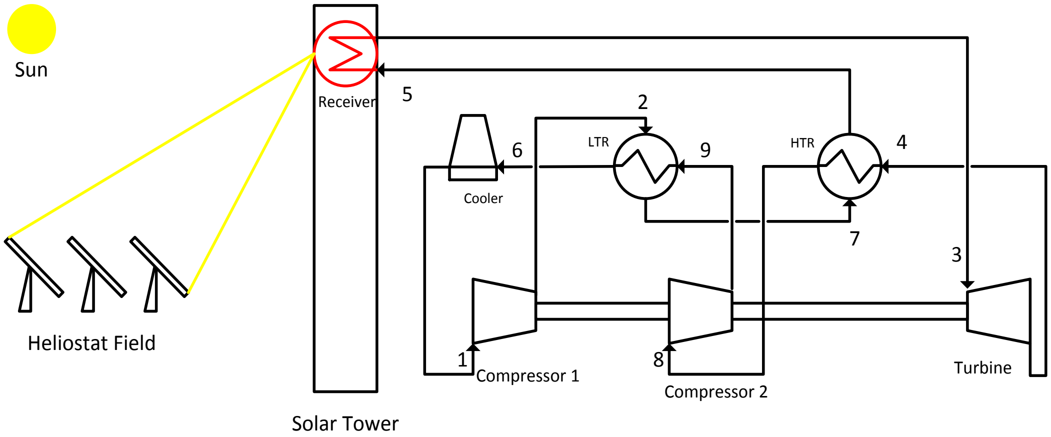

Figure 3.9 Pre-compression closed loop supercritical carbon dioxide Brayton cycle

3.6.4 Re-compression closed loop Brayton cycle

The recompression Brayton cycle (Figure 3.10) has the same number of components as the pre-compression Brayton cycle but with a different arrangement. In this cycle, the flow is split into two streams after the low temperature regenerator and before passing through the cooler. These two streams are the one that flows to the main compressor through the cooler and the other one flows to the recompression compressor. Consequently, the system rejects less heat and the compressor work is reduced, which in turn causes the thermal efficiency to improve. The modeling of this cycle is presented as follows.

The power input of the first compressor is defined as

$$W_c = x_{mass}\dot{m}(h_2 - h_1) \tag{88}$$

where x_{mass} is the fraction of the mass flow rate through the first compressor.

The power input of the second compressor is defined as

$$W_{c2} = (1 - x_{mass})\dot{m}(h_{10} - h_6) \tag{89}$$

The isentropic efficiency of the first compressor is defined as

$$\eta_c = \frac{h_{2s} - h_1}{h_2 - h_1} \tag{90}$$

The isentropic efficiency of the second compressor is defined as

$$\eta_{c2} = \frac{h_{10s} - h_6}{h_{10} - h_6} \tag{91}$$

The effectiveness of the high temperature regenerator is defined as

$$\varepsilon_{HTR} = \frac{h_5 - h_8}{h_4 - h_8} \tag{92}$$

The effectiveness of the low temperature regenerator is defined as

$$\varepsilon_{LTR} = \frac{h_7 - h_2}{h_9 - h_2} \tag{93}$$

The useful energy gained at the receiver is defined as

$$Q_u = \dot{m}(h_3 - h_5) \tag{94}$$

The turbine power can be defined as

$$W_T = \dot{m}(h_3 - h_4) \tag{95}$$

The isentropic efficiency of the turbine is defined as

$$\eta_T = \frac{h_3 - h_4}{h_3 - h_4} \tag{96}$$

Applying the energy balance on the high temperature regenerator to obtain

$$h_4 - h_9 = h_5 - h_8 \tag{97}$$

Applying the energy balance on the low temperature regenerator to obtain

$$x_{mass}(h_7 - h_2) = h_9 - h_6 \tag{98}$$

The energy rejected at the cooler is defined as

$$Q_{out} = x_{mass}\dot{m}(h_6 - h_1) \tag{99}$$

The net power output of the cycle is defined as

$$W_{net} = W_T - W_C - W_{C2} \tag{100}$$

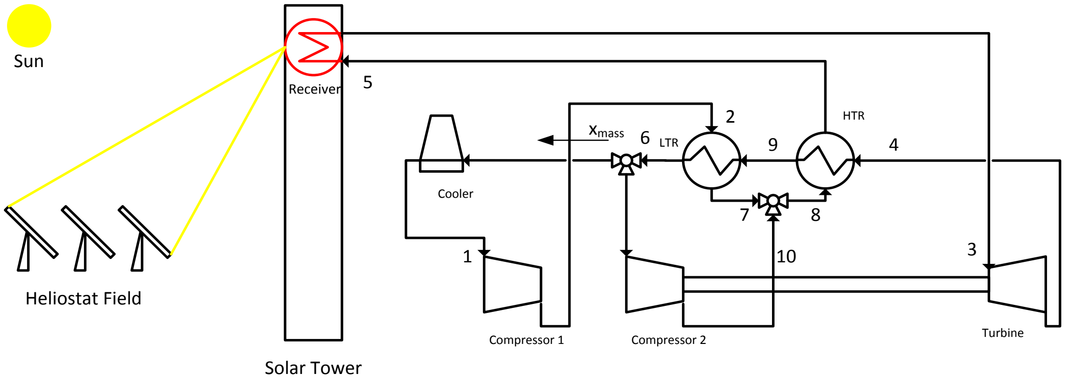

Figure 3.10 Re-compression closed loop supercritical carbon dioxide Brayton cycle

3.6.5 Split expansion closed loop Brayton cycle

Finally, the split expansion Brayton cycle (Figure 3.11) has the same configuration as that of the recompression cycle but the expansion is performed in two stages by introducing an additional turbine; and the heat addition process takes place in between the two stages of fluid expansion. This cycle can be modeled using the following equations.

The power input of the first compressor is defined as

$$W_c = x_{mass}\dot{m}(h_2 - \mathrm{h}_1) \tag{101}$$

The power input of the second compressor is defined as

$$W_{c2} = (1 - x_{mass})\dot{m}(h_{10} - \mathrm{h}_6) \tag{102}$$

The isentropic efficiency of the first compressor is defined as

$$\eta_c = \frac{h_{2s} - h_1}{h_2 - h_1} \tag{103}$$

The isentropic efficiency of the second compressor is defined as

$$\eta_{c2} = \frac{h_{10s} - h_6}{h_{10} - h_6} \tag{104}$$

The effectiveness of the high temperature regenerator is defined as

$$\varepsilon_{HTR} = \frac{h_5 - h_8}{h_4 - h_8} \tag{105}$$

The effectiveness of the low temperature regenerator is defined as

$$\varepsilon_{LTR} = \frac{h_7 - h_2}{h_9 - h_2} \tag{106}$$

The useful energy gained at receiver is defined as

$$Q_u = \dot{m}(h_3 - h_{11}) \tag{107}$$

The power of the first turbine is defined as

$$W_T = \dot{m}(h_5 - h_{11}) \tag{108}$$

The power of the second turbine can be defined as

$$W_{T2} = \dot{m}(h_3 - h_4) \tag{109}$$

The isentropic efficiency of the first turbine is defined as

$$\eta_T = \frac{h_5 - h_{11}}{h_5 - h_{11s}} \tag{110}$$

The isentropic efficiency of the second turbine is defined as

$$\eta_{T2} = \frac{h_3 - h_4}{h_3 - h_{4s}} \tag{111}$$

Applying the energy balance on the high temperature regenerator to obtain

$$h_4 - h_9 = h_5 - h_8 \tag{112}$$

Applying the energy balance on the low temperature regenerator to obtain

$$x_{mass}(h_7 - h_2) = h_9 - h_6 \tag{113}$$

The energy rejected at the cooler is defined as

$$Q_{out} = x_{mass}\dot{m}(h_6 - h_1) \tag{114}$$

The net power output of the cycle is defined as

$$W_{net} = W_T + W_{T2} - W_C - W_{C2} \tag{115}$$

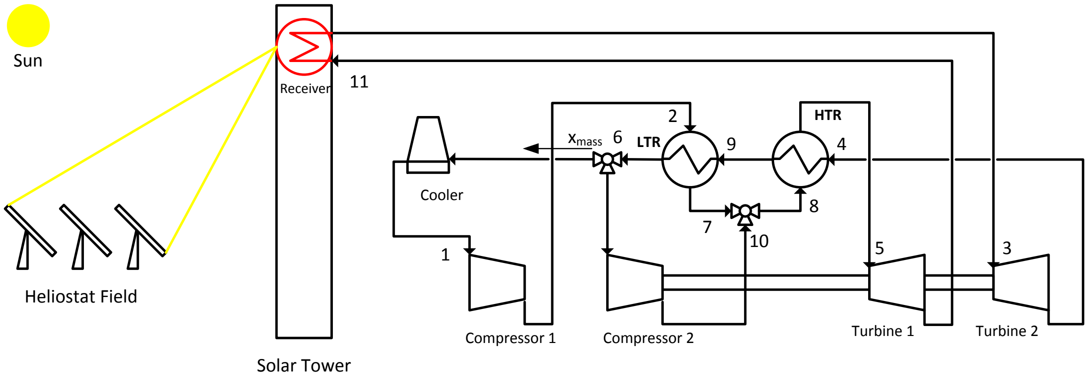

Figure 3.11 Split Expansion closed loop supercritical carbon dioxide Brayton cycle

3.6.6 Thermal efficiency of the Brayton cycles

The thermal efficiency for all the Brayton cycles is given by

$$\eta_{th} = \frac{W_{net}}{Q_u} \tag{116}$$

3.6.7 Validation of sCO_2 modeling

To validate our results for sCO_2 modeling, a recompression Brayton cycle was modeled using EES [99] and the results were compared with the data (Figure 3.12) presented in [100]. Temperature (T) – entropy (s) diagram was plotted to compare our modeling results with the aforementioned reference data as shown in Figure 3.13. It can be observed from the figure that our modeling is in a good agreement with the cycle in the reference presented. It should be further noted that in EES, the values of specific enthalpy and specific entropy are, by default, referred to values of 0 at 25° C and 101.325 kPa.

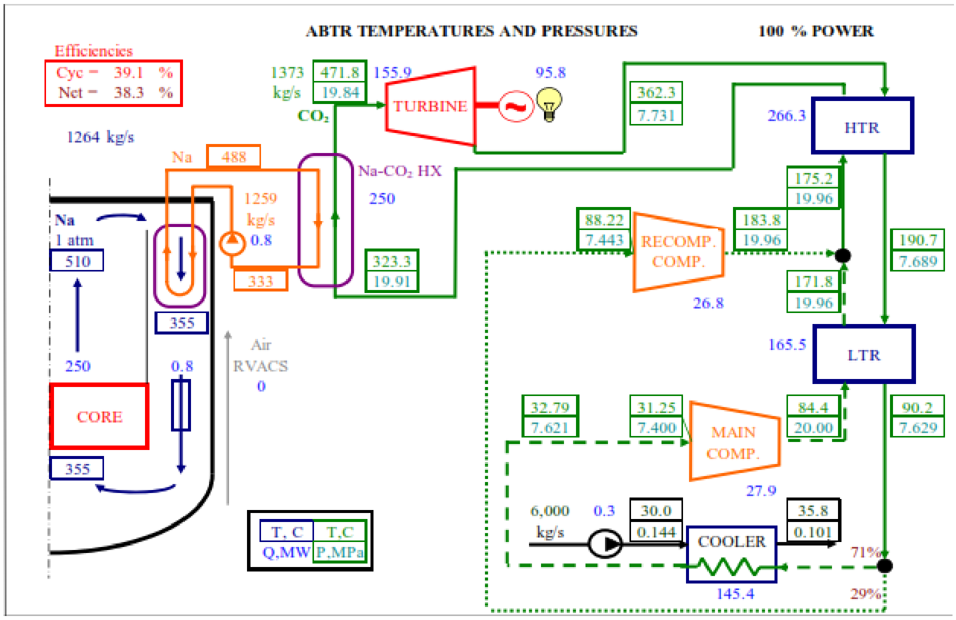

Figure 3.12 A re-compression closed loop sCO_2 Brayton cycle (Figure 2 of reference [100]**)**

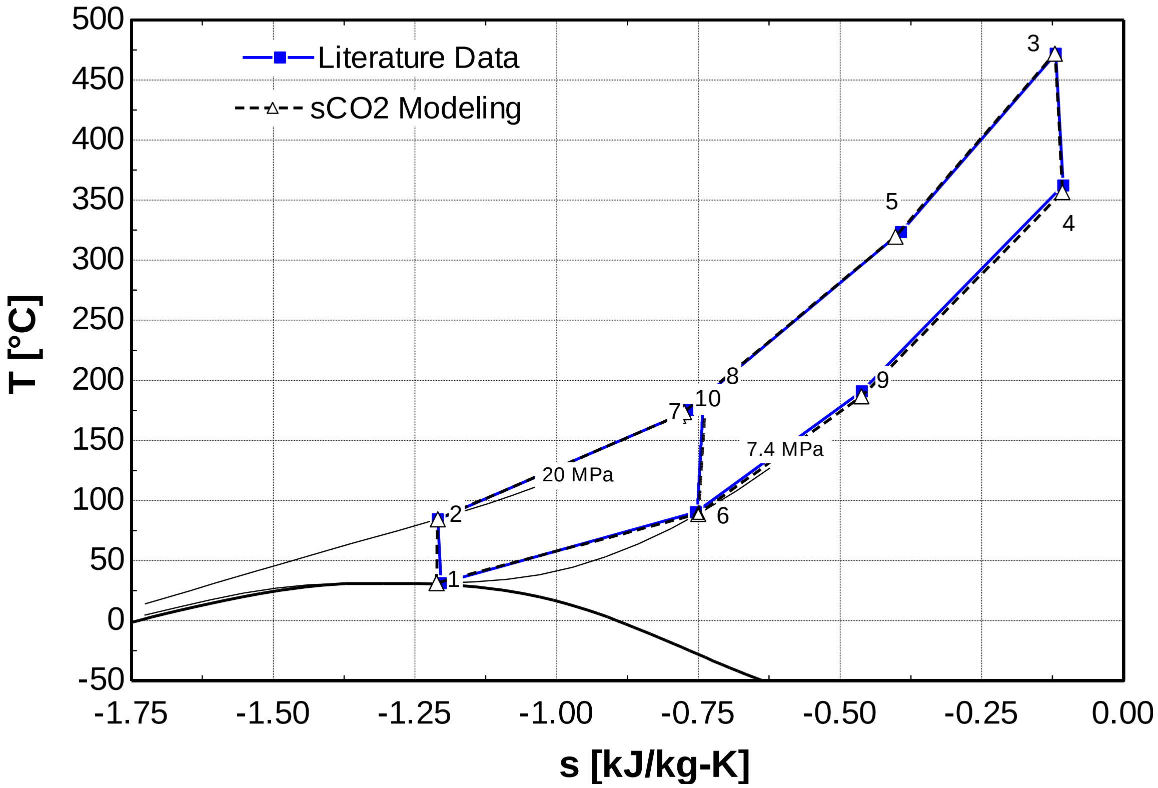

Figure 3.13 Temperature (T) – entropy (s) diagram for validation with figure 2 of reference [100]

3.7 Thermal efficiency of the integrated system

The thermal efficiency of the complete integrated system (without thermal storage) is defined as

$$\eta_{sys} = \frac{W_{net}}{Q_{solar}} \tag{117}$$

where Q_{solar} is the solar heat radiation input to the system.

3.8 Thermal storage

A two tank thermal storage was modeled using molten salt as a storage medium.

3.8.1 Hot storage tank

Applying energy balance on the hot storage tank to obtain

$$\frac{dU_{hst}}{dt} = Q_{1s} - Q_{hst} - Q_{2s} \tag{118}$$

where

$$U_{hst} = M_{hst} u_{hst} \tag{119}$$

where M_{hst} denotes the mass of storage fluid in the hot storage tank, u_{hst} denotes the internal energy of the storage medium in the hot storage tank and Q_{hst} are the losses to the ambient from the hot storage tank and it is defined as

$$Q_{hst} = (UA)_{hst}(T_{hst} - T_{amb}) \tag{120}$$

where $(UA)_{hst}$ is the loss coefficient area product of the hot storage tank.

If the thermal storage is integrated with the receiver, the energy gain rate at the receiver is

$$Q_u = \dot{m}_{1s}(h_{1s} - h_{4s}) \tag{121}$$

where $\dot{m}_{1s}$ is the mass flow rate through the central receiver.

3.8.2 Cold storage tank

Similarly, for the cold storage tank, applying energy balance to obtain [77]

$$\frac{dU_{cst}}{dt} = Q_{3s} - Q_{cst} - Q_{4s} \tag{122}$$

where

$$U_{cst} = M_{cst} u_{cst} \tag{123}$$

where M_{cst} denotes the mass of storage fluid in the cold storage tank, u_{cst} denotes the internal energy of the storage medium in the cold storage tank and Q_{cst} are the losses to the ambient from the cold storage tank and it is defined as

$$Q_{cst} = (UA)_{cst}(T_{cst} - T_{amb}) \tag{124}$$

where $(UA)_{cst}$ is the loss coefficient area product of the cold storage tank.

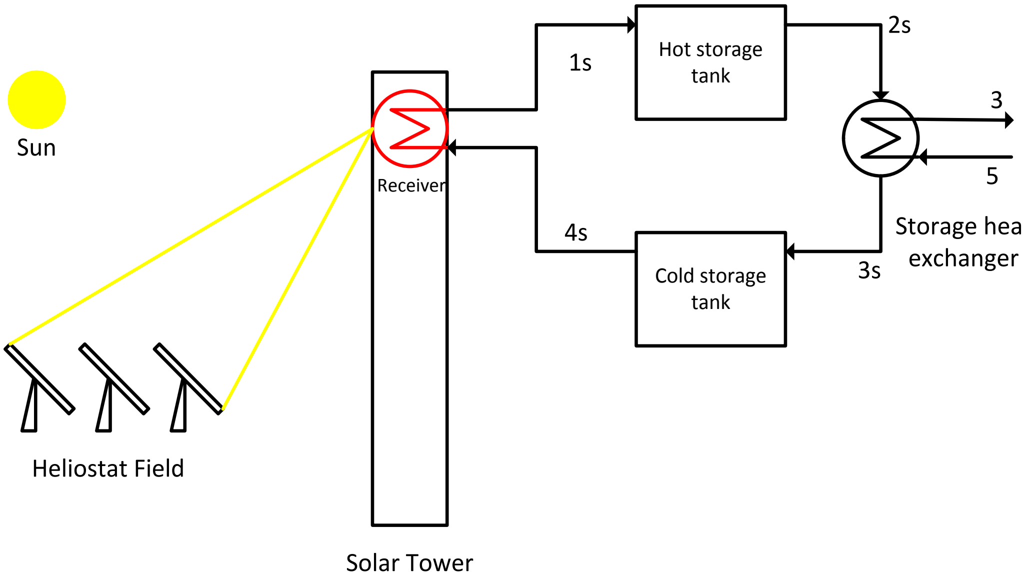

Figure 3.14 Two tank molten salt thermal storage integrated with the central receiver

3.8.3 Storage heat exchanger

For the modeling of the storage heat exchanger, the formula for the effectiveness of the heat exchanger is given as

$$\varepsilon_s = \frac{\dot{m}C_{p_{sco_2}}(T_3 - T_5)}{(\dot{m}C_p)_{\min}(T_{2s} - T_5)} \tag{125}$$

where $(\dot{m}C_p)_{\min}$ is the minimum capacitance of either the sCO$_2$ or the salt side, ε_s is effectiveness of the storage heat exchanger, $C_{p_{sco_2}}$ is the specific heat value of the sCO$_2$, and the subscript *s* denotes molten salt.

The storage medium used for the analysis was 60%NaNO$_3$ and 40%KNO$_3$, which is also known as solar salt [72]. The outer composition of the wall is taken as follows: alumina, stainless steel (SS304)[77] , and mineral wool[77] which is an insulation material. And the dimensions were taken as follow: 2cm of alumina lining, 5 cm of stainless steel (SS 304) lining [77] and 60 cm of mineral wool. The wind convective losses were also incorporated into the calculation of heat loss coefficient by assuming a constant wind velocity of 5 m/s. The average Nusselt number correlation for cross flow over a cylinder is given as [77,101]

$$\mathrm{Nu} = 0.3 + \frac{0.62\,\mathrm{Re}^{1/2}\,\mathrm{Pr}^{1/3}}{\left(1+\left(0.4/\mathrm{Pr}\right)^{2/3}\right)^{1/4}}.\left(1+\left(\mathrm{Re}/282000\right)^{5/8}\right)^{4/5} \tag{126}$$

where Re is the Reynolds number and Pr is the Prandtl number. This correlation is valid for (Re.Pr)>0.2, which is the case in this study.

CHAPTER 4

RESULTS AND DISCUSSION

In this chapter, results of the aforementioned mathematical modeling are presented and discussed in details. The discussion of the results proceeds as follows. It starts with the demonstration of optimization of the heliostat field using differential evolution using different approaches. Then, the heat collected at the central receiver is presented and its relation to the heliostat field size is discussed. Then, analysis of five different sCO_2 Brayton cycles when integrated with solar thermal power tower is carried out. Afterwards, comparison of the solar tower driven sCO_2 recompression Brayton cycle for different locations of Saudi Arabia is performed. Finally, analysis of the recompression sCO_2 Brayton cycle when integrated with solar thermal power tower through two tank thermal storage is performed and discussed.

4.1 Optimization of heliostat field layout

In this section, the results of optimizing the heliostat field using differential evolution are presented. Various optimizing parameters and other parameters which control the computation time are examined and discussed.

4.1.1 Optimization of heliostat field using one and two variables

In this section, a heliostat field was generated and this preliminary heliostat field was optimized using differential evolution. A mathematical code was developed for this purpose. Table 4.1 (Page 78) lists the basic design parameters of the heliostat field and the central receiver. For these cases, the total number of heliostats considered was 1932 in a surround field layout, and the tower optical height was taken as 120m. This optimization considers Dhahran city in Saudi Arabia as an illustrative example. A smaller field was selected to demonstrate two variables optimization. Later on, in this study higher field size will be selected to demonstrate more complex optimization approaches.

Equation (9) represents the minimum radial distance between heliostat rows; this equation was modified by introducing an optimizing parameter x_2 to optimize the radial distance as follows:

$$\Delta R_{\min} = x_2 DM \cos 30° \tag{127}$$

The optimizing parameter, x_2, is constant for all the zones.
Two time instants were considered for our analysis, i.e. June 21st at solar noon with sun altitude angle of 86.95° and December 21st at solar time 8:00 a.m. with sun altitude angle of 13.47°. This way both low and high sun altitude angles were considered for the optimization analysis. Further three cases each were taken into account for these time instants; first by considering x_1 variable only for optimization, secondly by considering x_2 variable only, and for the third and final case with optimizing both of these variables simultaneously.

For these cases, the population size was set equal to ten times the number of variables to be optimized. In addition, the termination criterion (stopping criterion) was set such that if after 50 continuous generations, the optimized results do not change, the code will halt.

The computation time can be reduced if the termination criterion is set such that the code will halt after less number of generations. Alternatively, it can be adjusted to stop the code by the user if the optimized results were not improved for the new generations; this gives the user more control over the optimization process.

Among the optical performance parameters, the shadowing and blocking factor is the most burdensome to calculate because it depends upon the problem heliostat (i.e. the heliostat that is being analyzed), as well as upon the surrounding heliostats that are its neighbors. Nevertheless, this computation becomes much more complex during the optimization process because the heliostat layout is changing throughout the process. The main advantage of this optimization procedure is that it calculates all the optical performance parameters of all the heliostats at every stage of optimization. The other advantage as compared to using the built-in optimization tool is that it is flexible and gives the user more control over the optimization process.

Other codes such as the one presented in [31] uses a discretization of the heliostats for the calculation of shadowing and blocking factor and the intercept factor. The surface was divided into cells ranging from 9 to 100 for the validation. This implies that in a complete optimization process, which includes thousands of heliostats, this approach can be time consuming, especially if the interception is calculated locally for each cell.

The code by Chinese academy of science [35] calculates the intercept using the Monte Carlo ray tracing method, and the accuracy of their code depends upon the number of rays traced and it will also increase the computation time.

Other codes do not specify what approach or algorithm they used for the optimization, how the optimization was carried out, and on what basis it was stopped. All of these factors are addressed in this study and explained.

Table 4.2 (Page 78) shows the results of all of the cases for both 21st June and 21st December. At solar time 8:00 a.m. on December 21st, the sun altitude angle is nearly equal to 15°. Due to low sun altitude angle, the shadowing and blocking factor (the fraction of area free of shadowing and blocking) is very low for the un-optimized field. After optimizing variable $x_{1,}$ the azimuthal distance between the adjacent heliostats varies and this improves the shadowing and blocking factor but as a consequence the heliostat field size increases from a maximum radius of about 400 meters to about 800 meters as shown in Figure 4.2. This is due to low sun altitude angles and consequently high nose blocking; hence the increase in heliostat field size is relatively high. We can also observe this from the results in Table 4.2 that as the shadowing and blocking factor improves the value of the other optical performance parameters decrease. This behavior is due to the shadowing and blocking factor trade-off as mentioned in[41].

For the second case, if variable x_2 is optimized, it controls the radial distance between the rows of the heliostats and we have slightly a better efficiency of the field as compared with the first case. This behavior is because of controlling the radial distance between the rows; unlike for case one where the change in azimuthal distance also caused the distance of the first ring from the tower to change and as a result the cosine, attenuation, and intercept factor decrease further because of this increased distance from the tower. These changes can be clearly observed in Figure 4.2 and Figure 4.3 where in the former the distance of the first row of heliostats from the tower has changed due to the change in the azimuthal spacing while in the latter this distance has not changed.

For June 21st, the optimization was carried out at solar noon. Due to high sun altitude angle for this instant of time, the shadowing and blocking factor is already very high.

After carrying out the optimization for case one and case two the heliostat field size (Figure 4.5 and Figure 4.6) does not increase as much as it increased when optimization for December 21st was carried out which is attributed to high sun altitude angle for June 21st. Similarly, optimizing x_2 variable yielded slightly better efficiency as compared to when x_1 was optimized.

As far as the case when both the variables were optimized simultaneously, the code returned the same results as that for when x_2 was optimized. This again is due to the increased radial distance of first row of heliostats when x_1 is increased and as a result of that only varying x_2 yields better efficiency (Figure 4.3 and Figure 4.6).

Moreover, the variables x_1 and x_2 can be divided into zones or further divided into rows and can be varied independently for the optimization process. This division has the probability of further increasing the heliostat field efficiency. Note that in this code, the relative shadowing and blocking heliostats are fixed by fixing their indexes and changing the variable x_1 independently for each zone or row may result in changing the relative position of the heliostats, which affects shadowing and blocking. This has to be considered strictly for efficient calculation of the shadowing and blocking factor if variable x_1 is optimized for each zone or row separately. All of these factors including the computation time by controlling the population size, the mutation factor, the crossover factor, and the termination criterion is explored and discussed next.

Table 4.1 Basic design and operating parameters of the heliostat field [41,102]

Heliostat height, *LH*	9.75 m
Heliostat width, *LW*	12.3 m
Receiver size, *LR*	9.44 m
Receiver diameter (cylindrical), *DR*	9.44 m
Mirror reflectivity × cleanliness, ρ	0.88 × 0.95
Standard deviation of sunshape errors, σ_{sun}	2.51mrad
Standard deviation of tracking errors, σ_t	0.63 mrad
Standard deviation of beam quality errors, σ_{bq}	1.88 mrad

Table 4.2 Optimization results of single and two variable optimization

	December 21 solar time 8				June 21 solar noon			
	Un-optimized	Case 1	Case 2	Case 3	Un-optimized	Case 1	Case 2	Case 3
		x_1=14.3803	x_2=2.1838	x_1=0, x_2=2.184		x_1=2.8763	x_2=1.2744	$x_1 \cong 0$, x_2=1.2744
$\cos\omega$	0.7043	0.6797	0.6819	0.6819	0.8414	0.8262	0.8270	0.8270
f_{sb}	0.5871	0.9214	0.9454	0.9454	0.9318	0.9769	0.9818	0.9818
f_{itc}	0.9841	0.9165	0.9148	0.9148	0.999	0.9963	0.9958	0.9958
η_{field}	0.3062	0.4504	0.4641	0.4641	0.6285	0.6414	0.6448	0.6448

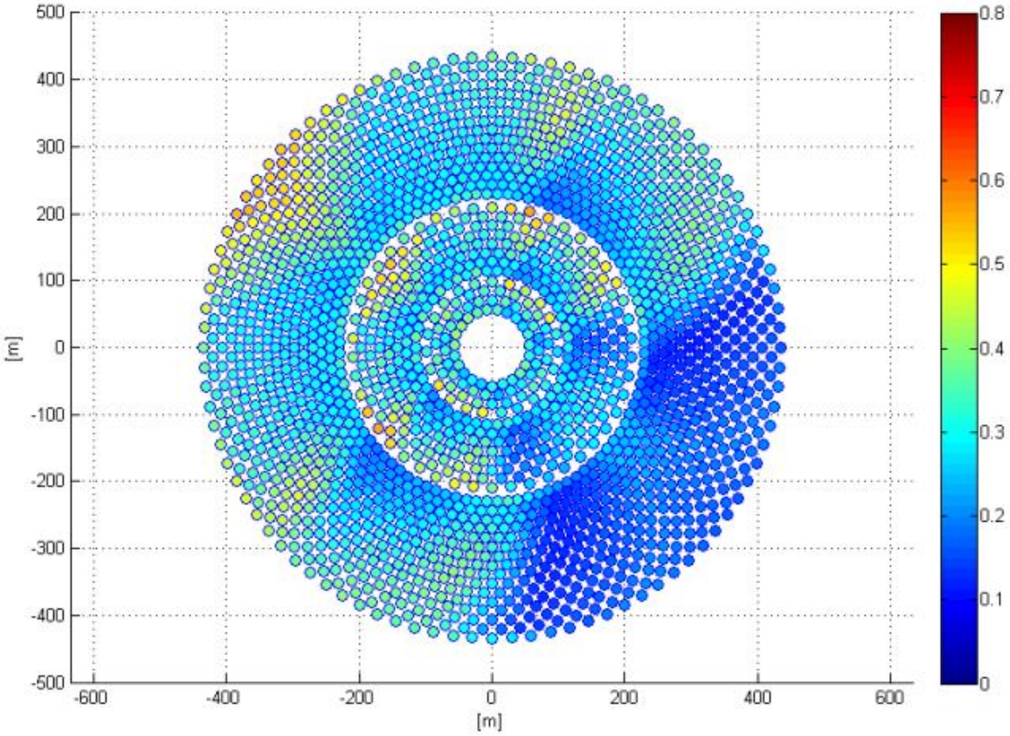

Figure 4.1 Contours of the optical efficiency of the un-optimized heliostat field for 21st December, solar time 8:00 a.m.

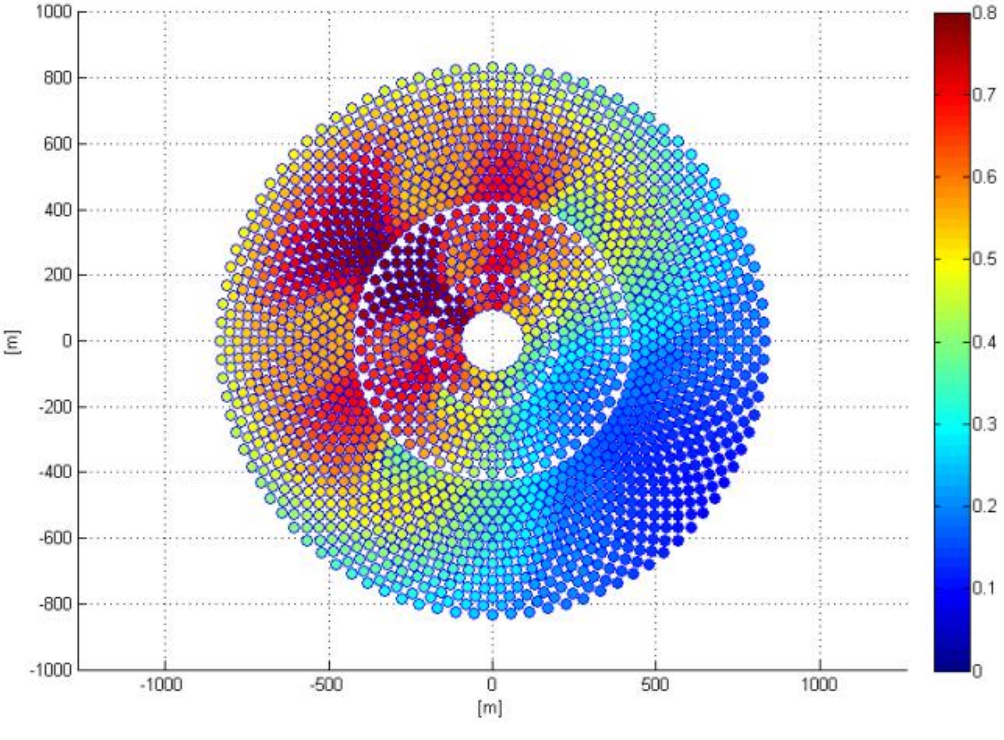

Figure 4.2 Contours of the optical efficiency of the optimized heliostat field for 21st December, solar time 8:00 a.m. with x_1 = 14.3803 (Case 1)

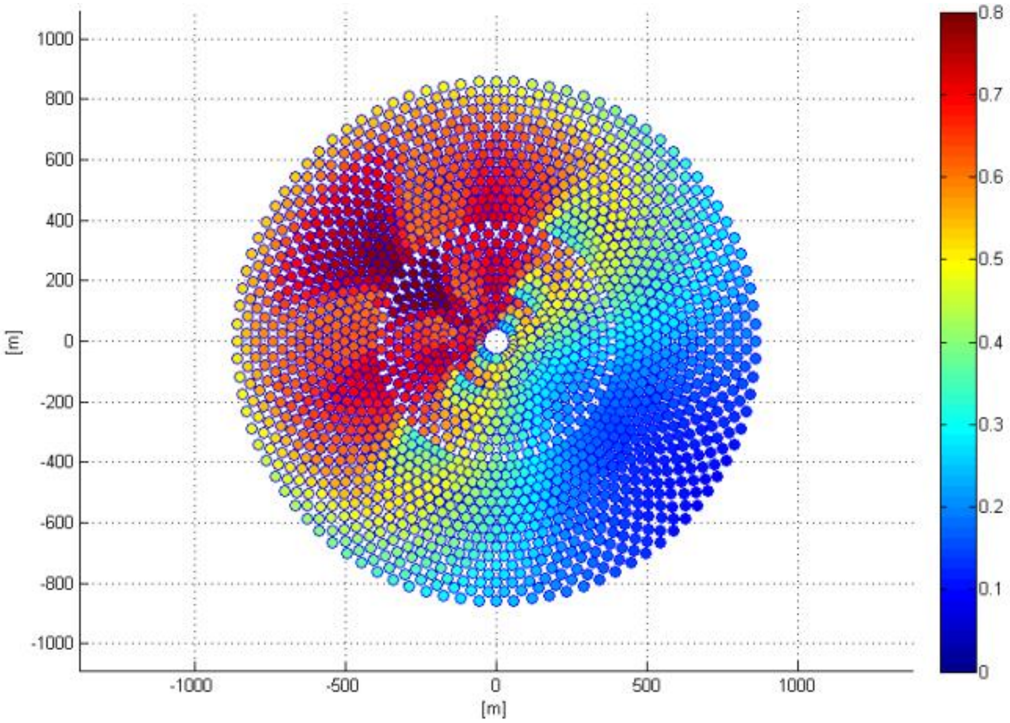

Figure 4.3 Contours of the optical efficiency of the optimized heliostat field for 21st December, solar time 8:00 a.m. with x_1 =0 and x_2 = 2.1838 (Case 2 and Case 3)

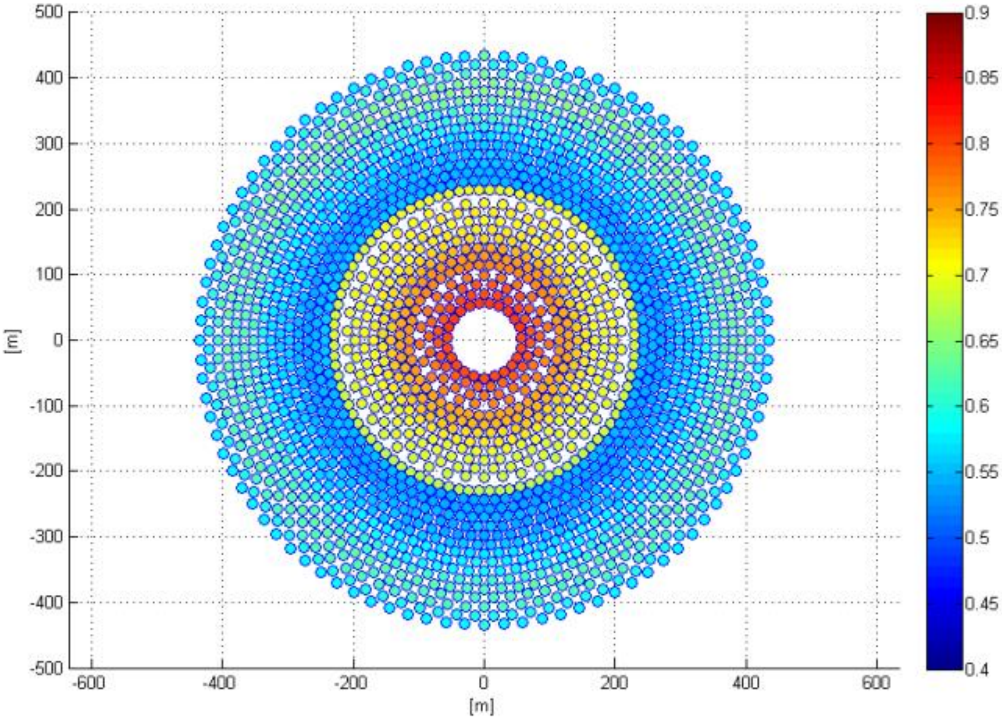

Figure 4.4 Contours of the optical efficiency of the un-optimized heliostat field for 21st June, solar noon

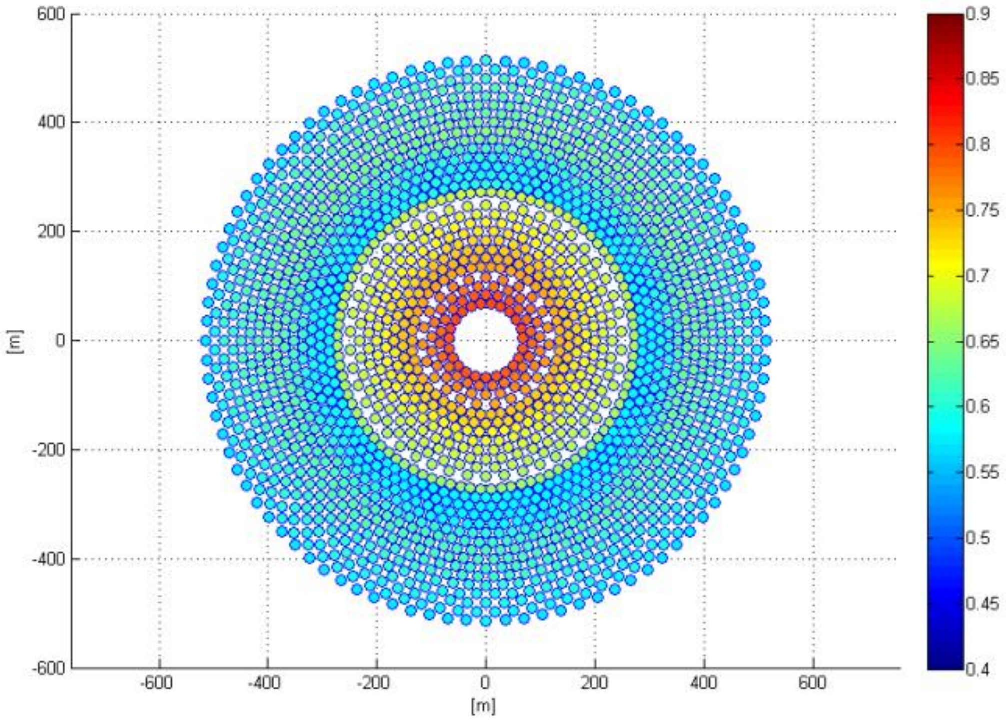

Figure 4.5 Contours of the optical efficiency of the optimized heliostat field for 21st June, solar noon with x_1 = 2.87633 (Case 2)

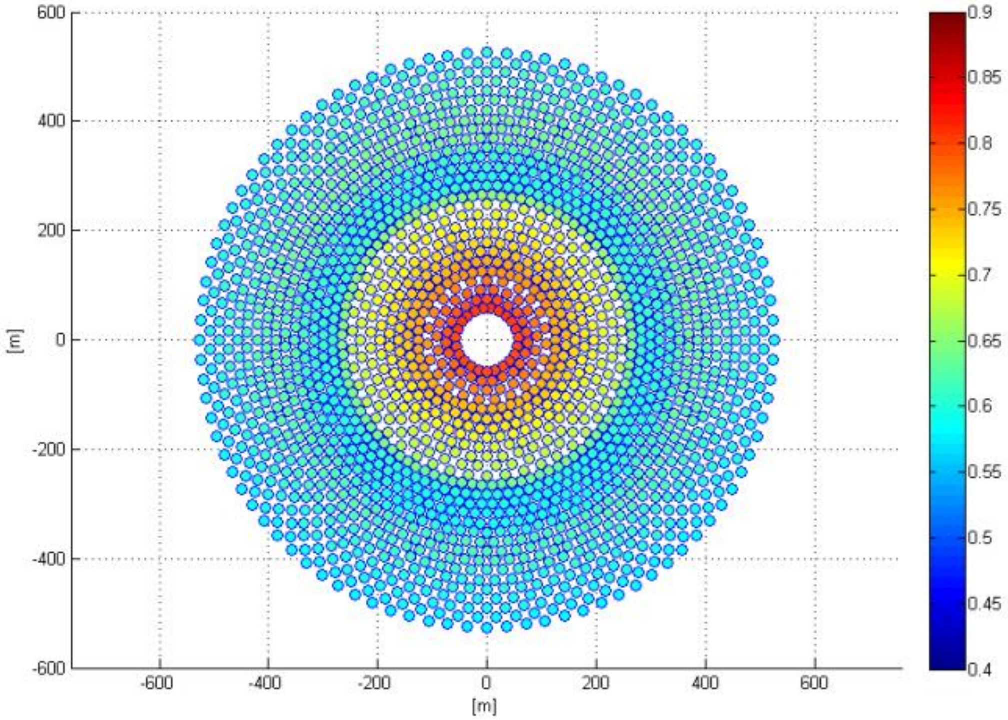

Figure 4.6 Contours of the optical efficiency of the optimized heliostat field for 21st June, solar noon with x_1 = 0 and x_2 = 1.2744 (Case 2 and Case 3)

4.1.2 Optimization of heliostat field using four variables

In this section, using the developed Matlab code, optimization of a preliminary generated heliostat field using DE was demonstrated when four variables are optimized. This code calculates all the necessary optical performance parameters of all the heliostats at every step of the optimization until the best layout of the generated heliostat field is found. Table 4.1 (Page 78) lists the design parameters of the heliostat and the central receiver which were used in this study. For these cases, higher number of heliostats was considered; 2646 in a surround field layout, and the tower optical height was taken as 130m. Furthermore, for these cases the *dsep* value was neglected. The computation costs of the optimization for all the cases considered are presented in Table 4.4 (Page 89). Table 4.3 (Page 88) shows all the results obtained after optimization of the heliostat field using differential evolution.

Three particular days were chosen for the analysis: summer solstice (June 21), winter solstice, (December 21), and spring equinox (March 21). These were selected to demonstrate the DE for different time instants and to check the effect of un-optimized against the optimized cases due to the characteristic change in solar altitude angles for these days, which represent two extreme angles and one middle angle.

For all the time instants considered for optimization, two cases were examined. In the first case, the radial spacing between the rows of the heliostats and the azimuthal spacing between adjacent heliostats was checked for optimization, i.e. two variables were considered for optimization in the first case. For the second case, in addition to controlling the azimuthal spacing, the radial spacing (which is function of two variables) was varied independently for each zone; thus, optimization of four variables was performed simultaneously. Because the shadowing and blocking factor and the intercept factor are considered, which are the most controversial factors [41] that affect the optical efficiency of the heliostat field, their values are also plotted and discussed for the cases considered. Figure 4.7 to Figure 4.9 illustrate, respectively, the shadowing and blocking factor, the intercept factor, and the optical efficiency of the un-optimized heliostat field for December 21 at solar time 8:00 a.m. with solar altitude angle of 13.47°. Figure 4.10, to Figure 4.12; and Figure 4.13 to Figure 4.15 demonstrate the optical performance parameters for the optimized heliostat field considering two variables and considering four variables for the same time instant. It can be observed from these figures and from the results presented in Table 4.3 that the shadowing and blocking factor is very low for the un-optimized field. On the other hand, after performing two variable optimization (case 1), the shadowing and blocking factor rises, and consequently the other optical performance parameters, which are the intercept, the cosine, and the attenuation factor decrease (Table 4.3). This result is due to the shadowing and blocking trade-off as mentioned in [41]. Alternatively, when the radial spacing is optimized independently for each zone of the heliostat field, the shadowing and blocking factor increases again; however, in this case the rest of the optical performance parameters increase as well. This result can be attributed to more freedom in placing of the heliostats as compared to when the radial spacing was fixed for all the zones. Accordingly, we have a better efficiency of the heliostat field when optimizing four variables (case 2). Figure 4.16 was plotted to conveniently show a zoomed in view of specifically the first and the second zone of the optimized heliostat field for the case shown in Figure 4.15. As mentioned before, the DE was programmed as a minimization function; hence, in our case it optimizes the negative of the objective function, i.e. the optical efficiency in order to maximize it. It took a total of 193 generations to reach at the optimum value for case 2 of this time instant. Note that the population size and termination criteria can be defined by the user to decrease or control the calculation time. Otherwise, decreasing the population size beyond a certain point will have an effect on the quality of result.

For the same day (December 21), solar time 9:00 a.m. was also considered in our analysis when the solar altitude angle is more than 20°, i.e. 23.765°, to check the effect of the optimization on the shadowing and blocking factor and the rest of the optical performance parameters. It can be observed from the results in Table 4.3 that the shadowing and blocking factor is quite high for the un-optimized field (Figure 4.17) as compared to before because of the higher solar altitude angle as compared to the previous time instant considered. Figure 4.18 and Figure 4.19 depict the optical efficiency of the heliostat field after optimization for case 1 and case 2, respectively. For these cases, similarly, the shadowing and blocking factor further increase but at the cost of other optical performance parameters as can be observed from the results presented in Table 4.3. It should be noted that the increase in the size of the heliostat field layout, i.e. the outermost radius for this time instant was not as much as before; this decrease in the heliostat field size is attributed to high solar altitude angle for this time instant. As compared with the previous case, it only took 96 generations to find the optimum value for case 2 of this time instant. This reduction in the generation number is because the DE generates the initial solution using random numbers within the control limits and the optimum value is found through an evolutionary process. This process progresses until the optimum value is obtained for the defined problem. It is not necessary that the same problem will again find the optimum value after the same number of generations.

For June 21, at solar noon when the solar altitude angle is the highest, it can be seen that the shadowing and blocking factor is already very high for the un-optimized field. The contours of the un-optimized field for this case are shown in Figure 4.20. Similarly, after optimization, the shadowing and blocking factor increases while the other optical performance parameters worsen which is the same observation as discussed above. Figure 4.21 and Figure 4.22 show the optimized heliostat field with optimizing two and four variables, respectively. However, this time there is only a slight increase in the size of the heliostat field layout as compared to the previous cases because of relatively high solar altitude angle. For the case 2 of this time instant, it took 98 generations to find the optimal solution.

Lastly, the analysis was carried out for March 21 solar noon. Similarly, it is observed that the shadowing and blocking factor is improved at the price of worsening the other optical performance parameters (Table 4.3). Figure 4.23 depicts the un-optimized heliostat field; whereas Figure 4.24 shows the optimized heliostat field with optimizing two variables and Figure 4.25 illustrates the optimized heliostat field with optimizing four variables. The altitude angle for this time instant is slightly lower than the case of June 21 solar noon. For this reason, the efficiency after optimization is slightly less. The optimization of case two for this time instant took 121 generations to find the global best solution using DE, as shown in Figure 4.25.

For the three particular days considered: on summer solstice (June 21) at solar noon, the optical efficiency of the un-optimized case was 0.6027; while for first optimized case, it was 0.6270; and for the second optimized case, it was 0.6394. Similar observations of optical efficiencies improvement were noticed in the other two days. It should be noted here that the overall optical efficiency is slightly less than some other optimized fields since we have not eliminated the heliostats that have relatively low optical efficiency; otherwise, the optical efficiency will be higher. The elimination of heliostats that have low optical efficiency can be performed to increase the optical performance of the whole heliostat field.

Optimizing the radial spacing independently for each zone of the heliostat field layout yielded slightly better results as compared to when the radial spacing was fixed for all zones. Moreover, the size of the heliostat field for time instant optimization is dependent on sun's altitude angle.

As a recommendation, for a quick estimation of the performance of the heliostat field, the time instant optimization should be carried out for low solar altitude angles or on December 21st when the altitude angle is the lowest. Moreover, the computation time depends upon various factors like the population size, the mutation factor, the crossover factor, and the termination criterion. In this section, the population size and the termination criterion were taken high to illustrate the application of the differential evolution method on the optimization of the heliostat field layout. This computation time can be reduced drastically by reducing the population size and controlling the aforementioned factors. Furthermore, note that taking the population size too low or lower than a certain point can affect the quality of result. These factors are explored in the next section.

Table 4.3 Optimization results of four variable optimization

	Un-optimized	Optimized	
		Case 1	Case 2
	December 21, solar time 8 $(\alpha_s = 13.471°)$		
		x_1=5.4353e-7	x_1=7.6881e-14 $x_{2,1}$=1.9357
		x_2=2.0940	$x_{2,2}$=1.6572 $x_{2,3}$=2.4555
$\cos\omega$	0.7000	0.6814	0.6834
f_{at}	0.9568	0.9374	0.9394
f_{sb}	0.5847	0.9208	0.9327
f_{itc}	0.9769	0.8902	0.8941
η_{filed}	0.2989	0.4377	0.4441
	December 21, solar time 9 $(\alpha_s = 23.765°)$		
		x_1=2.5352e-6	x_1=0 $x_{2,1}$=1.3296
		x_2=1.5559	$x_{2,2}$=1.2931 $x_{2,3}$=1.7908
$\cos\omega$	0.7309	0.7170	0.7202
f_{at}	0.9568	0.9476	0.9493
f_{sb}	0.8083	0.9558	0.9626
f_{itc}	0.9833	0.9537	0.9556
η_{filed}	0.4501	0.5169	0.5239
	June 21, solar noon $(\alpha_s = 86.949°)$		
		x_1=1.128e-4	x_1=2.5912e-6 $x_{2,1}$=1.002
		x_2=1.2836	$x_{2,2}$=1.0625 $x_{2,3}$=1.5204
$\cos\omega$	0.8324	0.8219	0.8237
f_{at}	0.9568	0.9530	0.9532
f_{sb}	0.9105	0.9721	0.9913
f_{itc}	0.9960	0.9890	0.9865
η_{filed}	0.6027	0.6270	0.6394
	March 21, solar noon $(\alpha_s = 63.096°)$		
		x_1=0	x_1=2.4576e-9 $x_{2,1}$=1.0215
		x_2=1.2891	$x_{2,2}$=1.0271 $x_{2,3}$=1.5327
$\cos\omega$	0.8150	0.8048	0.8068
f_{at}	0.9568	0.9529	0.9531
f_{sb}	0.9126	0.9710	0.9905
f_{itc}	0.9948	0.9868	0.9842
η_{filed}	0.5881	0.6112	0.6241

Table 4.4 Computation configuration of the optimization

		Mutation factor	Crossover factor	No. of generations
December 21, solar time 8	Case 1	0.8	0.7	253
	Case 2	0.8	0.1	192
December 21, solar time 9	Case 1	0.8	0.1	90
	Case 2	0.8	0.1	96
June 21, solar noon	Case 1	0.8	0.1	60
	Case 2	0.8	0.1	98
March 21, solar noon	Case 1	0.8	0.1	78
	Case 2	0.8	0.1	121

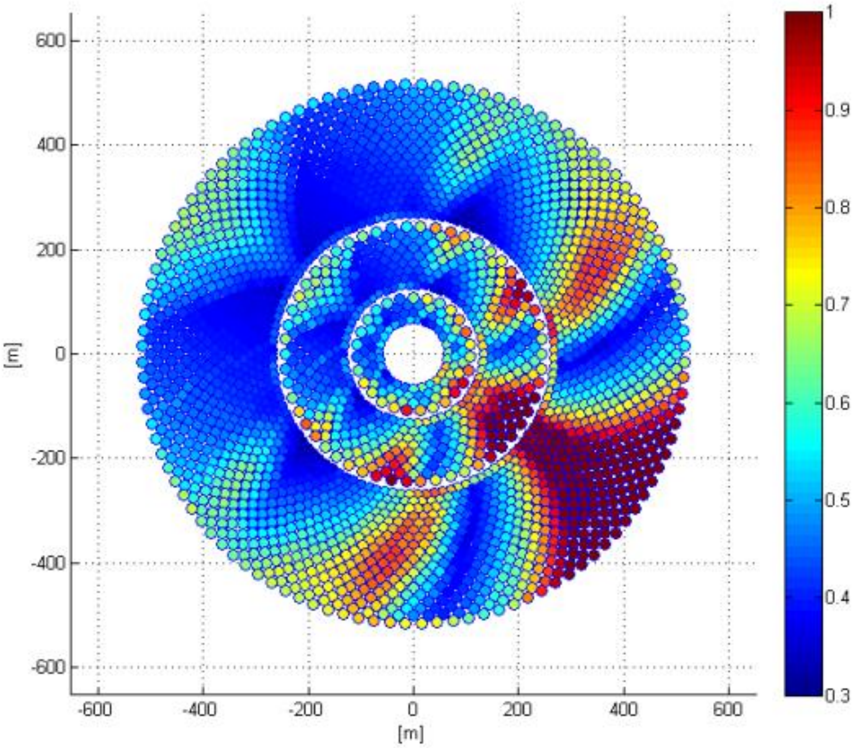

Figure 4.7 Contours of the shadowing and blocking factor of the un-optimized heliostat field for 21st December, solar time 8:00 a.m.

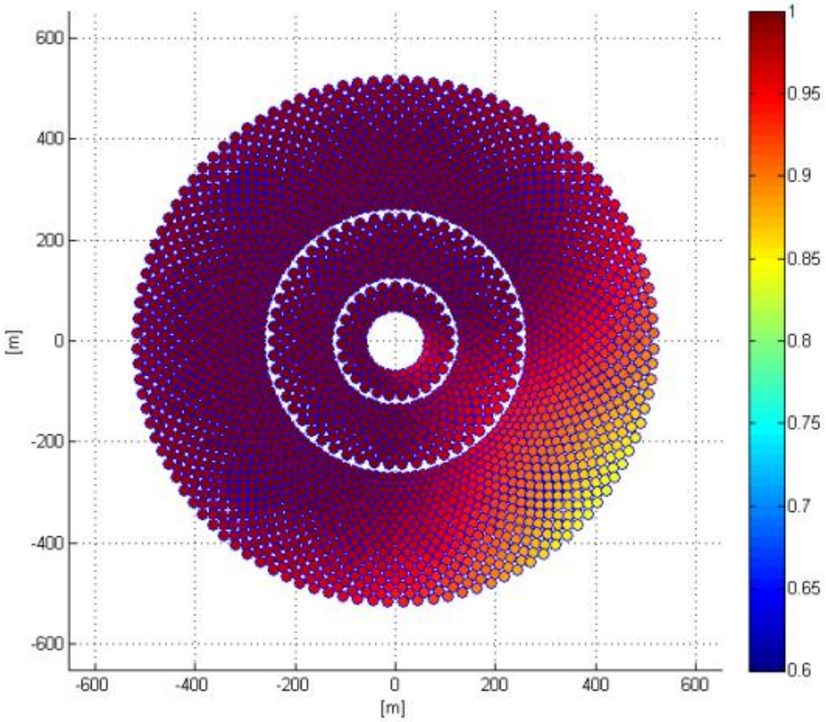

Figure 4.8 Contours of the intercept factor of the un-optimized heliostat field for 21st December, solar time 8:00 a.m.

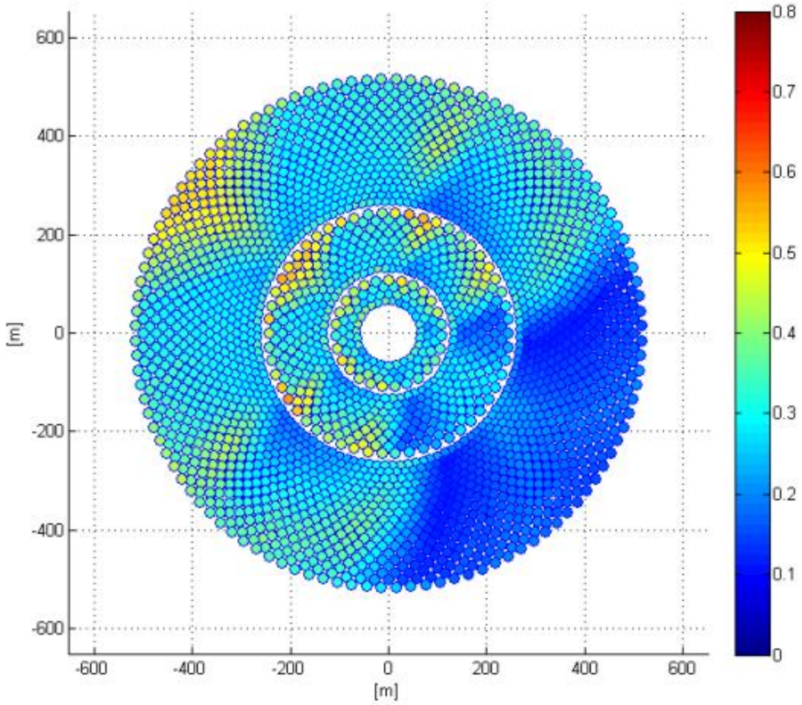

Figure 4.9 Contours of the optical efficiency of the un-optimized heliostat field for 21st December, solar time 8:00 a.m.

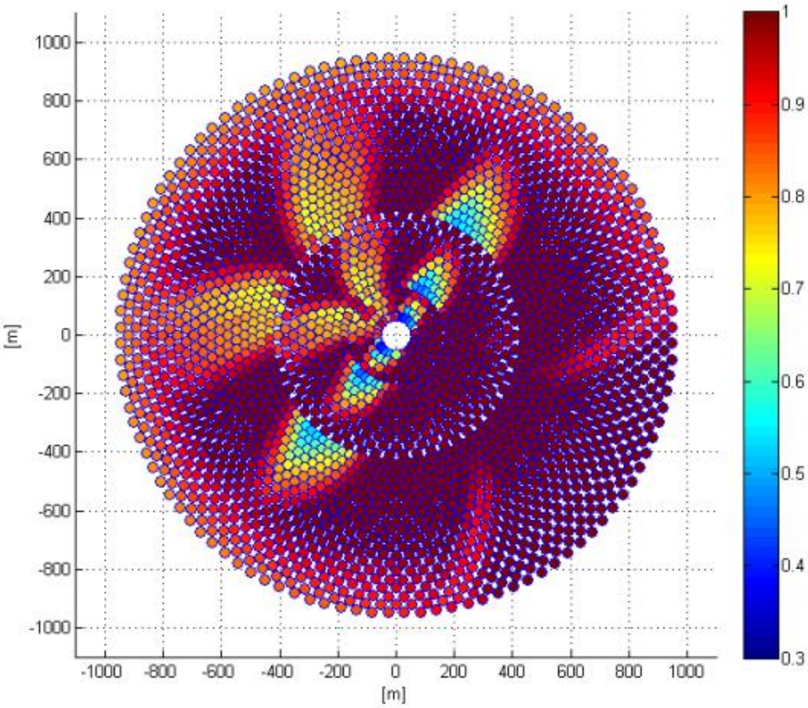

Figure 4.10 Contours of the shadowing and blocking factor of the optimized heliostat field for 21st December, solar time 8:00 a.m. (Case 1)

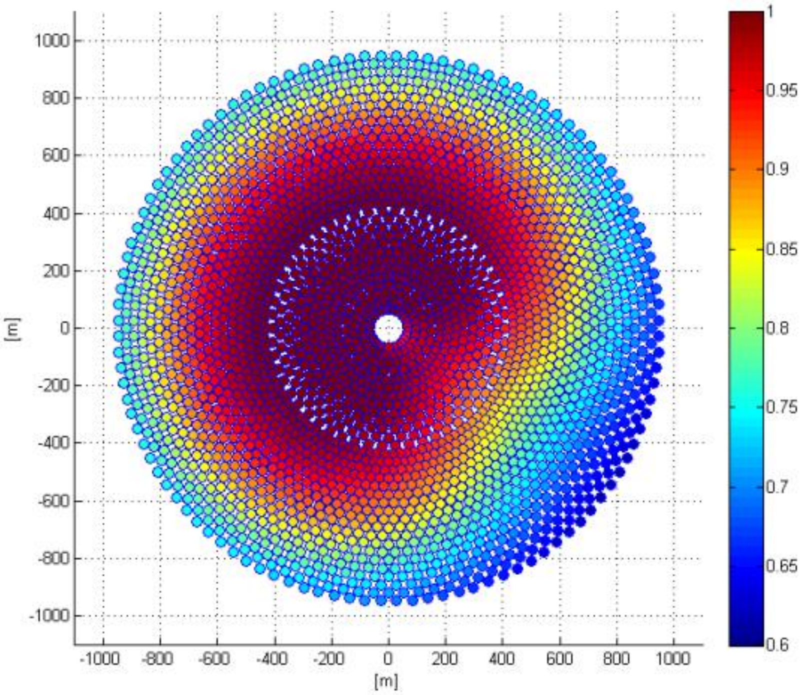

Figure 4.11 Contours of the intercept factor of the optimized heliostat field for 21st December, solar time 8:00 a.m. (Case 1)

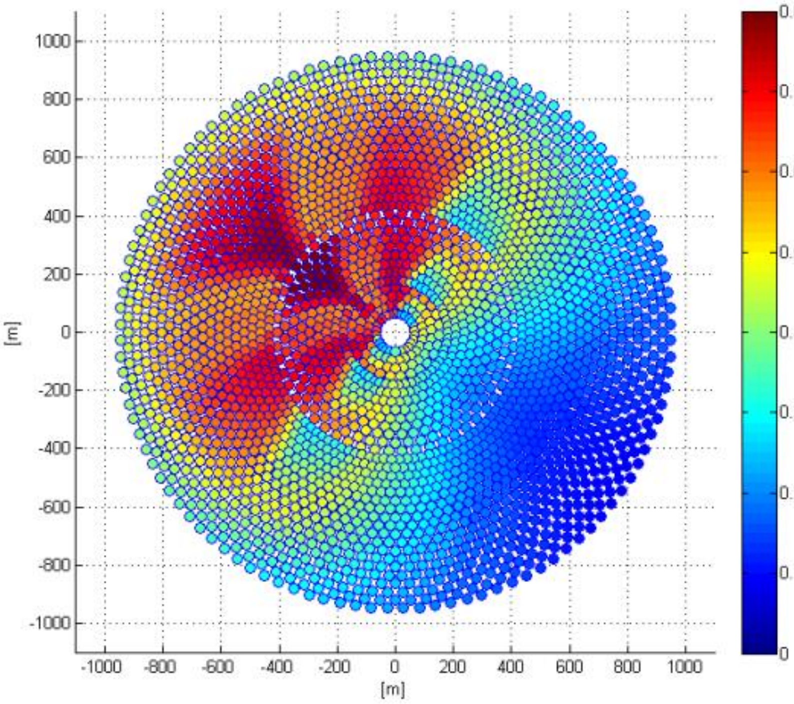

Figure 4.12 Contours of the optical efficiency of the optimized heliostat field for 21st December, solar time 8:00 a.m. (Case 1)

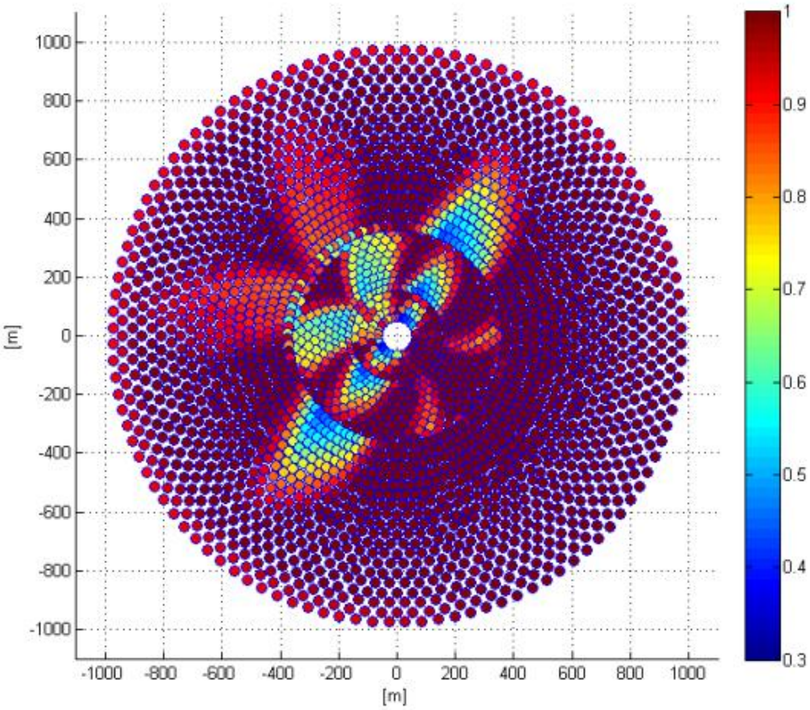

Figure 4.13 Contours of the shadowing and blocking factor of the optimized heliostat field for 21st December, solar time 8:00 a.m. (Case 2)

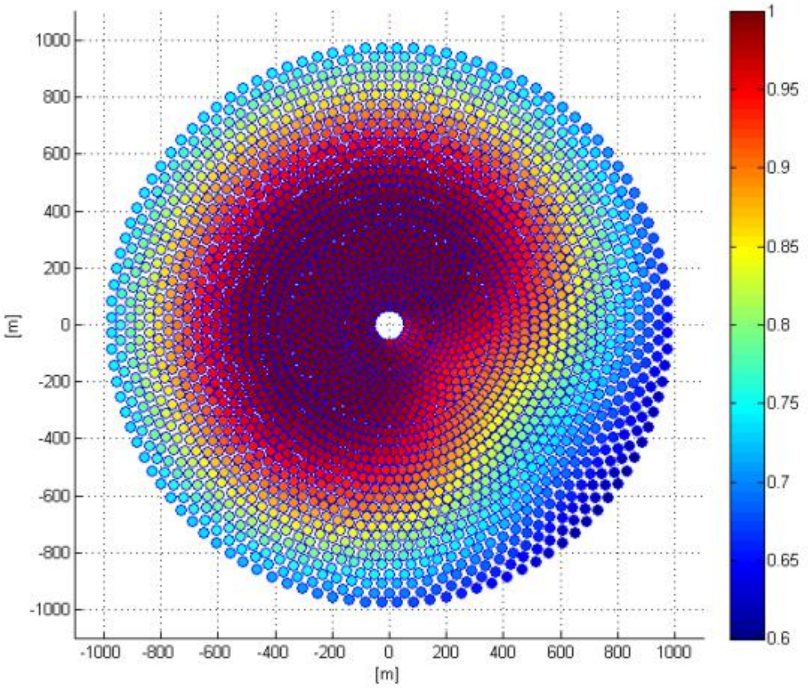

Figure 4.14 Contours of the intercept factor of the optimized heliostat field for 21st December, solar time 8:00 a.m. (Case 2)

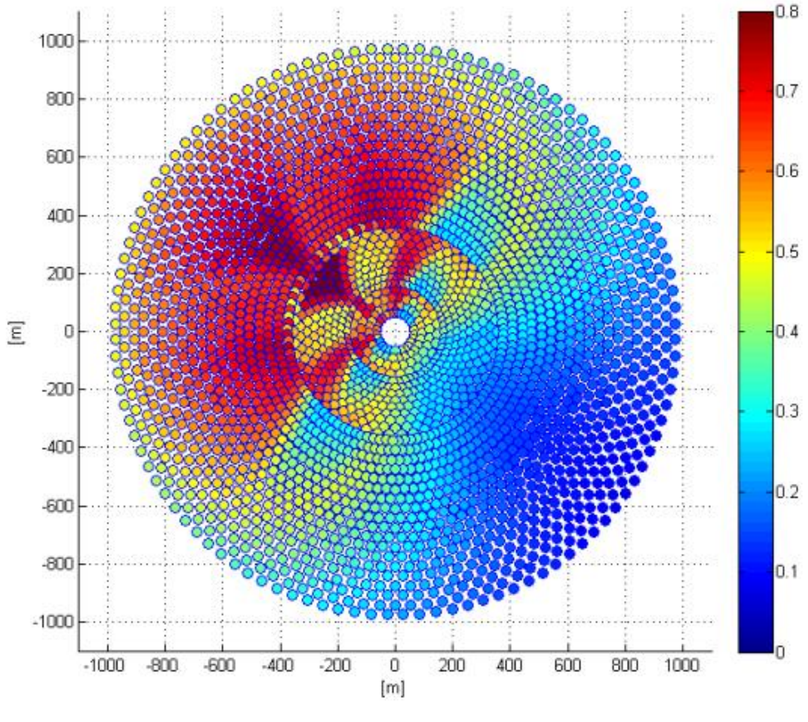

Figure 4.15 Contours of the optical efficiency of the optimized heliostat field for 21st December, solar time 8:00 a.m. (Case 2)

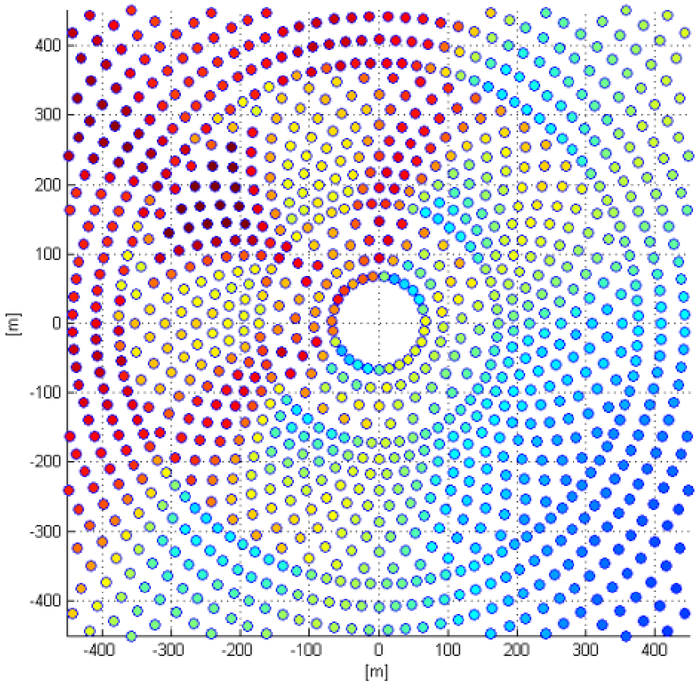

Figure 4.16 A zoomed view of the contours of the optical efficiency of the optimized heliostat field of first two zones for 21st December, solar time 8:00 a.m. (Case 2)

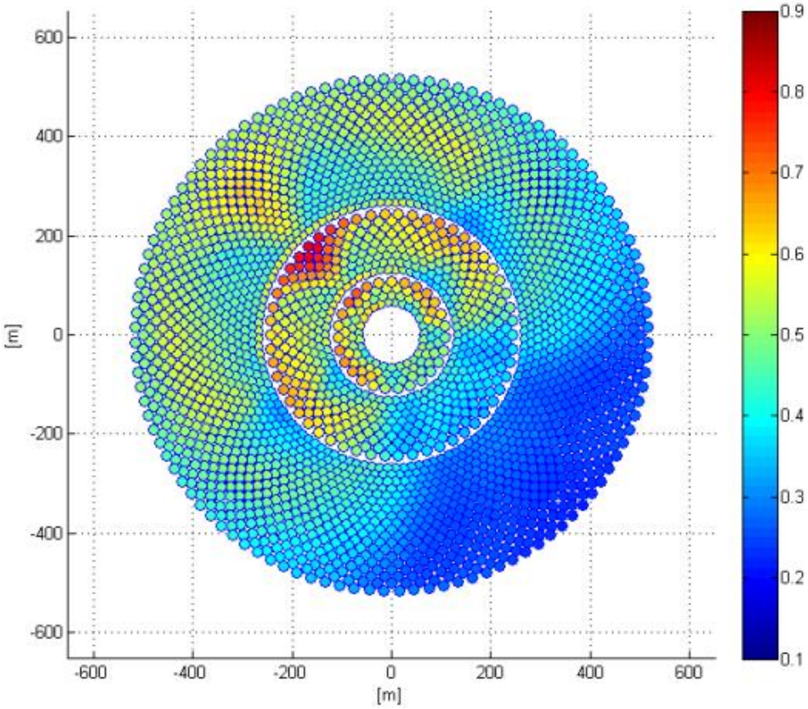

Figure 4.17 Contours of the optical efficiency of the un-optimized heliostat field for 21st December, solar time 9:00 a.m.

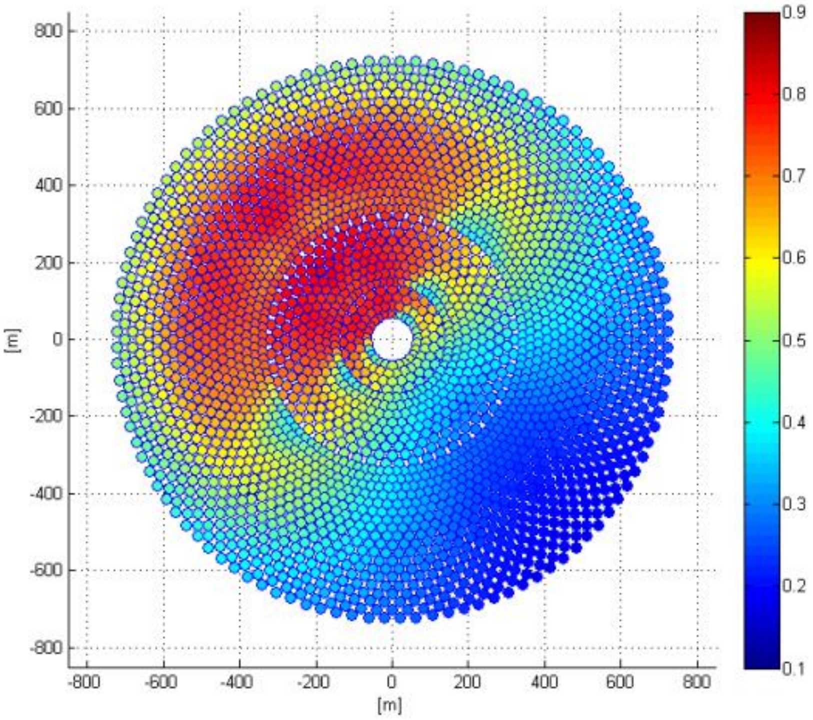

Figure 4.18 Contours of the optical efficiency of the optimized heliostat field for 21st December, solar time 9:00 a.m. (Case 1)

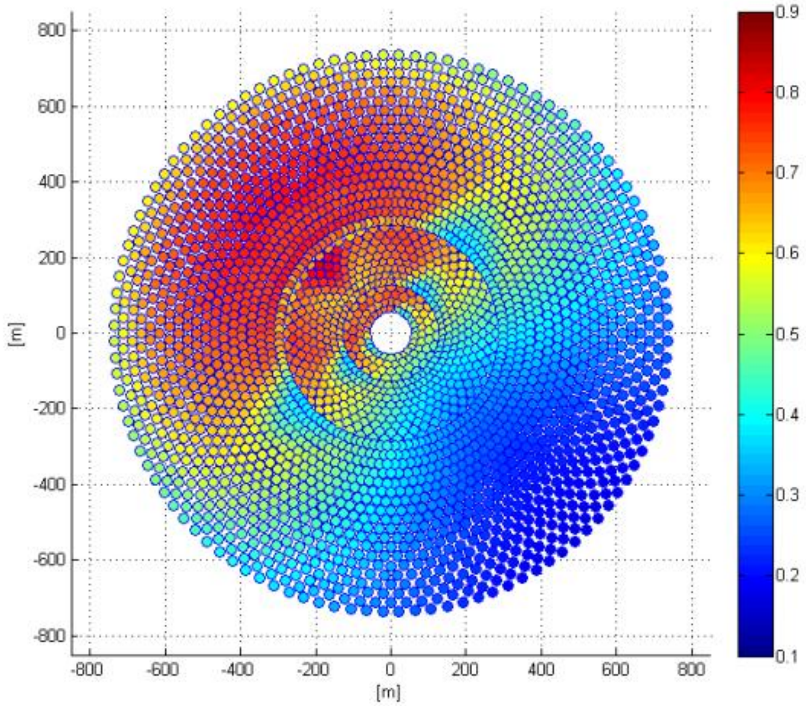

Figure 4.19 Contours of the optical efficiency of the optimized heliostat field for 21st December, solar time 9:00 a.m. (Case 2)

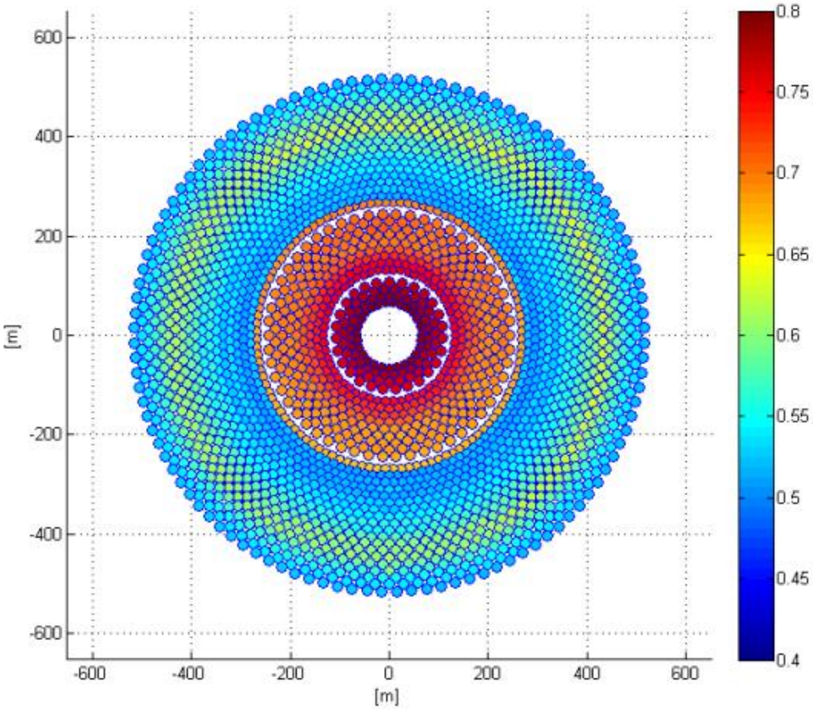

Figure 4.20 Contours of the optical efficiency of the un-optimized heliostat field for 21st June, solar noon

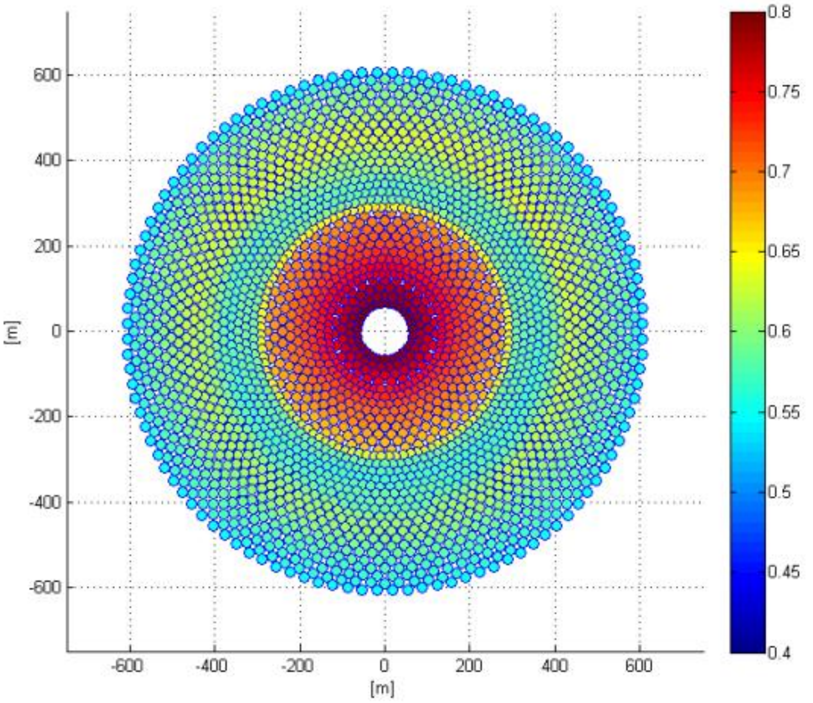

Figure 4.21 Contours of the optical efficiency of the optimized heliostat field for 21st June, solar noon (Case 1)

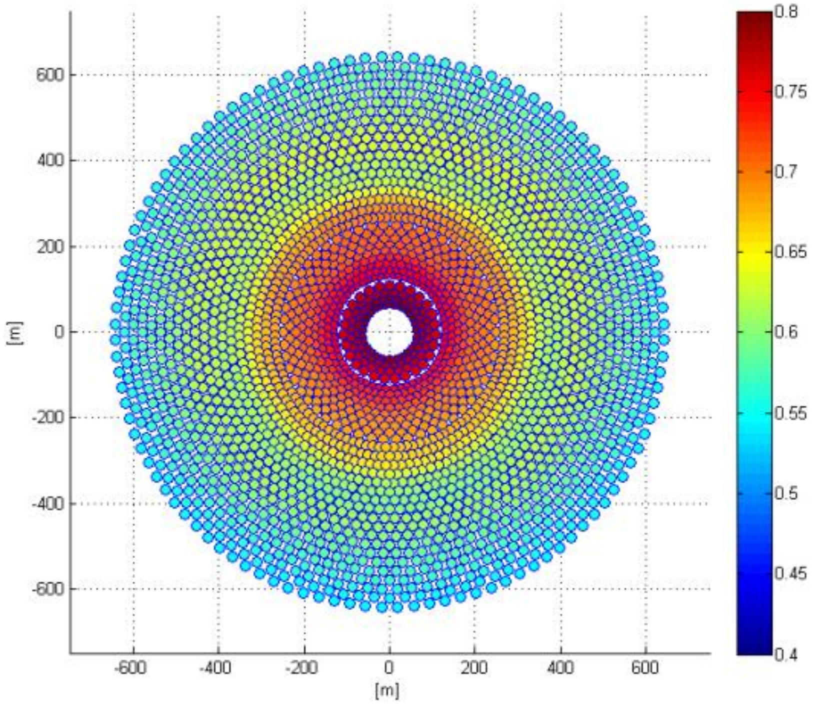

Figure 4.22 Contours of the optical efficiency of the optimized heliostat field for 21st June, solar noon (Case 2)

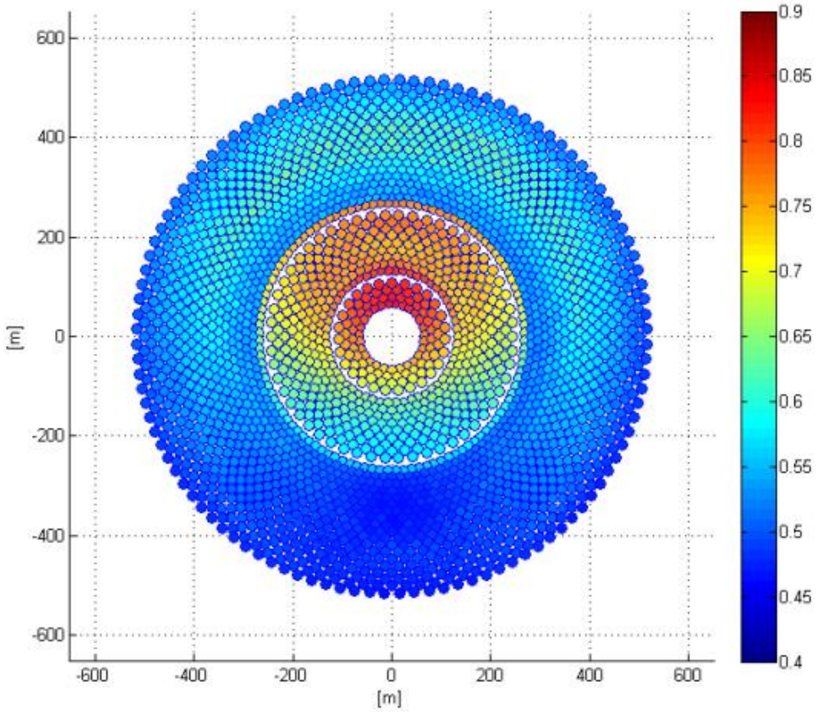

Figure 4.23 Contours of the optical efficiency of the un-optimized heliostat field for 21st March, solar noon

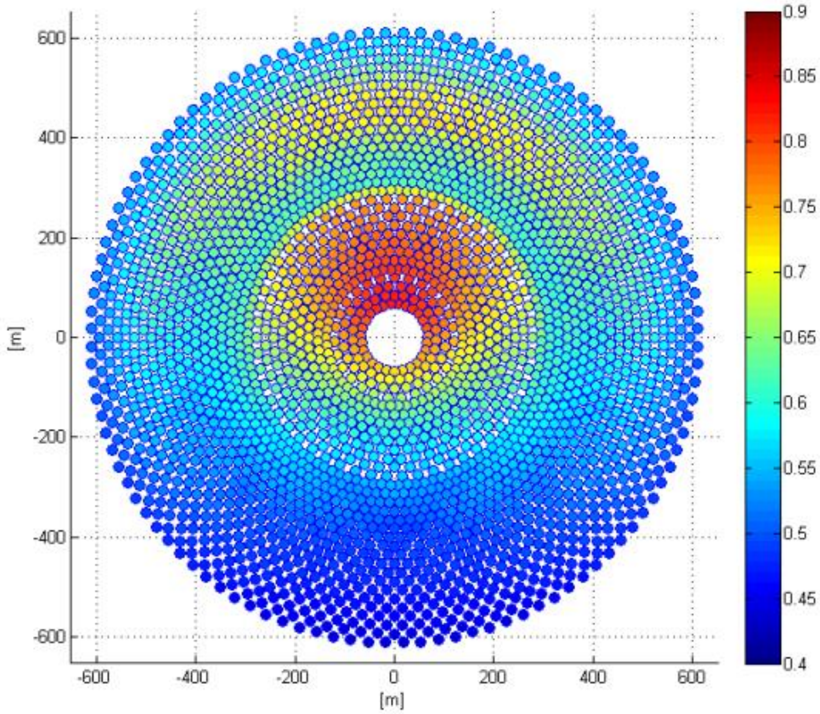

Figure 4.24 Contours of the optical efficiency of the optimized heliostat field for 21st March, solar noon (Case 1)

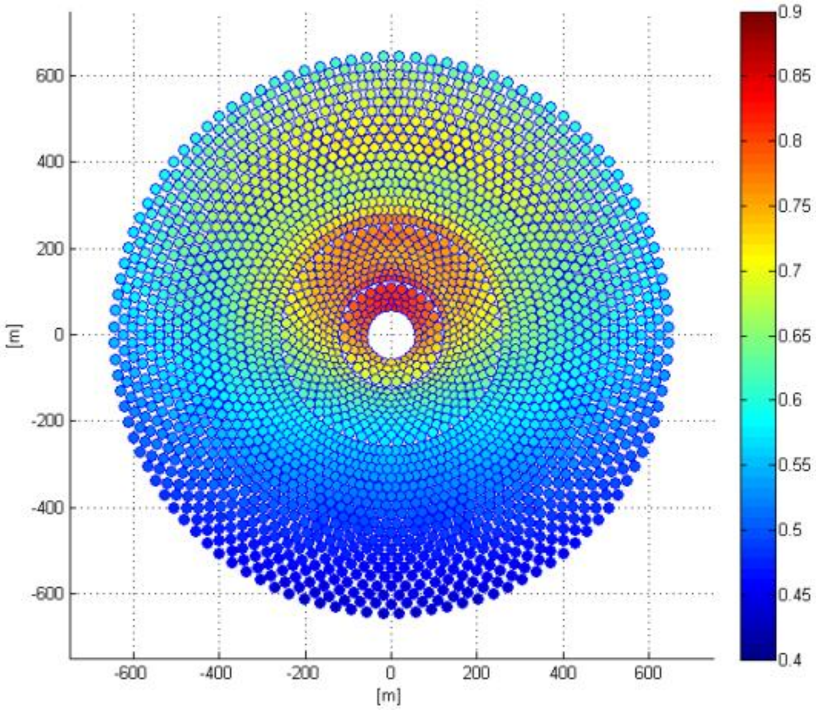

Figure 4.25 Contours of the optical efficiency of the optimized heliostat field for 21st March, solar noon (Case 2)

4.1.3 Optimization of normalized ratio of optical performance to the land area covered by the heliostat field

In this section, using the developed Matlab code, optimization of a preliminary generated heliostat field versus optimization of the normalized ratio of optical efficiency to the land area covered by the heliostat field using DE was demonstrated when four variables are optimized. This code calculates all the necessary optical performance parameters of all the heliostats at every step of the optimization until the best layout of the generated heliostat field is found. This optimization considers Dhahran city in Saudi Arabia as an illustrative example. Furthermore, the value selected for the crossover factor was 0.5 and that for the mutation factor was 0.6. These particular values were selected because it was observed after many runs that this particular combination of these two values reduces the computation time for this particular mathematical problem.

Table 4.1 (Page 78) lists the design parameters of the heliostat and the central receiver which were used in this study. For these cases, same number of heliostats as in the previous section that is 2646 in a surround field layout was considered, and the tower optical height was taken as 130m. The computation costs of the optimization for all the cases considered are presented in Table 4.6 (Page 105). Table 4.5 (Page 104) shows all the results obtained after optimization of the heliostat field using differential evolution.

In the first set of cases, *dsep* was taken equal to zero, whereas in the second set of cases the value of *ds* (the ratio of extra security distance to the height of the heliostat as given by equation(5)) was taken equal to 0.3 [40]. That is, the value of $dsep = 2.925 \approx 3$m.

Again, three particular days were chosen for the analysis: summer solstice (June 21), winter solstice, (December 21), and spring equinox (March 21). These were selected to demonstrate the DE for different time instants and to check the effect of un-optimized case against the optimized cases due to the characteristic change in the solar altitude angles for these days, which represent two extreme angles and one middle angle. The required number of generations (computation costs) to find the optimal solution for all of these cases are listed in Table 4.6. Note that the population size and termination criteria can be defined by the user to decrease or control the calculation time. Otherwise, decreasing the population size beyond a certain point will have an effect on the quality of the result.

For all the time instants considered for optimization, two sets each of two cases were examined. In all the cases, four variables were used for optimization, the parameter x_1 which is used to control the azimuthal spacing between adjacent heliostats and the parameter $x_{2,i}$ was considered separately for each zone which is used to control the radial spacing between the rows of the heliostats. In the first set of cases, the optimization was performed considering zero security distance between the heliostats, whereas for the second set of cases, a suitable value, 3m [40], was taken for the extra security distance between the heliostats. Some studies do not consider this extra secrity distance in their optimization process. This issue has been adressed and has been taken into account in this study. In addition, the un-optimized case was compared with the optimized case considering optical efficiency alone or considering the ratio of the optical performance to that of the covered land area by the heliostats. December 21, solar time 9:00 a.m. was considered in the analysis when the solar altitude angle is more than 20°, i.e. 23.765°, to check the effect of the optimization on the shadowing and blocking factor and the rest of the optical performance parameters, which are listed in Table 4.5. It can be observed from the results in Table 4.5 for *dsep=0* that the shadowing and blocking factor is quite high for the un-optimized field (Figure 4.26) because of the higher solar altitude angle. Figure 4.27 and Figure 4.28 depict the optical efficiency of the heliostat field after optimization for case 1 and case 2, respectively. In the first case, only the optical performance was optimized whereas in the second case, the ratio of the optical performance to that of the land area covered by the heliostat field was optimized. For the first case, the initial field size increases from $0.8570\times10^6(\mathrm{m}^2)$ to $1.7115\times10^6(\mathrm{m}^2)$ whereas the optical performance also increases from 0.4501 to 0.5239. Alternatively, for the second case if the ratio is maximized, the field size remains the same as the un-optimized case, but the optical performance increases from 0.4501 to 0.4540. In addition, if the same analysis is performed with considering the extra security distance between the heliostats, the second set of cases, the field size changes from $1.2160\times10^6(\mathrm{m}^2)$ to 1.8140 $\times10^6(\mathrm{m}^2)$ for the first optimization case; and the optical efficiency increases from 0.4871 to 0.5230. Figure 4.29 and Figure 4.30 depict the optical efficiency with *dsep=3* for the un-optimized case and with the optical performance optimized. Note that the initial field size with *dsep =3* is already high because of the incorporation of the extra security distance. Furthermore, the optimized optical efficiency is not as high as when the extra security distance was neglected, this is because of the increase in the distance of the overall heliostat field from the tower due to the incorporation of the extra security distance. On the other hand, when the ratio of the optical performance to the land area was maximized (Figure 4.31), the land area remained the same as that of the un-optimized heliostat field but the optical performance improved from 0.4871 to 0.4896.

For June 21, at solar noon when the solar altitude angle is the highest, it can be seen that the shadowing and blocking factor is already very high for the un-optimized field. The contours of the un-optimized field with *dsep=0* for this case are shown in Figure 4.32. Similarly, after optimization, the shadowing and blocking factor increases while the other optical performance parameters worsen which is due to the shadowing and blocking tradeoff as mentioned in [41]. Figure 4.33 and Figure 4.34 show the optimized heliostat field for case 1 and case 2 with *dsep=0* , respectively. However, this time the heliostat field layout size increased from $0.8570\times10^{6}(\mathrm{m}^{2})$ to $1.3227\times10^{6}(\mathrm{m}^{2})$, whereas the optical performance improved from 0.6026 to 0.6395. There was not much increase in the heliostat field size or the optical performance as compared to the previous cases because of relatively high solar altitude angle. Additionally, for the second case, the land area remained the same, while the optical performance improved from 0.6026 to 0.6033. On the other hand, with *dsep = 3*, for case 1 (Figure 4.36) the initial land area that is 1.2160 $\times10^{6}(\mathrm{m}^{2})$ increased to $1.4560\times10^{6}(\mathrm{m}^{2})$, and the optical efficiency increased from 0.6167 to 0.6241. On the contrary, the optimization of the ratio of optical performance to the land area yielded the same results as that of the un-optimized case for this time instant with *dsep=3*, which has been depicted in Figure 4.35. This behavior was observed because of very high solar altitude angle for this time instant. Moreover, the land area that was considered was calculated from the center of the tower towards the last row of the heliostat field and not from the first row. This land area is dependent on both the azimuthal spacing and the radial spacing, which in turn are dependent upon the optimization parameters namely x_1 and $x_{2,i}$. If the value of the parameter x_1 is increased, the overall distance of all the heliostats from the tower increases because of the increase in the azimuthal spacing. On the other hand, if the parameter $x_{2,i}$ is varied independently for each zone for optimization, the radial spacing is controlled for the specific zone for which this parameter is varied. The number of generations it took to converge to an optimal solution for these cases is shown in Table 4.6.

Lastly, the analysis was carried out for March 21 solar noon. Figure 4.37 to Figure 4.39 depict the contours of the heliostat field with $dsep=0$ for the un-optimized case and optimized cases respectively. The altitude angle for this time instant is slightly lower than the case of June 21 solar noon. For this reason, the efficiency after optimization is slightly less for case 1 (Table 4.5). However, the increase in the field size for case 1 (Figure 4.41) as compared to the case for June 21 was higher, again because of the lower solar altitude angle for this case. In addition, for the cases with $dsep=3$, for this time instant, the increase in the field size was from $1.2160\times10^6(\mathrm{m}^2)$ to $1.5679\times10^6(\mathrm{m}^2)$. Nevertheless, for case 2, when the ratio was maximized, again it yielded the same results as the un-optimized case, Figure 4.40.

Table 4.5 Optimization results using four variables for optimizing the normalized ratio

	Un-optimized	Optimized		Un-optimized	Optimized	
	dsep =0			*dsep* = 3		
		Case 1	Case 2		Case 1	Case 2
December 21, solar time 9 $(\alpha_s = 23.765°)$						
		x_1=0.7385 $x_{2,1}$=1.3798 $x_{2,2}$=1.1214 $x_{2,3}$=1.6845	x_1=0 $x_{2,1}$=1.2253 $x_{2,2}$=1.0914 $x_{2,3}$=1.0000		x_1=0.0001 $x_{2,1}$=1.1974 $x_{2,2}$=1.0660 $x_{2,3}$=1.4971	x_1=0.0001 $x_{2,1}$=1.2008 $x_{2,2}$=1.0814 $x_{2,3}$=1.0000
$\cos\omega$	0.7309	0.7200	0.7305	0.7216	0.7170	0.7212
f_{at}	0.9568	0.9493	0.9566	0.9515	0.9474	0.9513
f_{sb}	0.8083	0.9618	0.8150	0.8907	0.9695	0.8947
f_{itc}	0.9833	0.9566	0.9833	0.9709	0.9501	0.9709
η_{filed}	0.4501	0.5239	0.4540	0.4871	0.5230	0.4896
$A_l \times 10^6 (\mathrm{m}^2)$	0.8570	1.7115	0.8570	1.2160	1.8482	1.2160
June 21, solar noon $(\alpha_s = 86.949°)$						
		x_1=0 $x_{2,1}$=1.0001 $x_{2,2}$=1.0625 $x_{2,3}$=1.5173	x_1=0 $x_{2,1}$=1.0459 $x_{2,2}$=1.0619 $x_{2,3}$=1.0000		x_1=0 $x_{2,1}$=1.0002 $x_{2,2}$=1.0000 $x_{2,3}$=1.2012	x_1=0 $x_{2,1}$=1.0000 $x_{2,2}$=1.0000 $x_{2,3}$=1.0000
$\cos\omega$	0.8324	0.8238	0.8320	0.8171	0.8140	0.8171
f_{at}	0.9568	0.9532	0.9567	0.9515	0.9499	0.9515
f_{sb}	0.9104	0.9912	0.9118	0.9636	0.9882	0.9636
f_{itc}	0.9960	0.9866	0.9960	0.9876	0.9811	0.9876
η_{filed}	0.6026	0.6395	0.6033	0.6167	0.6241	0.6167
$A_l \times 10^6 (\mathrm{m}^2)$	0.8570	1.3227	0.8570	1.2160	1.4560	1.2160
March 21, solar noon $(\alpha_s = 63.096°)$						
		x_1=0 $x_{2,1}$=1.0000 $x_{2,2}$=1.0261 $x_{2,3}$=1.5324	x_1=0 $x_{2,1}$=1.0000 $x_{2,2}$=1.0261 $x_{2,3}$=1.0000		x_1=0 $x_{2,1}$=1.008 $x_{2,2}$=1.002 $x_{2,3}$=1.2893	x_1=0 $x_{2,1}$=1.0000 $x_{2,2}$=1.0000 $x_{2,3}$=1.0000
$\cos\omega$	0.8150	0.8069	0.8148	0.8006	07965	0.8006
f_{at}	0.9568	0.9531	0.9568	0.9515	0.9492	0.9515
f_{sb}	0.9123	0.9905	0.9126	0.9563	0.9897	0.9563
f_{itc}	0.9948	0.9842	0.9948	0.9855	0.9752	0.9855
η_{filed}	0.5879	0.6241	0.5880	0.5972	0.6078	0.5972
$A_l \times 10^6 (\mathrm{m}^2)$	0.8570	1.3378	0.8570	1.2160	1.5679	1.2160

Table 4.6 Computation costs of the optimization

		Number of generations	
		dsep=0	*dsep=3*
December 21, solar time 9	Case 1	90	120
	Case 2	66	163
June 21, solar noon	Case 1	136	135
	Case 2	118	33
March 21, solar noon	Case 1	160	137
	Case 2	478	26

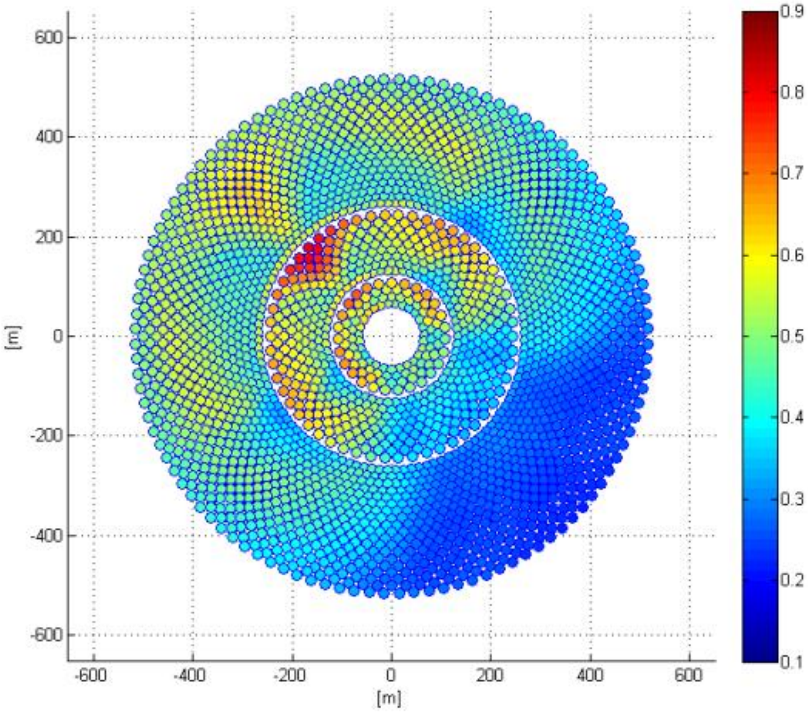

Figure 4.26 Contours of the optical efficiency of the un-optimized heliostat field with *dsep =0* for 21st December, solar time 9:00 a.m.

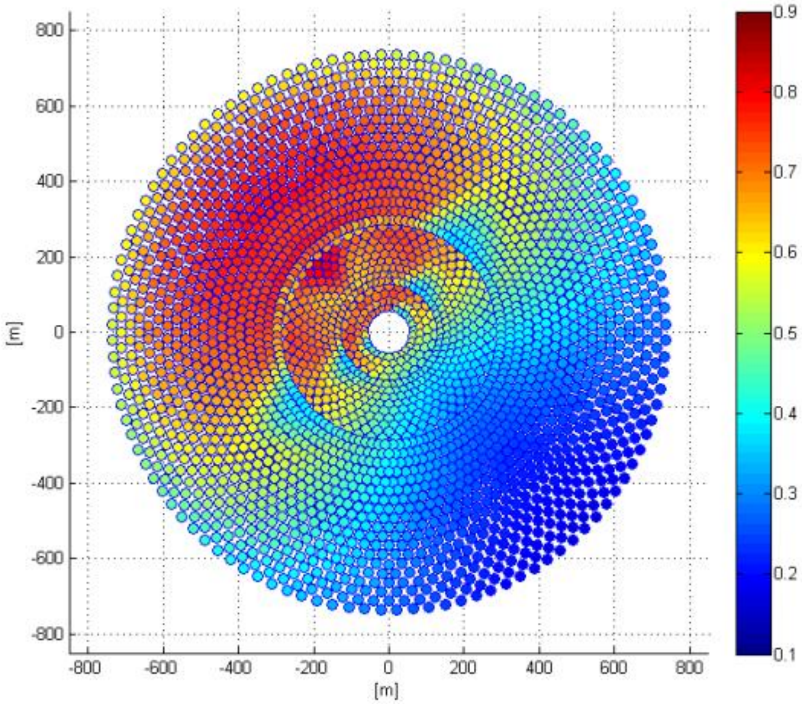

Figure 4.27 Contours of the optical efficiency of the optimized heliostat field with *dsep =0* for 21st December, solar time 9:00 a.m.(Case 1)

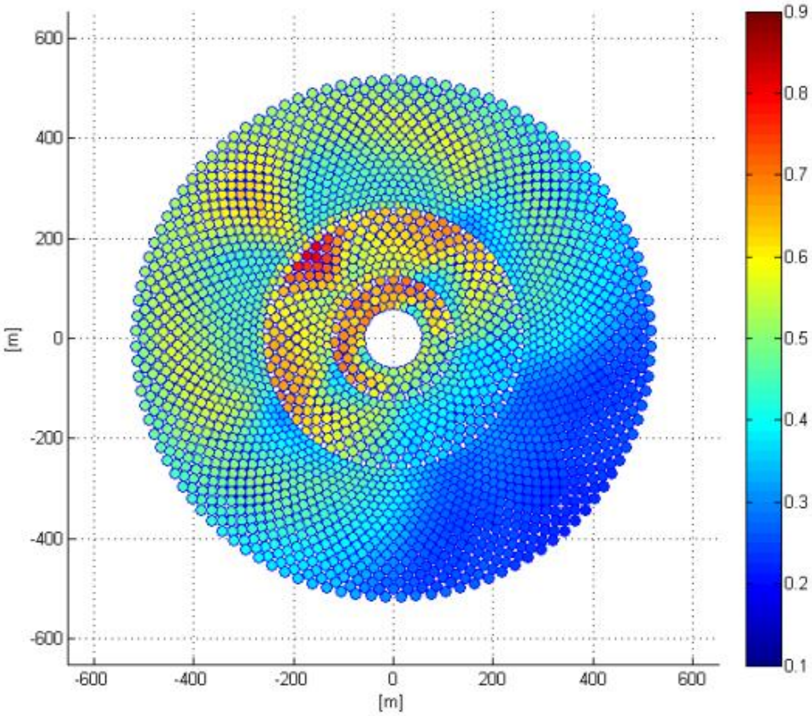

Figure 4.28 Contours of the optical efficiency of the optimized heliostat field with *dsep =0* for 21st December, solar time 9:00 a.m.(Case 2)

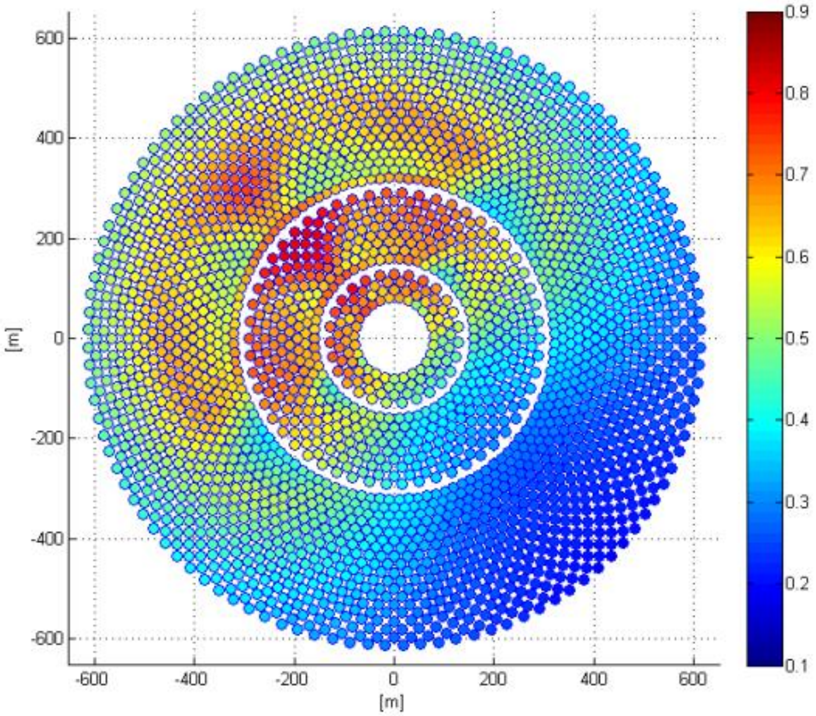

Figure 4.29 Contours of the optical efficiency of the unoptimized heliostat field with *dsep =3* for 21st December, solar time 9:00 a.m.

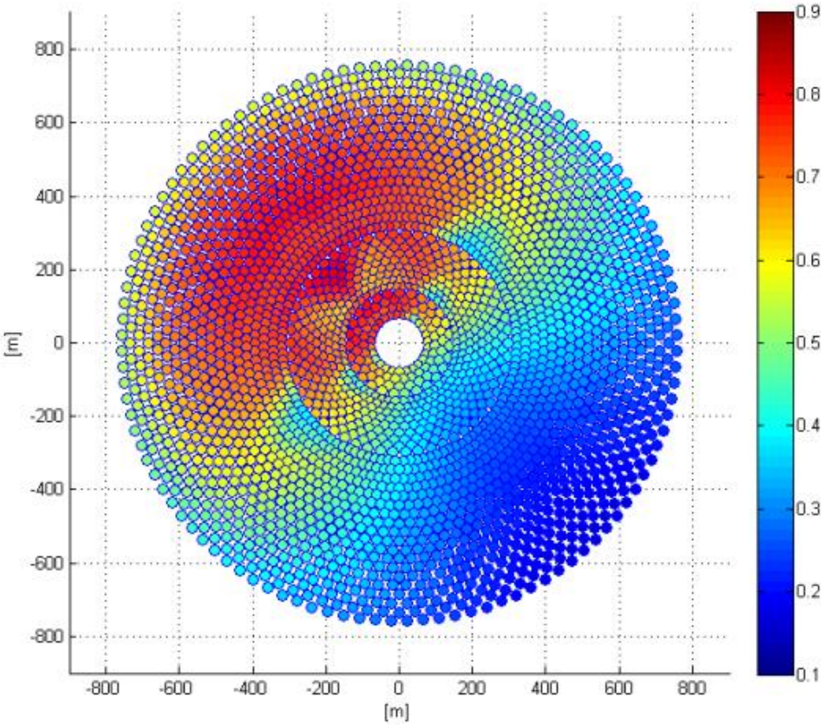

Figure 4.30 Contours of the optical efficiency of the optimized heliostat field with *dsep =3* for 21st December, solar time 9:00 a.m.(Case 1)

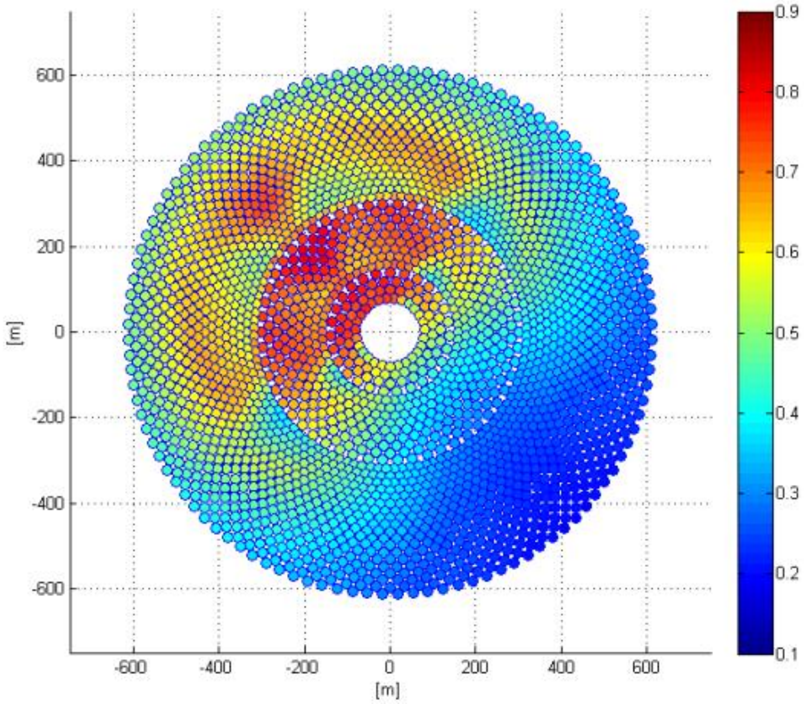

Figure 4.31 Contours of the optical efficiency of the optimized heliostat field with *dsep =3* for 21st December, solar time 9:00 a.m.(Case 2)

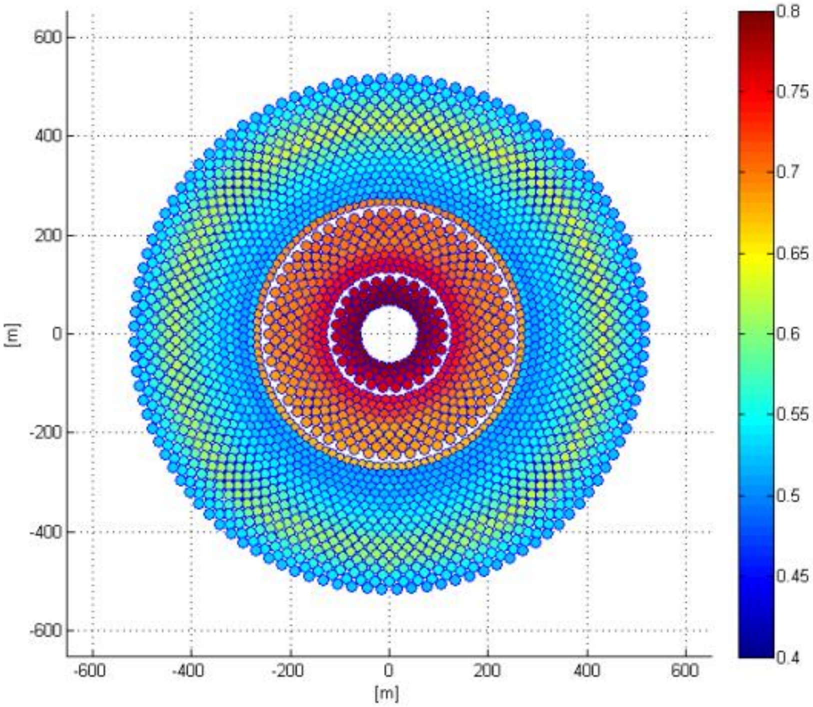

Figure 4.32 Contours of the optical efficiency of the un-optimized heliostat field with *dsep =0* for 21st June, solar noon

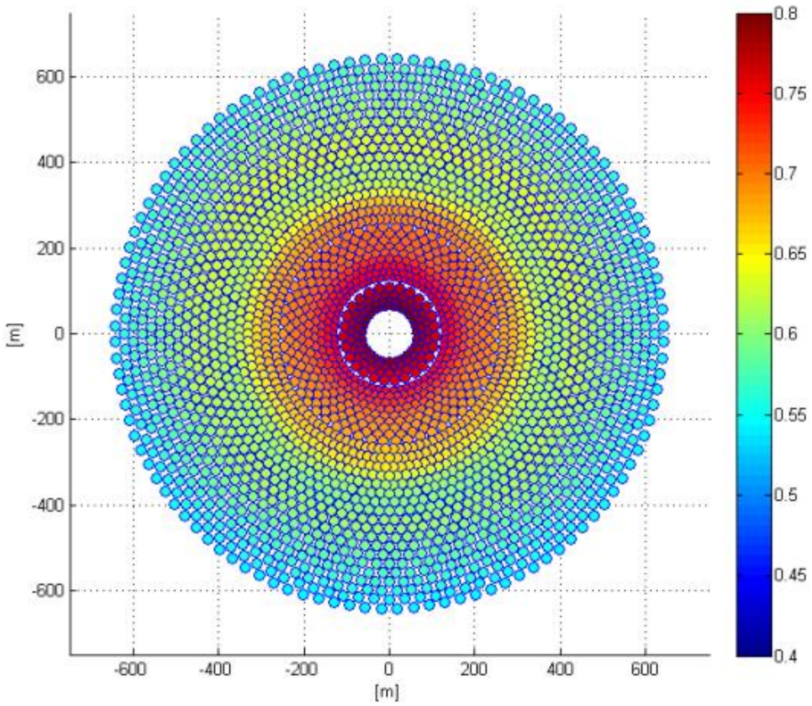

Figure 4.33 Contours of the optical efficiency of the optimized heliostat field with *dsep =0* for 21st June, solar noon (Case 1)

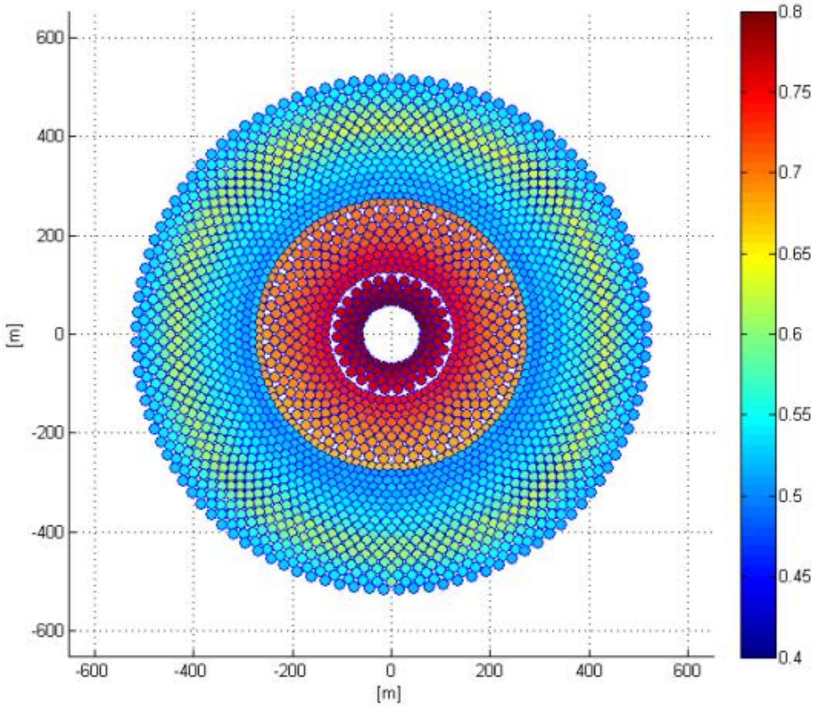

Figure 4.34 Contours of the optical efficiency of the optimized heliostat field with *dsep =0* for 21st June, solar noon (Case 2)

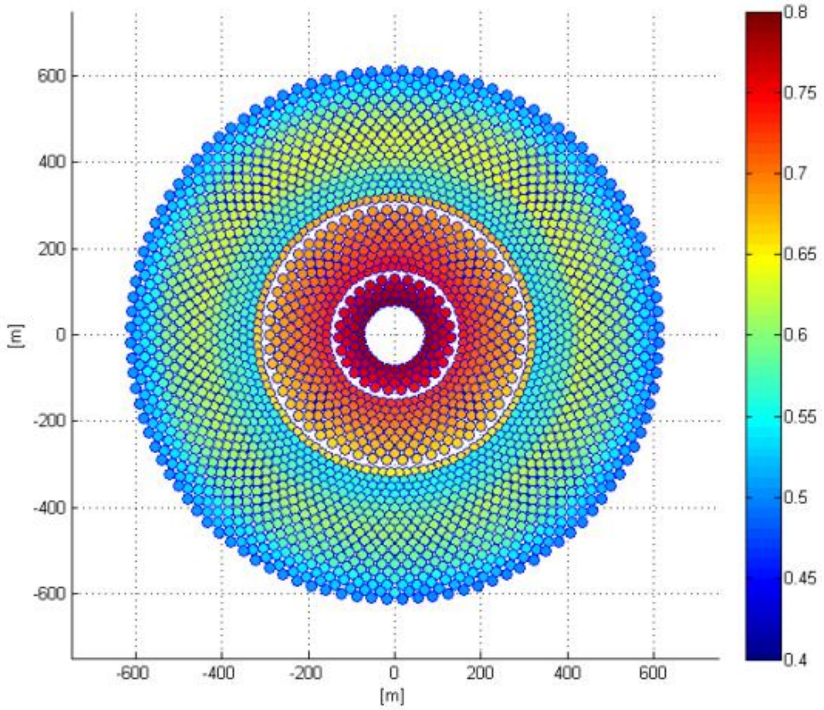

Figure 4.35 Contours of the optical efficiency of the un-optimized heliostat field with *dsep =3* for 21st June, solar noon (same as Case 2)

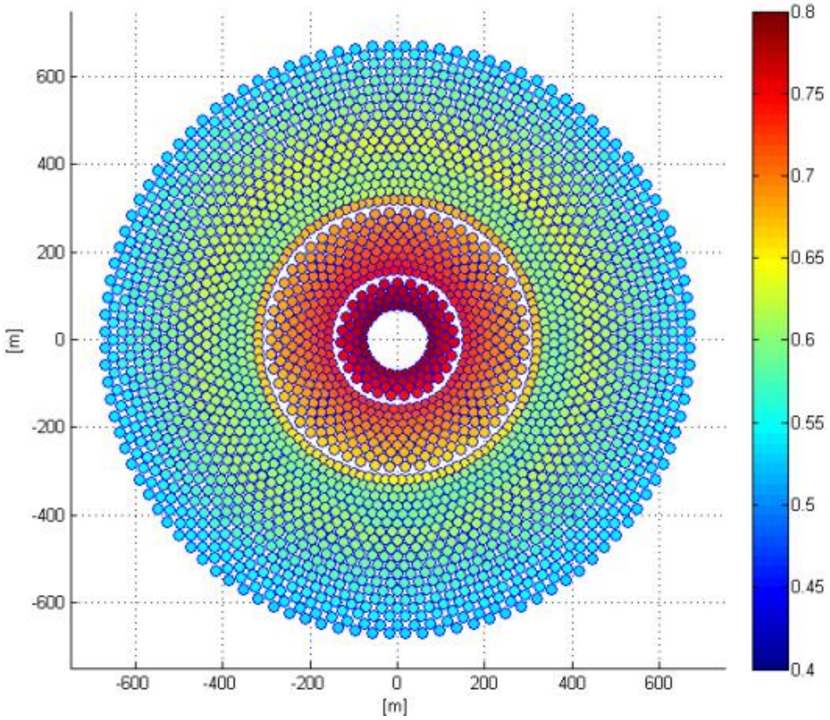

Figure 4.36 Contours of the optical efficiency of the optimized heliostat field with *dsep =3* for 21st June, solar noon (Case 1)

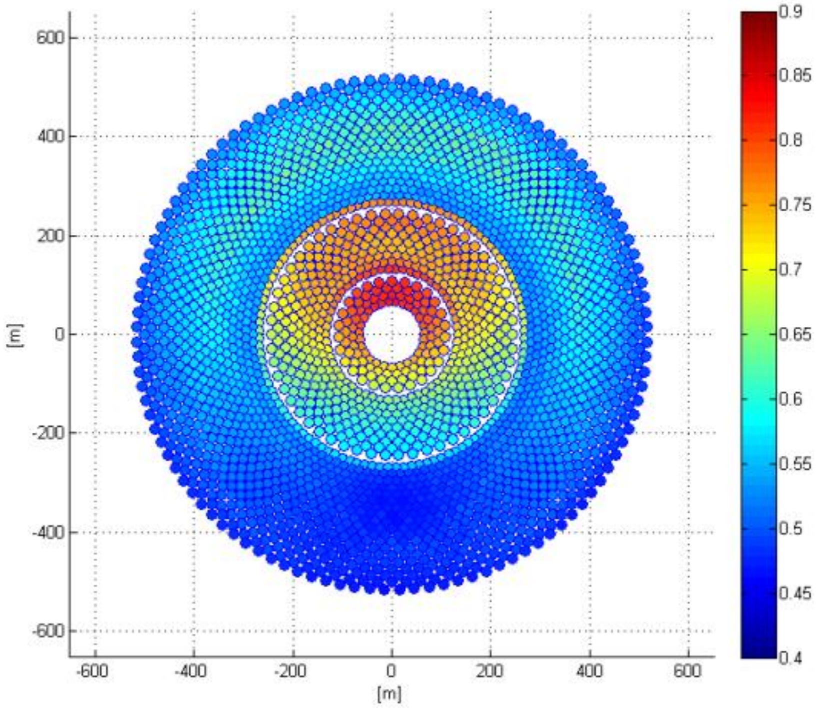

Figure 4.37 Contours of the optical efficiency of the un-optimized heliostat field with *dsep =0* for 21st March, solar noon

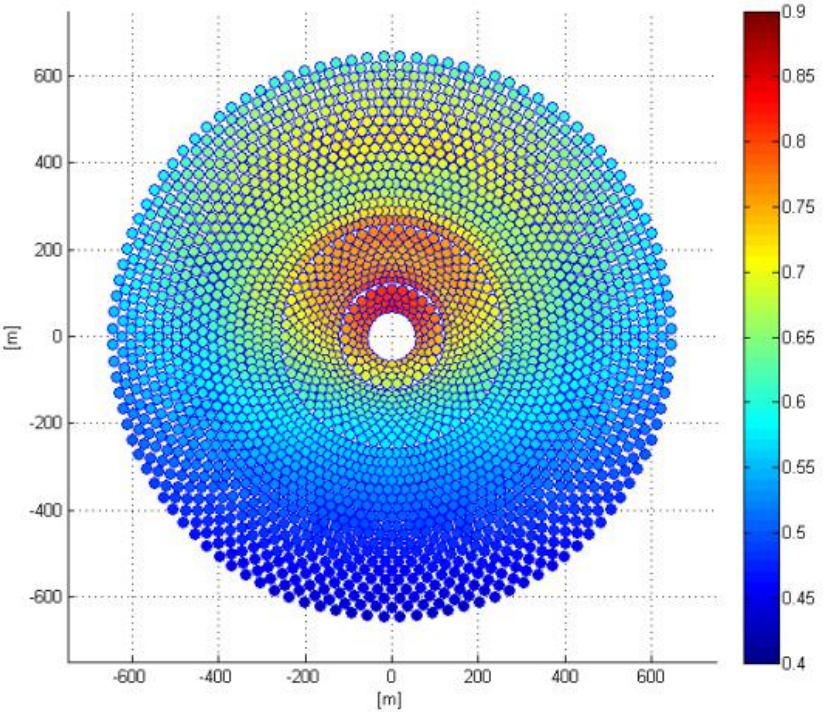

Figure 4.38 Contours of the optical efficiency of the optimized heliostat field with *dsep =0* for 21st March, solar noon (Case 1)

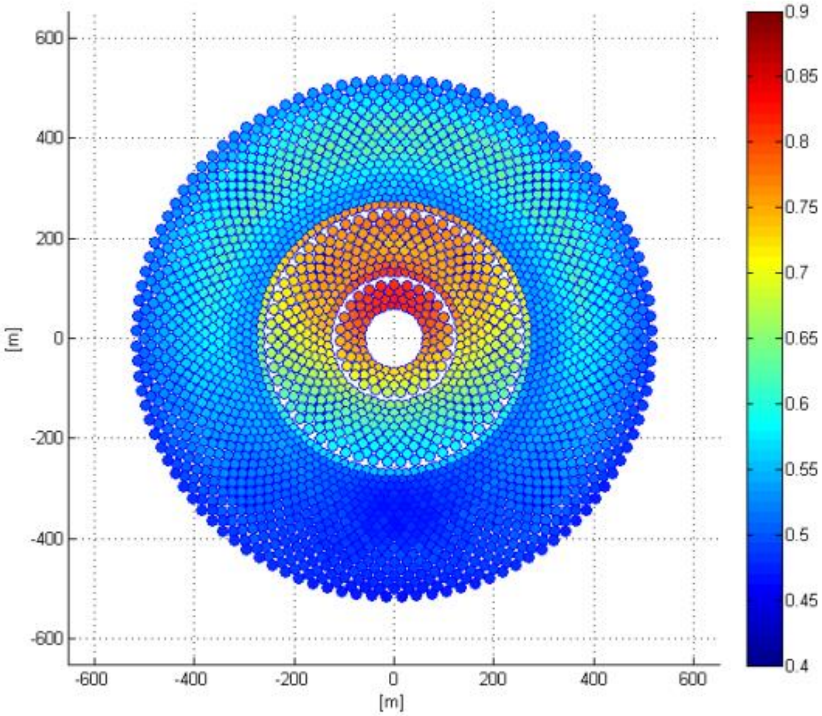

Figure 4.39 Contours of the optical efficiency of the optimized heliostat field with *dsep =0* for 21st March, solar noon (Case 2)

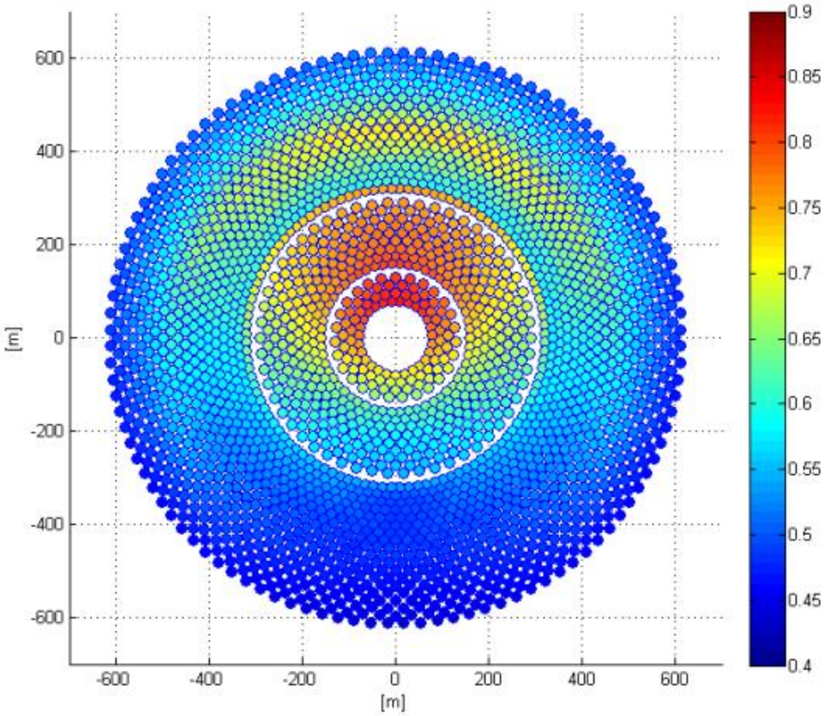

Figure 4.40 Contours of the optical efficiency of the un-optimized heliostat field with *dsep =3* for 21st March, solar noon (same as case 2)

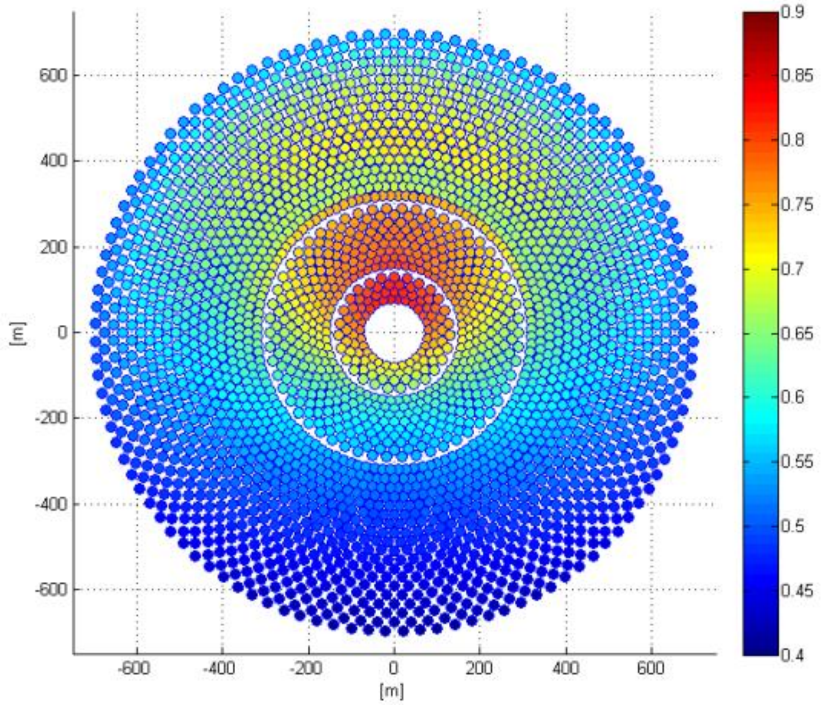

Figure 4.41 Contours of the optical efficiency of the optimized heliostat field with *dsep =3* for 21st March, solar noon (Case 1)

4.1.4 Annual Optimization of heliostat field

In this section, using the developed Matlab code, annual optimization of the preliminary generated heliostat field using DE when four variables are optimized is presented. This code calculates all the necessary optical performance parameters of all the heliostats at every step of the optimization until the best layout of the generated heliostat field is found. Table 4.1 (Page 78) lists the design parameters of the heliostat and the central receiver which were used in this study. Table 4.7 (Page 118) shows all the results obtained after optimizing the heliostat field using differential evolution. For the annual optimization, the number of heliostats considered was 2940 in a surround field layout, the tower optical height was taken as 130m. This optimization considers Dhahran city in Saudi Arabia as an illustrative example.

The mathematical model was adjusted so that the optimization could be carried out using differential evolution. In our model, the distance at the zone boundaries was also taken into account in the optimization process. Furthermore, two different ways were used for the demonstration of the heliostat field layout optimization using DE (HFLODE): one with optimizing the insolation weighted heliostat field efficiency and the other with optimizing un-weighted heliostat field efficiency. In addition, an alternate fast approach was also proposed and discussed for the optimization of the heliostat field. Other studies, such as the one by Collado and Guallar [42], did not take into account the extra security distance (*dsep*) in a complete optimization process; whereas this study also considers the extra security distance in the optimization process. Moreover, the effect of neglecting the extra security distance has also been discussed and presented.

As it can be observed from Table 4.7 that the un-weighted daily averaged annual heliostat field efficiency is 0.4746; and after optimization, using Equation (49), it becomes 0.5023. Figure 4.42 and Figure 4.43 depict the contours of the un-optimized and the optimized heliostat field efficiency on daily averaged basis. On the other hand, when the optimization was performed using Equation (51) as the objective function, the optimized heliostat field efficiency was 0.5025. The findings show that there is only a negligible difference in the two approaches because we have selected the average representative day for each month as suggested in[84,97]. Figure 4.44 and Figure 4.45 depict the contours of the un-optimized and the optimized heliostat field efficiency on monthly averaged basis. In addition, it takes a total of 144 time steps for the calculation of numerator of Equation (51); nevertheless, it takes a total of 3651 time steps for the calculation of numerator of Equation (49). Hence, the number of time steps was considerably reduced and thus the computation time was reduced significantly. It can be observed from Table 4.7 that the un-optimized heliostat field has low shadowing and blocking factor, whereas after optimization the shadowing and blocking factor improves but the rest of the optical performance parameters worsen. After optimization, the heliostat positions are arranged in such a way so as to reduce the blocking and shadowing caused by the other heliostats. However, as a result of increasing the distance between the heliostats, the overall distance of the heliostats from the tower increases, and consequently, the other optical performance parameters decrease. This is called the shadowing and blocking trade-off.

On the other hand, optimization was also carried out when neglecting the extra security distance between the heliostats to illustrate the difference between the two approaches with neglecting or considering the extra security distance. Table 4.8 (Page 118) depicts the optimization results of annual heliostat field efficiency using Equation (51) when the extra security distance was taken into account. It can be observed from Table 4.7 and Table 4.8, that there is a difference in both the un-optimized and the optimized heliostat field efficiencies as compared to the case when extra security distance is considered. Figure 4.46 and Figure 4.47 show the contours of the optical efficiency of the un-optimized and the optimized heliostat field when $dsep = 0$, respectively. The heliostat field efficiency improved from 0.4750 to 0.5025 after optimization when the extra security distance was taken into account. On the other hand, it improves from 0.4530 to 0.5075 if the extra security distance is neglected. In addition, it can be observed from Table 4.8 that the shadowing and blocking factor is relatively low as compared to the case when the extra security distance was considered (Table 4.7). By considering the extra security distance, the azimuthal spacing between the adjacent heliostats increases, and as a result, the shadowing and blocking factor initially is higher due to this increased distance between the heliostats. Furthermore, after optimization, the annual heliostat field efficiency is relatively higher as opposed to the case when the extra security distance was considered; this is because the heliostats have more freedom in placement during the optimization process due to the initial lower spacing between the adjacent heliostats. Thus, the heliostat field efficiency appears to be larger if the extra security distance is neglected, and this should be strictly checked when performing survey or feasibility study for the installation of solar tower plant in a complete optimization process.

Furthermore, the insolation weighted efficiency was calculated to be 0.5634 after optimization. Figure 4.48 and Figure 4.49 illustrate the contours of the un-optimized and the optimized insolation weighted daily averaged annual heliostat field efficiency, respectively. Note that the solar resource data was obtained from the weather station at King Fahd University of Petroleum & Minerals, Dhahran, Saudi Arabia. The DNI data used had been collected at hourly intervals. This study considered the calculation of the annual heliostat field efficiency from sunrise to sunset; however, other studies such as the one by Collado and Guallar [42] calculates the annual heliostat field efficiency considering time of the day when the solar elevation angle is equal to or more than 15°. If the insolation weighted annual heliostat field efficiency is calculated using this approach, the calculated heliostat field efficiency after optimization is 0.5912.

Table 4.7 Optimization results of heliostat field on annual basis with considering the extra security distance

	Un-optimized	Optimized
	Monthly averaged annual optimization	
$(\cos\omega)_{\_annual}$	*0.7438*	*0.7388*
f_{at_annual}	*0.9506*	*0.9464*
f_{sb_annual}	*0.8335*	*0.9097*
f_{itc_annual}	*0.9713*	*0.9464*
η_{maa}	*0.4750*	*0.5025*
	Daily averaged annual optimization	
$(\cos\omega)_{\_annual}$	*0.7437*	*0.7385*
f_{at_annual}	*0.9506*	*0.9462*
f_{sb_annual}	*0.8329*	*0.9114*
f_{itc_annual}	*0.9713*	*0.9448*
η_{daa}	*0.4746*	*0.5023*
	Insolation weighted daily averaged daily annual optimization	
η_{iwaa}	*0.5458*	*05634*

Table 4.8 Optimization results of the heliostat field on monthly averaged annual basis with *dsep=0*

	Un-optimized	Optimized
	Monthly averaged annual optimization	
$(\cos\omega)_{\_annual}$	*0.7544*	*0.7458*
f_{at_annual}	*0.9561*	*0.9501*
f_{sb_annual}	*0.7709*	*0.8970*
f_{itc_annual}	*0.9844*	*0.9582*
η_{maa}	*0.4530*	*0.5075*

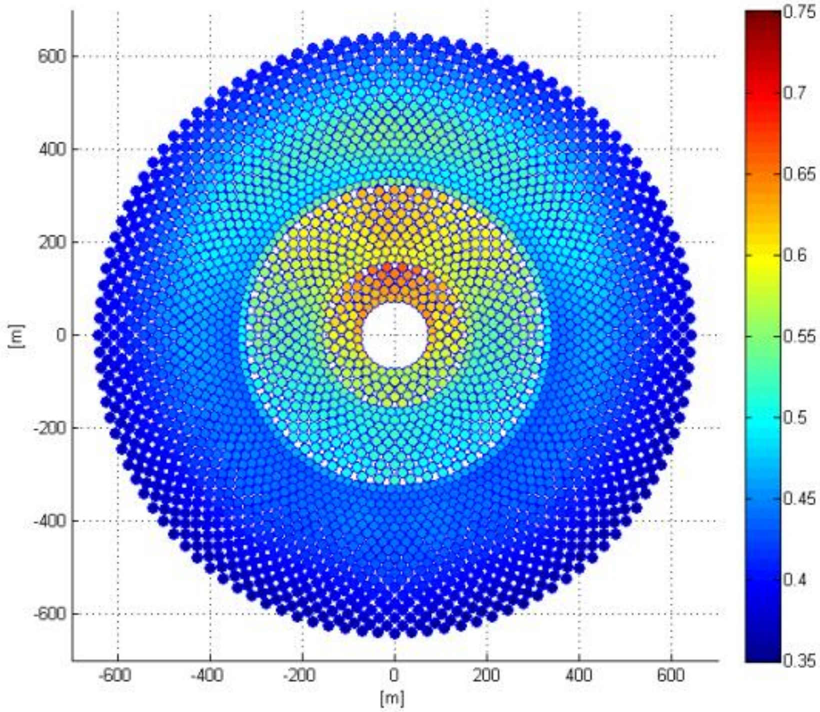

Figure 4.42 Contours of the optical efficiency of the annually un-optimized heliostat field on daily averaged basis

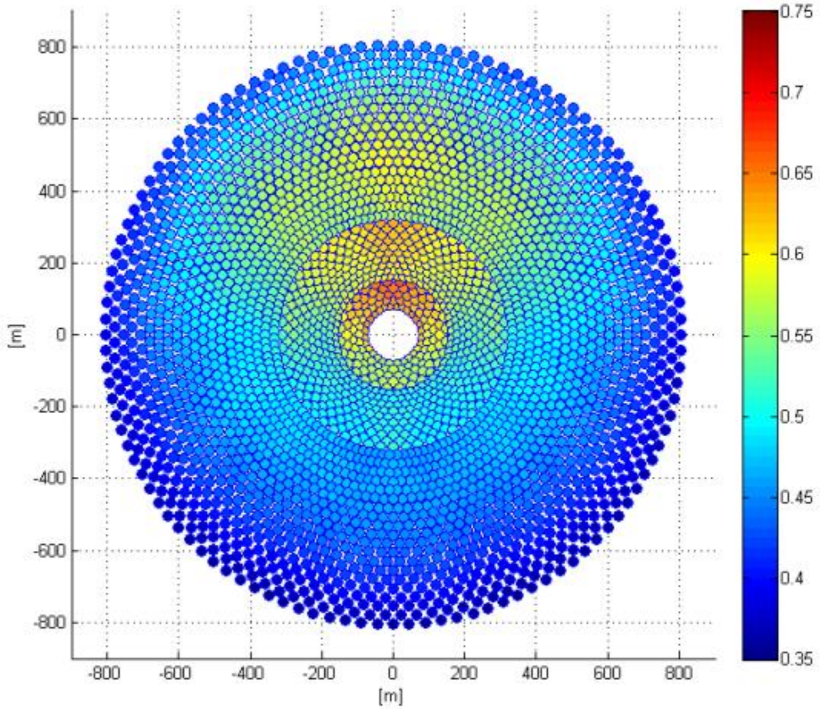

Figure 4.43 Contours of the optical efficiency of the annually optimized heliostat field on daily averaged basis

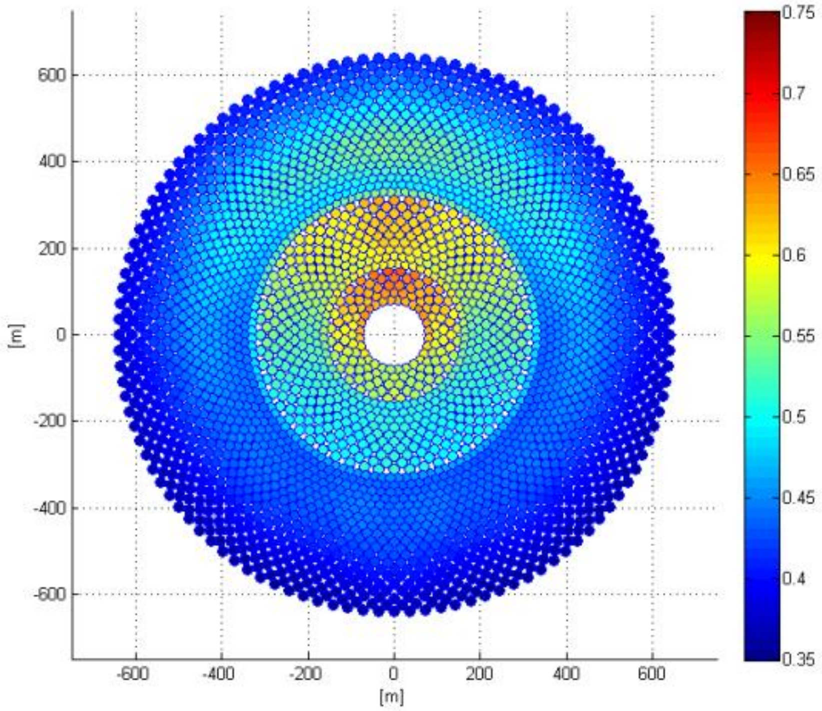

Figure 4.44 Contours of the optical efficiency of the annually un-optimized heliostat field on monthly averaged basis

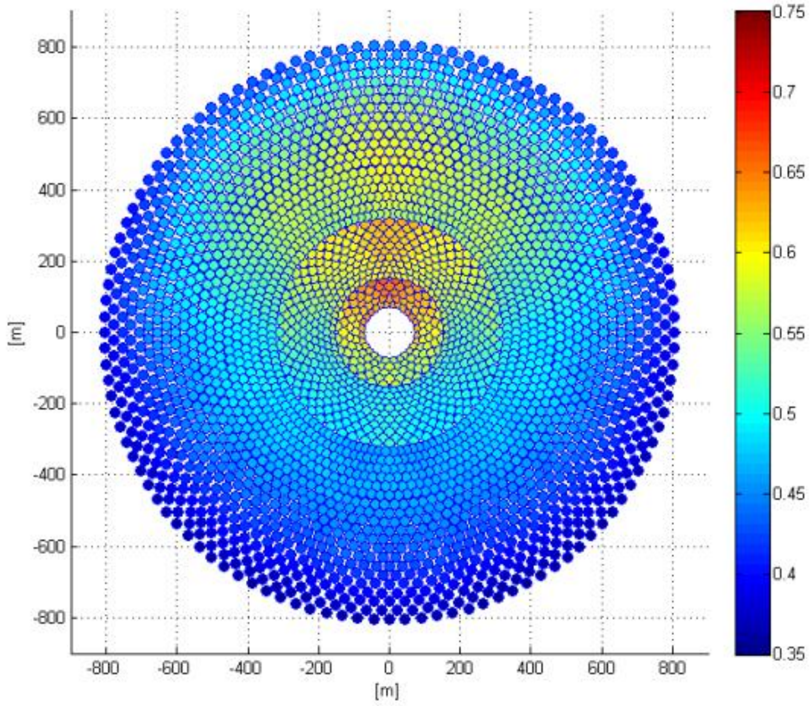

Figure 4.45 Contours of the optical efficiency of the annually optimized heliostat field on monthly averaged basis

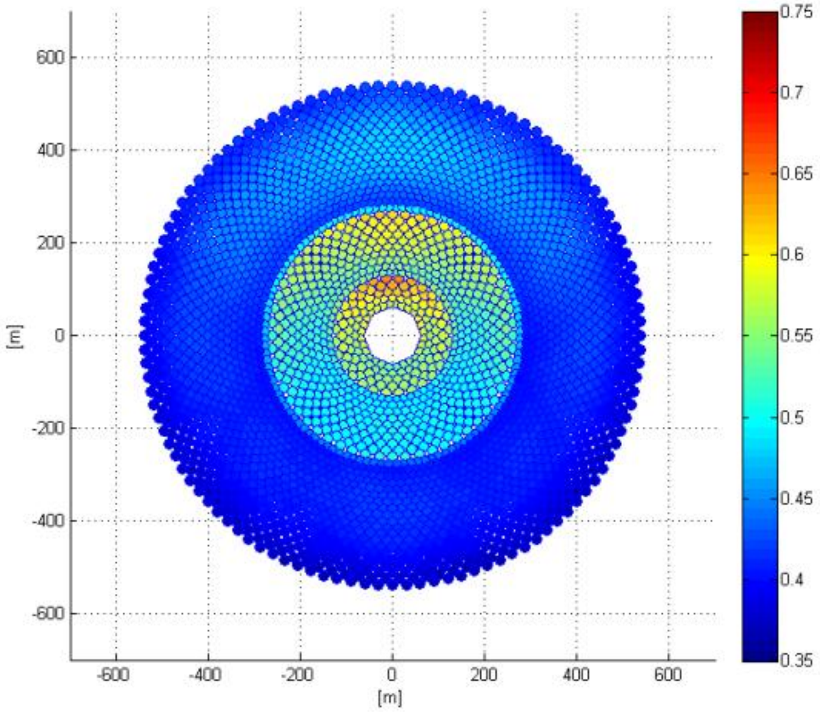

Figure 4.46 Contours of the optical efficiency of the annually unoptimized heliostat field on monthly averaged basis with *dsep=0*

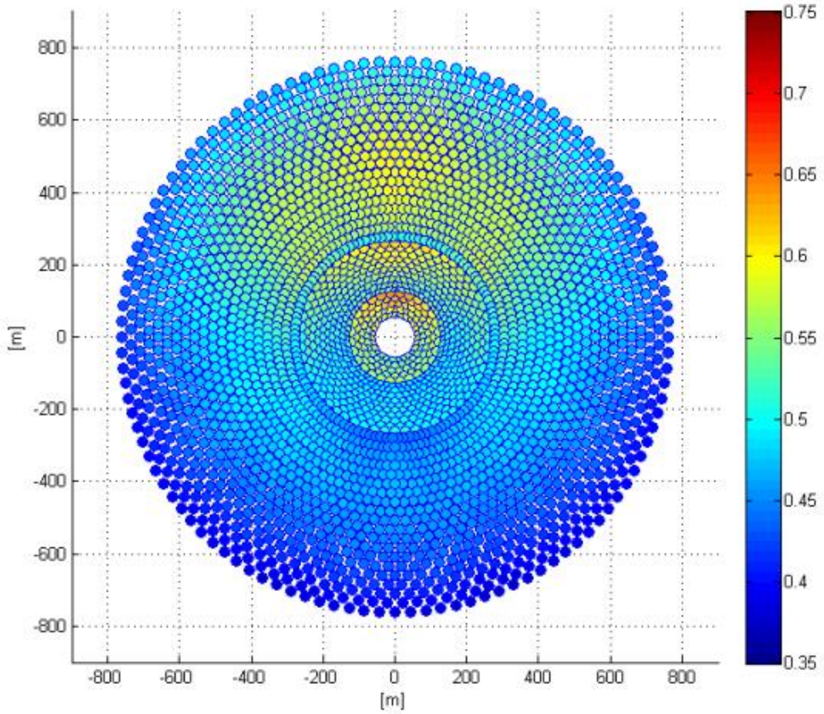

Figure 4.47 Contours of the optical efficiency of the annually optimized heliostat field on monthly averaged basis with *dsep=0*

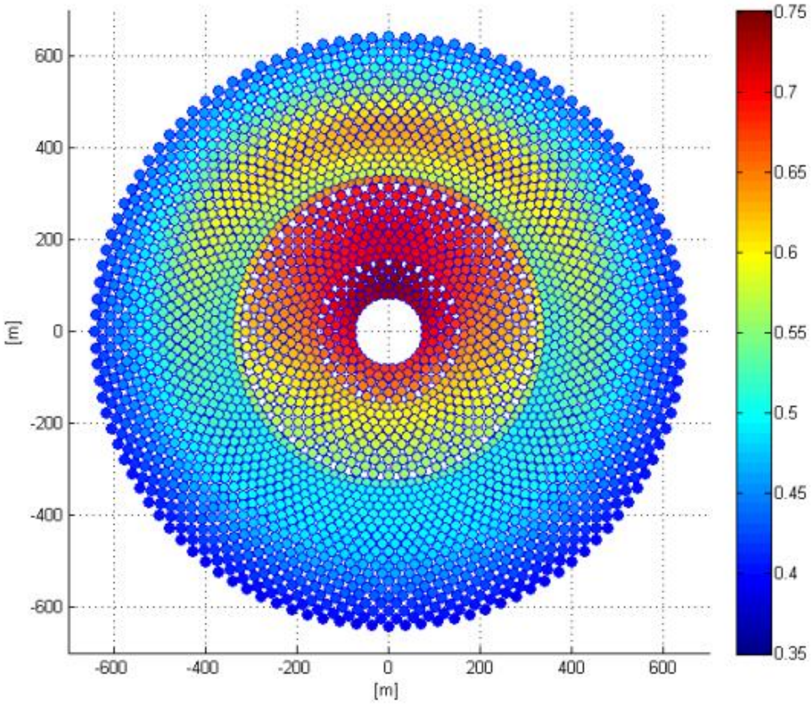

Figure 4.48 Contours of the optical efficiency of the annually un-optimized heliostat field on insolation weighted daily averaged basis

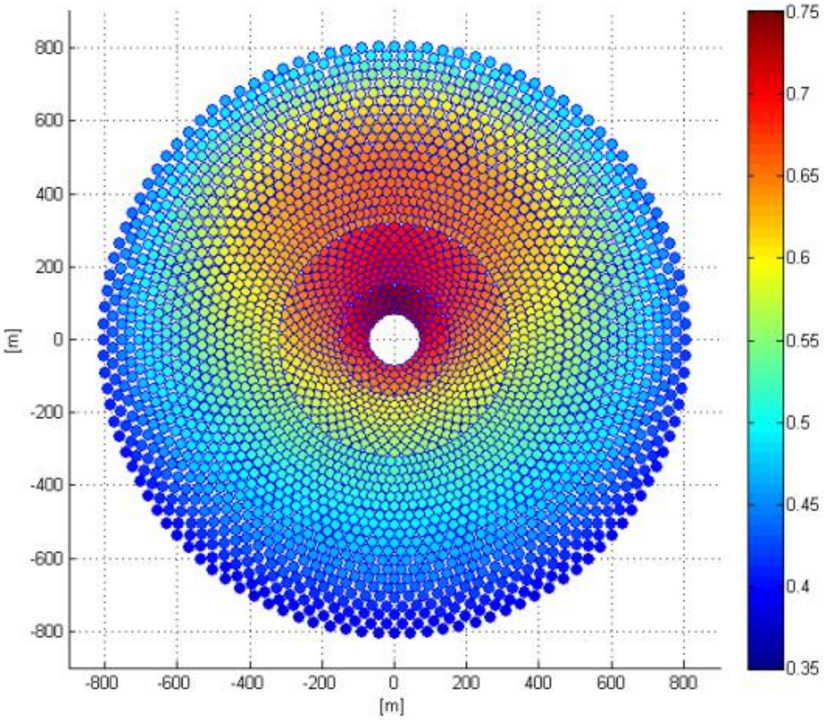

Figure 4.49 Contours of the optical efficiency of the annually optimized heliostat field on insolation weighted daily averaged basis

4.2 Central receiver

An EES [99] code was developed to model the central receiver. The values of the optical efficiency from the MATLAB code were used in the EES code as an input. Table 4.1(Page 78) lists all the design parameters used for the modeling of the central receiver. Furthermore, the value selected for the emissivity and the absorptivity of the receiver surface was 0.85 and 0.95, respectively [17].

There are four types of losses which concern the central receiver: optical losses, radiation heat losses, convection heat losses, and conduction heat losses. The conduction heat losses are insignificant as compared to the other two losses, so the conduction heat losses have been neglected in this study. On the other hand, due to very high concentration ratios of central receiver systems, radiation heat losses are more prominent as compared to the convection heat losses.

A total of 2940 heliostats were generated and optimized on an annual basis. The analysis was made for three days which are 16th of March, 11th of June, and 10th of December. These particular days were selected because they represent the solar radiation monthly average day of March, June, and December, respectively [84]. The net energy gained at the receiver for these three days are depicted in Figure 4.50 to Figure 4.52, respectively. Note that perfect weather conditions were not assumed and the actual DNI (direct normal irradiance) data was used which was obtained from the weather station at King Fahd University of Petroleum & Minerals, Dhahran, Saudi Arabia. The DNI data used had been collected for hourly intervals. These figures demonstrate the total incident energy onto the receiver from the heliostat field and the net energy gained or the useful energy gained at the receiver after the radiation losses have been accounted for. The DNI data is also illustrated in the same figures for comparative purposes.

On the other hand, Figure 4.53 to Figure 4.55 represent the relation of the net energy collected at the receiver and the optical efficiency of the heliostat field versus the area of the heliostat field. Again, these figures are also plotted for the same aforementioned days but at noon time. It can be observed from these figures that as the heliostat field size increases, the optical performance of the field decreases. This is because of the increasing number of heliostats focusing on the same tower. When number of heliostats increases, the new heliostats have to be placed further away from the tower. Thus their optical performance is low because of this increased distance from the tower. And hence, the overall efficiency of the heliostat field decreases.

On the contrary, increasing the heliostat area increases the net energy gained at the receiver. The variables x_1 and $x_{2,i}$ were optimized for a total of 2940 heliostats, and then the same values for these optimized variables were used to plot Figure 4.53 to Figure 4.55. It can be observed from these figures that there does not seem to be any decrease or the profile does not seem to decrease asymptotically. This is not true, the net energy gained worsens but the decrease is not much significant because adding more rows of heliostats increases the heliostat area exponentially.

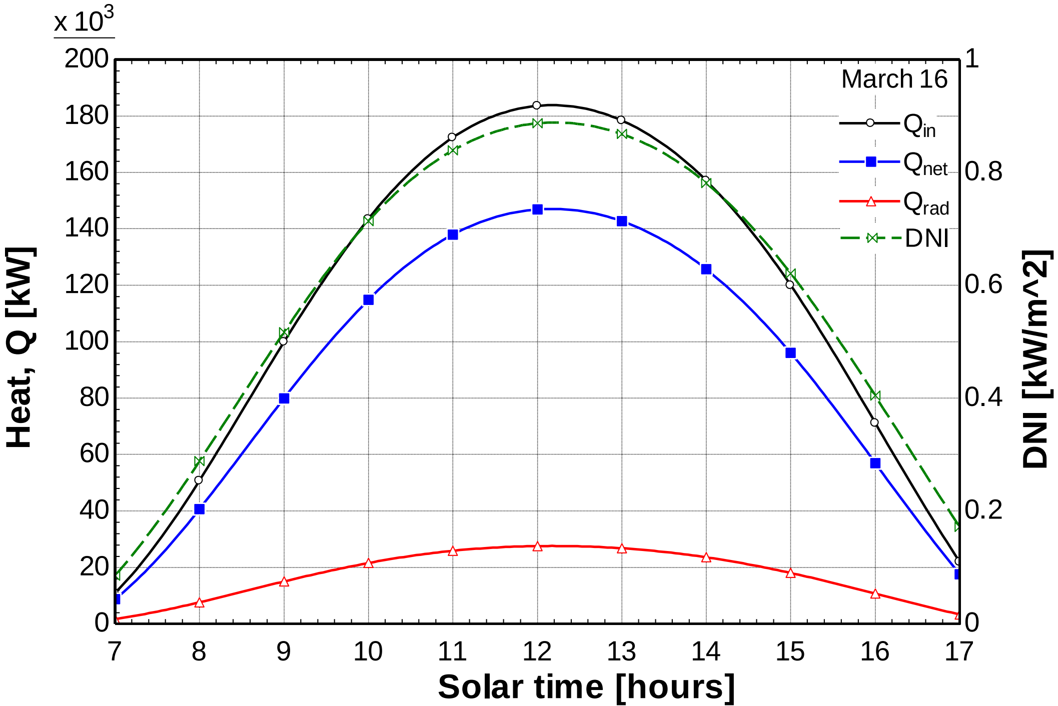

Figure 4.50 Net energy gained for 16th March, Dhahran, Saudi Arabia

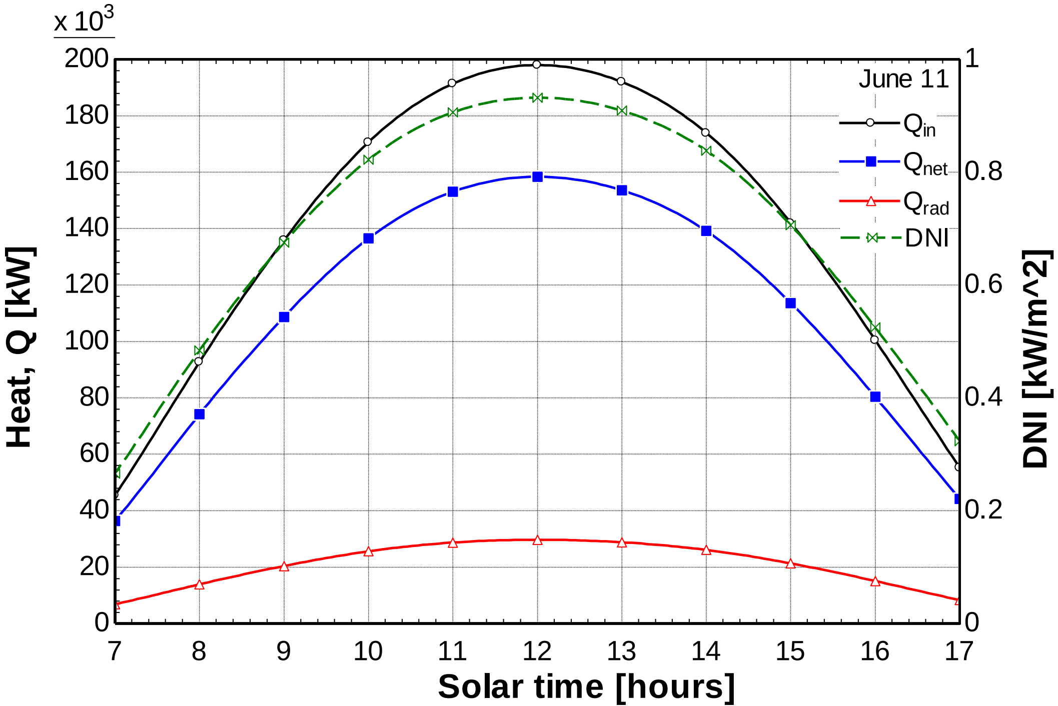

Figure 4.51 Net energy gained for 11th June, Dhahran, Saudi Arabia

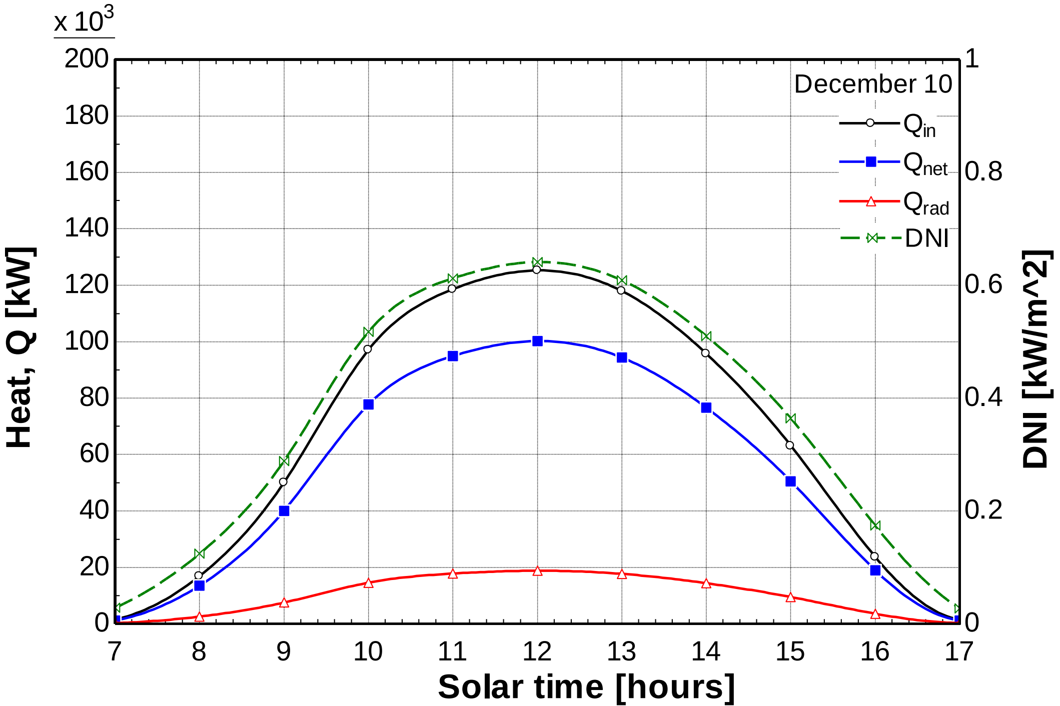

Figure 4.52 Net energy gained for 10th December, Dhahran, Saudi Arabia

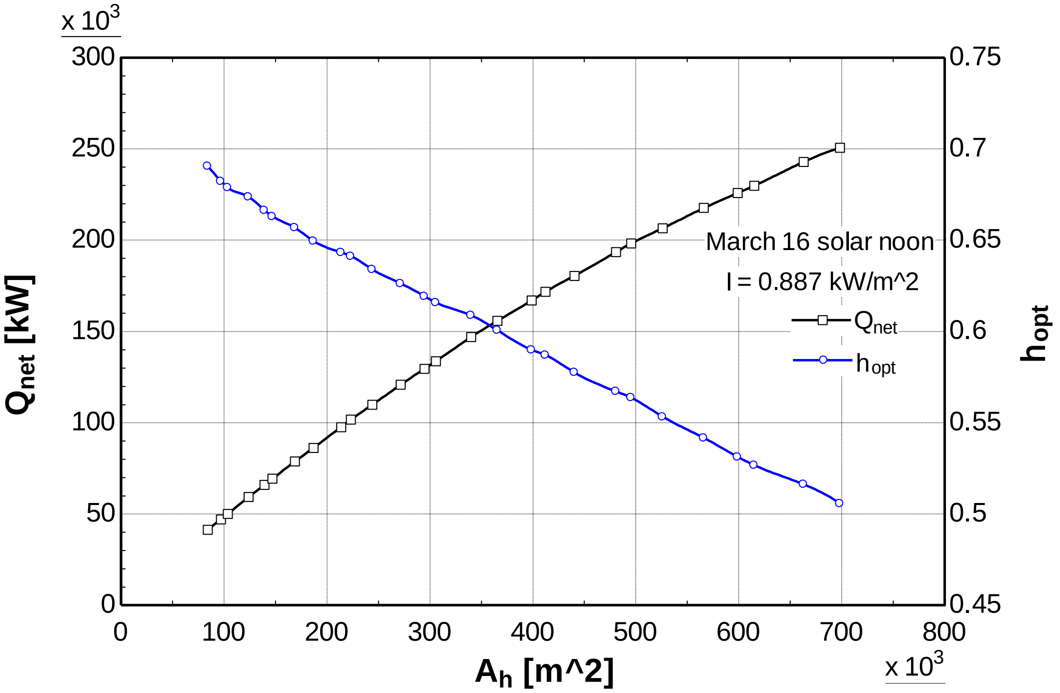

Figure 4.53 Optical efficiency of the heliostat field and the net energy gained at the receiver for 16th March, solar noon, Dhahran, Saudi Arabia

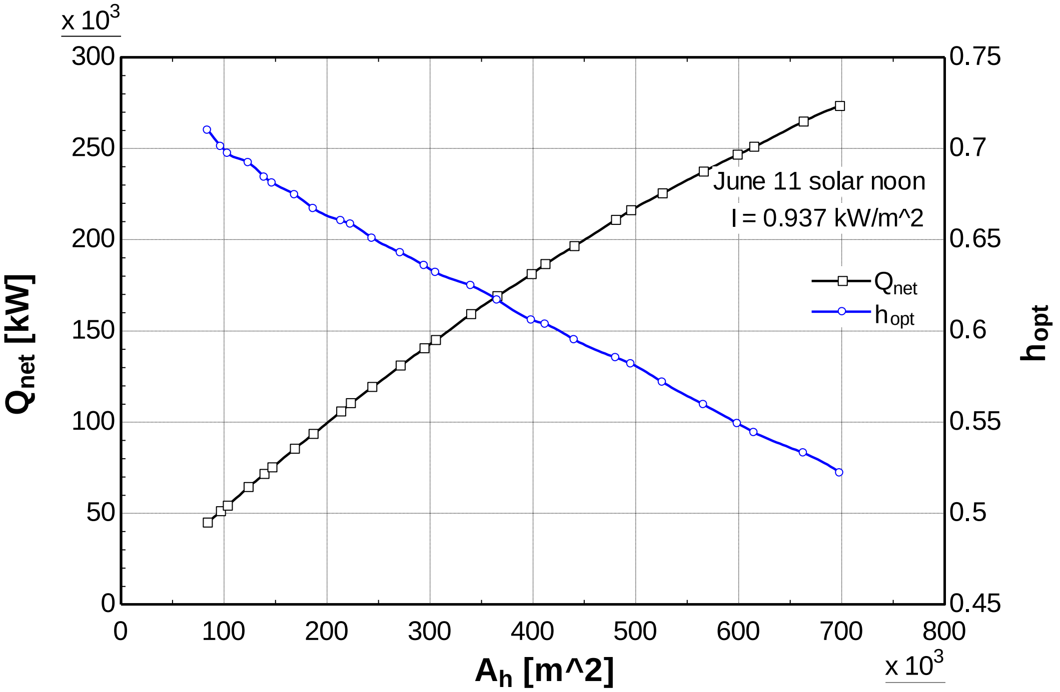

Figure 4.54 Optical efficiency of the heliostat field and the net energy gained at the receiver for 11th June, solar noon, Dhahran, Saudi Arabia

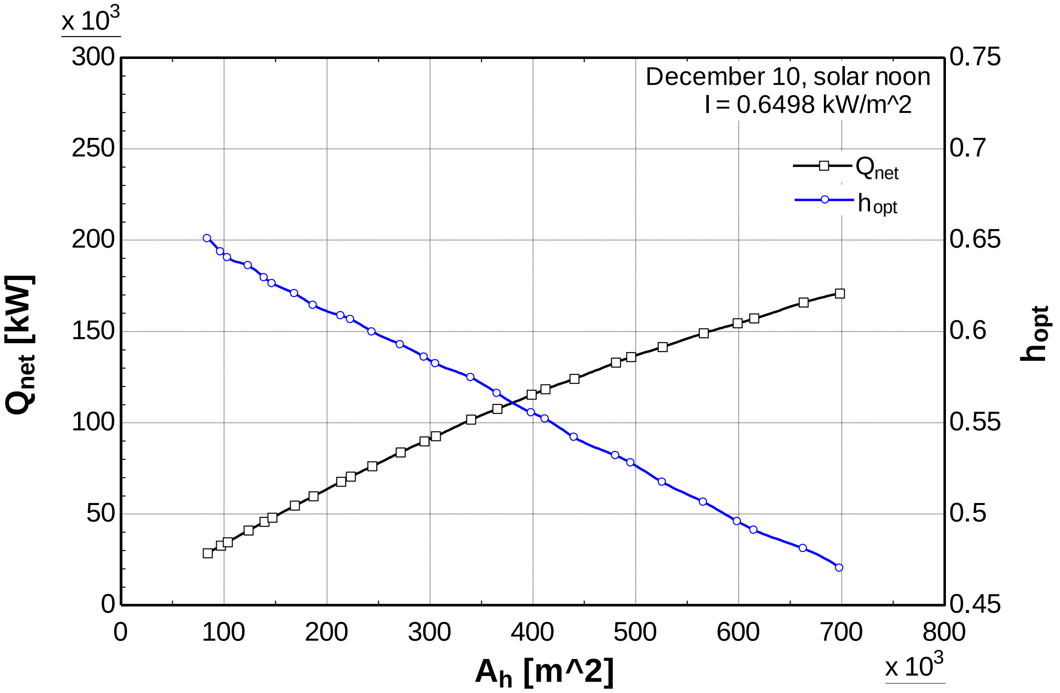

Figure 4.55 Optical efficiency of the heliostat field and the net energy gained at the receiver for 10th December, solar noon, Dhahran, Saudi Arabia

4.3 Supercritical CO_2 Brayton cycles

A complete thermodynamic analysis of the integrated solar tower power system and supercritical CO_2 cycles was performed for three days of the year. These days are 16th of March, 11th of June, and 10th of December. These particular days were selected because they represent the solar radiation monthly average day of March, June, and December, respectively [84]. Table 4.9 (Page 133) lists the basic design and operating parameters of the heliostat field and the central receiver whereas the operating conditions of the supercritical CO_2 Brayton cycles are listed in Table 4.10 (Page 133). The mass flow rate of sCO_2 for all the cycles was 600 kg/s.

A total of 2940 heliostats were generated and optimized on an annual basis. Higher number of heliostats were optimized to integrate the solar field to thermal storage and perform analysis. This is discussed in detail in the next section. The contours of the net optical efficiency of the heliostat field are illustrated in Figure 4.56 to Figure 4.58 for 16th of March, 11th of June, and 10th of December at solar noon, respectively. The heliostat field depicted in the discussed figures is annually optimized. As can be observed from the figures that the highest optical performance is achieved on 11th of June at solar noon while the lowest optical performance is achieved on 10th of December at solar noon. On the other hand, the optical performance is in the medium range for 16th of March at solar noon. This observation can be attributed to the solar altitude angle of these days. The sun altitude angle for June 11 is the highest at noon time as compared to March 16 and December 10; that is why most of the heliostats on June 11 depict high optical efficiency.

The net energy gained at the receiver for these three days are depicted in Figure 4.50 to Figure 4.52 respectively. Note that perfect weather conditions were not assumed and the actual DNI (direct normal irradiance) data was used which was obtained from the weather station at King Fahd University of Petroleum & Minerals, Dhahran, Saudi Arabia. The DNI data used had been collected for hourly intervals. These figures demonstrate the total incident energy onto the receiver from the heliostat field and the net energy gained or the useful energy gained at the receiver after the radiation losses have been accounted for. The DNI data is also illustrated in the same figures for comparative purposes.

The net power outputs for all the cycles with varying heat input for these different days are depicted in Figure 4.59 to Figure 4.61. On the other hand, comparative thermal efficiencies of all the cycles of these days are illustrated in Figure 4.62 to Figure 4.64. Moreover, the integrated overall thermal system efficiency of all the cycles is also depicted in Figure 4.65 to Figure 4.67. Additionally, for the sake of analysis and comparison, the change in turbine inlet temperature with time due to varying heat input to the thermodynamic cycles was also portrayed because it was not fixed, as shown in Figure 4.68 to Figure 4.70. The sCO_2 Brayton cycles were modeled in such a way that instead of fixing the turbine inlet temperature, varying energy gain with respect to time at the receiver was taken as the input value to the integrated thermodynamic Brayton cycles. The mass flow rate of sCO_2 for the Brayton cycles was taken as a constant value for all the cases. These figures are discussed in details next.

The solar time on the x-axis of Figure 4.50 to Figure 4.52 is taken from 07:00 hours to 17:00 hours. On the other hand, for other Figures (Figure 4.59 - Figure 4.70), it varies from day to day. The reason of choosing different time on x-axis is that the output turbine work rate was lower as compared to the required compressor work rate because of the low solar radiation for that instant of time; thus the cycle was producing no net useful power output outside these time frames.

As can be observed from Figure 4.59 and Figure 4.60, the recompression cycle has the highest amount of net power for the same operating conditions on 16th of March and 11th of June, respectively. Subsequently, the highest thermal efficiency and system efficiency occur around solar noon for the same days, as revealed in Figure 4.62 and Figure 4.63 and in Figure 4.65 and Figure 4.66, respectively. The maximum net power produced from the recompression cycle is around 82 MW while the highest thermal efficiency is 52% and the highest system efficiency is 40%, all for June 11. However, this was not the case for 10th of December. It can be observed that the regenerative cycle exhibits higher amount of net power and thermal efficiencies, as shown in Figure 4.61, Figure 4.64, and Figure 4.67. This anomalous behavior occurred because of the fixed amount of mass flow rate through the Brayton cycles. This mass flow rate was more suited to the regenerative cycle, which has a simpler configuration, and due to the low DNI on 10th of December as presented in Figure 4.52. For this case, the net heat gained is relatively low as compared to the other two days and subsequently the performance of the regenerative Brayton cycle is higher as compared to the other Brayton cycles. On the other hand, the split expansion cycle and the regenerative cycle have almost overlapping curves for both the net power obtained and the thermal efficiency for 16th of March and 11th of June. Nevertheless, for low heat input values, right after sunrise or before sunset, the regenerative cycle exhibits higher amount of power and thermal efficiency as compared to the split expansion cycle.

The pre-compression cycle does not demonstrate high amount of power for 16th of March and 11th of June. This relative low performance is attributed to the configuration of the cycle. This behavior is due to the addition of the second compressor after the high temperature regenerator which makes place for further regeneration, but as a consequence, the amount of work consumed by this second compressor is much higher as compared to the first compressor; because it is compressing sCO_2 at the critical point. Unlike the recompression and split expansion cycle, where the consumed work by the second compressor is much lower because of splitting the flow stream and allowing only a fraction of the total to be passed through the second compressor. On the other hand, although the recompression cycle and the pre-compression cycle have the same number of components, the placement of an additional compressor between the two regenerators in the pre-compression cycle makes room for additional regeneration and helps in avoiding pinch point problems. For low heat inputs during 10th of December, the net power obtained by the pre-compression cycle is very close to that of the split expansion cycle as demonstrated in Figure 4.61.

Although the thermal efficiency of the pre-compression cycle is low, this cycle has the highest turbine inlet temperature (TIT) for 16th of March and 11th of June, which is again because of the arrangement of the second compressor between the regenerators, as shown in Figure 4.68 and Figure 4.69. This arrangement causes the temperature of the high-pressure side to rise because it has recuperated heat at higher temperature and consequently the TIT is the highest for the pre-compression cycle. The recompression cycle, similarly, has almost the same TIT, and both cycles have almost overlapping curves for TIT. The TIT of the split expansion Brayton cycle’s second turbine is also close to the pre-compression and the recompression cycles; but the TIT of the first turbine for the same cycle is low because the fluid expands before any heat is added to the cycle, and only recuperated heat from the regenerators is used to expand in the first turbine. Nevertheless, for the case of December 10, due to low net heat gained at the receiver, the recompression cycle exhibits the highest TIT, although the regenerative cycle has the highest net power gained and the highest thermal efficiencies for this day, as shown in Figure 4.61, Figure 4.64, and Figure 4.67.

Each of these cycles is discussed at component level next for better understanding through the use of graphs.

Table 4.9 Basic design and operating parameters used for the heliostat field and the central receiver [17,42,102]

Tower optical height, *THT*	130 m
Heliostat height , *LH*	9.75m
Heliostat width, *LW*	12.3m
Fraction of mirror area of heliostat	0.9642
Receiver diameter (cylindrical), *DR*	9.44
Receiver size, *LR*	9.44
Mirror reflectivity × cleanliness, ρ	0.88×0.95
Standard deviation of sunshape errors, σ_{sun}	2.51 mrad
Standard deviation of tracking errors, σ_t	0.63 mrad
Standard deviation of beam quality errors, σ_{bq}	1.88 mrad
Emissivity of the receiver surface, ε	0.85
Absorptivity of the receiver surface, α_R	0.95

Table 4.10 Basic design and operating parameters used for the sCO$_2$ Brayton cycles

Temperature at the inlet of compressor (first compressor)	31.25° C
Pressure at the inlet of the compressor (first compressor)	7.4 MPa
Pressure ratio	2.7
High temperature regenerator effectiveness [71]	0.85
Low temperature regenerator effectiveness	0.7
Isentropic efficiencies of the compressors[71]	0.8
Isentropic efficiencies of the turbines[71]	0.9

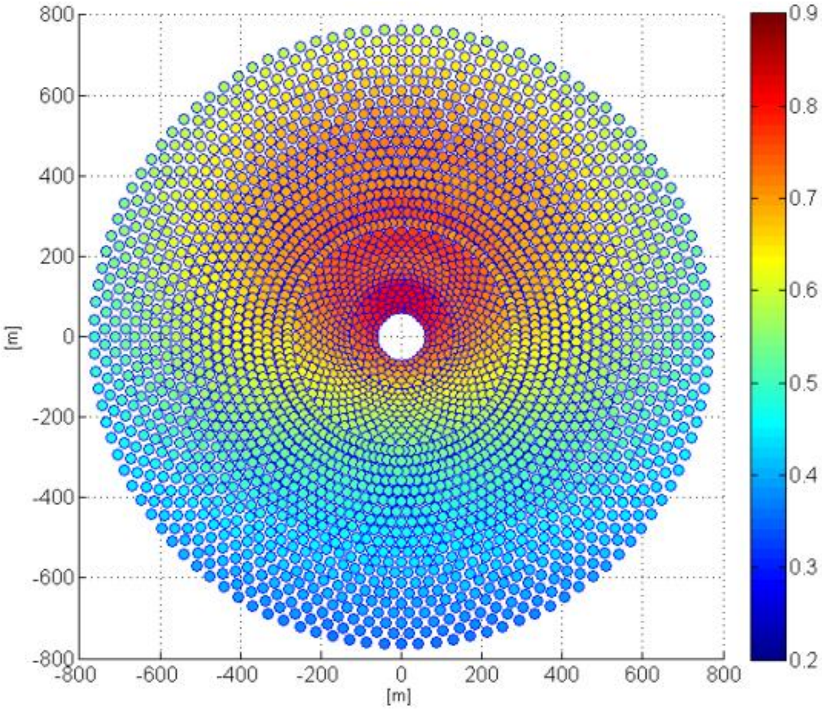

Figure 4.56 Contours of the net optical efficiency of the heliostat field at solar noon, March 16, Dhahran, Saudi Arabia

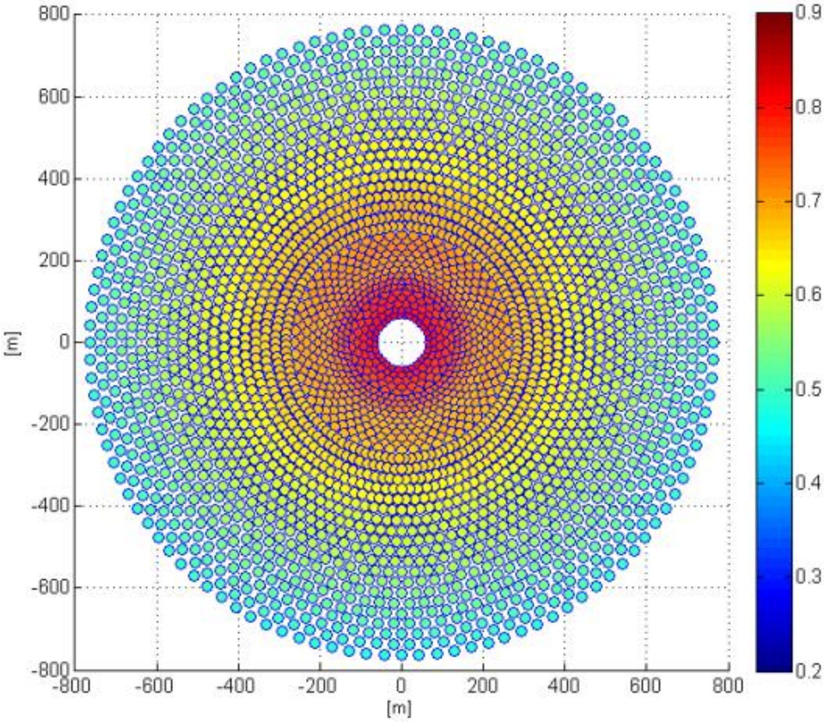

Figure 4.57 Contours of the net optical efficiency of the heliostat field at solar noon, June 11, Dhahran, Saudi Arabia

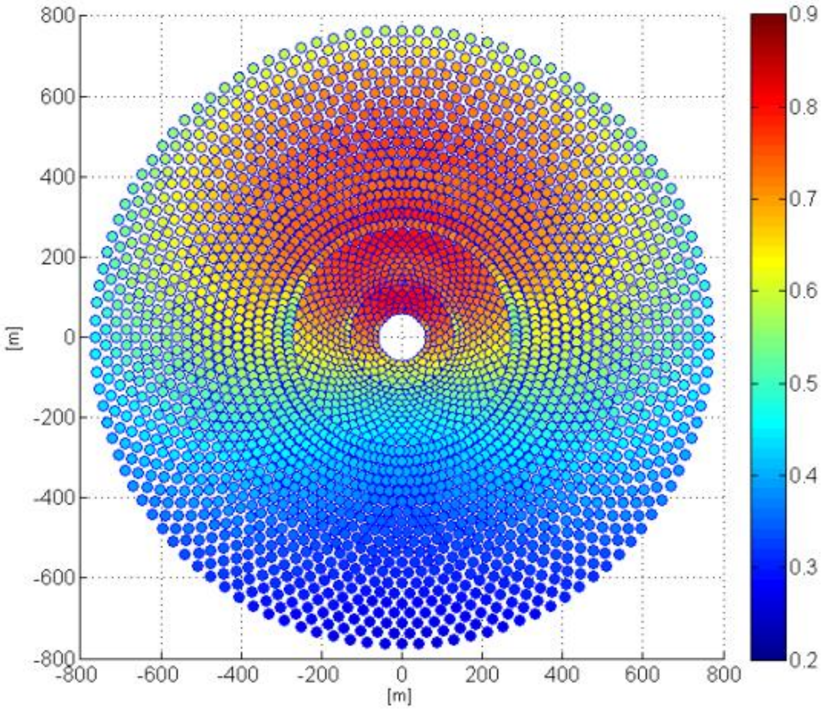

Figure 4.58 Contours of the net optical efficiency of the heliostat field at solar noon, December 10, Dhahran, Saudi Arabia

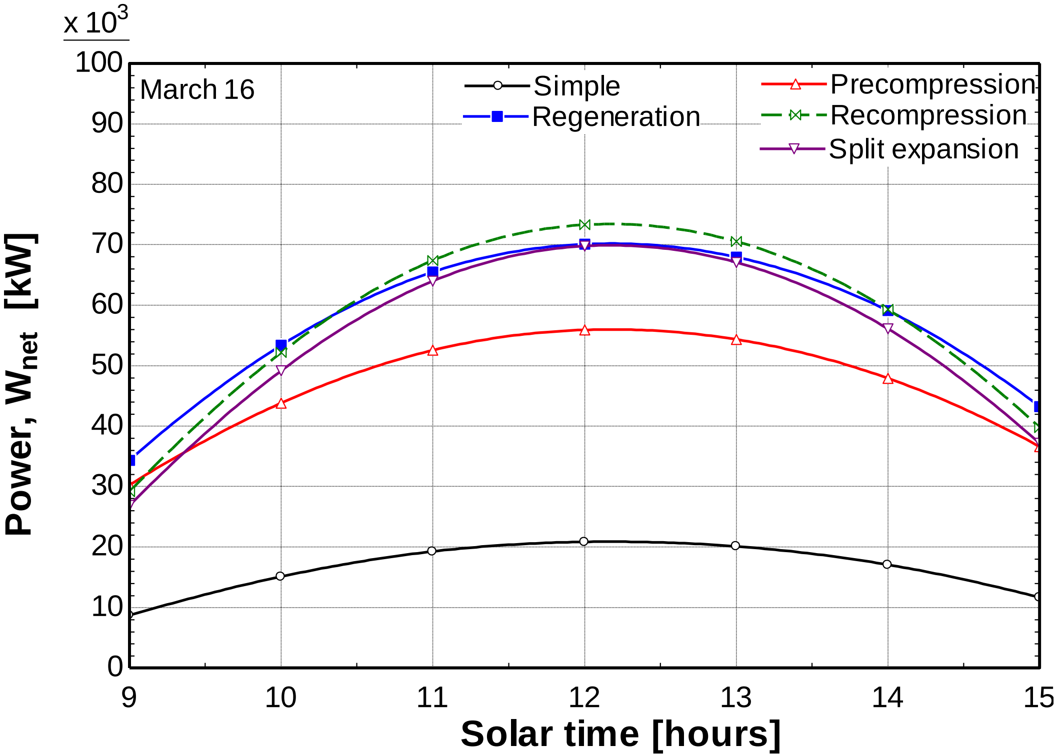

Figure 4.59 Comparison of net power output for 16th of March, Dhahran, Saudi Arabia

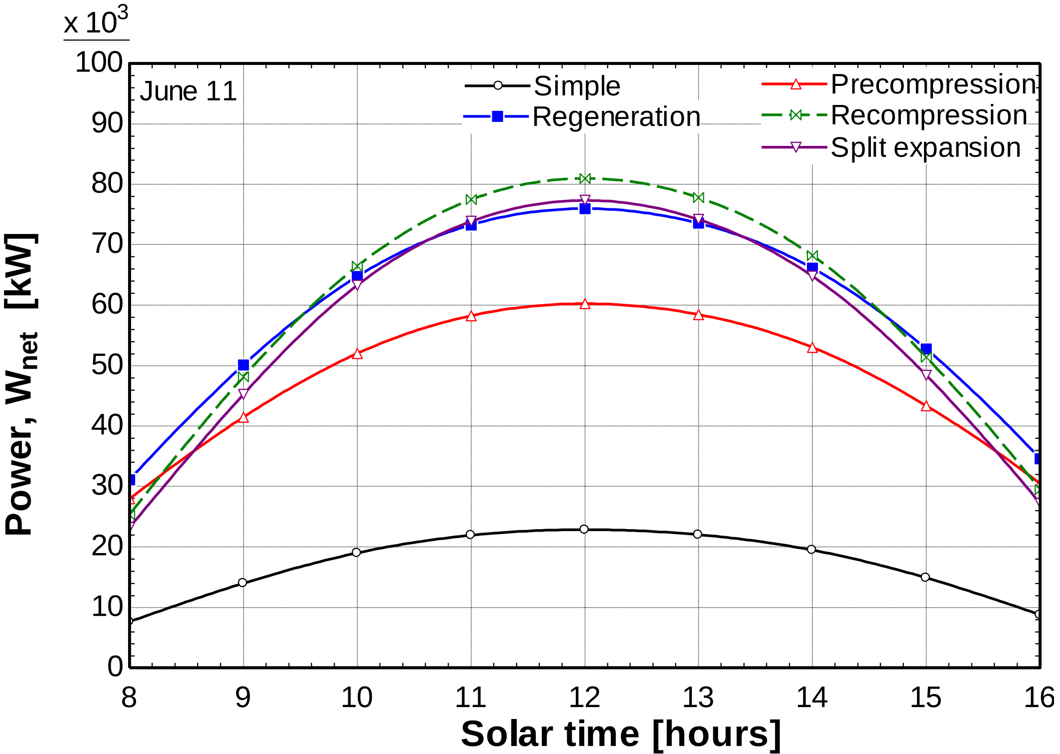

Figure 4.60 Comparison of net power output for 11th of June, Dhahran, Saudi Arabia

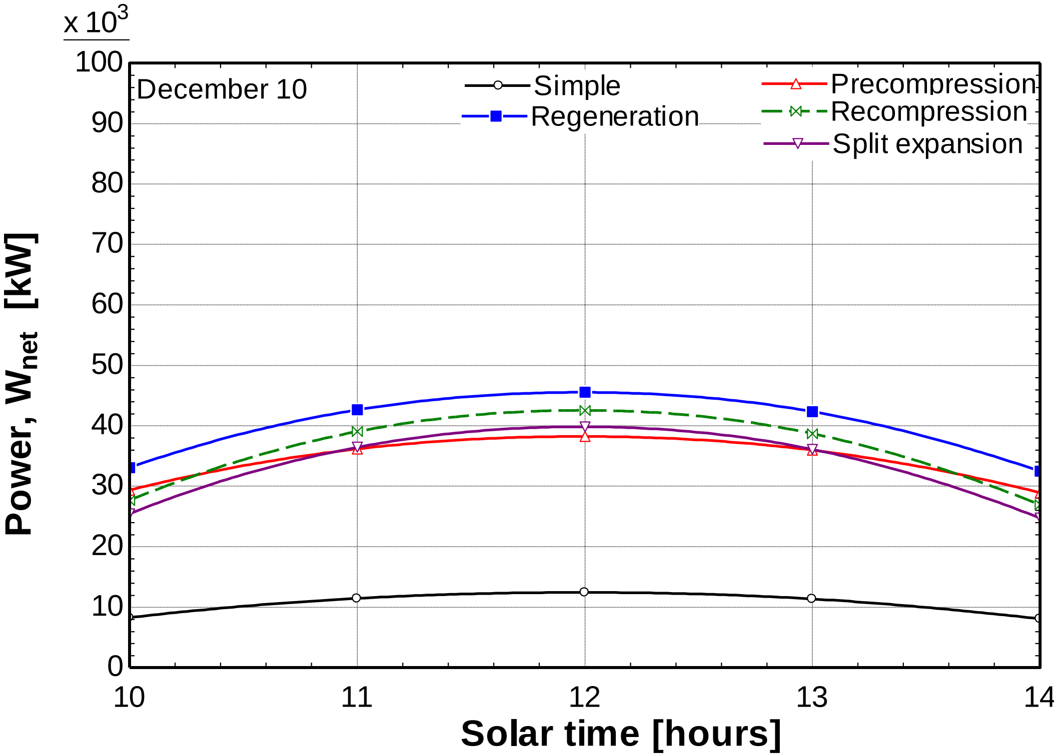

Figure 4.61 Comparison of net power output for 10th of December, Dhahran, Saudi Arabia

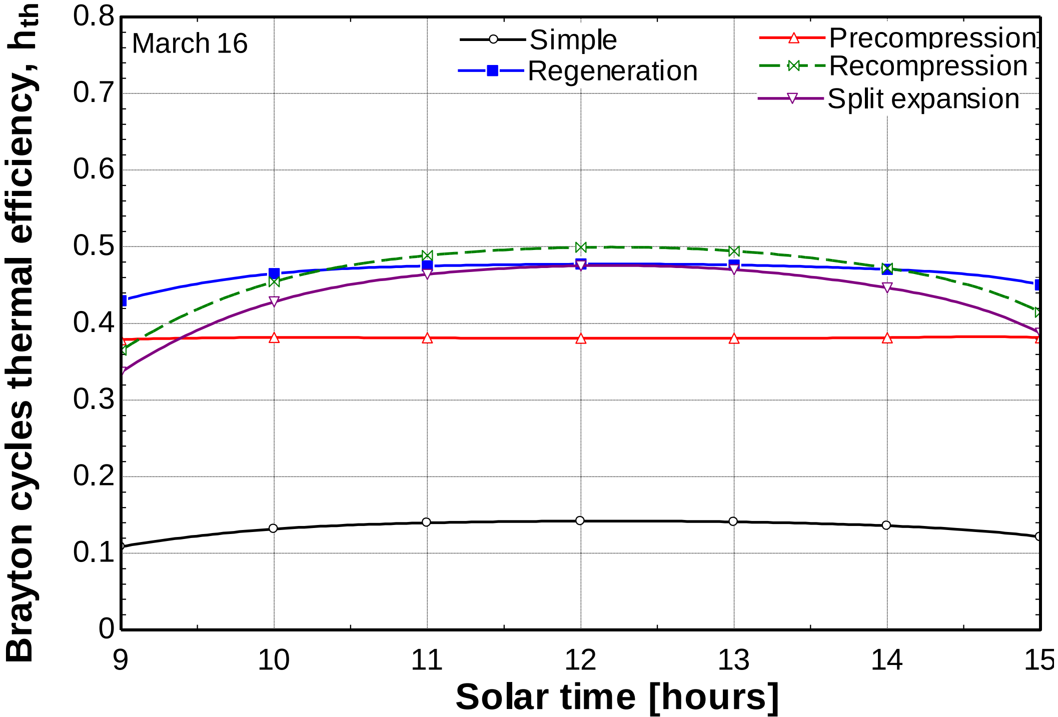

Figure 4.62 Comparison of thermal efficiency for 16th of March, Dhahran, Saudi Arabia

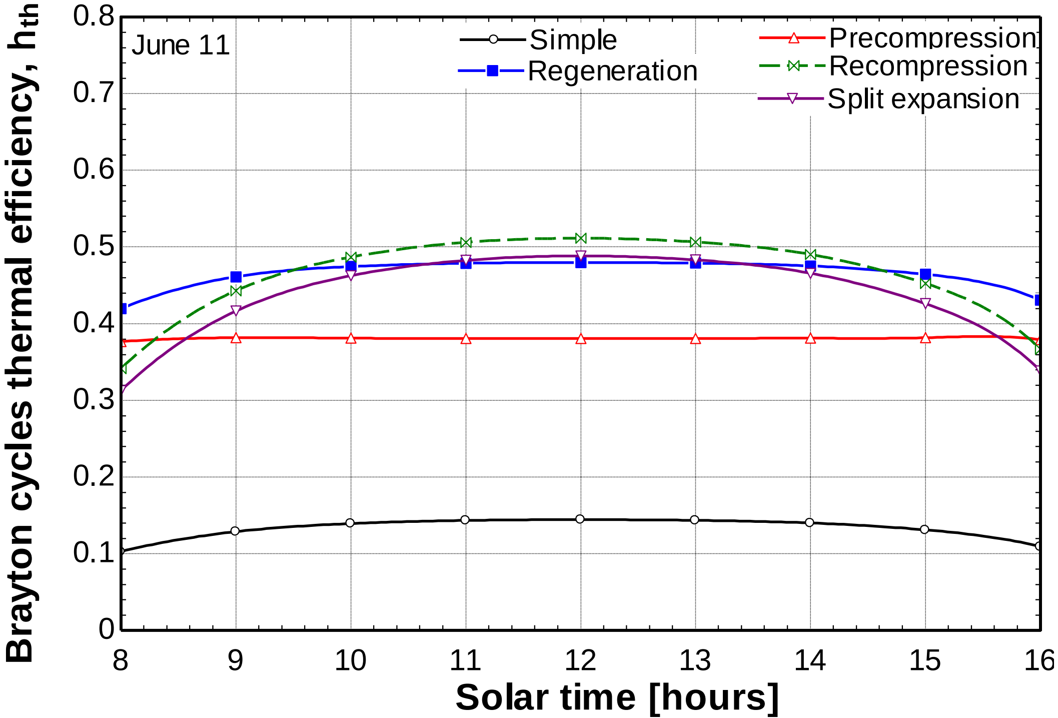

Figure 4.63 Comparison of thermal efficiency for 11th of June, Dhahran, Saudi Arabia

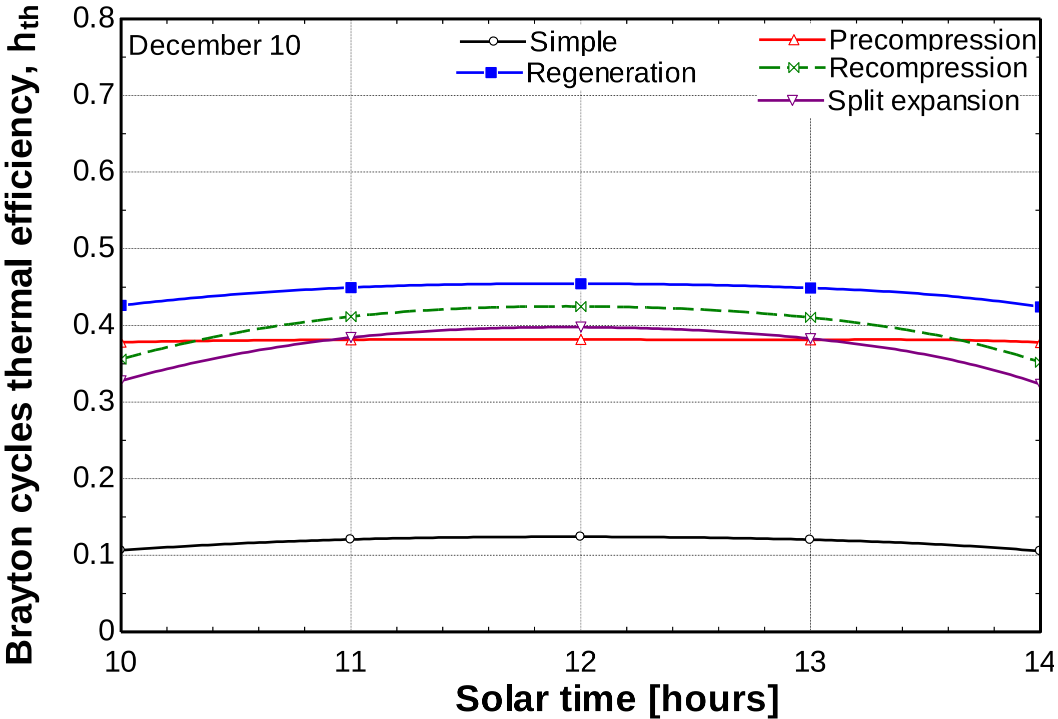

Figure 4.64 Comparison of thermal efficiency for 10th of December, Dhahran, Saudi Arabia

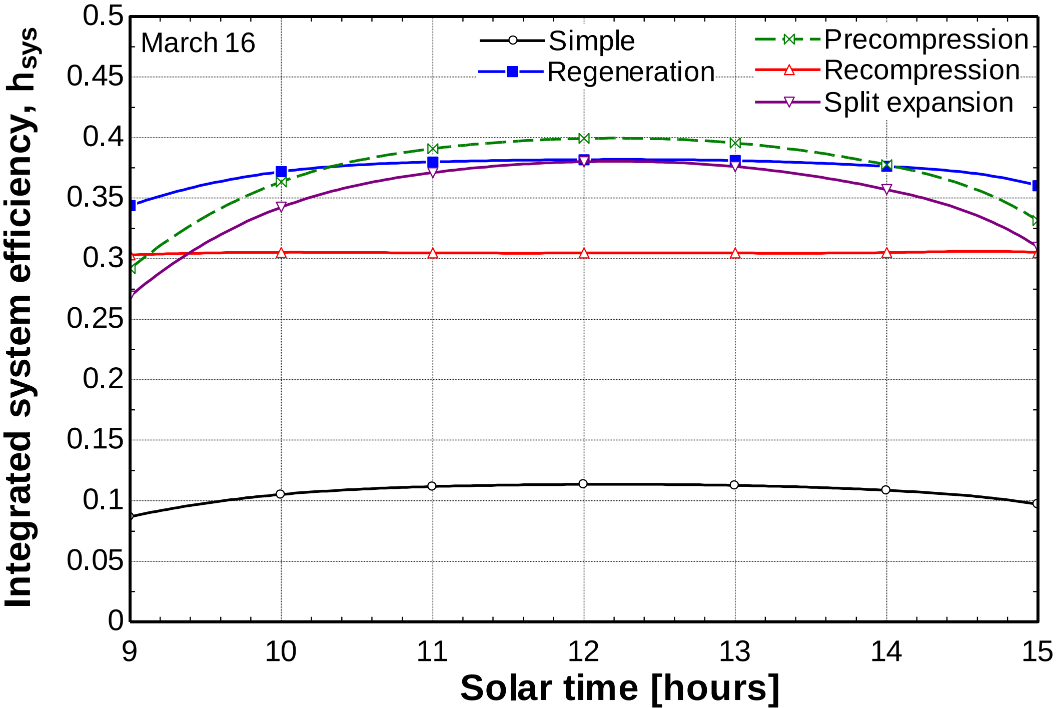

Figure 4.65 Comparison of system efficiency for 16th of March, Dhahran, Saudi Arabia

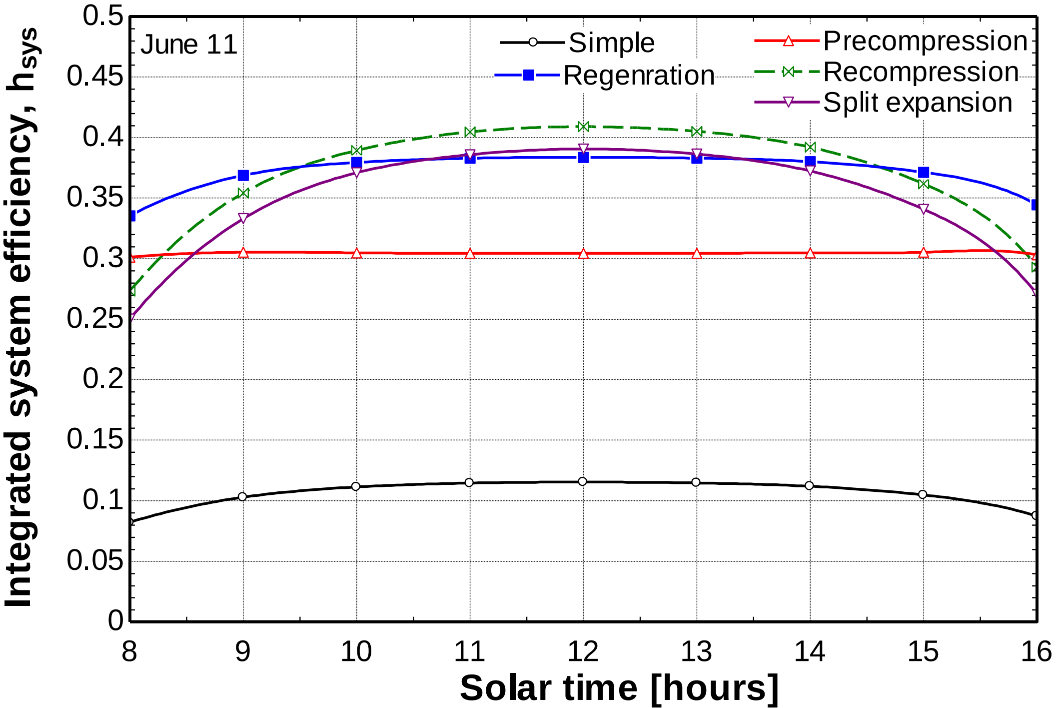

Figure 4.66 Comparison of system efficiency for 11th of June, Dhahran, Saudi Arabia

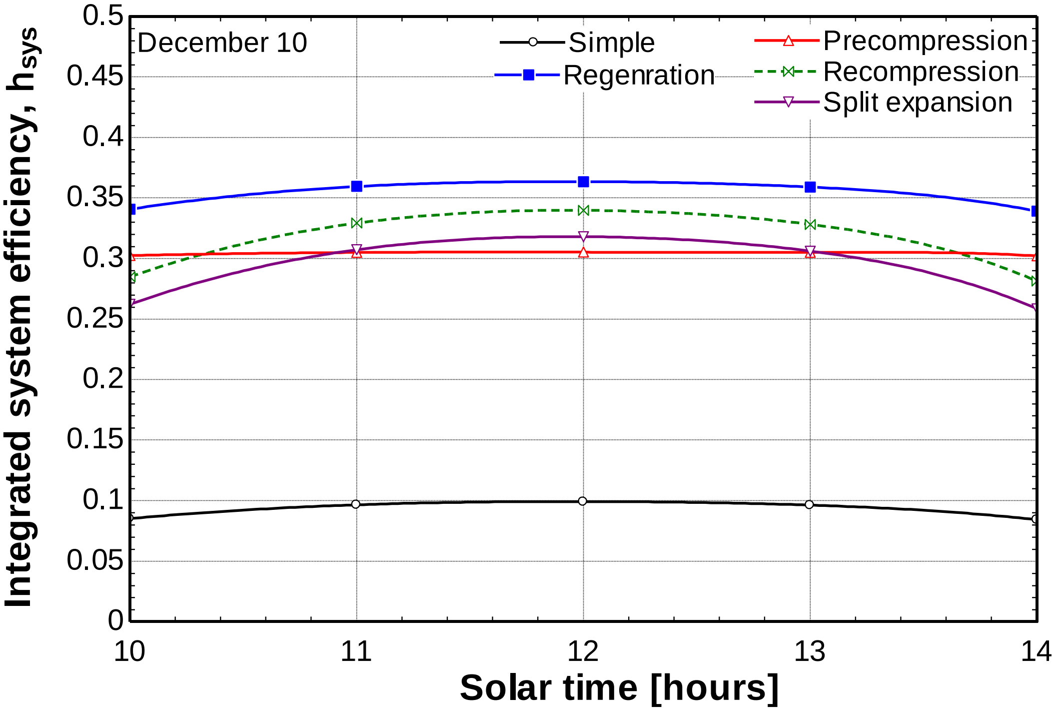

Figure 4.67 Comparison of system efficiency for 10th of December, Dhahran, Saudi Arabia

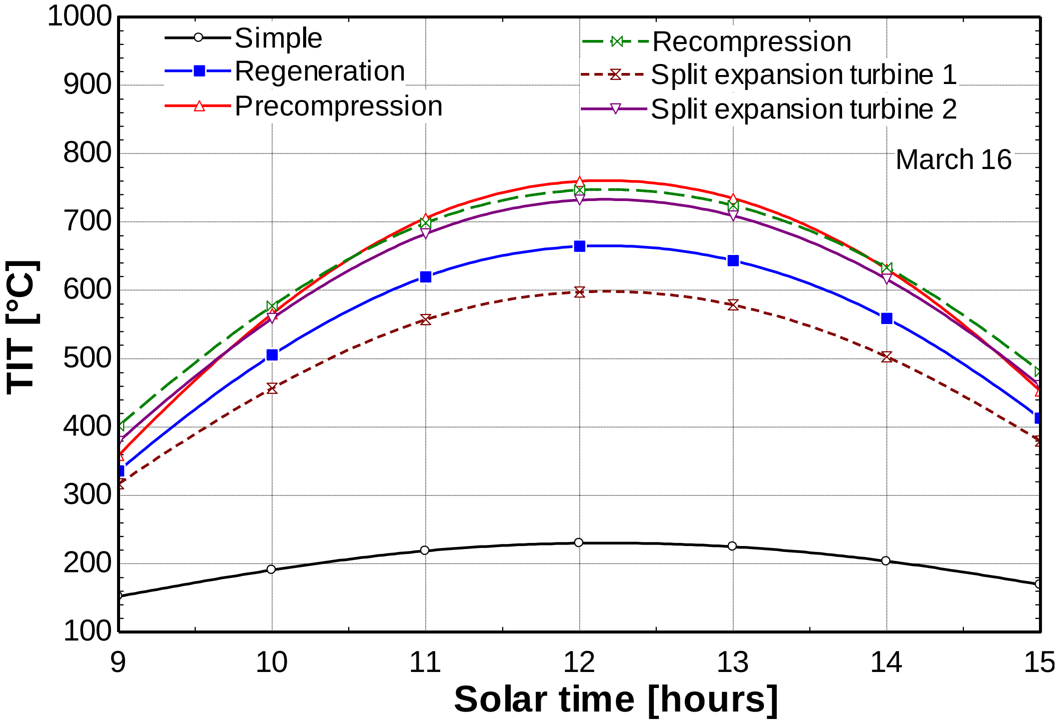

Figure 4.68 Comparison of turbine inlet temperature (TIT) for 16th of March, Dhahran, Saudi Arabia

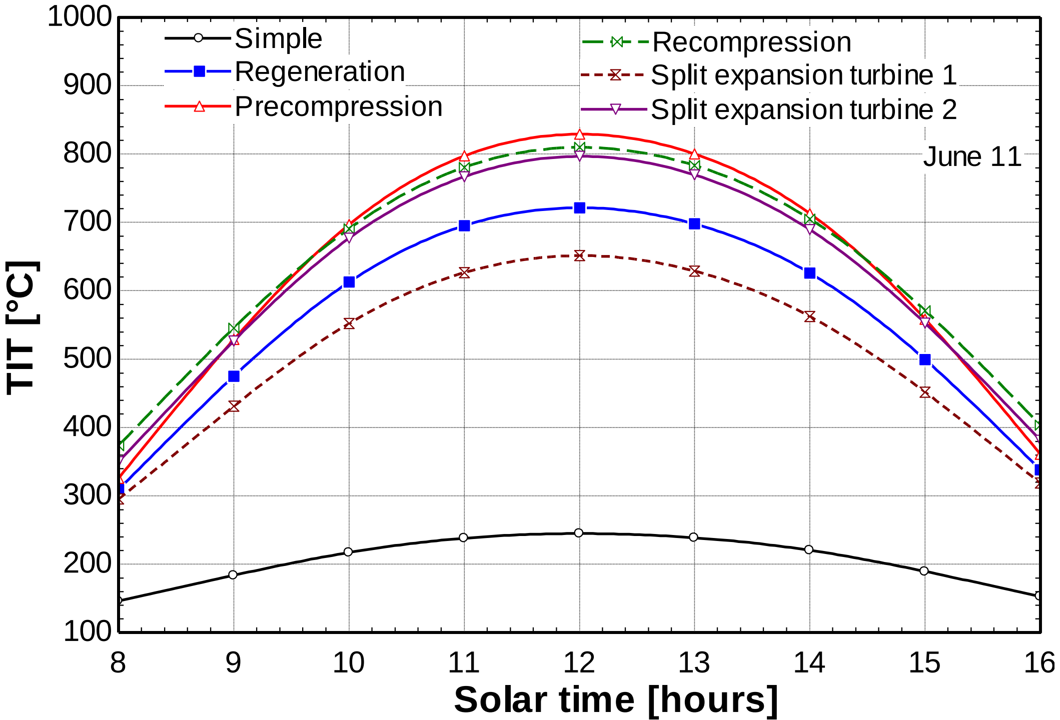

Figure 4.69 Comparison of turbine inlet temperature (TIT) for 11th of June, Dhahran, Saudi Arabia

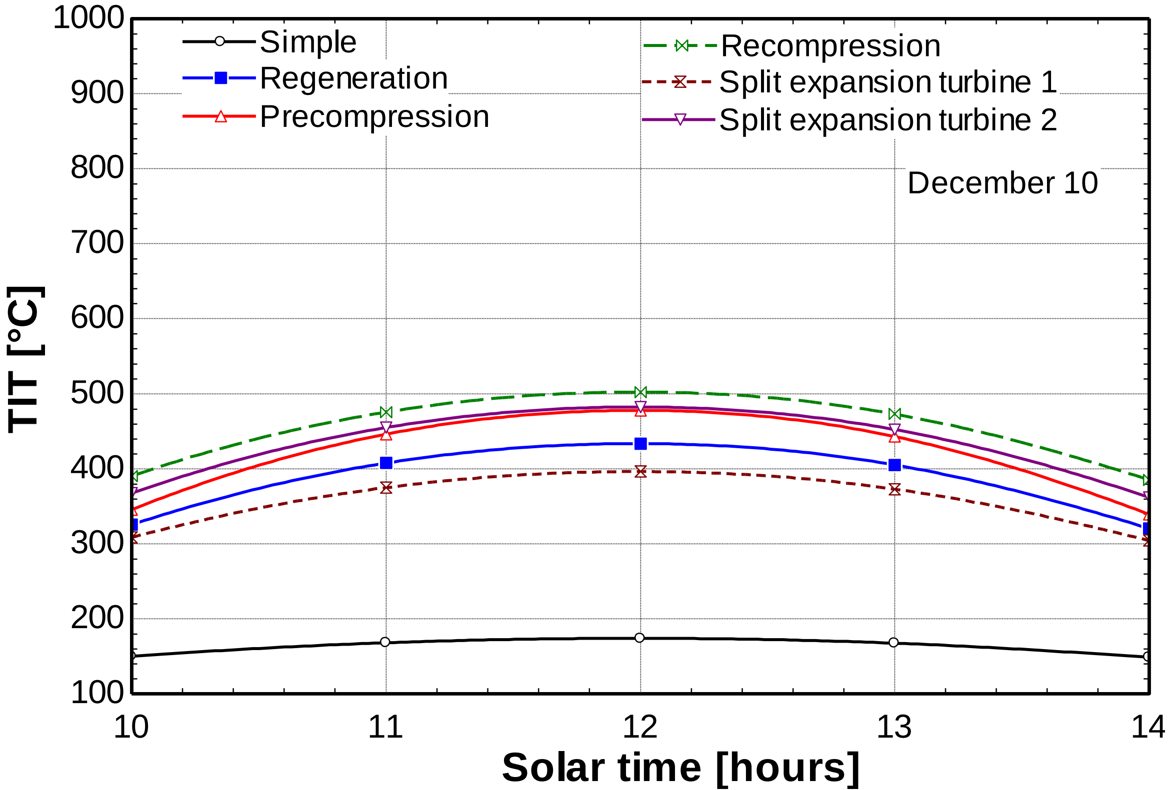

Figure 4.70 Comparison of turbine inlet temperature (TIT) for 10th of December, Dhahran, Saudi Arabia

4.3.1 Simple closed loop sCO_2 Brayton cycle

The simple Brayton cycle (Figure 3.7) consists of a single compressor, a single turbine, a cooler and a heat source, which is the central receiver in our case. The net power output, the thermal efficiency, and the turbine inlet temperature are not high for this cycle because a lot of energy, which can be recuperated, is wasted.

The power (kW) of all components of this cycle for March 16, June 11, and December 10 is depicted in Figure 4.71 to Figure 4.73. It can be observed from these figures that a lot of energy is being rejected at the cooler, and there is room for regeneration or recuperation. Moreover, the net power output is very low for this cycle due to the aforementioned reason. It is also inferred that the required compressor work remains constant throughout and its power consumed is very low because of compressing the carbon dioxide near its critical point.

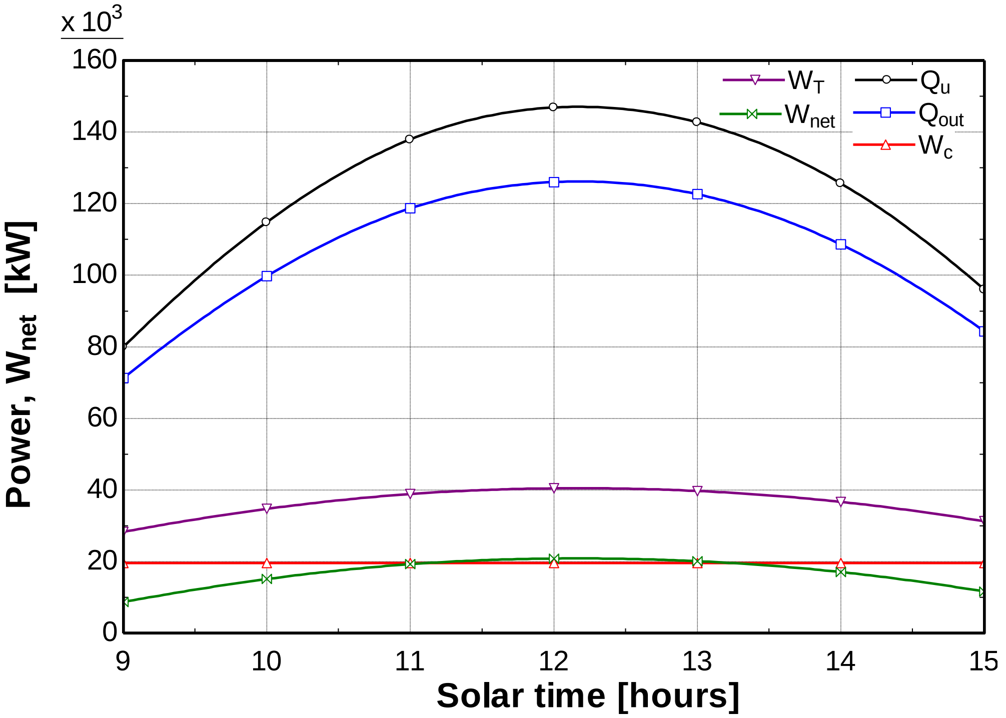

Figure 4.71 Simple sCO$_2$ cycle's components energy analysis for 16th of March, Dhahran, Saudi Arabia

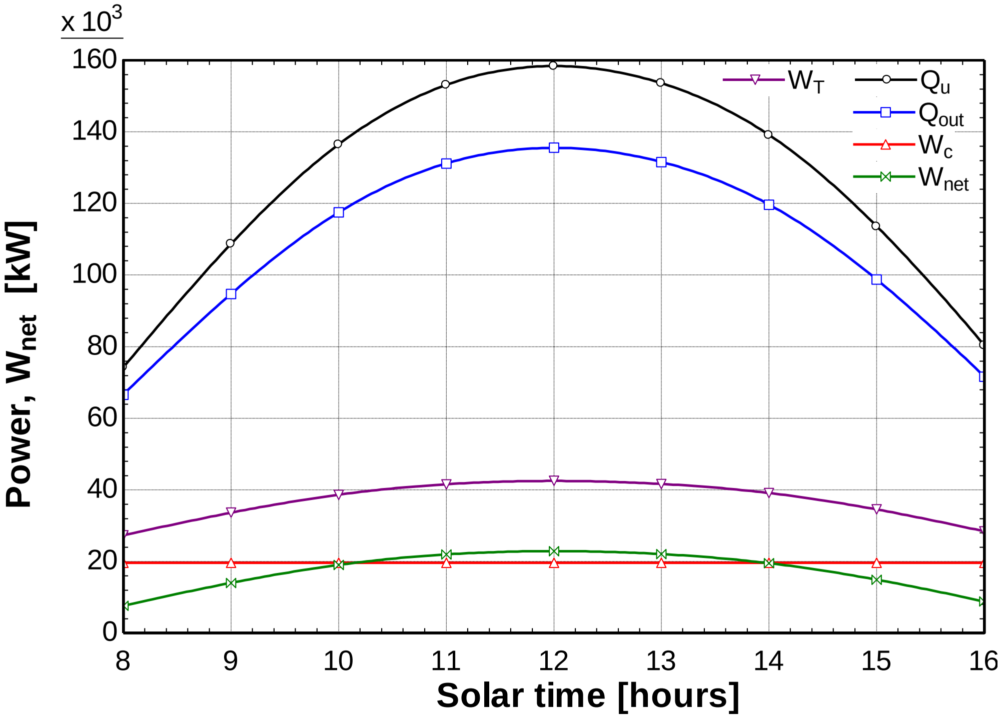

Figure 4.72 Simple sCO$_2$ cycle's components energy analysis for 11th of June, Dhahran, Saudi Arabia

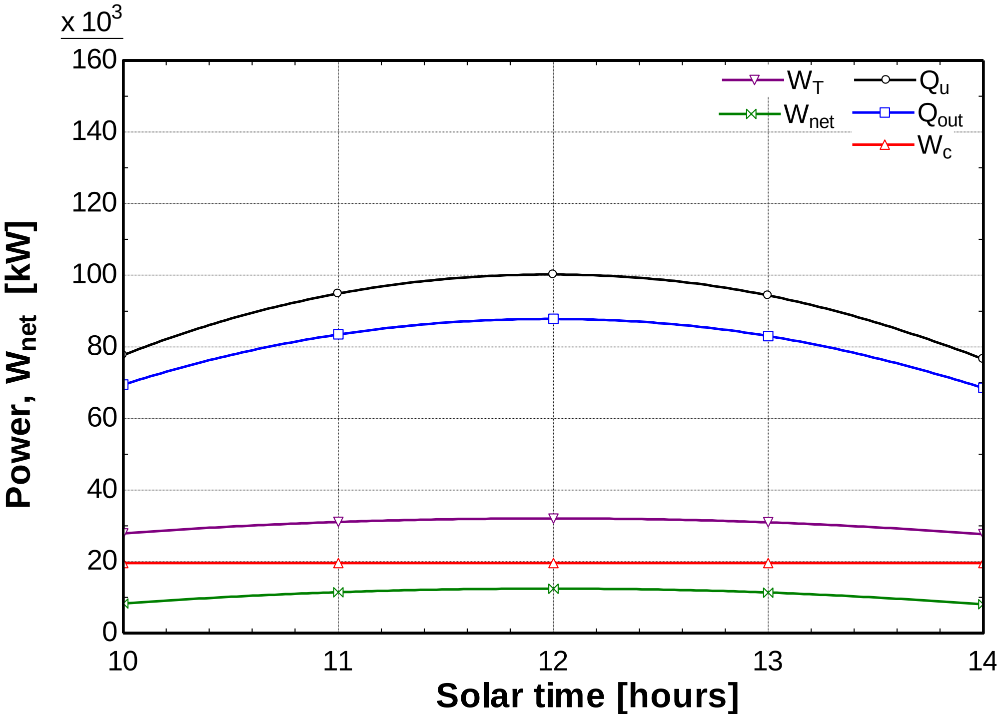

Figure 4.73 Simple sCO_2 cycle's components energy analysis for 10th of December, Dhahran, Saudi Arabia

4.3.2 Regenerative closed loop sCO_2 Brayton cycle

For the case of regenerative Brayton cycle (Figure 3.8), one extra component is added to the configuration called the regenerator. The regenerator helps to recuperate the excess energy at the turbine exhaust.

The power (kW) of all components of this cycle for March 16, June 11, and December 10 is depicted in Figure 4.74 to Figure 4.76. For this cycle, it can be observed that the curve for turbine work output is higher as compared to the heat rejected due to the addition of a single regenerator as compared to simple closed loop cycle. Hence, the net power outputs are also higher as compared to the simple closed loop cycle.

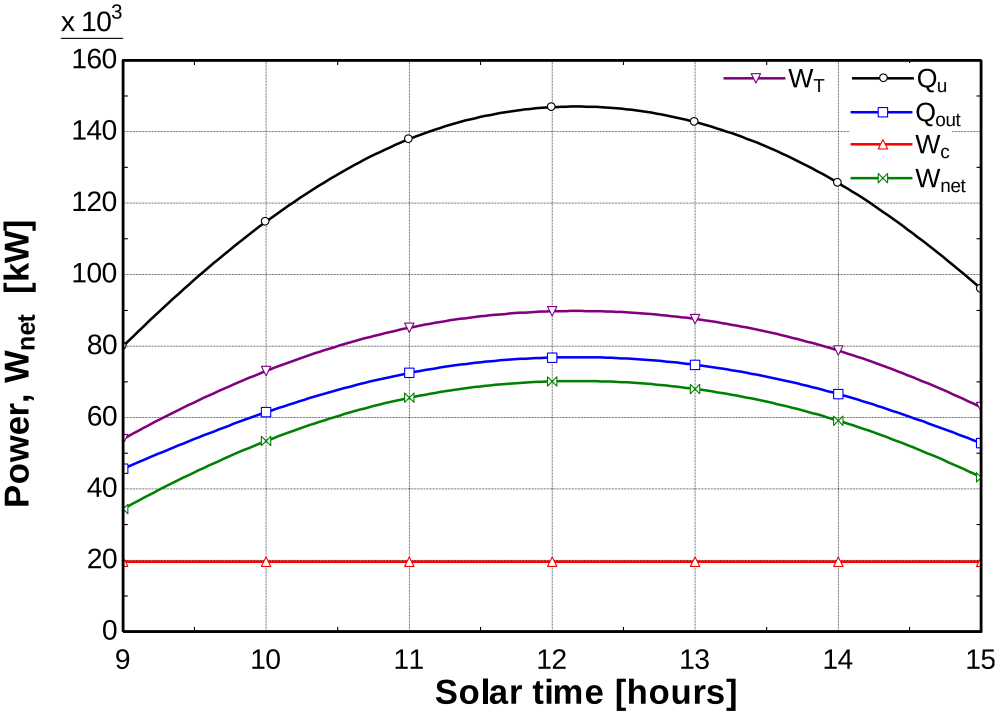

Figure 4.74 Regenerative sCO_2 cycle's components energy analysis for 16th of March, Dhahran, Saudi Arabia

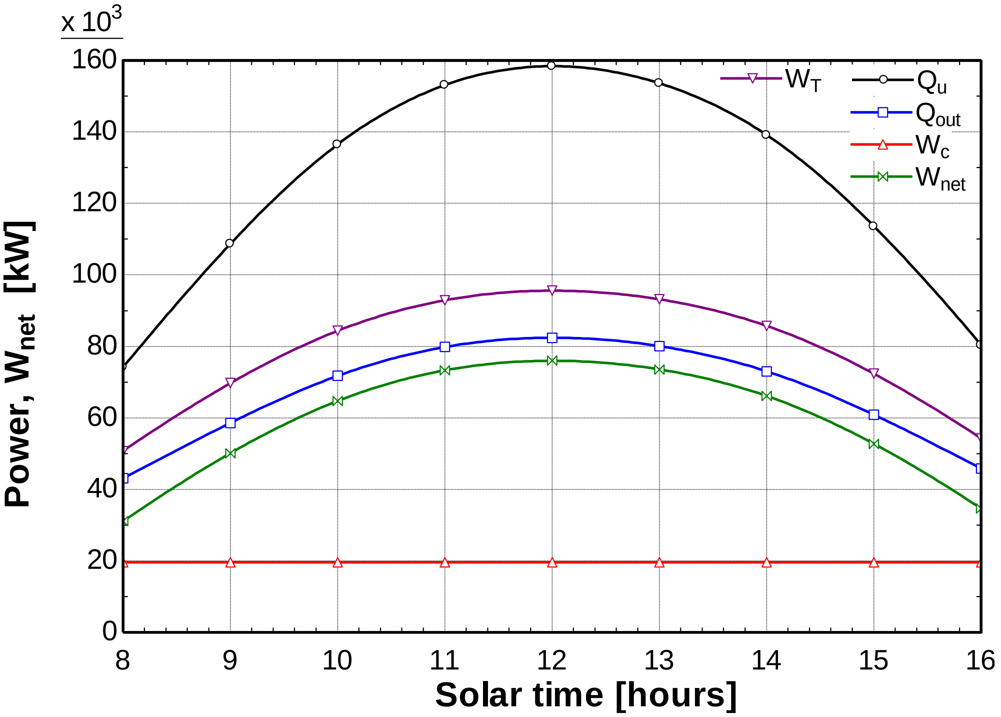

Figure 4.75 Regenerative sCO_2 cycle's components energy analysis for 11th of June, Dhahran, Saudi Arabia

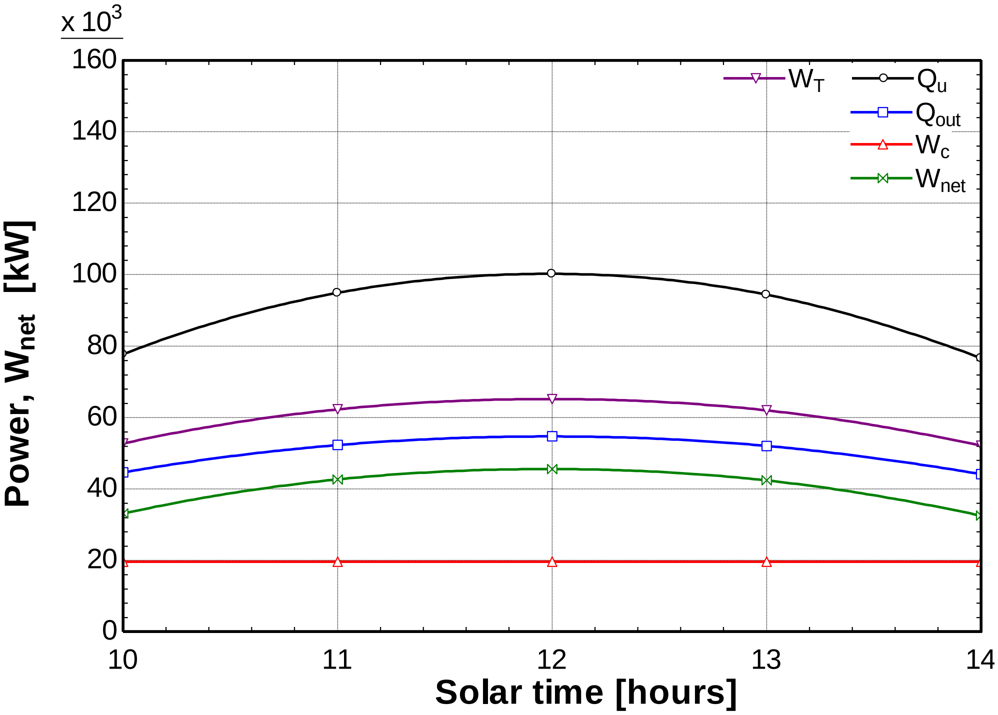

Figure 4.76 Regenerative sCO_2 cycle's components energy analysis for 10th of December, Dhahran, Saudi Arabia

4.3.3 Pre-compression closed loop sCO_2 Brayton cycle

The pre-compression Brayton cycle (Figure 3.9) has two regenerators: one is a high temperature regenerator and the other is a low temperature regenerator; and two compressors. The advantage of this arrangement is the placement of the additional compressor, which makes place for further regeneration.

The power (kW) of all components of this cycle for March 16, June 11, and December 10 is depicted in Figure 4.77 to Figure 4.79. For this cycle, the same observation is made that the curve for turbine work output is higher as compared to the heat rejected due to the addition of two regenerators; high temperature regenerator (HTR) and low temperature regenerator (LTR). Hence, the net work output is also higher as compared to the simple closed loop cycle. On the contrary, this cycle has lower net power output except at solar noon hours because of the required power consumed by the addition of the second compressor. Note that this compressor is consuming more power as compared to the other compressor, because it is not compressing carbon dioxide at the critical point. This power output is not uniform and changes according to the heat input to the cycle.

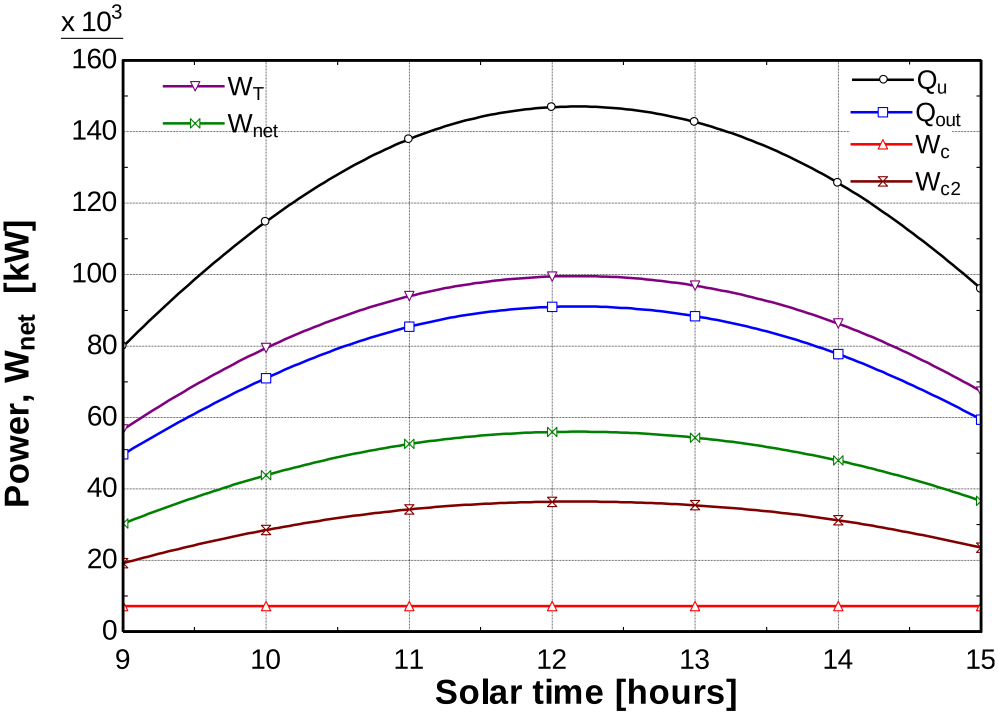

Figure 4.77 Pre-compression sCO_2 cycle's components energy analysis for 16th of March, Dhahran, Saudi Arabia

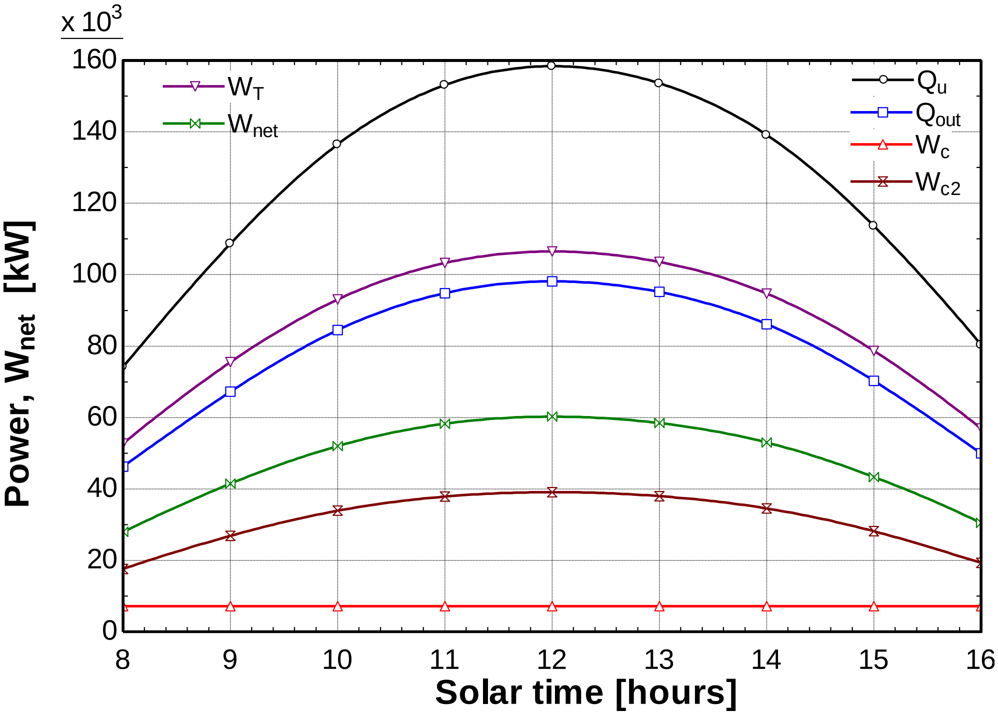

Figure 4.78 Pre-compression sCO_2 cycle's components energy analysis for 11th of June, Dhahran, Saudi Arabia

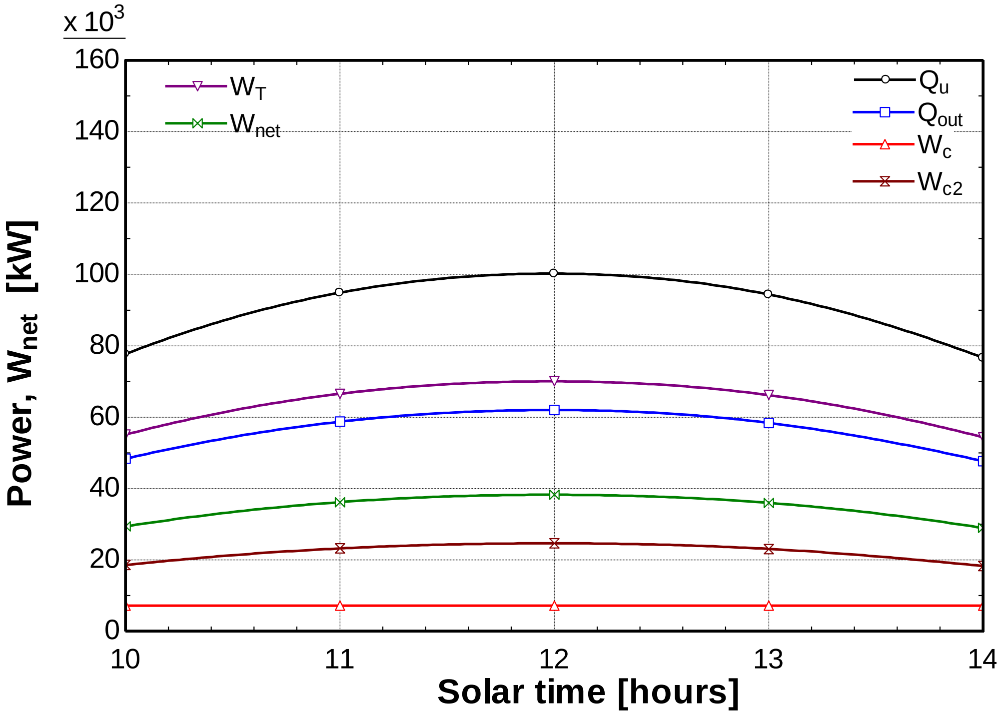

Figure 4.79 Pre-compression sCO_2 cycle's components energy analysis for 10th of December, Dhahran, Saudi Arabia

4.3.4 Re-compression closed loop sCO_2 Brayton cycle

The recompression Brayton cycle (Figure 3.10) has the same number of components as the pre-compression Brayton cycle but with a different arrangement. In this cycle, the flow is split into two streams after the low temperature regenerator and before passing through the cooler. These two streams are the one that flows to the main compressor through the cooler and the other one flows to the recompression compressor. Consequently, the system rejects less heat and the compressor work is reduced, which in turn causes the thermal efficiency to improve.

The power (kW) of all components of this cycle for March 16, June 11, and December 10 is depicted in Figure 4.80 to Figure 4.82. It is observed for this cycle, that the curve for net work output reaches a higher value as compared to the heat rejected around solar noon hours, thus efficiently utilizing the heat added to the cycle and increasing the efficiency. This can be attributed to the position of the second compressor, and the splitting of the mass flow stream. It is observed from the figures that around solar noon hours higher mass fraction passes through the first compressor, and thus reducing the work consumed by the second compressor as opposed to the pre-compression cycle.

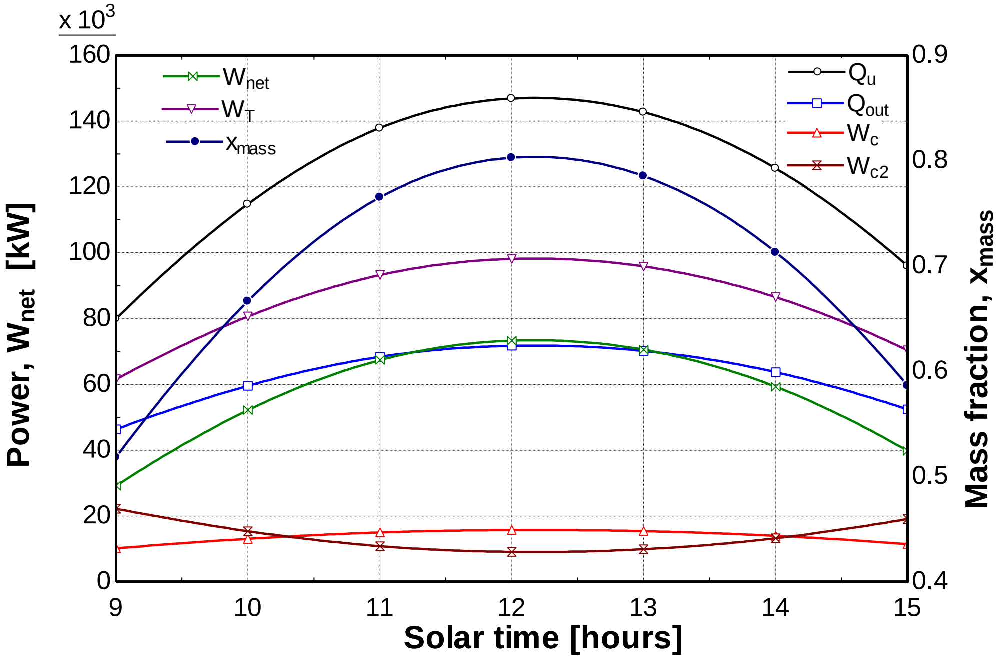

Figure 4.80 Re-compression sCO_2 cycle's components energy analysis for 16th of March, Dhahran, Saudi Arabia

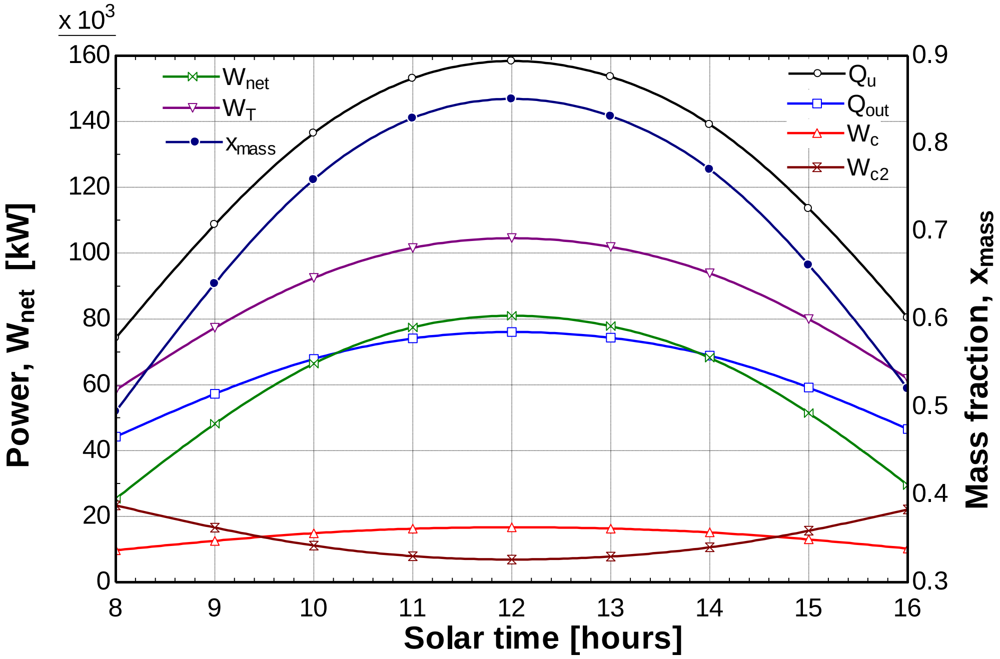

Figure 4.81 Re-compression sCO_2 cycle's components energy analysis for 11th of June, Dhahran, Saudi Arabia

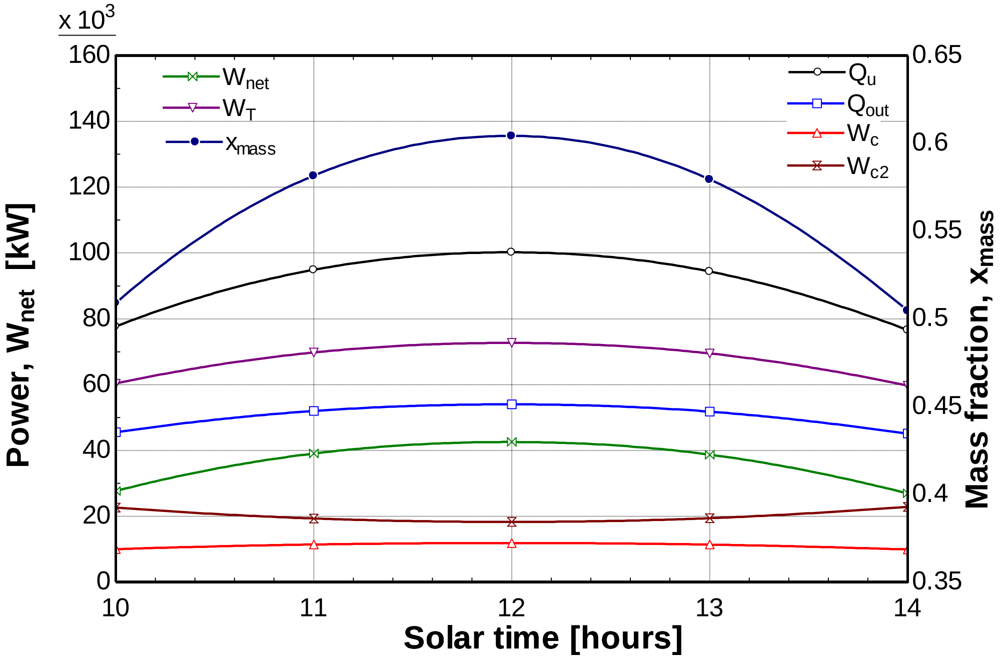

Figure 4.82 Re-compression sCO_2 cycle's components energy analysis for 10th of December, Dhahran, Saudi Arabia

4.3.5 Split expansion closed loop sCO_2 Brayton cycle

Finally, the split expansion Brayton cycle (Figure 3.11) has the same configuration as that of the recompression cycle but the expansion is performed in two stages by introducing an additional turbine; and the heat addition process takes place in between the two stages of fluid expansion.

The power (kW) of all components of this cycle for March 16, June 11, and December 10 is depicted in Figure 4.83 to Figure 4.85. This cycle has a lower efficiency curve as compared to the re-compression cycle. In this cycle, the fluid is expanded in two stages and heat addition takes place in between. The expansion in the first stage is carried out utilizing the heat recuperated through the regenerator, and expansion in the second stage is carried out using the heat added externally (using solar tower). The cycle efficiency is almost equal to the regeneration cycle but lower than the re-compression cycle.

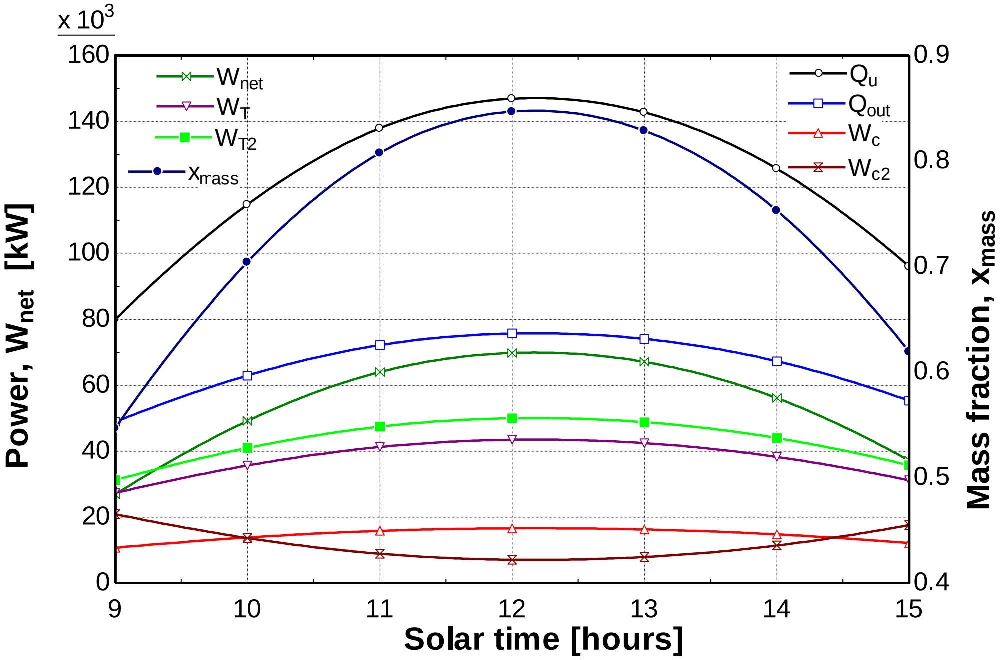

Figure 4.83 Split expansion sCO_2 cycle's components energy analysis for 16th of March, Dhahran, Saudi Arabia

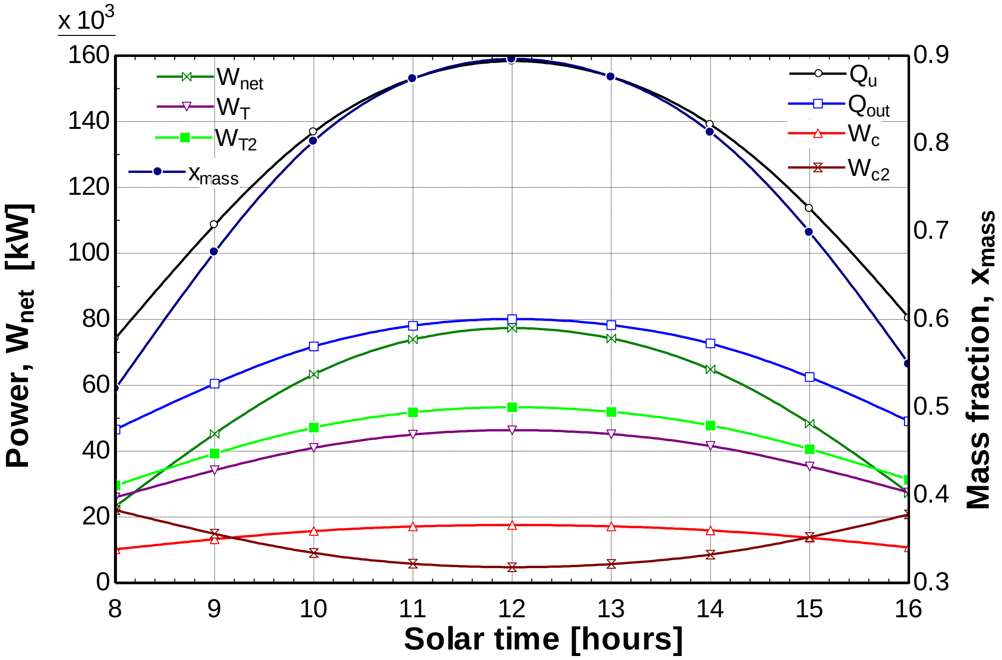

Figure 4.84 Split expansion sCO_2 cycle's components energy analysis for 11th of June, Dhahran, Saudi Arabia

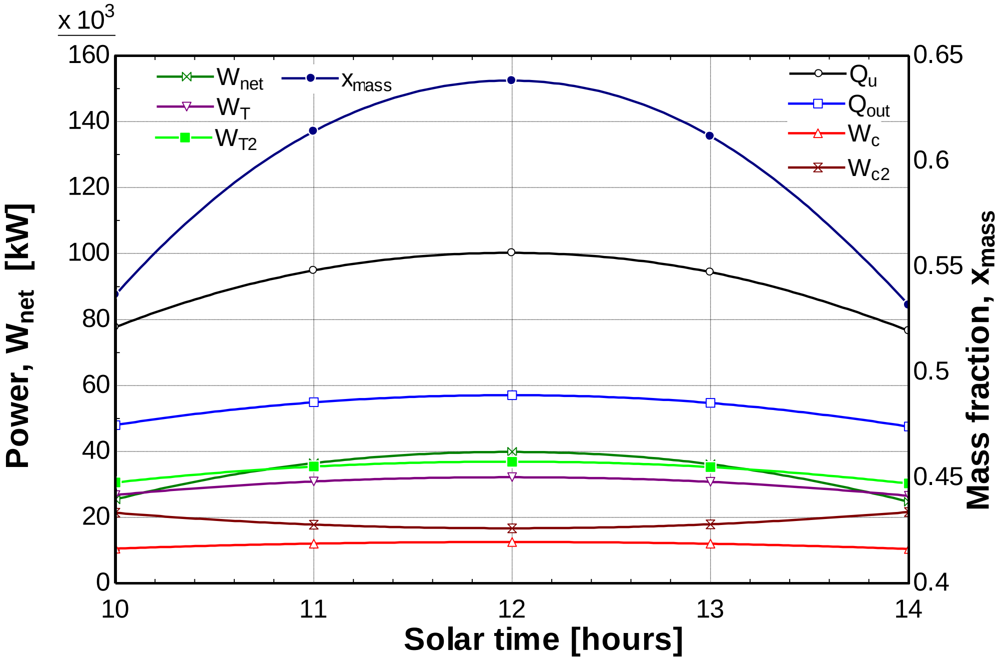

Figure 4.85 Split expansion sCO_2 cycle's components energy analysis for 10th of December, Dhahran, Saudi Arabia.

4.4 sCO$_2$ recompression Brayton cycles for different locations in Saudi Arabia

In this section, a complete thermodynamic analysis of the solar thermal tower system integrated with a closed loop sCO$_2$ recompression Brayton cycle was performed. This analysis was carried out for six different locations of Saudi Arabia taking into account each of the locations' direct normal irradiation. The selected locations were Tabouk (North), Madinah (West North), Dhahran (central), Riyadh (central), Bishah (South) and Najran (South). The target net power output was 40 MW and the analysis was carried out in accordance with this net power output. This net power output was made uniform and for this purpose an auxiliary heat source was added. This plant would be operational with the input solar energy and auxiliary heat source for daylight hours; nonetheless for night time operation the plant would operate on auxiliary heat source. Detailed analysis of the input solar share and the auxiliary heat provided has also been performed. Table 4.9 (Page 133) lists the design parameters of the heliostat and the central receiver which were used in this study whereas the operating conditions of the recompression sCO$_2$ Brayton cycle are listed in Table 4.10 (Page 133). For the annual optimization, the number of heliostats considered was 2646 in a surround field layout, the tower optical height was taken as 130m, and the *dsep* value was taken as 3m. Finally, in Table 4.11 (Page 161) all of the acquired results of the analysis are tabulated including the latitude and longitude of the concerned cites.

From Figure 4.86, it can be observed that the useful energy gain rate at the receiver is

$$Q_u = \dot{m}(h_3' - h_5) \tag{128}$$

And the heat added by the auxiliary heater is defined as

$$Q_{aux} = \dot{m}(h_3 - h_3') \tag{129}$$

In case if there is an auxiliary heat exchanger present, the thermal efficiency of the Brayton cycle is defined as

$$\eta_{th} = \frac{W_{net}}{Q_u + Q_{aux}} \tag{130}$$

Furthermore, the fraction of fuel hybridization required to keep a constant power output is given by

$$f_{hybrid} = \frac{Q_{aux}}{Q_{solar} + Q_{aux}} \tag{131}$$

The input solar share is

$$X_{solar} = \frac{Q_{solar}}{Q_{solar} + Q_{aux}} \tag{132}$$

The solar resource data for each of the locations aforementioned was taken from a renewable energy resource website sponsored by NASA [103]. The data available on this website is averaged over a period of 22 years from 1983 until 2005. The averaged values over a month of direct normal irradiation are available there. A preliminary generated heliostat field was optimized on monthly averaged annual basis. Therefore, Equation (51) was used for the annual optimization for all the locations considered in this study. This code calculates all the necessary optical performance parameters of all the heliostats at every step of the optimization until the best layout of the generated heliostat field is found. The optimized heliostat fields for all of selected locations have been depicted in Figure 4.87 - Figure 4.92.

As the data available on the aforementioned website was available on monthly basis, the average efficiencies of each month for all the locations were calculated after the heliostat fields were annually optimized. These efficiencies were used as an input to the EES code for the analysis of the receiver and recompression Brayton cycle. In this study; optical, convection heat, and radiation heat losses were taken into account, whereas the conduction heat losses were neglected from the receiver.

Figure 4.93 to Figure 4.98 depicts bar graphs for the average heat collected for each month, for Tabouk, Madinah, Dhahran, Riyadh, Bishah, and Najran, respectively. Moreover, it can be observed (Table 4.11) that Madinah has the highest annual average heat collected in kWh/day, whereas Tabouk has the second highest and Dhahran has the lowest. For Tabouk, Madinah, Dhahran, and Riyadh; the highest heat collected is in the month of June, whereas for Bishah and Najran it is not the case. Furthermore, it will be more preferable to install a plant where there are fewer fluctuations in the solar irradiation such as Madinah and Bishah.

A closed loop sCO_2 recompression Brayton cycle was integrated with the central receiver where the net heat collected was used as an input to the Brayton cycle. The modeling of the Brayton cycle was performed in such a way that heat gained at the receiver was used as an input value to the cycle rather than the turbine inlet temperature. Consequently, the temperature T_3' will not remain constant and will depend upon the irradiation of a particular location. Thus, the power output will not be uniform. To address this, an auxiliary heat exchanger was added before the turbine so that if the net heat gained at the receiver is low, extra heat will be added to keep the turbine inlet temperature constant and hence to keep the power output uniform. For this study, the turbine inlet temperature was fixed at 570 ° C and the net power output was fixed at 40MW. Figure 4.99 - Figure 4.104 illustrate the percent hybridization required for all the cities for each month during daylight hours. In other words, these bar graphs also show indirectly the amount of auxiliary heat required to keep a uniform power output. From Table 4.11, it can be observed that Madinah requires least amount of external fuel hybridization, i.e. only 5.82%, whereas Tabouk requires second least 6.34% and Najran requires third least i.e. 7.62%.

Table 4.11 Performance comparison of different locations of Saudi Arabia

City	Latitude	Longitude	Annual un-weighted optical efficiency	Average annual heat collected at the central receiver (kWh/day)	Annual hybridization fraction	Annual input solar share
Tabouk	28.5 ° N	36.5 ° E	0.5089	933103	6.34%	93.66%
Madinah	24.5 ° N	39.5 ° E	0.5132	938388	5.82%	94.18%
Dhahran	26.5 ° N	50.5 ° E	0.5111	827420	11.51%	88.49%
Riyadh	24.5 ° N	46.5 ° E	0.5132	855262	10.16%	89.84%
Bishah	20.5 ° N	42.5 ° E	0.5147	882216	8.55%	91.45%
Najran	17.5 ° N	44.5 ° E	0.5191	893359	7.62%	92.38%

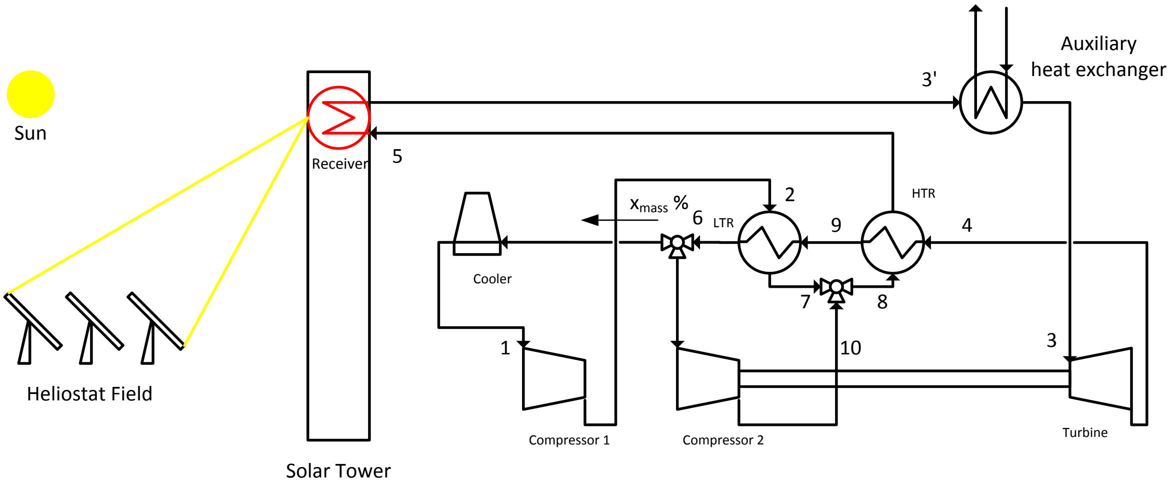

Figure 4.86 Re-compression closed loop supercritical carbon dioxide Brayton cycle with auxiliary heater.

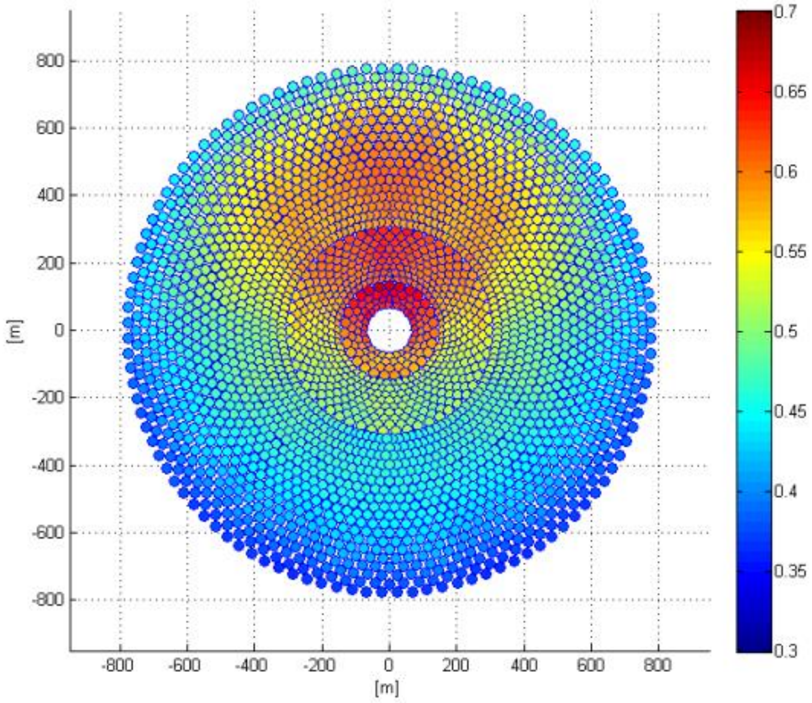

Figure 4.87 Contours of the optical efficiency of the optimized heliostat field on annual basis for Tabouk, Saudi Arabia

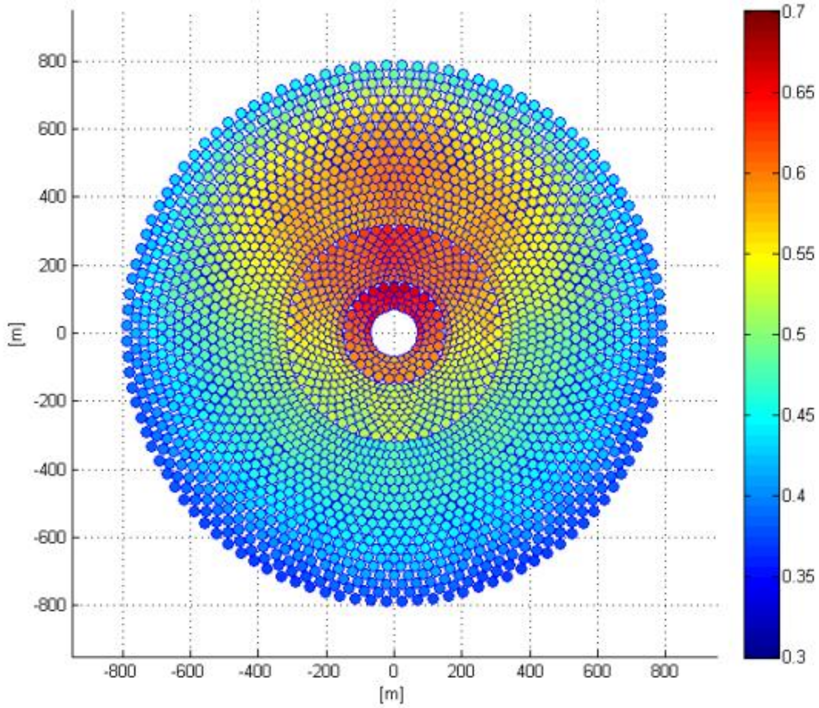

Figure 4.88 Contours of the optical efficiency of the optimized heliostat field on annual basis for Madinah, Saudi Arabia

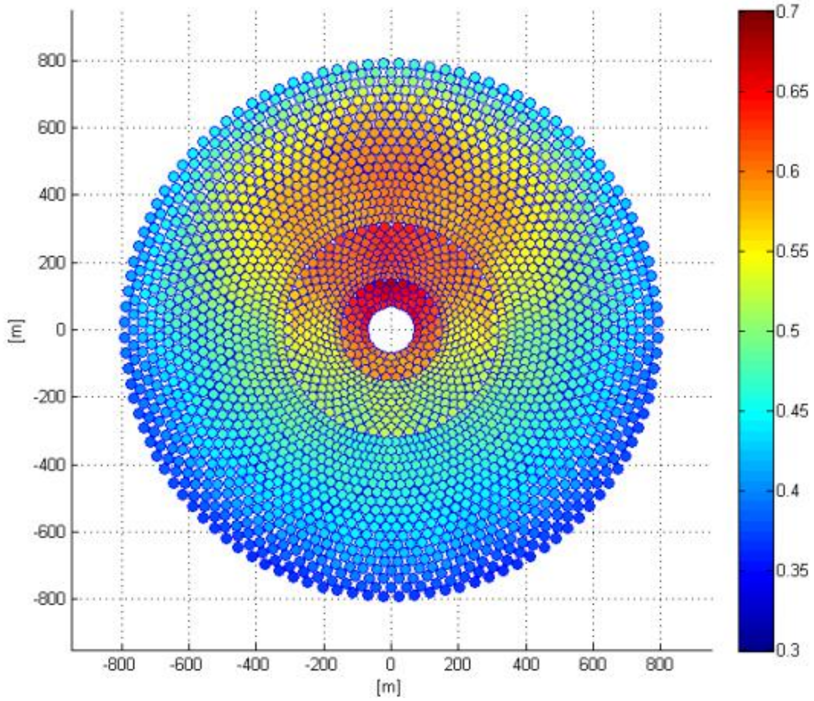

Figure 4.89 Contours of the optical efficiency of the optimized heliostat field on annual basis for Dhahran, Saudi Arabia

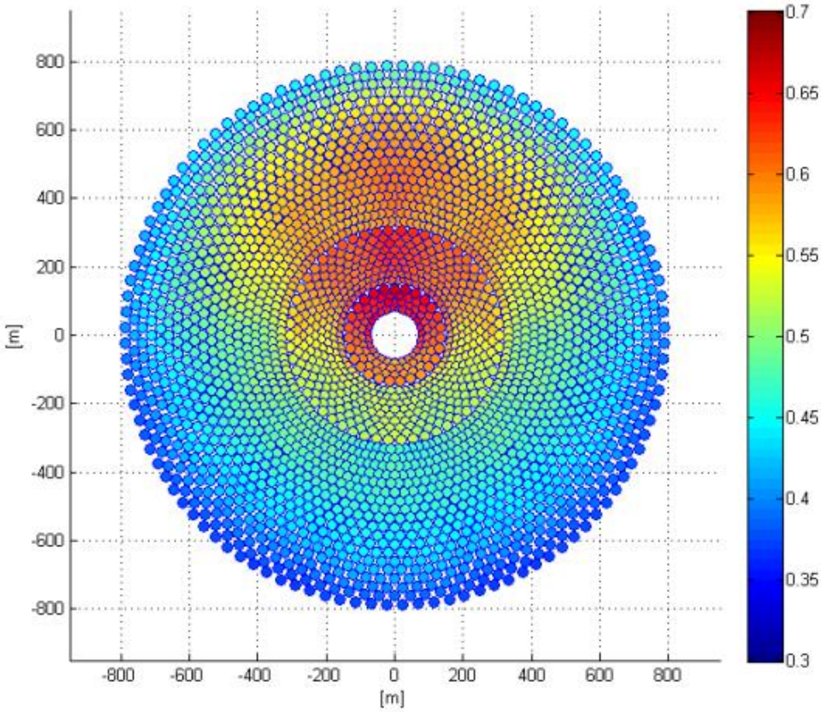

Figure 4.90 Contours of the optical efficiency of the optimized heliostat field on annual basis for Riyadh, Saudi Arabia

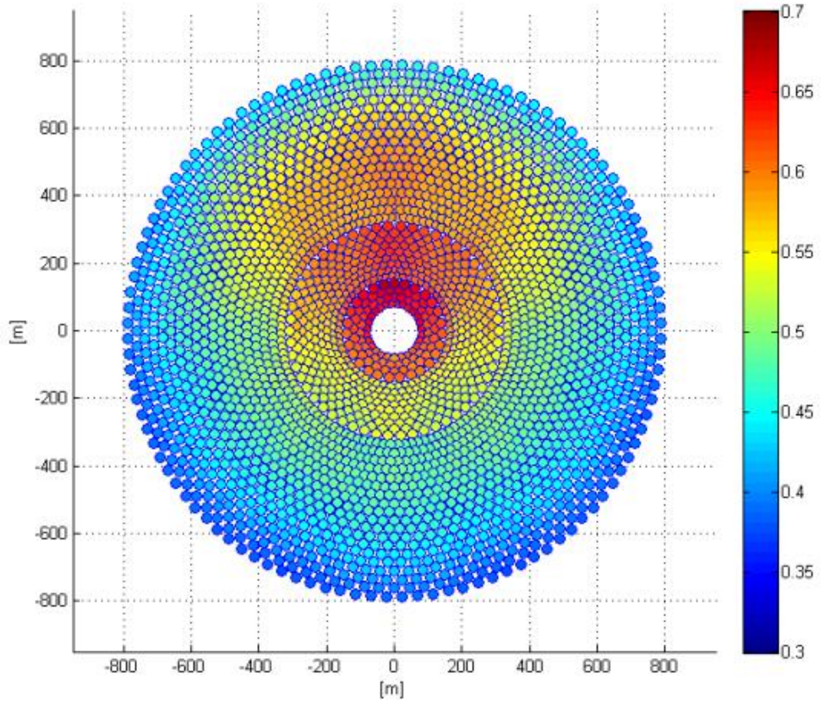

Figure 4.91 Contours of the optical efficiency of the optimized heliostat field on annual basis for Bishah, Saudi Arabia

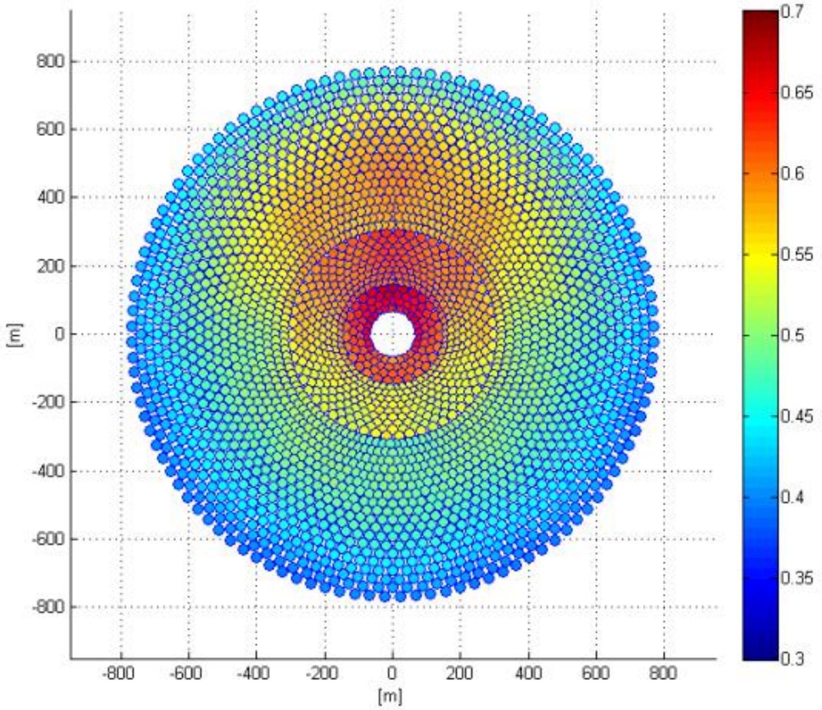

Figure 4.92 Contours of the optical efficiency of the optimized heliostat field on annual basis for Najran, Saudi Arabia

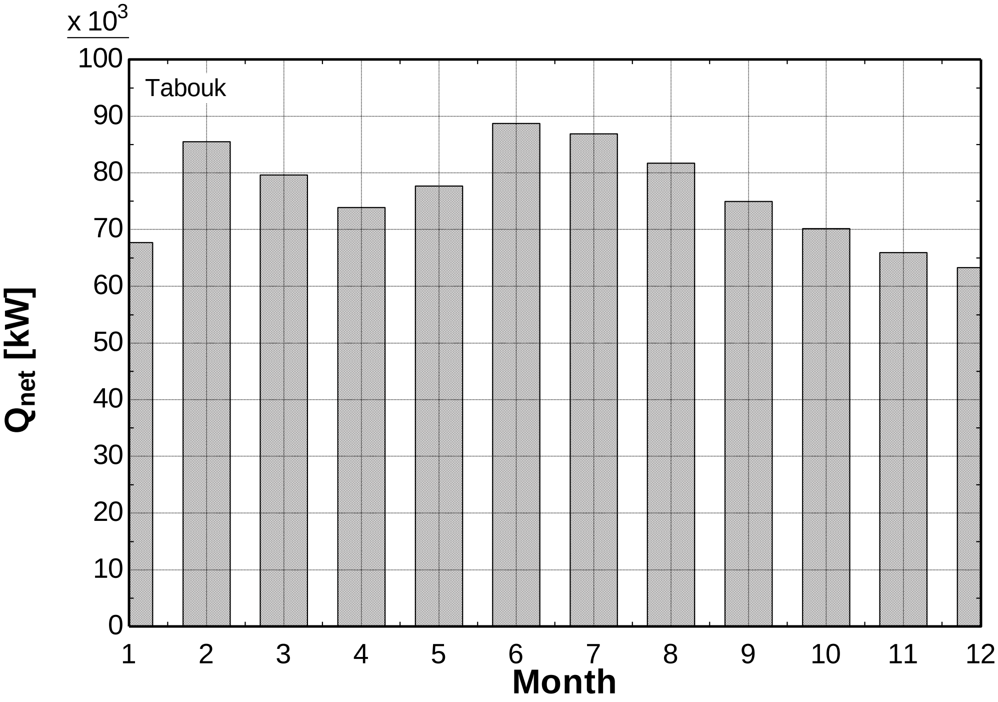

Figure 4.93 Average heat collected at the central receiver for Tabouk, Saudi Arabia

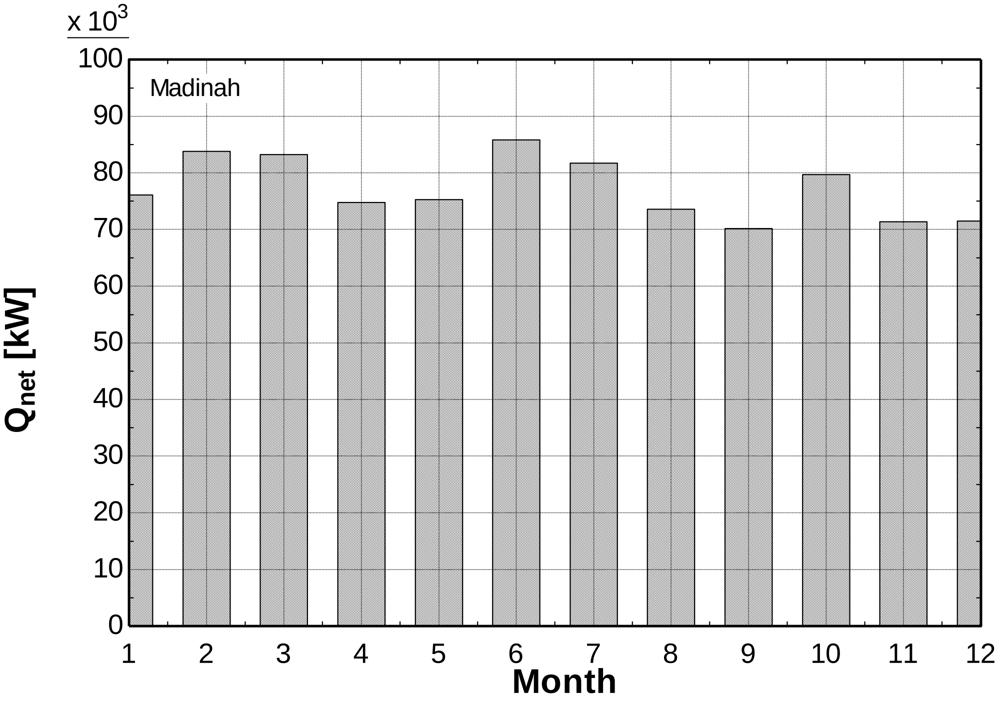

Figure 4.94 Average heat collected at the central receiver for Madinah, Saudi Arabia

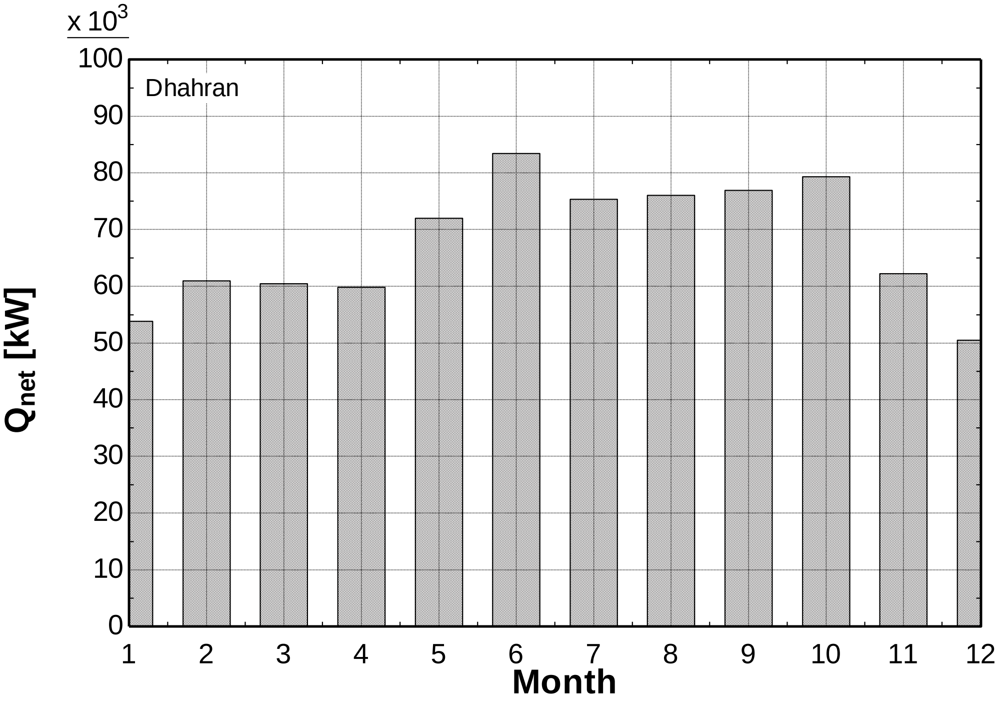

Figure 4.95 Average heat collected at the central receiver for Dhahran, Saudi Arabia

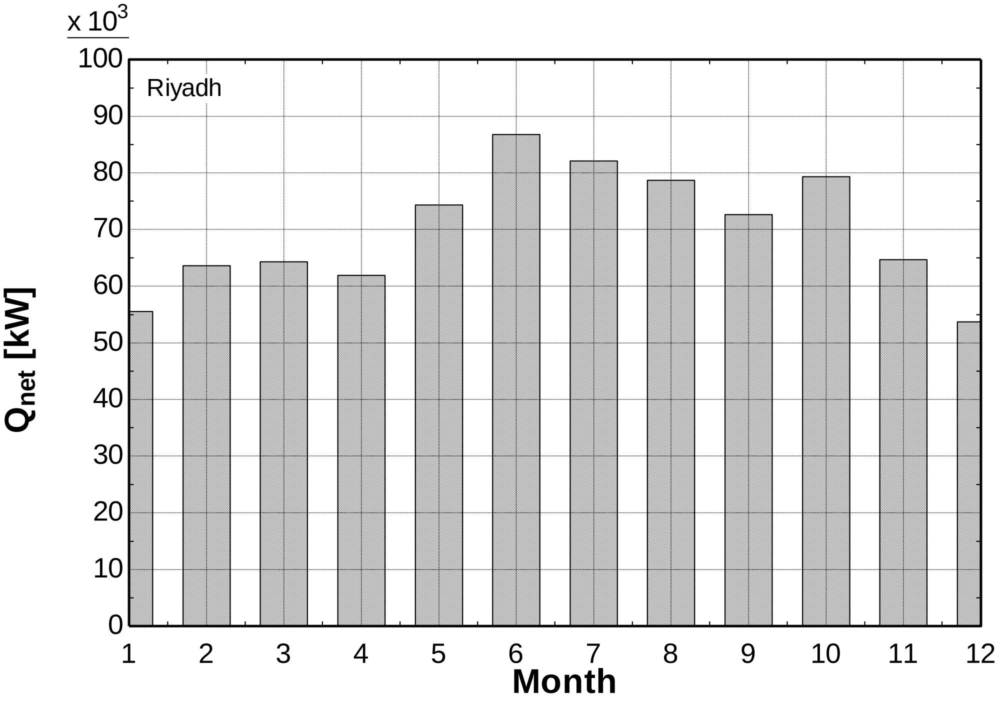

Figure 4.96 Average heat collected at the central receiver for Riyadh, Saudi Arabia

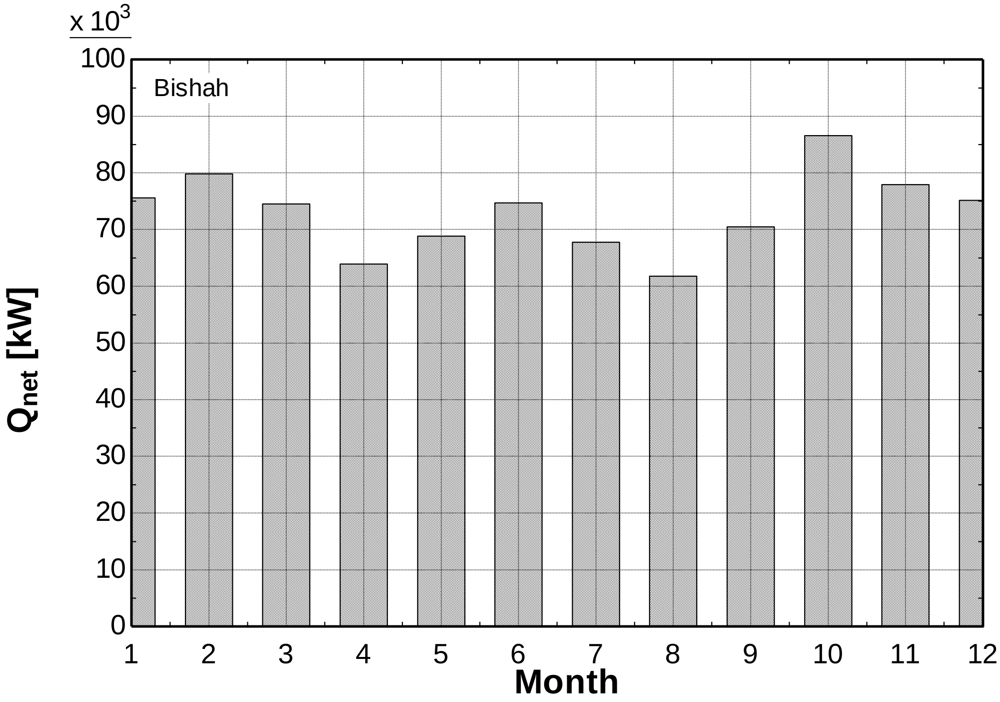

Figure 4.97 Average heat collected at the central receiver for Bishah, Saudi Arabia

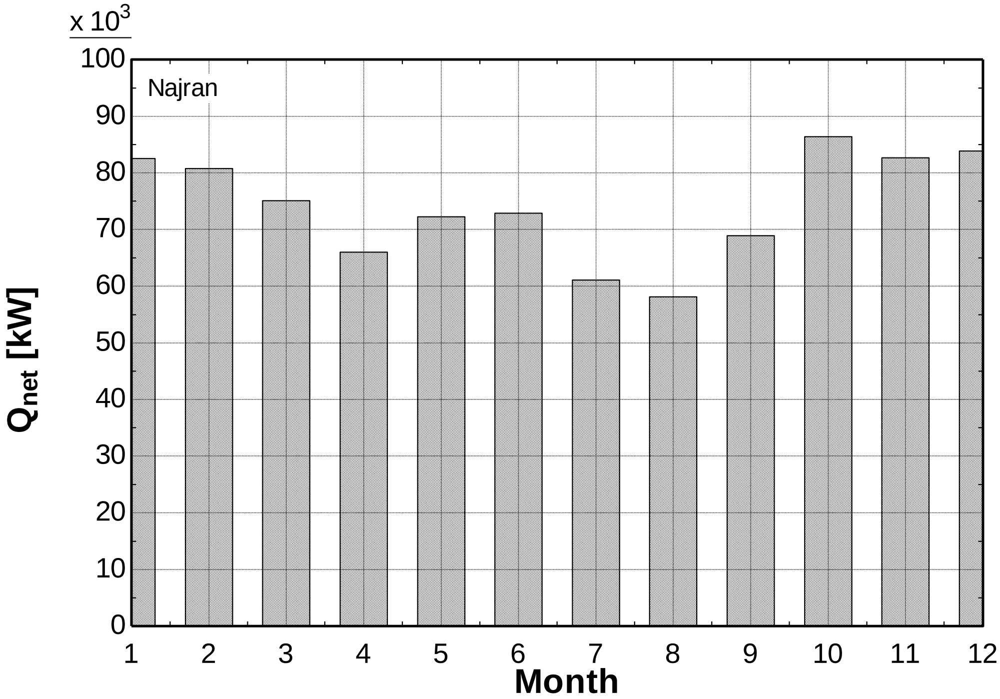

Figure 4.98 Average heat collected at the central receiver for Najran, Saudi Arabia

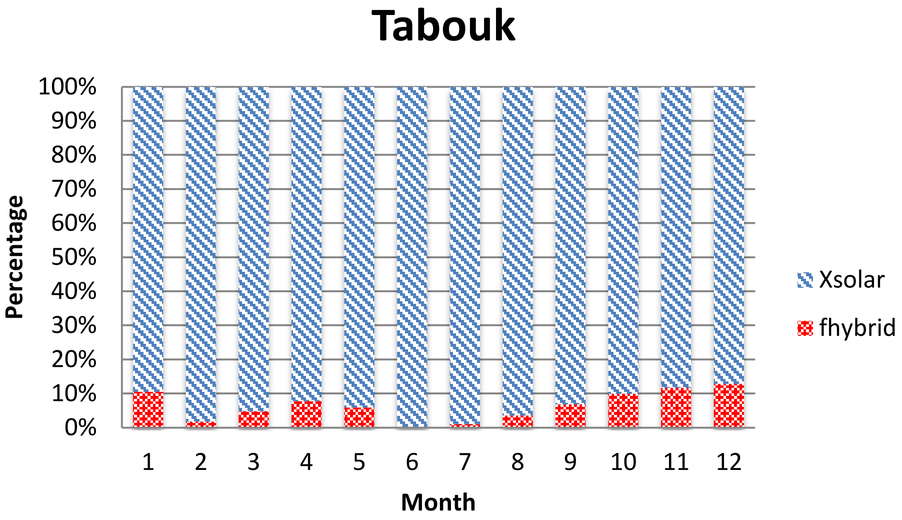

Figure 4.99 Percentage of hybridization required for Tabouk, Saudi Arabia

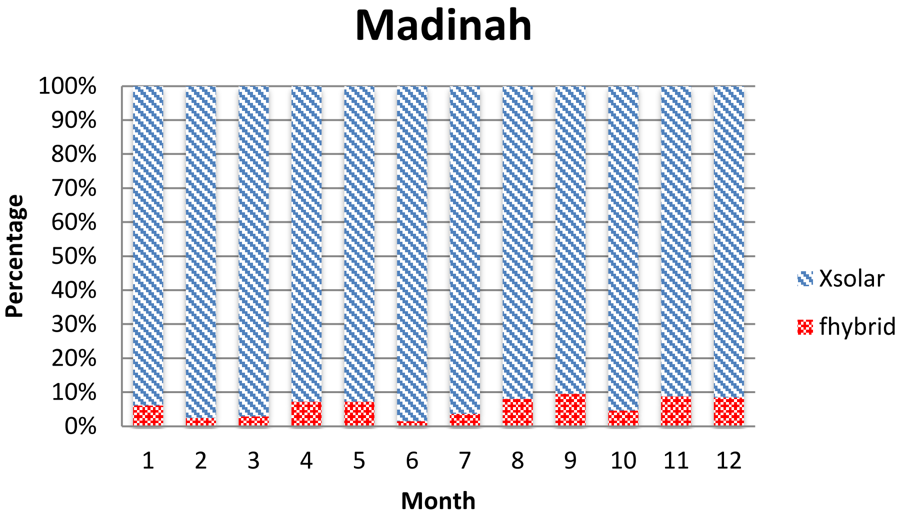

Figure 4.100 Percentage of hybridization required for Madinah, Saudi Arabia

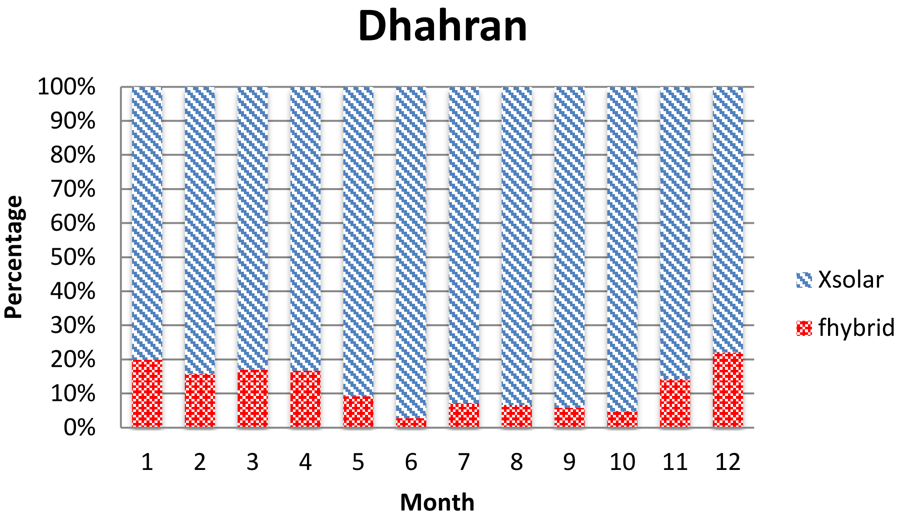

Figure 4.101 Percentage of hybridization required for Dhahran, Saudi Arabia

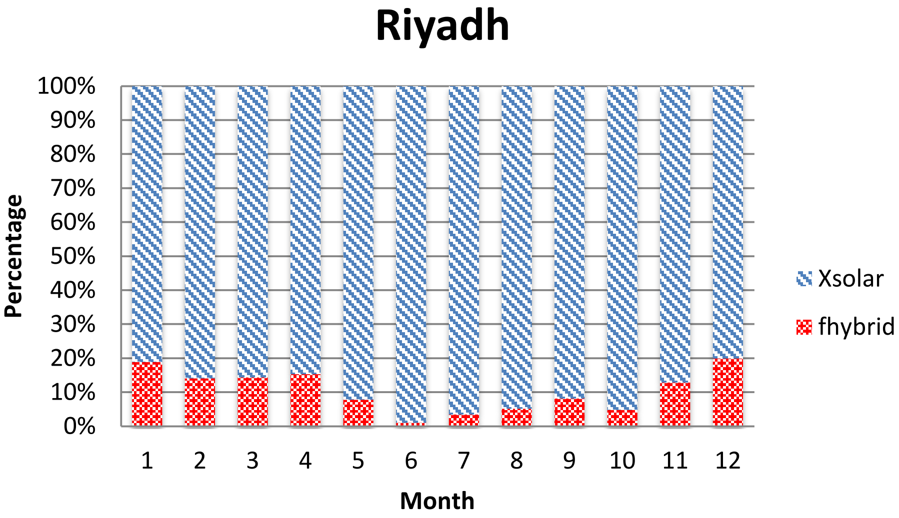

Figure 4.102 Percentage of hybridization required for Riyadh, Saudi Arabia

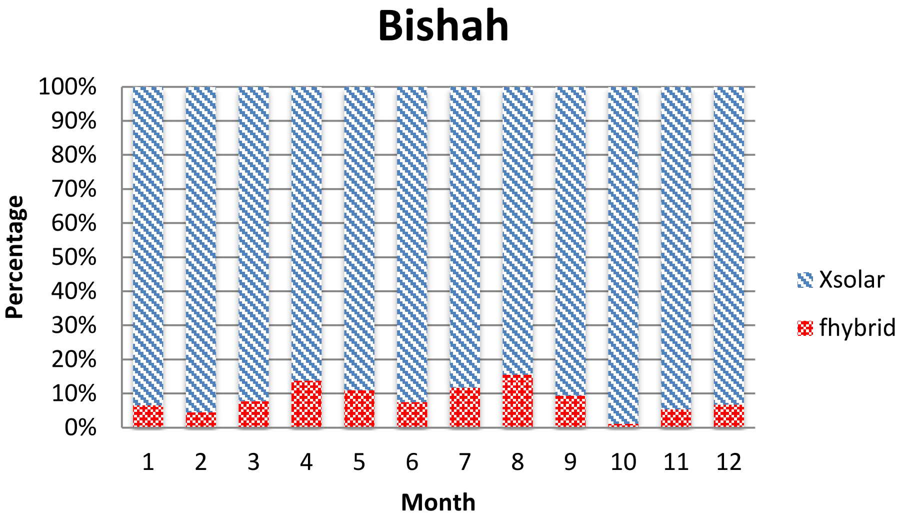

Figure 4.103 Percentage of hybridization required for Bishah, Saudi Arabia

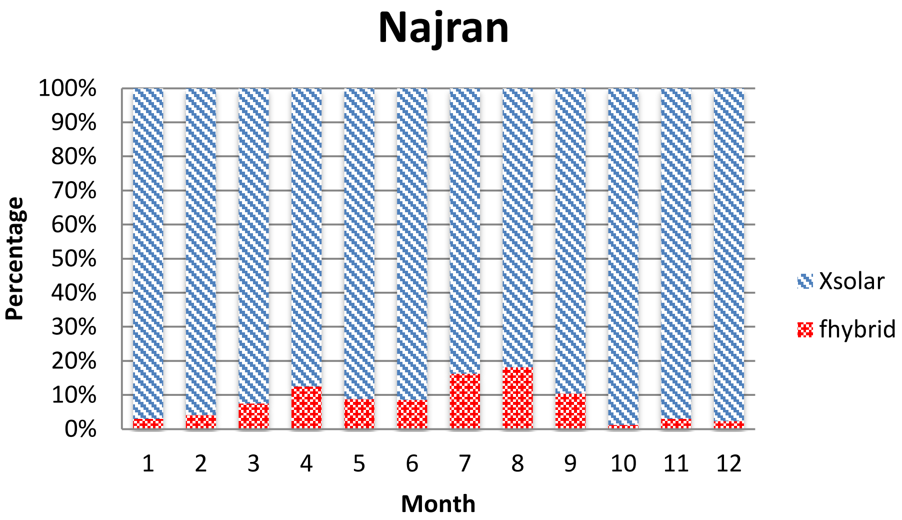

Figure 4.104 Percentage of hybridization required for Najran, Saudi Arabia

4.5 sCO_2 Brayton cycle integrated with two tank thermal storage

In this section, a complete thermodynamic analysis of the solar thermal power tower system integrated with recompression supercritical CO_2 Brayton cycle through two tank thermal storage was performed for three typical days of the year, i.e. 11th of June, 16th of March, and 10th of December respectively. These particular days were selected because they represent the solar radiation monthly average day of June, March, and December, respectively [84]. Table 4.9 (Page 133) lists the basic design and operating parameters of the heliostat field and the central receiver whereas the operating conditions of the supercritical CO_2 Brayton cycles are listed in Table 4.10 (133). For the annual optimization, the number of heliostats considered was 2940 in a surround field layout, the tower optical height was taken as 130m. The value for the storage heat exchanger effectiveness was taken as 0.9. Figure 4.105 represents the recompression cycle integrated with solar tower through two tank thermal storage.

A total of 2940 heliostats were generated and optimized on an annual basis. Higher number of heliostats were optimized to integrate the solar field to thermal storage and perform analysis. The contours of the net optical efficiency of the heliostat field are illustrated in Figure 4.56 to Figure 4.58 for 16th of March, 11th of June, and 10th of December at solar noon, respectively. The heliostat field depicted in the discussed figures is annually optimized. As can be observed from the figures that the highest optical performance is achieved on 11th of June at solar noon while the lowest optical performance is achieved on 10th of December at solar noon. On the other hand, the optical performance is in the medium range for 16th of March at solar noon. This observation can be attributed to the solar altitude angle of these days. The sun altitude angle for June 11 is the highest at noon time as compared to March 16 and December 10; that is why most of the heliostats on June 11 depict high optical efficiency.

Thermal analysis was carried out by applying transient energy balance on the two tanks. For this purpose, heat loss coefficient area product for both the tanks was calculated. The wind convective losses were also incorporated into the calculation of heat loss coefficient. Furthermore, the losses from the top were neglected, as the tank doesn't remain completely filled with the storage medium and air works as an excellent insulator.

The net energy gained at the receiver for these three days are depicted in Figure 4.50 to Figure 4.52 respectively. Note that perfect weather conditions were not assumed and the actual DNI (direct normal irradiance) data was used which was obtained from the weather station at King Fahd University of Petroleum & Minerals, Dhahran, Saudi Arabia. The DNI data used had been collected for hourly intervals. These figures demonstrate the total incident energy onto the receiver from the heliostat field and the net energy gained or the useful energy gained at the receiver after the radiation losses have been accounted for. The DNI data is also illustrated in the same figures for comparative purposes.

Since the size of the heliostat field is constant and cannot be changed because the heliostat field is deployed after finding the best positions for heliostats through optimization; therefore, the analysis was carried out for three different cases after the solar tower system was integrated with the recompression cycle. In the first case, the analysis was carried out when the net power output is uniform only for daylight hours, whereas in the second case the analysis was performed when net power output is uniform from sunrise till the end of the day, and lastly when the net power output is uniform for the whole day.

Figure 4.106 to Figure 4.108 represent the uniform net power output for all the three cases for March, June, and December, respectively. It can be observed from these figures that there is noticeable difference in the net power output for all the three days due to the variation in the incident solar irradiation. For the first case, when the net power output is uniform for the whole day, 17 MW is produced in March, 22 MW in June, and 10 MW in December. On the other hand, for the second case, when the net power output is uniform from sunrise till the end of the day, 23 MW is produced in March, 28 MW in June, and 13 MW in December. And lastly, when the net power output is uniform from sunrise till sunset, 38 MW is produced in March, 41 MW in June, and 22 MW in December. The rated power output depends upon the requirement for which the plant is designed. If the storage is operational only for daylight hours, higher power output can be targeted but the plant would have to be operational on fossil fuel resources for the rest of the hours of the day. Furthermore, for the days with low incident solar irradiation fossil fuel can be employed to achieve the rated power capacity.

On the other hand, Figure 4.109 represents the mass flow rate of molten salt through the central receiver for different days. The mass flow rate changes in accordance with the solar flux so that the temperature in the hot storage tank remains constant. The temperature in the hot storage tank is $564.4 \pm 0.6^\circ$ C, whereas the temperature in the cold storage tank remains $413 \pm 0.6^\circ$ C. The fluctuation in the temperature is due to the thermal losses associated with the storage tanks. Moreover, the mass flow rate through the storage heat exchange stays constant so that the heat transferred through the storage medium to the recompression Brayton cycle is constant. The changes in mass in both storage tanks are illustrated in Figure 4.110 to Figure 4.112 when full day operation is considered. Note that for our modeling, initial mass of molten salt was taken equal in both tanks. It can be observed that the molten salt in the hot storage tank rises during the daylight hours and it starts to decrease after the sun has set. This trend is observed because the molten salt is always flowing through the storage heat exchanger at a constant rate during the thermal storage operation, whereas the mass flow rate of the molten salt through the receiver varies according to the solar flux and it flows through the receiver only during daylight hours. Finally, at the end of operation the molten salt reaches its initial value in both tanks.

Furthermore, for the cases when the storage is operational only for daylight hours, similar trend is observed. These trends are demonstrated in Figure 4.113 to Figure 4.115. The mass of molten salt in the hot storage tank decreases at first when the solar flux is slow meanwhile some mass is withdrawn from the tank to operate the power cycle; and it starts to increase after the passage of time as the solar flux starts increasing and consequently the mass flow rate through the central receiver. Likewise, when the storage operates from sunrise till the end of the day, it can be observed from Figure 4.116 to Figure 4.118 that the total mass in the hot storage tank decreases at first and then again it starts increasing. And finally, it reaches its initial value. It should be noted here that storage operation hours depend upon the rated power capacity of the plant on which it was designed and the incident solar irradiation. If the plant is to be designed for a higher power capacity, the storage can be operational for less number of hours. Additionally, if the solar irradiation is low, low heat will be stored in the storage medium and as a result the storage will be operational for less number of hours. In our study, we have demonstrated three different cases for three different days to show the effect of solar irradiation and the output power capacity as a result of changing the storage operation hours and the change in direct normal irradiation for different days.

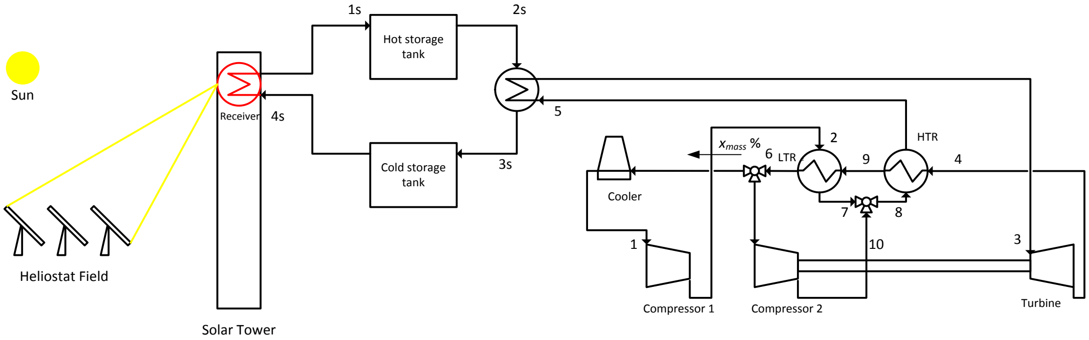

Figure 4.105 Re-compression closed loop supercritical carbon dioxide Brayton cycle integrated with solar tower through two tank thermal storage

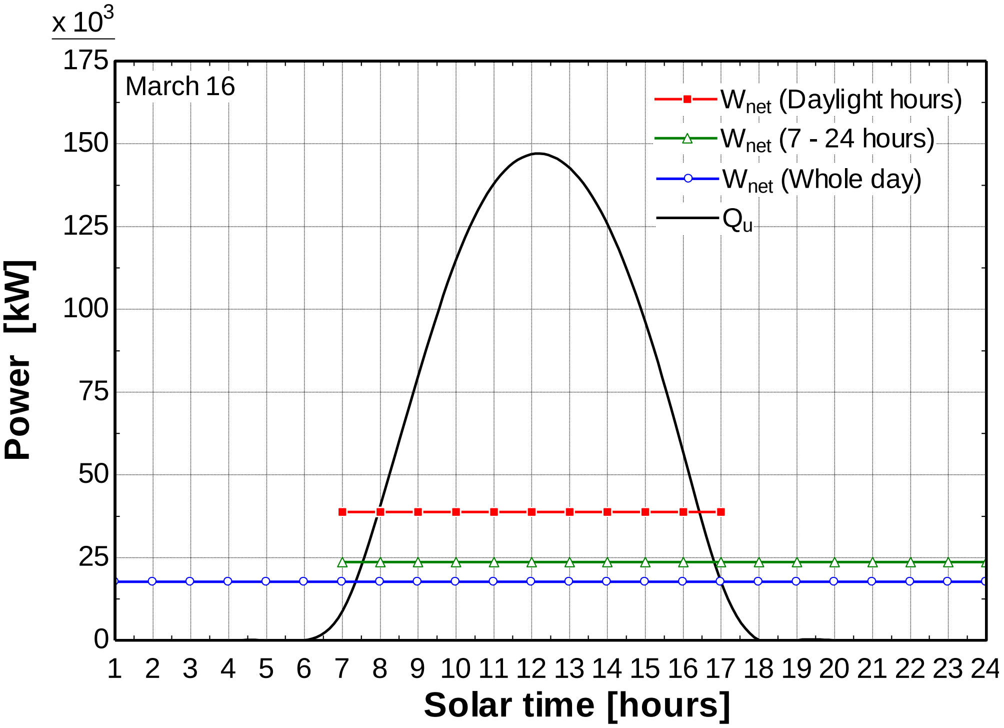

Figure 4.106 Net power gained on 11th of June for different storage options

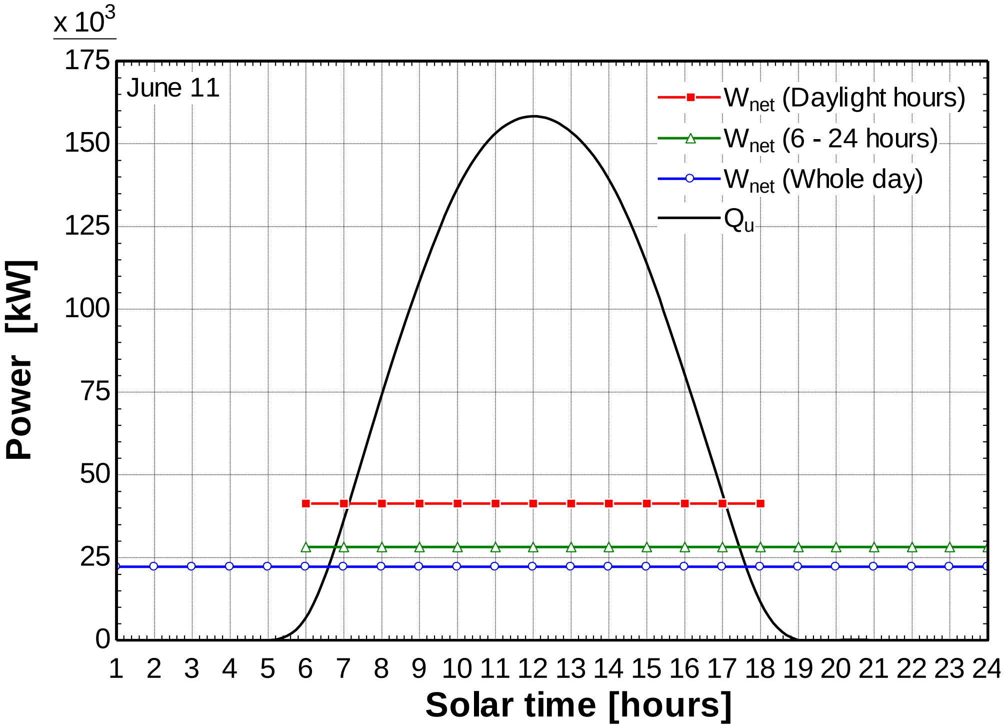

Figure 4.107 Net power gained on 11th of June for different storage options

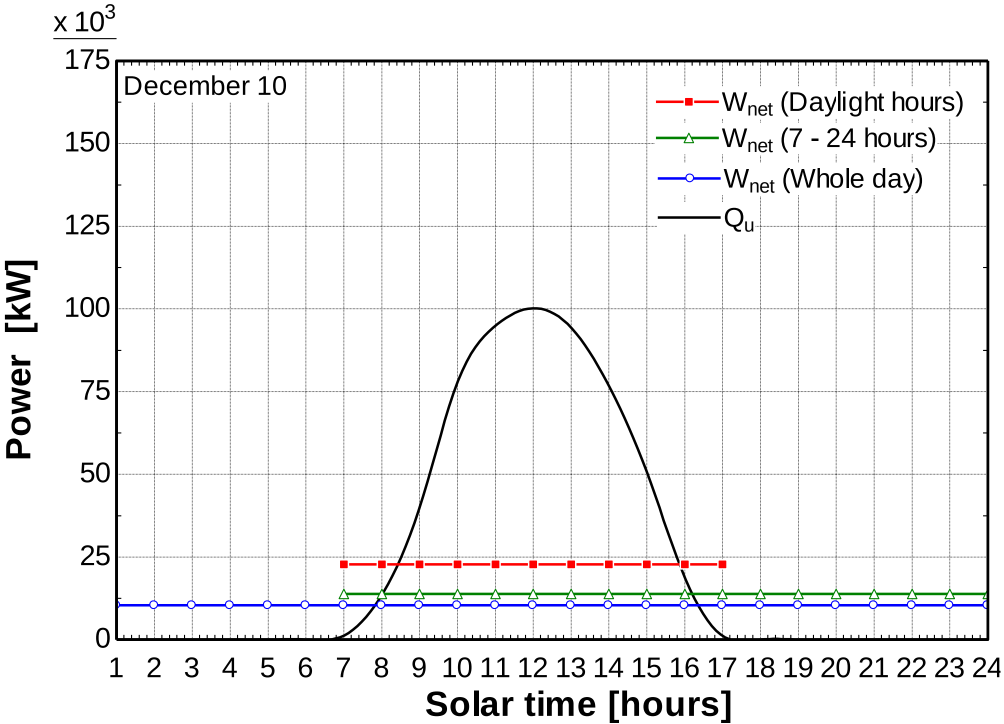

Figure 4.108 Net power gained on 10th of December for different storage options

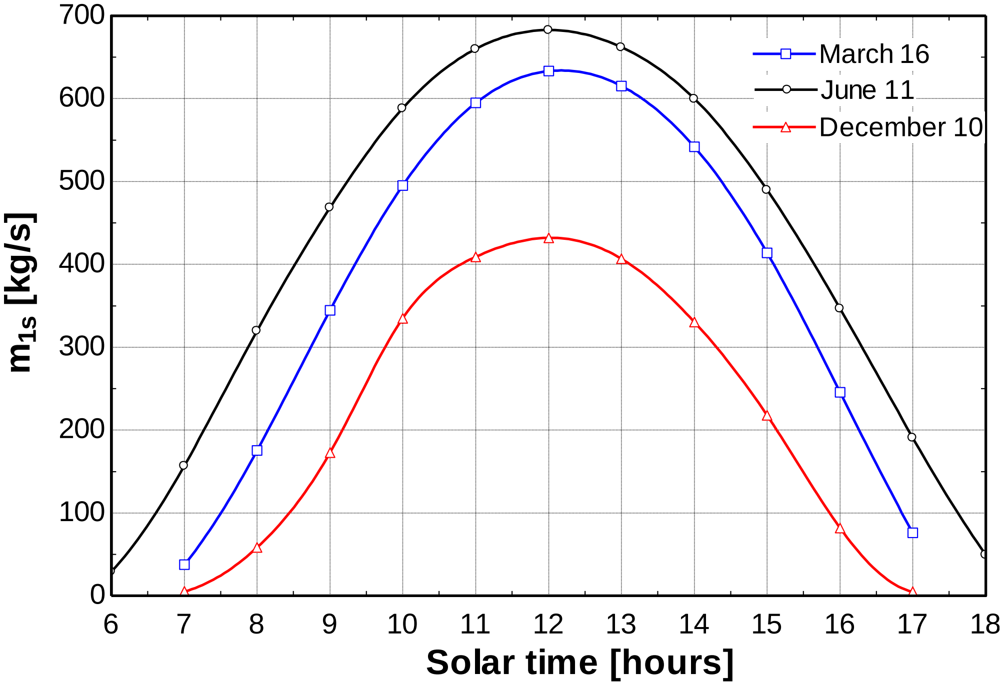

Figure 4.109 Mass flow rate of the storage medium through the receiver

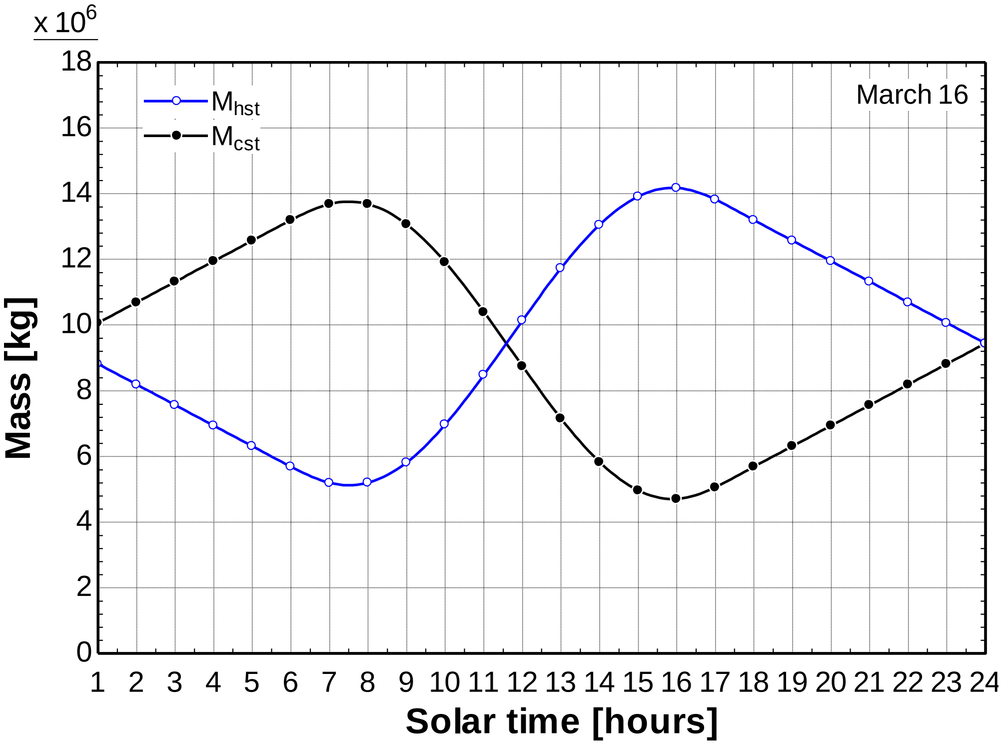

Figure 4.110 Change in mass of molten salt in the storage tanks with time for whole day operation on 16th of March

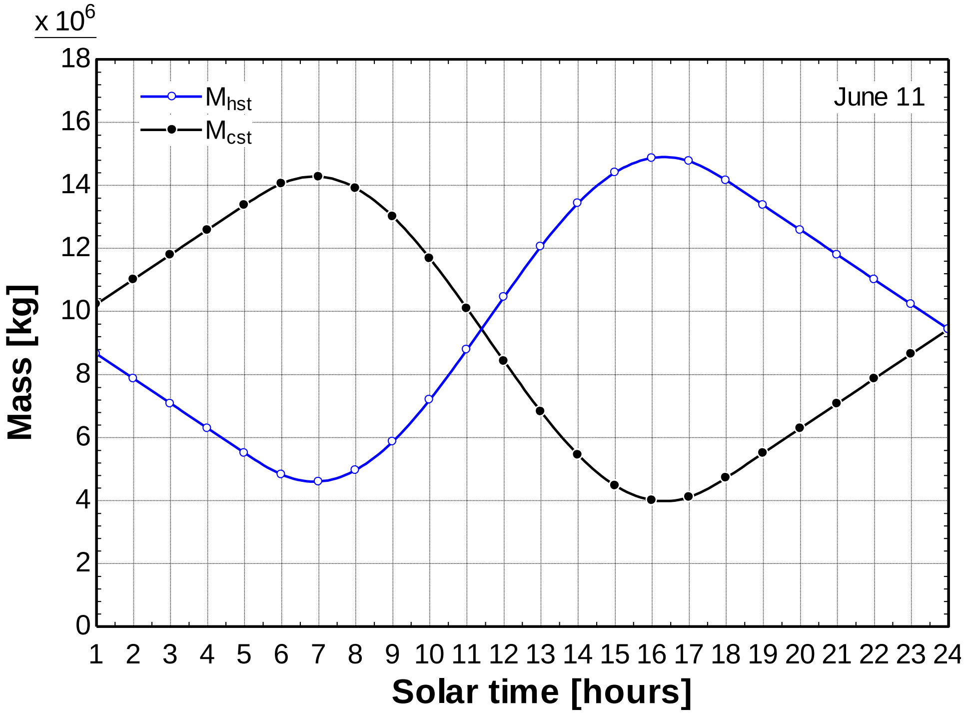

Figure 4.111 Change in mass of molten salt in the storage tanks with time for whole day operation on 11th of June

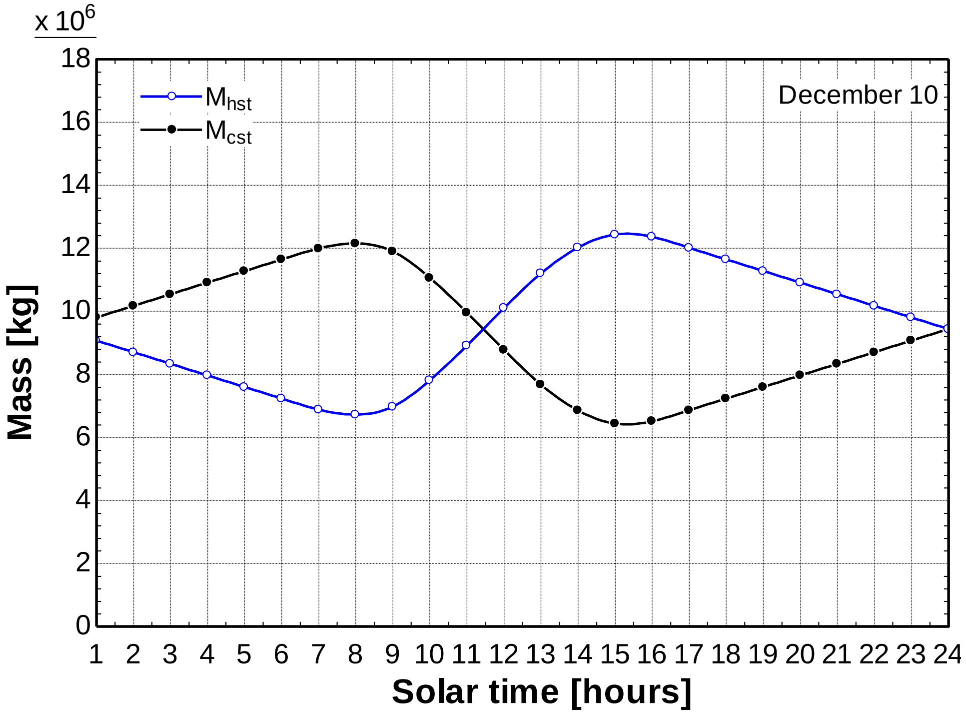

Figure 4.112 Change in mass of molten salt in the storage tanks with time for whole day operation on 10th of December

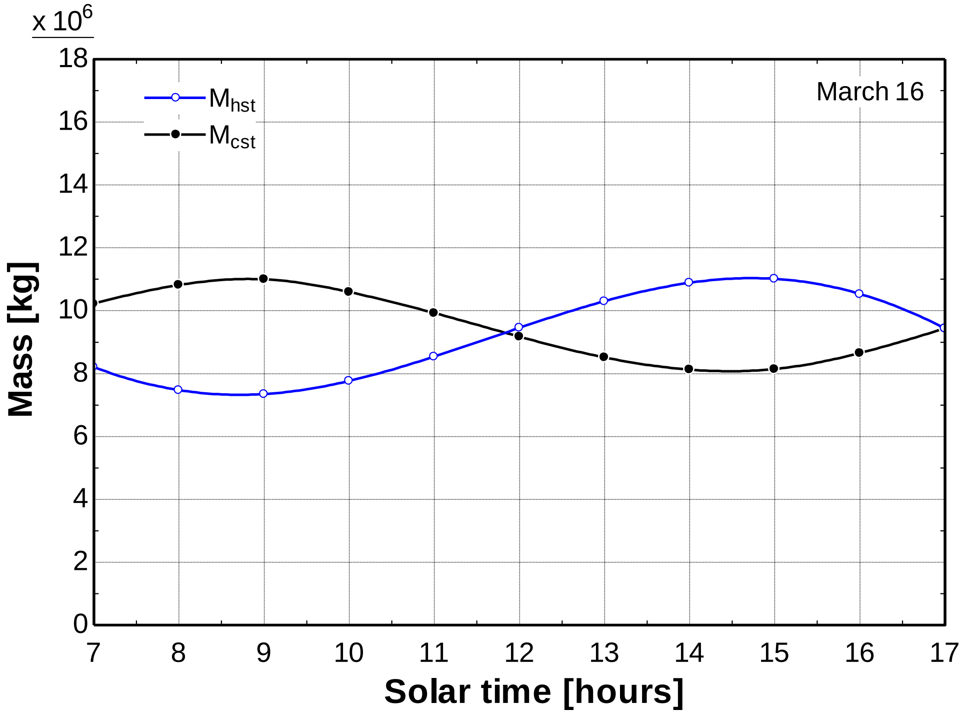

Figure 4.113 Change in mass of molten salt in the storage tanks with time for daylight hours operation on 16th of March

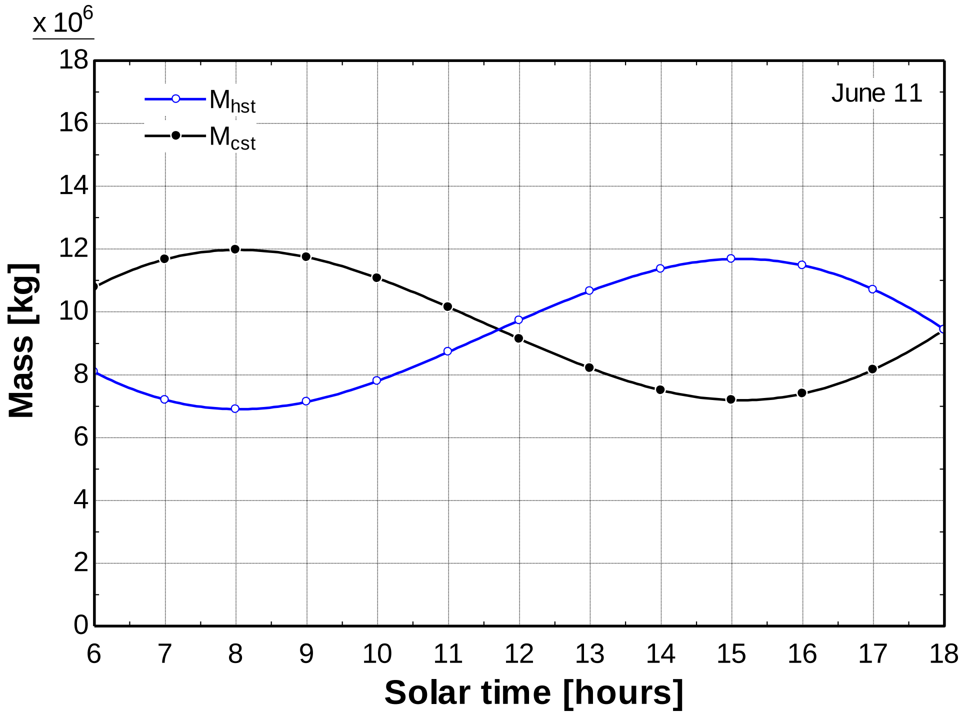

Figure 4.114 Change in mass of molten salt in the storage tanks with time for daylight hours operation on 11th of June

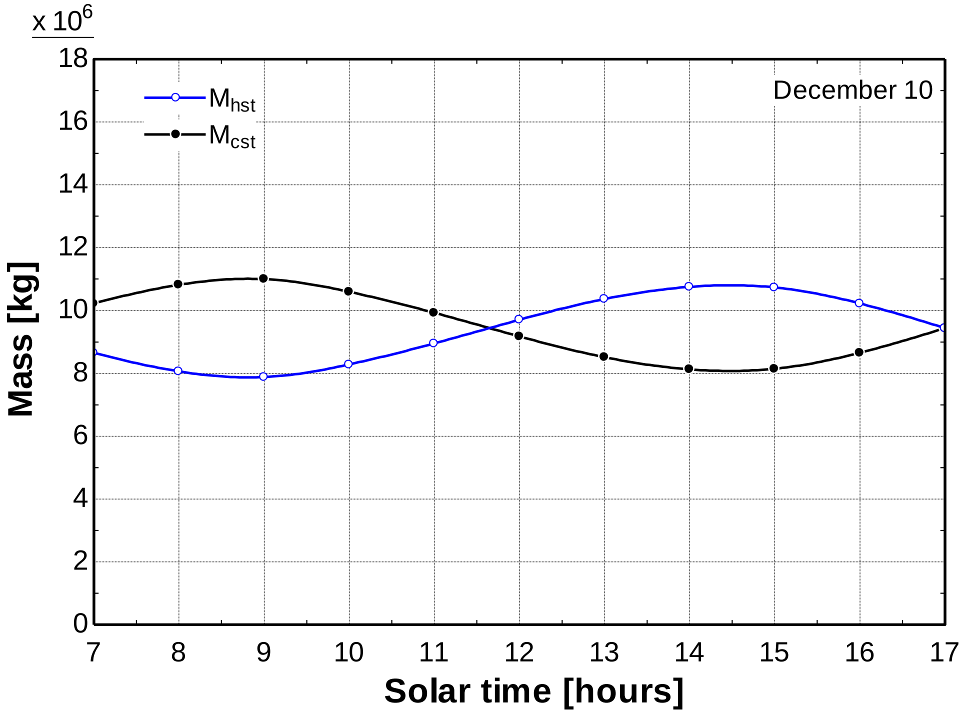

Figure 4.115 Change in mass of molten salt in the storage tanks with time for daylight hours operation on 10th of December

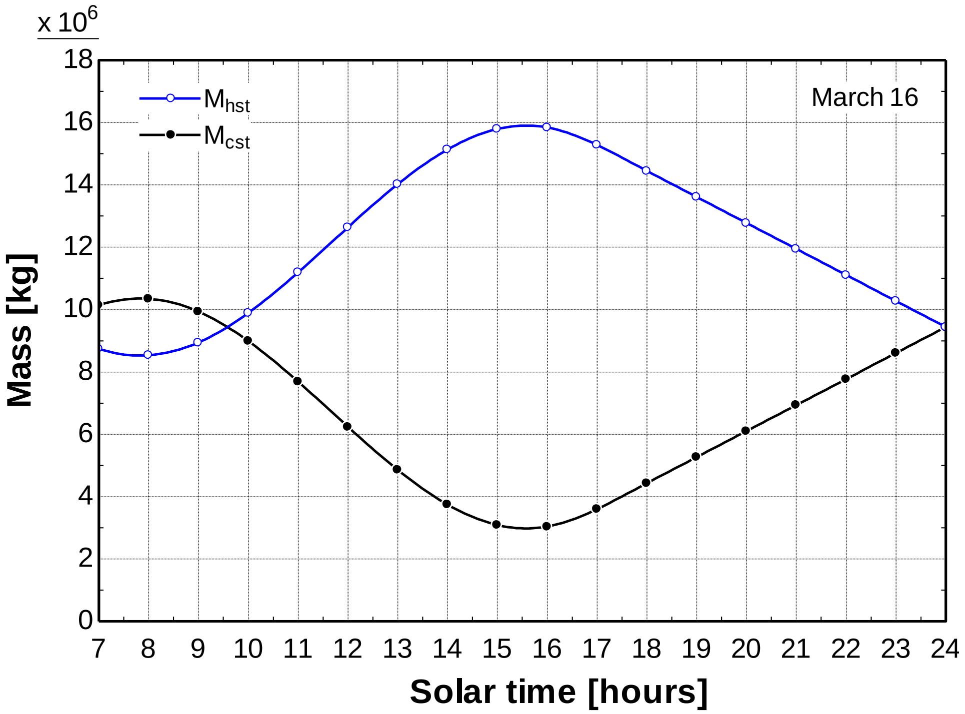

Figure 4.116 Change in mass of molten salt in the storage tanks with time for sunrise till the end of the day operation on 16th of March

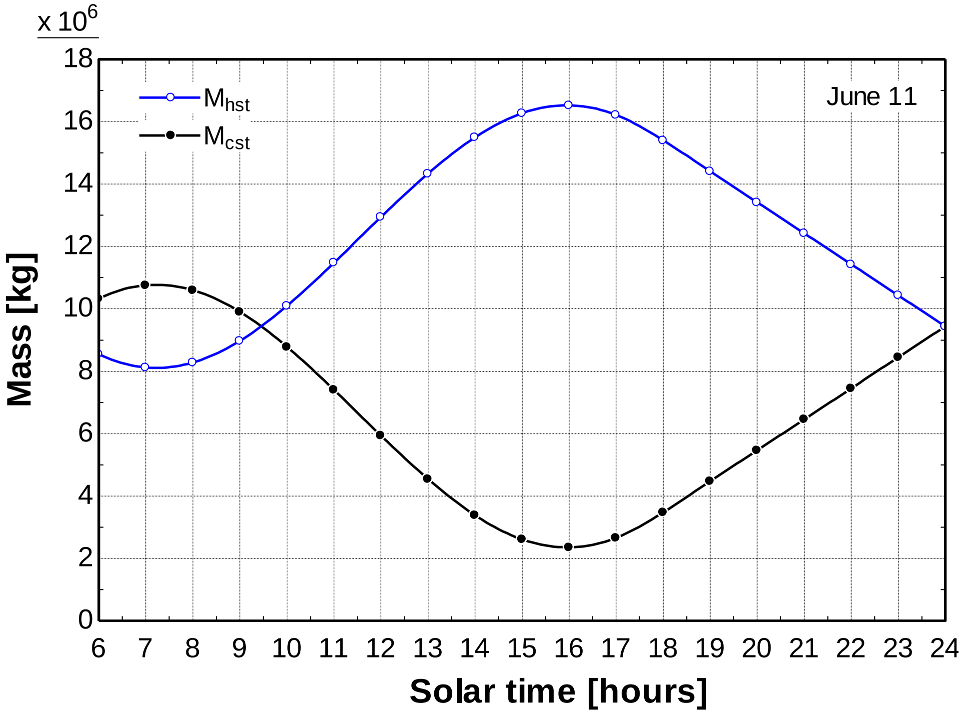

Figure 4.117 Change in mass of molten salt in the storage tanks with time for sunrise till the end of the day operation on 11th of June

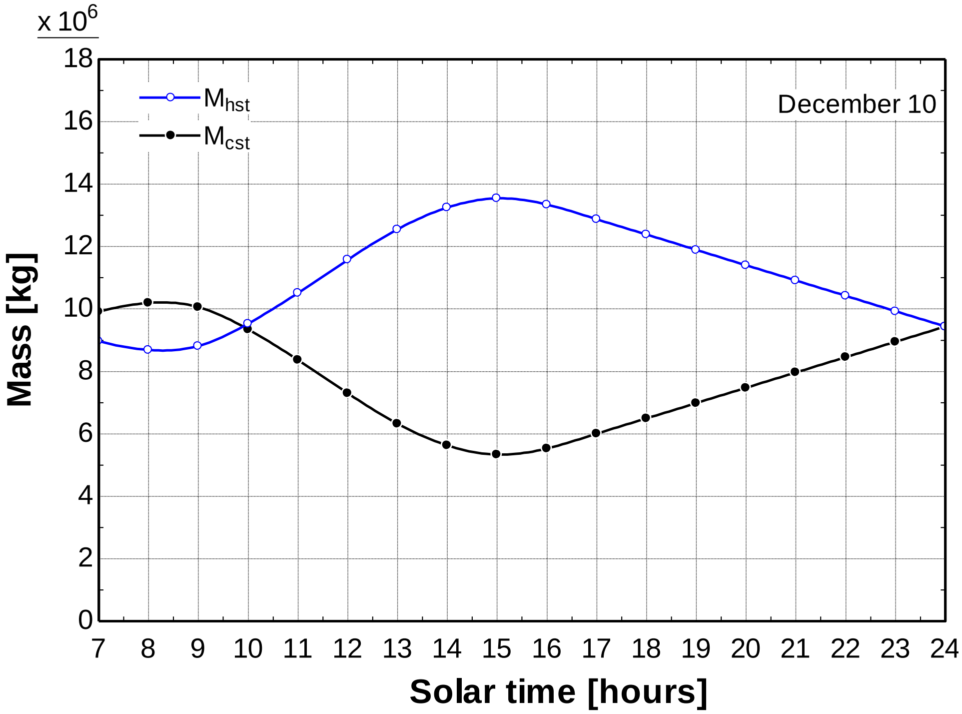

Figure 4.118 Change in mass of molten salt in the storage tanks with time for sunrise till the end of the day on 10th of December

CHAPTER 5

CONCLUSIONS AND RECOMMENDATIONS

In this chapter, the conclusions of this study and the results that were elaborated in the previous chapter have been presented and discussed. Furthermore, future work and recommendations are also presented.

5.1 Conclusions

A mathematical code was developed in Matlab which generates and optimizes a heliostat field effectively. This code was developed to demonstrate the optimization of a heliostat field using differential evolution, which is an evolutionary algorithm. The current study illustrates how to employ the model developed and its advantages. The optimization process calculates the optical performance parameters at every step of the optimization considering all the heliostats; thus yields accurate results as discussed in this study. The optimization was also executed for different time instants to check the effect of sun's altitude angle on the heliostat field efficiency. The efficiency of the un-optimized heliostat field with that of the optimized heliostat field was compared when:

- two variables were optimized i.e. the radial and the azimuthal spacing taken as constant for all the zones.
- four variables were optimized i.e. constant azimuthal spacing for all the zones and the radial spacing independently for each zone.

- normalized ratio of optical efficiency to the land area covered by the heliostat field was maximized using four variables.
- heliostat field layout was optimized on annual basis using four variables.

Moreover, the insolation weighted daily averaged annual efficiency of the heliostat field was 0.5634 for Dhahran, Saudi Arabia.

On the other hand, complete thermodynamic analysis of supercritical CO_2 Brayton cycles when integrated with solar thermal power tower system was performed. The heliostat field layout generated was optimized on an annual basis and was tested for its optical performance as discussed previously. Furthermore, five closed loop sCO_2 Brayton cycles were modeled: the simple cycle, the regenerative cycle, the recompression cycle, the pre-compression cycle, and the split expansion cycle. These cycles were evaluated and compared for their net power outputs and thermal efficiencies. The operating conditions were the same for all the cycles. This analysis was carried out for three selected days of the year: 16th of March, 11th of June, and 10th of December, which are the average day of radiation for each month. The results demonstrate that the recompression cycle reached the highest thermal efficiency and the highest net power output at peak hours, around solar noon, when the solar radiation is high. The highest cycle thermal efficiency is 52% and the highest integrated system efficiency is 40% both in June noontime for this cycle. The regenerative cycle, although simpler in configuration, also showed promising results and its thermal efficiency and net power output were the second highest and comparable to that of the split expansion cycle.

Furthermore, a complete thermodynamic analysis of a solar thermal tower system when integrated with a sCO_2 recompression Brayton cycle was performed for six different locations in Saudi Arabia considering the local solar irradiation intensity for each location. The selected locations for the analysis were Tabouk (North), Madinah (West), Dhahran (East), Riyadh (Central), Bishah (South), and Najran (South). In addition, to keep the net power output uniform, an auxiliary heat exchanger was added before the expansion turbine. The findings indicated that the highest annual average heat collected was for Madinah (938,400 kWh/day) and the second highest was for Tabouk, (933,100 kWh/day). Similarly, the least amount of annual average fuel hybridization required was 5.82% for Madinah, and 6.34% for Tabouk during daytime.

Because the recompression cycle has the highest thermal efficiency around solar noon hours when integrated with solar thermal power tower system; this cycle was selected for integration with two tank thermal storage. This analysis was carried out for three selected days of the year: 16th of March, 11th of June, and 10th of December, which are the average days of radiation for each month. The integrated heliostat field was optimized on annual basis and tested for its optical efficiency. The storage medium which was used in this study was 60%$NaNO_3$ and 40%KNO_3. Three cases were studied in which the thermal storage was operational for different ranges of time. Firstly, when it was operational only for daylight hours, secondly when it was operational from sunrise till the end of the day, and lastly when it was operational for the whole day. For the first case, when the net power output is uniform for the whole day, 17 MW is produced in March, 22 MW in June, and 10 MW in December. And for the case when the net power output is uniform from sunrise till sunset, 38 MW is produced in March, 41 MW in June, and 22 MW in

December. Similar observations were made for the other case. It can be observed that the amount of net power yielded at the recompression cycle depends upon the incident solar energy. Nonetheless, this can accounted for by adding an auxiliary boiler to reach the target power.

5.2 Recommendations

The recommendations of future research are given below:

- It was observed that increasing the number of optimizing parameters increased the optical efficiency of the heliostat field; therefore, more number of optimizing parameters can be introduced by modifying the Matlab code to examine if the heliostat field efficiency further improves or not.
- The intercept factor depends upon the receiver dimensions, nevertheless, the convection and the radiation heat losses also depend upon the receiver dimensions. Hence, the receiver dimensions should also be incorporated in the optimization process on annual basis.
- The feasibility of sCO2 Brayton cycles should be examined for heat cogeneration.
- For the storage analysis, phase change material should be employed as the storage medium and sCO_2 as the heat transfer fluid.

NOMENCLATURE

A_h	Total area of the heliostats, m^2
A_l	Land area covered by the heliostat field, m^2
A_R	Surface area of the central receiver, m^2
C_p	Specific heat, kJ/kg-K
CR	Crossover factor
$\hat{d}_{sun}$	Unit vector pointing towards the sun
$\hat{d}_{rec}$ (or $\hat{t}$)	Unit vector pointing towards the receiver
$\hat{d}_n$ (or $\hat{n}$)	Unit normal vector of the heliostat surface
d_g	General dimension of the heliostat
DH	Heliostat diagonal, m
DM	Characteristic diameter, m
DR	Receiver diameter (cylindrical), m
$dsep$	Extra security distance between heliostats, m
ds	Ratio of extra security distance to heliostat height
f	Focal length of the heliostat, m
F	Mutation factor
f_{at}	Atmospheric attenuation factor
f_{hybrid}	Fraction of fuel hybridization required to keep a constant power output
f_{sb}	Shadowing and blocking factor
f_{itc}	Intercept factor
f_{at_annual}	Annual atmospheric attenuation factor
f_{sb_annual}	Annual shadowing and blocking factor

f_{itc_annual}	Annual Intercept factor
F_{view}	Radiation view factor
h	Specific enthalpy, kJ/kg
h_{clear}	Horizontal clearance between the heliostats, m
h_{conv}	Convective heat transfer coefficient at the central receiver, kW/m^2-$^\circ$C
H_t	Image dimension in the tangential plane, m
H_{tower}	Total height of the tower, m
I	Incident normal radiation, kW/m^2
LH	Height of the heliostat, m
LR	Receiver size, m
LW	Width of the heliostat, m
M_{cst}	Mass of the storage medium in cold storage tank, kg
M_{hst}	Mass of the storage medium in hot storage tank, kg
$\dot{m}$	Mass flow rate of sCO_2 in the Brayton cycle, kg/s
$\dot{m}_{1s}$	Mass flow rate of the storage medium through central receiver, kg/s
$\dot{m}_{2s}$	Mass flow rate of the storage medium through storage heat exchanger, kg/s
n_d	A day in the year
$Nhel_i$	Number of heliostats per row in ith zone
$Nrows_i$	Number of rows of heliostats in ith zone
Nu	Nusselt number
Pr	Prandtl number
Q_{aux}	Auxiliary heat addition rate, kW
Q_{conv}	Rate of convection heat losses from the central receiver, kW
Q_{cst}	Heat loss rate from the cold storage tank to the ambient, kW

Q_{hst}	Heat loss rate from the hot storage tank to the ambient, kW
Q_{in}	Total energy interception rate by the central receiver, kW
Q_{out}	Energy rejection rate at the cooler of the Brayton cycle, kW
Q_{rad}	Rate of radiation heat losses from the central receiver, kW
Q_u (Q_{net})	Net useful energy gain rate at the central receiver, kW
Q_{solar}	Total incident solar radiation on the solar field, kW
Re	Reynolds number
random#	A random number
R_i	Radius of first row of heliostats of ith zone, m
R_{last}	Radius of the last row of heliostats of the last zone from the solar tower, m
S_{rec}	Slant distance between the heliostat and the central receiver, m
t	Time
T_{amb}	Ambient temperature, $^\circ$C
T_{cst}	Temperature of the storage medium in cold storage tank, $^\circ$C
T_{hst}	Temperature of the storage medium in hot storage tank, $^\circ$C
THT	Tower optical height or aim point height, m
T_R	Temperature at the central receiver surface, $^\circ$C
$(UA)_{cst}$	Loss coefficient area product of the cold storage tank, kW/$^\circ$C
$(UA)_{hst}$	Loss coefficient area product of the hot storage tank, kW/$^\circ$C
u_{cst}	Specific internal energy of the storage medium in the cold storage tank, kJ/kg
u_{hst}	Specific internal energy of the storage medium in the hot storage tank, kJ/kg
V	Mutant vector
v_{clear}	Vertical clearance between the heliostats, m

W_C	Compressor power, kW
$W_{C,i}$	Compressor power of ith compressor, kW
W_{net}	Net power output of the Brayton cycle, kW
wr	Ratio of heliostat width to heliostat height
W_s	Image dimension in the sagittal plane, m
W_T	Turbine power, kW
$W_{T,i}$	Turbine power of ith turbine, kW
X	Control variable vector
x	X co-ordinate
x'	X co-ordinate on the receiver plane
x_{mass}	Fraction of mass flow rate of sCO_2 through the cooler
X_{solar}	The input solar share
y	Y co-ordinate
y'	Y co-ordinate on the receiver plane

List of Greek symbols

α_s	Solar altitude angle, radians
α_n	Altitude angle of unit normal vector of heliostat, radians
α_R	Absorptivity of the central receiver
δ	Solar declination angle, radians
$\Delta\alpha z_i$	Azimuthal spacing between adjacent heliostats in ith zone, radians
$\Delta R_{\min}$	Minimum radial distance between the rows of heliostats, m
ΔR_i	Radial distance between the rows of heliostats in ith zone, m
ε	Emissivity of the central receiver
ε_s	Effectiveness of storage heat exchanger

ε_R	Effectiveness of the regenerator
ε_{HTR}	Effectiveness of the high temperature regenerator
ε_{LTR}	Effectiveness of the low temperature regenerator
η_{opt}	Optical efficiency of the heliostat
η_{daa}	Daily averaged annual heliostat field layout efficiency
η_{iwaa}	Insolation weighted daily averaged annual heliostat field layout efficiency
η_{maa}	Monthly averaged annual heliostat field layout efficiency
$\eta_{th,R}$	Thermal efficiency of the central receiver
η_T	Isentropic efficiency of the turbine
$\eta_{T,i}$	Isentropic efficiency of ith turbine
η_C	Isentropic efficiency of the compressor
$\eta_{\mathrm{C},i}$	Isentropic efficiency of ith compressor
η_{sys}	Thermal efficiency of the complete integrated system (without thermal storage)
η_{th}	Thermal efficiency of the Brayton cycle
γ_s	Solar azimuthal angle, radians
γ_n	Azimuthal angle of unit normal vector of heliostat, radians
ω_s	Solar hour angle, radians
$\omega_{sunrise}$	Sunrise hour angle, radians
ω_{sunset}	Sunset hour angle, radians
ω	Incidence angle, radians
$(\cos\omega)_{\_annual}$	Annual cosine factor

ϕ	Latitude angle, radians
$\psi_{\max}$	Angular distance from the north axis to the last heliostat in the polar field, radians
ρ	Reflectivity of the heliostat surface
σ	Stefan-Boltzmann constant, kW/m^2- K
σ_s	Mirror slope error
σ_h	Horizontal elliptical Gaussian distribution for of the slope error
σ_v	Vertical elliptical Gaussian distribution for of the slope error
σ_{tot}	Standard deviation of total error on the receiver plane
σ_{bq}	Standard deviation of beam quality error
σ_{ast}	Standard deviation of astigmatic error
σ_t	Standard deviation of tracking error
σ_{sun}	Standard deviation of sunshape error
θ_n	Zenith angle of unit normal vector of heliostat, radians

REFERENCES

[1] IEA, 2010, Technology Roadmap: Concentrating Solar Power, OECD Publishing.

[2] IRENA, 2012, Renewable Power Generation Costs in 2012 : An Overview, Abu Dhabi, United Arab Emirates.

[3] Fernández-García A., Zarza E., Valenzuela L., and Pérez M., 2010, “Parabolic-trough solar collectors and their applications,” Renew. Sustain. Energy Rev., **14**(7), pp. 1695–1721.

[4] Pavlović T. M., Radonjić I. S., Milosavljević D. D., and Pantić L. S., 2012, “A review of concentrating solar power plants in the world and their potential use in Serbia,” Renew. Sustain. Energy Rev., **16**(6), pp. 3891–3902.

[5] Ummadisingu A., and Soni M. S., 2011, “Concentrating solar power – Technology, potential and policy in India,” Renew. Sustain. Energy Rev., **15**(9), pp. 5169–5175.

[6] DLR, 2005, European concentrated solar thermal road-mapping.

[7] Sargent, and Lundy, 2003, Assessment of parabolic trough and power tower solar technology cost and performance forecasts.

[8] Liqreina A., and Qoaider L., 2014, “Dry cooling of concentrating solar power (CSP) plants, an economic competitive option for the desert regions of the MENA region,” Sol. Energy, **103**, pp. 417–424.

[9] Li J., 2009, “Scaling up concentrating solar thermal technology in China,” Renew. Sustain. Energy Rev., **13**(8), pp. 2051–2060.

[10] Mahia R., de Arce R., and Medina E., 2014, “Assessing the future of a CSP industry in Morocco,” Energy Policy, **69**, pp. 586–597.

[11] Squire Sanders, The future for renewable energy in the MENA region.

[12] Kalogirou S. A., 2004, “Solar thermal collectors and applications,” Prog. Energy Combust. Sci., **30**(3), pp. 231–295.

[13] IEA, 2014, Technology Roadmap Energy storage.

[14] IRENA, 2013, Thermal Energy Storage Technology Brief.

[15] Behar O., Khellaf A., and Mohammedi K., 2013, “A review of studies on central receiver solar thermal power plants,” Renew. Sustain. Energy Rev., **23**, pp. 12–39.

[16] Kulhanek M., and Dostal V., 2011, “Supercritical carbon dioxide cycles thermodynamic analysis and comparison,” Supercrit. CO 2 Power Cycle Symp. ….

[17] Ho C. K., and Iverson B. D., 2014, “Review of high-temperature central receiver designs for concentrating solar power,” Renew. Sustain. Energy Rev., **29**, pp. 835–846.

[18] Persichilli M., Kacludis A., Zdankiewicz E., and Held T., 2012, “Supercritical CO2 Power Cycle Developments and Commercialization: Why sCO2 can Displace Steam Steam,” pp. 19–21.

[19] Chiesi M., Vanzolini L., Franchi Scarselli E., and Guerrieri R., 2013, “Accurate optical model for design and analysis of solar fields based on heterogeneous multicore systems,” Renew. Energy, **55**, pp. 241–251.

[20] Garcia P., Ferriere A., and Bezian J.-J., 2008, “Codes for solar flux calculation dedicated to central receiver system applications: A comparative review,” Sol. Energy, **82**(3), pp. 189–197.

[21] Romero M., and Steinfeld A., 2012, “Concentrating solar thermal power and thermochemical fuels,” Energy Environ. Sci., **5**(11), p. 9234.

[22] Renzi M., Bartolini C. M., Santolini M., and Arteconi A., 2014, “Efficiency assessment for a small heliostat solar concentration plant,” Int. J. Energy Res.

[23] Ali B. F., 1990, “Theoretical study of main factors affecting the heliostat field design of tower power plant,” Energy Convers. Manag., **30**(2), pp. 101–106.

[24] Lipps F. W., and Vant-Hull L. L., 1978, “A cellwise method for the optimization of large central receiver systems,” Sol. Energy, **20**(6), pp. 505–516.

[25] Lipps F. W., and Vant-Hull L. L., 1974, “Shadowing and blocking geometry for a solar tower concentrator with rectangular mirrors,” ASME Pap., p. 74–WA/Sol–11.

[26] Lipps F. W., 1985, “Theory of cellwise optimization fo solar central receivers,” Albuquerque, **SAND85-817**.

[27] Siala F. M. ., and Elayeb M. ., 2001, “Mathematical formulation of a graphical method for a no-blocking heliostat field layout,” Renew. Energy, **23**(1), pp. 77–92.

[28] Schwarzbözl P., Pitz-Paal R., and Schmitz M., 2009, "Visual HFLCAL—A Software Tool for Layout and Optimisation of Heliostat Fields," SolarPACES, SolarPACES, Berlin, Germany, pp. 15–18.

[29] Schmitz M., Schwarzbözl P., Buck R., and Pitz-Paal R., 2006, "Assessment of the potential improvement due to multiple apertures in central receiver systems with secondary concentrators," Sol. Energy, **80**(1), pp. 111–120.

[30] Pitz-Paal R., Botero N. B., and Steinfeld A., 2011, "Heliostat field layout optimization for high-temperature solar thermochemical processing," Sol. Energy, **85**(2), pp. 334–343.

[31] Noone C. J., Torrilhon M., and Mitsos A., 2012, "Heliostat field optimization: A new computationally efficient model and biomimetic layout," Sol. Energy, **86**(2), pp. 792–803.

[32] Besarati S. M., and Yogi Goswami D., 2014, "A computationally efficient method for the design of the heliostat field for solar power tower plant," Renew. Energy, **69**, pp. 226–232.

[33] Sassi G., 1983, "Some notes on shadow and blockage effects," Sol. Energy, **31**(3), pp. 331–333.

[34] Wei X., Lu Z., Wang Z., Yu W., Zhang H., and Yao Z., 2010, "A new method for the design of the heliostat field layout for solar tower power plant," Renew. Energy, **35**(9), pp. 1970–1975.

[35] Wei X., Lu Z., Yu W., and Wang Z., 2010, "A new code for the design and analysis of the heliostat field layout for power tower system," Sol. Energy, **84**(4), pp. 685–690.

[36] Huang W., and Xu Q., 2014, "Development of an analytical method and its quick algorithm to calculate the solar energy collected by a heliostat field in a year," Energy Convers. Manag., **83**, pp. 110–118.

[37] Sánchez M., and Romero M., 2006, "Methodology for generation of heliostat field layout in central receiver systems based on yearly normalized energy surfaces," Sol. Energy, **80**(7), pp. 861–874.

[38] Huang W., Li L., Li Y., and Han Z., 2013, "Development and evaluation of several models for precise and fast calculations of shadowing and blocking in heliostats field," Sol. Energy, **95**, pp. 255–264.

[39] Huang W., Li H., Li L., Hu P., and Chen Z., 2013, "Gauss–Legendre integration of an analytical function to calculate the optical efficiency of a heliostat," Sol. Energy, **92**, pp. 7–14.

[40] Collado F. J., 2009, “Preliminary design of surrounding heliostat fields,” Renew. Energy, **34**(5), pp. 1359–1363.

[41] Collado F. J., and Guallar J., 2012, “Campo: Generation of regular heliostat fields,” Renew. Energy, **46**, pp. 49–59.

[42] Collado F. J., and Guallar J., 2013, “A review of optimized design layouts for solar power tower plants with campo code,” Renew. Sustain. Energy Rev., **20**, pp. 142–154.

[43] Leonardi E., and D’Aguanno B., 2011, “CRS4-2: A numerical code for the calculation of the solar power collected in a central receiver system,” Energy, **36**(8), pp. 4828–4837.

[44] Benammar S., Khellaf A., and Mohammedi K., 2014, “Contribution to the modeling and simulation of solar power tower plants using energy analysis,” Energy Convers. Manag., **78**, pp. 923–930.

[45] Kribus a., Zaibel R., Carey D., Segal a., and Karni J., 1998, “A solar-driven combined cycle power plant,” Sol. Energy, **62**(2), pp. 121–129.

[46] Spelling J., Favrat D., Martin A., and Augsburger G., 2011, “Thermoeconomic optimization of a combined-cycle solar tower power plant,” Energy, **41**(1), pp. 1–8.

[47] Xu C., Wang Z., Li X., and Sun F., 2011, “Energy and exergy analysis of solar power tower plants,” Appl. Therm. Eng., **31**(17-18), pp. 3904–3913.

[48] Reddy V. S., Kaushik S. C., and Tyagi S. K., 2014, “Exergetic analysis and economic evaluation of central tower receiver solar thermal power plant,” Int. J. Energy Res., **38**(10), pp. 1288–1303.

[49] Agrawal S. K., Kumar R., and Khaliq A., 2014, “First and second law investigations of a new solar-assisted thermodynamic cycle for triple effect refrigeration,” Int. J. Energy Res., **38**(2), pp. 162–173.

[50] Sheu E. J., and Mitsos A., 2013, “Optimization of a hybrid solar-fossil fuel plant: Solar steam reforming of methane in a combined cycle,” Energy, **51**, pp. 193–202.

[51] Yao Z., Wang Z., Lu Z., and Wei X., 2009, “Modeling and simulation of the pioneer 1MW solar thermal central receiver system in China,” Renew. Energy, **34**(11), pp. 2437–2446.

[52] Yu Q., Wang Z., and Xu E., 2014, “Analysis and improvement of solar flux distribution inside a cavity receiver based on multi-focal points of heliostat field,” Appl. Energy, **136**, pp. 417–430.

[53] Avila-Marin A. L., Fernandez-Reche J., and Tellez F. M., 2013, "Evaluation of the potential of central receiver solar power plants: Configuration, optimization and trends," Appl. Energy, **112**, pp. 274–288.

[54] Peng S., Hong H., Wang Y., Wang Z., and Jin H., 2014, "Off-design thermodynamic performances on typical days of a 330MW solar aided coal-fired power plant in China," Appl. Energy, **130**, pp. 500–509.

[55] Le Moullec Y., 2013, "Conceptual study of a high efficiency coal-fired power plant with CO2 capture using a supercritical CO2 Brayton cycle," Energy, **49**, pp. 32–46.

[56] Niu X.-D., Yamaguchi H., Zhang X.-R., Iwamoto Y., and Hashitani N., 2011, "Experimental study of heat transfer characteristics of supercritical CO2 fluid in collectors of solar Rankine cycle system," Appl. Therm. Eng., **31**(6-7), pp. 1279–1285.

[57] Zhang X. R., Yamaguchi H., Uneno D., Fujima K., Enomoto M., and Sawada N., 2006, "Analysis of a novel solar energy-powered Rankine cycle for combined power and heat generation using supercritical carbon dioxide," Renew. Energy, **31**(12), pp. 1839–1854.

[58] Yamaguchi H., Zhang X. R., Fujima K., Enomoto M., and Sawada N., 2006, "Solar energy powered Rankine cycle using supercritical CO2," Appl. Therm. Eng., **26**(17-18), pp. 2345–2354.

[59] Zhang X. R., and Yamaguchi H., 2008, "An experimental study on evacuated tube solar collector using supercritical CO2," Appl. Therm. Eng., **28**(10), pp. 1225–1233.

[60] Niu X.-D., Yamaguchi H., Iwamoto Y., and Zhang X.-R., 2013, "Optimal arrangement of the solar collectors of a supercritical CO2-based solar Rankine cycle system," Appl. Therm. Eng., **50**(1), pp. 505–510.

[61] Zhang X.-R., Yamaguchi H., and Uneno D., 2007, "Experimental study on the performance of solar Rankine system using supercritical CO2," Renew. Energy, **32**(15), pp. 2617–2628.

[62] Wright S., Conboy A., Parma E., Lewis T., Rochau G., and Suo-Anttila A., 2011, "Summary of the Sandia supercritical CO2 development program," Proceedings of the Supercritical CO2 Power Cycle Symposium 2011, May 24-25, Boulder, Colorado, USA.

[63] Iverson B. D., Conboy T. M., Pasch J. J., and Kruizenga A. M., 2013, "Supercritical CO2 Brayton cycles for solar-thermal energy," Appl. Energy, **111**, pp. 957–970.

[64] Singh R., Miller S. A., Rowlands A. S., and Jacobs P. A., 2013, "Dynamic characteristics of a direct-heated supercritical carbon-dioxide Brayton cycle in a solar thermal power plant," Energy, **50**, pp. 194–204.

[65] Singh R., Rowlands A. S., and Miller S. A., 2013, "Effects of relative volume-ratios on dynamic performance of a direct-heated supercritical carbon-dioxide closed Brayton cycle in a solar-thermal power plant," Energy, **55**, pp. 1025–1032.

[66] Singh R., Kearney M. P., and Manzie C., 2013, "Extremum-seeking control of a supercritical carbon-dioxide closed Brayton cycle in a direct-heated solar thermal power plant," Energy, **60**, pp. 380–387.

[67] Chapman D. J., and Arias D. A., 2009, "An Assessment of the Supercritical Carbon Dioxide Cycle for Use in a Solar Parabolic Trough Power Plant," Proceedings of SCCO2 Power Cycle Symposium 2009, April 29-30, Troy, NY, USA.

[68] Turchi C., 2009, "Supercritical CO2 for application in concentrating solar power systems," Proceedings of SCCO2 Power Cycle Symposium 2009, April 29-30, Troy, NY, USA.

[69] Ma Z., and Turchi C. S., 2011, "Advanced Supercritical Carbon Dioxide Power Cycle Configurations for Use in Concentrating Solar Power Systems," Proceedings of the Supercritical CO2 Power Cycle Symposium 2011, May 24-25, Boulder, Colorado, USA.

[70] Garg P., Kumar P., and Srinivasan K., 2013, "Supercritical carbon dioxide Brayton cycle for concentrated solar power," J. Supercrit. Fluids, **76**, pp. 54–60.

[71] Chacartegui R., Muñoz de Escalona J. M., Sánchez D., Monje B., and Sánchez T., 2011, "Alternative cycles based on carbon dioxide for central receiver solar power plants," Appl. Therm. Eng., **31**(5), pp. 872–879.

[72] Liu M., Belusko M., Steven Tay N. H., and Bruno F., 2014, "Impact of the heat transfer fluid in a flat plate phase change thermal storage unit for concentrated solar tower plants," Sol. Energy, **101**, pp. 220–231.

[73] Gil A., Medrano M., and Martorell I., 2010, "State of the art on high temperature thermal energy storage for power generation. Part 1—Concepts, materials and modellization," … Sustain. Energy …, **14**(1), pp. 31–55.

[74] Medrano M., Gil A., and Martorell I., 2010, "State of the art on high-temperature thermal energy storage for power generation. Part 2—Case studies," … Sustain. Energy …, **14**(1), pp. 56–72.

[75] Kuravi S., Trahan J., Goswami D. Y., Rahman M. M., and Stefanakos E. K., 2013, “Thermal energy storage technologies and systems for concentrating solar power plants,” Prog. Energy Combust. Sci., **39**(4), pp. 285–319.

[76] Tian Y., and Zhao C. Y., 2013, “A review of solar collectors and thermal energy storage in solar thermal applications,” Appl. Energy, **104**, pp. 538–553.

[77] Zaversky F., García-Barberena J., Sánchez M., and Astrain D., 2013, “Transient molten salt two-tank thermal storage modeling for CSP performance simulations,” Sol. Energy, **93**, pp. 294–311.

[78] Yang Z., and Garimella S. V, 2010, “Thermal analysis of solar thermal energy storage in a molten-salt thermocline,” Sol. Energy, **84**(6), pp. 974–985.

[79] Yang Z., and Garimella S. V, 2013, “Cyclic operation of molten-salt thermal energy storage in thermoclines for solar power plants,” Appl. Energy, **103**, pp. 256–265.

[80] Rovira A., Montes M. J., Valdes M., and Martínez-Val J. M., 2011, “Energy management in solar thermal power plants with double thermal storage system and subdivided solar field,” Appl. Energy, **88**(11), pp. 4055–4066.

[81] Powell K. M., and Edgar T. F., 2012, “Modeling and control of a solar thermal power plant with thermal energy storage,” Chem. Eng. Sci., **71**, pp. 138–145.

[82] Heller L., and Gauché P., 2013, “Modeling of the rock bed thermal energy storage system of a combined cycle solar thermal power plant in South Africa,” Sol. Energy, **93**, pp. 345–356.

[83] Wagner S. J., and Rubin E. S., 2012, “Economic implications of thermal energy storage for concentrated solar thermal power,” Renew. Energy.

[84] Duffie J. A., and Beckman W. A., 2013, Solar Engineering of Thermal Processes, John Wiley & Sons, Inc., Hoboken, NJ, USA.

[85] Pacheco J. E., Reilly H. E., Kolb G. J., and Tyner C. E., 2000, “Summary of the Solar Two test and evaluation program,” Proceding of the Renewable Energy for the New Millenium, pp. 1–11.

[86] Leary P. L., and Hankins J. D., 1979, “User’s guide for MIRVAL: a computer code for comparing designs of heliostat-receiver optics for central receiver solar power plants,” SAND-77-8280, p. 14.

[87] Collado F., and Guallar J., 2009, “Design of solar tower Plants heliostat by heliostat: the blocking Factor,” SolarPACES, Berlin, Germany, pp. 15–18.

[88] Collado F., 2011, “Design of solar tower plants heliostat by heliostat: the shadowing and blocking factor,” SolarPACES, Granada, Spain, pp. 20–23.

[89] Guo M., and Wang Z., 2011, “On the analysis of an elliptical Gaussian flux image and its equivalent circular Gaussian flux images,” Sol. Energy, **85**, pp. 1144–1163.

[90] Collado F. J., 2010, “One-point fitting of the flux density produced by a heliostat,” Sol. Energy, **84**(4), pp. 673–684.

[91] Abido M. A., and Al-Ali N. A., 2009, “Multi-objective differential evolution for optimal power flow,” 2009 International Conference on Power Engineering, Energy and Electrical Drives, IEEE, pp. 101–106.

[92] Price K. V., Storn R. M., and Lampinen J. A., 2005, Differential Evolution: A Practical Approach to Global Optimization, Springer.

[93] Storn R., and Price K., 1997, “Differential Evolution – A Simple and Efficient Heuristic for global Optimization over Continuous Spaces,” J. Glob. Optim., **11**(4), pp. 341–359.

[94] Vesterstrom J., and Thomsen R., 2004, “A comparative study of differential evolution, particle swarm optimization, and evolutionary algorithms on numerical benchmark problems,” Proceedings of the 2004 Congress on Evolutionary Computation (IEEE Cat. No.04TH8753), IEEE, pp. 1980–1987.

[95] Das S., and Suganthan P. N., 2011, “Differential Evolution: A Survey of the State-of-the-Art,” IEEE Trans. Evol. Comput., **15**(1), pp. 4–31.

[96] Al-Ismail F. S., and Abido M. A., 2011, “The impact of STATCOM based stabilizers on Power System Stability, using intelligent computational optimization approach,” 2011 IEEE PES Innovative Smart Grid Technologies, IEEE, pp. 1–13.

[97] Klein S. A., 1977, “Calculation of monthly average insolation on tilted surfaces,” Sol. Energy, **19**(4), pp. 325–329.

[98] Segal A., and Epstein M., 1999, “Comparative performances of `tower-top’ and `tower-reflector' central solar receviers,” Sol. Energy, **65**(4), pp. 207–226.

[99] Klein S. A., “Engineering equation solver,” F-Chart Software, Madison, WI.

[100] Moisseytsev A., and Sienicki J., 2008, “Performance improvement options for the supercritical carbon dioxide brayton cycle,” Argonne Natl. Lab. ANL-GenIV-103.

[101] Cengel Y. A., 2006, Heat and Mass Transfer - A Practical Approach, McGraw-Hill, New York, USA.

[102] Collado F. J., 2008, “Quick evaluation of the annual heliostat field efficiency,” Sol. Energy, **82**(4), pp. 379–384.

[103] “Surface meterology and Solar energy” [Online]. Available: https://eosweb.larc.nasa.gov/cgi-bin/sse/sse.cgi?skip@larc.nasa.gov.

VITAE

Name :Maimoon Atif

Nationality :Pakistani

Date of Birth :3/30/1990

Address :P.I.S., P.O.Box. 1439, Al-Khobar, 31952, Saudi Arabia

Email address :maimoonatif@kfupm.edu.sa

maimoonatif@hotmail.com

Educational Qualification

M.Sc. Mechanical Engineering

October, 2014

King Fahd University of Petroleum and Minerals,

Dhahran, Saudi Arabia

B.Sc. Mechanical Engineering

June, 2012

University of Engineering and Technology,

Lahore, Pakistan

Thesis Contribution

Journal Papers

1. Development of a mathematical model for optimizing a heliostat field layout using differential evolution method.
2. Optimization of heliostat field layout in solar central receiver systems on annual basis using differential evolution algorithm.
3. Performance comparison of different supercritical carbon dioxide Brayton cycles integrated with a solar power tower.
4. Performance analysis of solar tower power plants driven supercritical carbon dioxide recompression cycles for six different locations in Saudi Arabia.
5. Performance analysis of recompression Brayton cycles integrated with solar thermal power tower systems under different thermal storage options.

Conference papers

1. M. Atif and F. A. Al-Sulaiman, “Performance analysis of supercritical CO_2 Brayton cycles integrated with solar central receiver system”, IEEE IREC, Hammamet Tunisia, 25 - 27th March, 2014. (Published)
2. M. Atif and F. A. Al-Sulaiman, “Time instant optimization of a heliostat field using a heuristic algorithm”, ASME, Boston USA, 30th June - 2nd July, 2014. (Published)